DYNAMIC SIMULATION AND CONTROL DESIGN TOOLS FOR HEAT PUMP SYSTEMS

A Dissertation

by

CHAO WANG

Submitted to the Office of Graduate and Professional Studies of
Texas A&M University
in partial fulfillment of the requirements for the degree of

DOCTOR OF PHILOSOPHY

Chair of Committee,	Bryan Rasmussen
Committee Members,	Partha Mukherjee
	Sivakumar Rathinam
	Wei Zhan
Head of Department,	Andreas Polycarpou

August 2016

Major Subject: Mechanical Engineering

ABSTRACT

In heating, ventilating, and air conditioning applications, heat pump systems are devices that provide cooling and heating to residential and commercial buildings. Control-oriented models and control tools are essential to meet load requirements and to maximize coefficient of performance. The main challenges include complex system nonlinearities and multivariable interactions.

This dissertation presents dynamic modeling and control design tools for heat pump systems. The first part introduces the dynamic modeling and development of a graphical user interface. The system-level dynamic model is developed based on component models, including compressors, expansion valves, finite control volume heat exchangers, etc. Validation results show that the models are effective tools to capture the dynamic characteristics in cooling, heating, and defrosting modes. A graphical user interface is developed for the dynamic models to facilitate parameter inputs and to generate steady-state operating conditions.

The second part introduces energy optimal control and intelligent defrost control. Three energy optimal control algorithms are proposed: single-input, single-output control with fan scheduling; multiple single-input, single-output control; and multi-input, multi-output control. These strategies, with varying levels of complexity, range from decoupled proportional-integral-derivative control to linear quadratic Gaussian multivariable control. Validation results show that all three algorithms are effective for heat pump control. The goal of the intelligent defrost control is to maximize both system efficiency and human comfort during defrosting cycles. Experimental results show that there exists an optimal combination of frost growth time and defrost termination temperature. Under a higher moisture rate or lower ambient temperature, the optimal frost growth time becomes more sensitive.

DEDICATION

To my parents.

ACKNOWLEDGEMENTS

I would like to thank my advisor, Professor Bryan Rasmussen, for his excellent mentoring and financial support. Four years' research experience in Dr. Rasmussen's group is valuable and unforgettable for me. I learned not only knowledge but also the right attitude toward research. Thank my committee members, Professors Partha Mukherjee, Sivakumar Rathinam, and Wei Zhan, for their guidance and support throughout the course of this research.

I want to thank all members at the Thermo-Fluids Control Lab. Thanks to Shuangshuang Liang and Eric Rodriguez for their instructions. Thanks also go to my friends and colleagues at Texas A&M University. I also want to extend my gratitude to Emerson Climate Technologies for the financial and technical support.

Finally, thanks to my parents for their encouragement and love.

NOMENCLATURE

A	Area
c	Coefficient
dfr	Defrost
D	Hydraulic Diameter
E	Expectation Operator
fr	Frost
h	Enthalpy
L	Length
$m/\dot{m}$	Mass/Mass Flow Rate
P	Pressure
Q	Cooling Capacity/Heating Capacity/Weighting Matrix
r	Refrigerant
RH	Relative Humidity
t	Time
T	Temperature
u	Control Signal
U	Internal Energy
UA	UA value
V/v	Volume/Valve

W/w	Power consumption/Water Vapor
x	Quality

Greek Letters

α	Heat Transfer Coefficient
ε	Human Discomfort
ρ	Density
η	Inverse Efficiency
ω	Compressor Speed
τ	Transport Delay

Subscripts

$1, 2, 3$ ...	First, Second, Third…
acc	Accumulator
amb	Ambient
$adia$	Adiabatic
cc	Charge Compensator
$comp$	Compressor
cs	Cross Section
dp	Dew Point
ex	Exterior
in	Inlet/Interior

n	Number of Control Volume
out	Outlet
r	Refrigerant
$tran$	Transitional
vol	Volumetric
w	Wall/Water

TABLE OF CONTENTS

Page

LIST OF FIGURES

LIST OF TABLES

Page

1. INTRODUCTION AND LITERATURE REVIEW

Heating, venting, and air conditioning (HVAC) systems provide thermal comfort and acceptable indoor air quality by adjusting temperature and relative humidity. HVAC systems are widely used in industrial, commercial, and residential sectors and account for more than 40% of the energy consumed in buildings [1]. Increasing the performance of HVAC systems can lower energy consumption and environmental costs.

Heat Pump Systems

Most heat pump systems run in a vapor compression cycle. The typical cycle has four processes, as shown in Figure 1-1 and Figure 1-2:

1–2 Isentropic compression in a compressor

2–3 Isobaric heat rejection in a condenser

3–4 Isenthalpic throttling in an expansion valve

4–1 Isobaric heat absorption in an evaporator

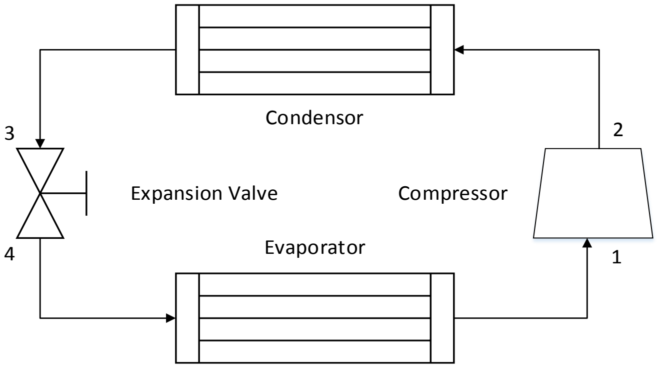

Figure 1-1 Vapor compression system.

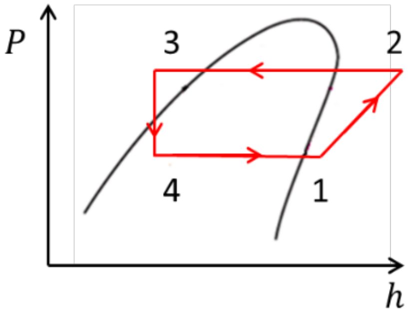

Figure 1-2 P-h diagram of vapor compression cycle.

Heat pump systems have four basic components and accessories. The four basic components are compressor, condenser, expansion valve, and evaporator. Typical accessories include accumulator, charge compensator, fans, pipes, and reversing valve. Figure 1-3 and Figure 1-4 show the schematics of a typical heat pump system running in cooling and heating modes. During cooling mode, the indoor (ID) heat exchanger works as an evaporator while the outdoor (OD) heat exchanger works as a condenser. During heating mode, the ID heat exchanger works as a condenser while the OD heat exchanger works as an evaporator.

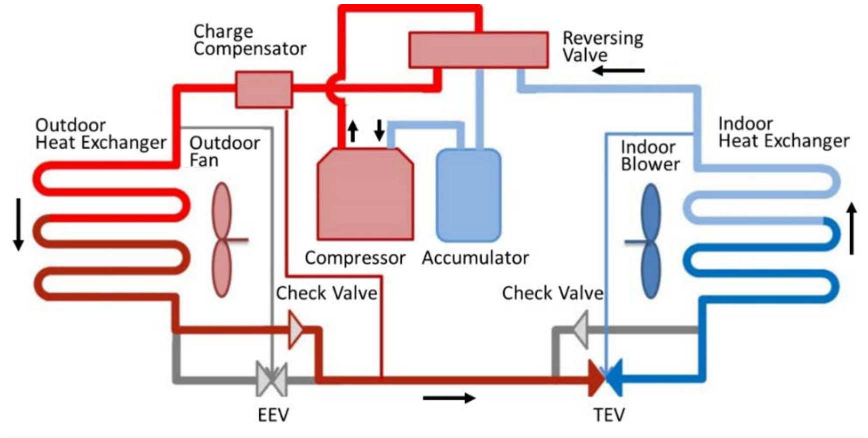

Figure 1-3 Schematic of a typical heat pump system in cooling mode.

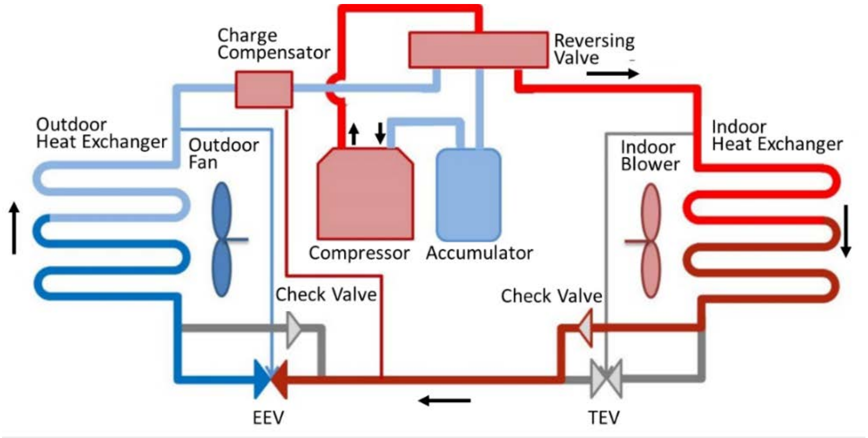

Figure 1-4 Schematic of a typical heat pump system in heating mode.

Literature Review

Dynamic Modeling of Heat Pump Systems

Studies on dynamic modeling of heat pump systems have made significant progress. Static relationships between refrigerant mass flow rate and outlet enthalpy are usually applied for compressor models [2, 3]. Thermal expansion valves (TXVs) and electronic expansion valves (EXVs) are two common types of valves used in HVAC systems. Different models have been presented for TXVs, such as a linear model [4], fourth-order model [5], and first-order model [6]. For EXVs, studies are mainly related to superheat control algorithm design.

Heat exchangers have higher complexities and slower thermal dynamics compared with compressors and expansion valves. The moving boundary (MB) model and finite control volume (FCV) model are widely applied for heat exchanger modeling [7, 8].

The MB approach captures the dynamics of fluid phase regions by dividing heat exchangers into different zones [9-15]. This approach minimizes the number of differential equations and computational costs. A fixed number of zones could limit the operating ranges. Zhang et al. [10] developed an MB model with a time-variant mean void fraction to improve robustness. McKinley et al. [9] developed a nonlinear switched heat exchanger model using the MB method to improve accuracy and robustness. The switched MB heat exchanger model was modified by Li et al. [15]. Validation results show that the dynamic model can predict dynamics during the shut-down and start-up processes. Compared with MB approaches, FCV approaches have higher accuracy and robustness, as well as higher computational cost [16]. Many researches on FCV models have been presented [17-21].

Condensation is a common phenomenon for heat pump systems running in cooling mode. Different models have been developed to study heat transfer performance and dynamic characteristics of heat exchangers with condensation [22-24].

Defrost Cycle Modeling

Air-source heat pump systems operating under cold-moist conditions have frost formation on OD units when the surface temperature is lower than the dewpoint and below 0℃. Frost accumulation leads to higher pressure drop [25], less air flow rate, and lower heat transfer performance [26-28]. The outdoor heat exchanger must be defrosted periodically.

A reverse defrosting cycle is commonly used to defrost by switching the system from heating mode to cooling mode. Studies on modeling defrosting cycles can be divided into two parts: frost growth and frost melting. Frost growth models usually focus on three aspects: frost properties, factors affecting frost formation, and system performance under frosting conditions. Sami et al. [29] developed a model to calculate frost thickness and frost density for flat surfaces and showed that higher relative humidity or lower surface temperature accelerates frost formation. Sherif et al. [30] developed a differential continuous model and calculated frost thickness and surface temperature for flat plates operating under forced convection. Kondepudi et al. [31] described an analytical model and predicted frost accumulation and its effects on heat exchanger performance. Yao et al. [32] and Seker et al. [33] reported frost formation under different air inlet temperatures, humidities, flow rates, and refrigerant temperatures, as well as the effects of frost on total conductivity of heat exchangers. Chen et al. [34] studied the blockage of air flow and air side pressure drop resulting from frost growth. Tso et al. [35] and Padhmanabhan et al. [36] presented nonuniform frost models to predict heat exchanger performance.

Different models have been developed for the frost melting process. Krakow et al. [37] developed a hot-gas defrosting model with four stages: preheating, melting, vaporizing, and dry heating. Dopazo et al. [38] reported a transient simulation model of a hot-gas defrosting model with six stages: preheating, tube frost melting start, fin frost melting start, air presence, tube-fin water film, and dry heating. Qu et al. [39] presented a model including three stages: frost melting without water flow, frost melting with water flow, and water layer vaporizing. The effects on defrosting performance of downward-flowing melted frost along a multicircuit outdoor coil surface were analyzed. Hoffenbecker et al. [40] developed a transient model for predicting heat and mass transfer effects and time required for frost melting.

Control of Heat Pump Systems

Control design for heat pump systems aims to meet the heating or cooling load requirement, maximize efficiency, and prevent component damage. Hence, both capacity control and superheat control are widely studied. Actuators of typical heat pump systems include compressor, expansion valve, ID blower, OD fan, and reversing valve. The compressor and expansion valve are widely used as control signals for cooling/heating capacity control and superheat control [41-43]. Limited researches show that fan speed is also used for superheat control [44] and for improving system efficiency [45].

Both single-input, single-output (SISO) and multi-input, multi-output (MIMO) controllers are widely applied in vapor compression systems. Common SISO control pairings include compressor speed–evaporator pressure, expansion valve opening–superheat, etc. The basic type is proportional-integral-derivative (PID) or proportional-integral (PI) control. The drawback of the above SISO controllers is obvious when inherent cross-coupling exists [44]. Because heat pump systems are highly coupled systems with nonlinearities, interactions among traditional control pairings cause a decrease in performance and reliability [46]. Systems nonlinearities can change system behaviors significantly, leading to researchers proposing adaptive, predictive, or auto-tuning approaches to control design [47-53].

Researches on SISO control include advanced control schemes and decentralized feedback structures using relative gain array (RGA). The cascaded control algorithm has been verified as an effective way of eliminating the system nonlinearities of HVAC systems [50, 54]. The outer loop uses a PI controller to track the superheat setpoint while the inner loop uses a proportional controller to track the pressure setpoint generated by the outer loop. Keir et al. [55] tested a decentralized control approach for compressor speed using the difference between the condenser and evaporator pressure as the feedback. Jain et al. [56, 57] proposed decentralized feedback structures containing three unconventional input/output control pairings: the expansion valve with average system pressure, the compressor speed with differential pressure, and the evaporator fan speed with average evaporator temperature. The new control strategy gave a better tracking performance.

MIMO control is considered an effective approach to eliminate the limits on SISO control and increase system performance [58-62]. Common types of multivariable control include linear quadratic regulator (LQR) control [44], linear quadratic Gaussian (LQG) control, $\mathcal{H}_\infty$ control [41, 63, 64], model predictive control [65, 66], etc.

The LQG method has been widely applied for vapor compression systems. He et al. [67] designed MIMO feedback control for superheat and evaporating temperature. Experimental results show that the system performance can be improved. Keir [42] developed LQG control for superheat and evaporator pressure. Schurt et al. [68] designed a LQG control algorithm for evaporator superheat and cooling capacity. Validation results also show that LQG control performed well for both reference tracking and disturbance rejection. LQG has also been used to control room temperature and humidity by adjusting the compressor speed and ID fan speed [69].

$\mathcal{H}_\infty$ control has also been applied for HVAC systems. Rasmussen [37] designed an $\mathcal{H}_\infty$ control that coordinates cooling capacity and superheat. $\mathcal{H}_\infty$ control has been proved to be an effective method for improving the performance of HVAC systems [38].

Defrosting Control

Defrosting technologies include the reverse cycle defrosting[39, 70-73], hot gaseous refrigerant [40, 74], electric resistance heating [75-77], sensible heat defrost [78], compressor shut-down defrosting [79], etc. The reverse cycle defrosting is the most widely used method. Defrost is triggered and terminated by switching the direction of the refrigerant flow in heat pump systems. Parameters used to evaluate defrosting cycles include average Coefficient of Performance (COP) during the frosting and defrosting [80], defrosting efficiency [73, 81], thermal comfort (predicted mean vote [82] and predicted percentage dissatisfied [83], etc. Zakrzewski et al. [81] defined the defrost efficiency as the ratio of energy used for frost melting and total energy input. The control logic for the reverse cycle in industries is based on fixed timing schedules, defrost thermostat, or a combination of the two. The time points at which to trigger and terminate defrosting are critical for system efficiency and human comfort [80, 84]. Usually the time points depend on a lot of parameters, including ambient temperature, air relative humidity, air flow rate, heat exchanger properties, compressor speed, ([85], [86], etc.

Researchers have proposed many methods to trigger and terminate defrost. Muller et al. [87] proposed a fan power sending method. Jiang et al. [88] reported a defrosting method based on superheat. The basic idea is to trigger defrosting when the fluctuation of superheat is higher than a setpoint estimated based on the data during the first 20 minutes. Frost thickness is also used as a signal to control defrost. Existing technologies include photoelectric technique [89], microscopic image system [90, 91], micrometer [92], photocoupler [93], etc.

Temperature-time (T-T) control is the most widely applied method [81, 94]. The disadvantages of the control logic is that defrosting may be triggered even without frost formation [95]. The disadvantage of the control logic is that defrosting may be triggered without frost formation ([95], [96]). Zhu et al. [97, 98] developed a temperature-humidity-time defrosting control method. A frosting map is created based on a temperature-humidity chart, which contains a nonfrosting region, condensing region, mild frosting zone, moderate frosting zone, and severe frosting zone. The optimal frost growth time of each zone is found experimentally.

Organization of Dissertation

This dissertation focuses on dynamic modeling, control design and validation, intelligent defrost control, and graphical user interface (GUI) development for heat pump systems. Chapter 2 presents the development of dynamic models for heat pump systems. Chapter 3 describes the GUI development. Chapter 4 shows the experimental setup. Chapter 5 introduces the model validation based on the experimental data. Chapter 6 and Chapter 7 show the energy-optimal control design and validation. Chapter 8 shows the defrost control. Conclusions and future work are shown in Chapter 9.

2. DYNAMIC MODEL DEVELOPMENT

This chapter presents dynamic model development for heat pump systems. First, dynamic models of components are introduced, including a heat exchanger model (with accumulator/charge compensator), compressor model, expansion valve model, pipe model, and fan model. Then the dynamic model is built based on the above component models. Model verification is performed to show the step responses of compressor speed, valve opening, room air temperature, and ID air flow rate.

A defrosting model is developed to study system performance and characteristics during defrosting cycles. A defrost cycle is divided into four steps: frost growth stage, switching, defrost stage, and switching back. Frost properties, the influences of frost formation on system performance, and characteristics during defrosting cycles are presented.

Component Models

Compressor

The compressor is assumed to be a positive displacement system. The refrigerant mass flow rate can be expressed as a function of the compressor speed, displacement, volumetric efficiency, and refrigerant density at the inlet (Equation (2.1)):

$$\dot{m}_{comp} = \omega_{comp} V_{comp} \rho_{comp} \eta_{vol} \tag{2.1}$$

The compression process is assumed to be an adiabatic process with an isentropic efficiency. The outlet enthalpy is given by Equation (2.2), where $h_{out,adia}$ is the outlet enthalpy of an isentropic process.

$$h_{k,out} = \frac{1}{\eta_{adia}}[h_{k,out,adia} + h_{k,in}(\eta_{adia} - 1)] \tag{2.2}$$

Both volumetric efficiency and adiabatic efficiency are interpolated as functions of the pressure ratio and the compressor speed from semi-empirical maps. Figure 2-1 and Figure 2-2 show typical efficiency maps. Both volumetric efficiency and adiabatic efficiency become higher as the compressor speed increases and the pressure ratio decreases.

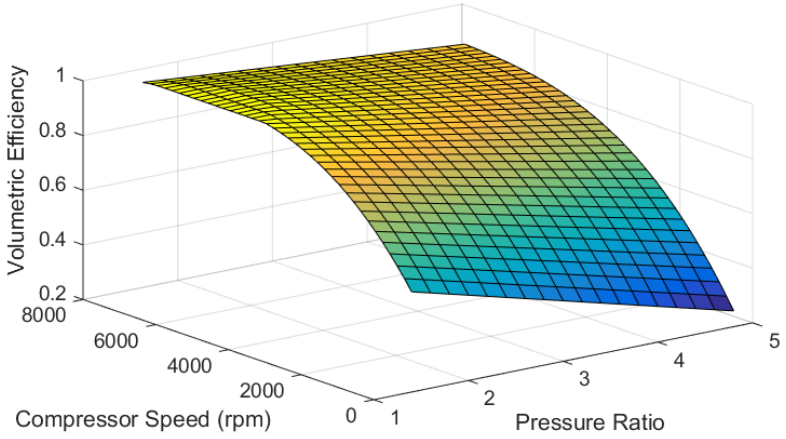

Figure 2-1 Volumetric efficiency map.

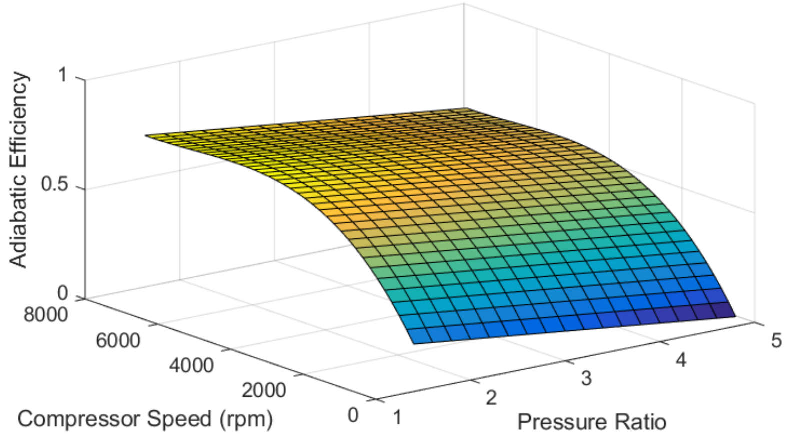

Figure 2-2 Adiabatic efficiency map.

Expansion Valves

TXVs and EXVs are two common types of expansion valves used in heat pump systems. The TXV uses the bulb pressure of a sensing bulb at the outlet of the evaporator to regulate the valve opening, while the EXV uses a step motor to adjust the valve opening. Throttling is assumed to be an isenthalpic process, that is, the outlet enthalpy equals the inlet enthalpy:

$$h_{v,out} = h_{v,in} \tag{2.3}$$

The refrigerant mass flow rate is a function of the pressure differential across the valve and the inlet refrigerant density. The mass flow rate through a TXV is modeled by Equation (2.4). For a specified TXV, c_1 and c_2 are constant.

$$\dot{m}_v = (c_1 + c_2(P_{bulb} - P_{v,out}))\sqrt{\rho_{v,in}(P_{v,in} - P_{v,out})} \tag{2.4}$$

Similarly, the refrigerant mass flow rate through an EXV is given by Equation (2.5), where $A_v C_d$ is the discharge coefficient.

$$\dot{m}_v = A_v C_d \sqrt{\rho_{v,in}(P_{v,in} - P_{v,out})} \tag{2.5}$$

The discharge coefficient is a semi-empirical map that depends on the valve opening and the pressure differential across the valve. (2.6) shows a typical discharge coefficient map. A higher pressure differential or larger valve opening indicates a larger discharge coefficient.

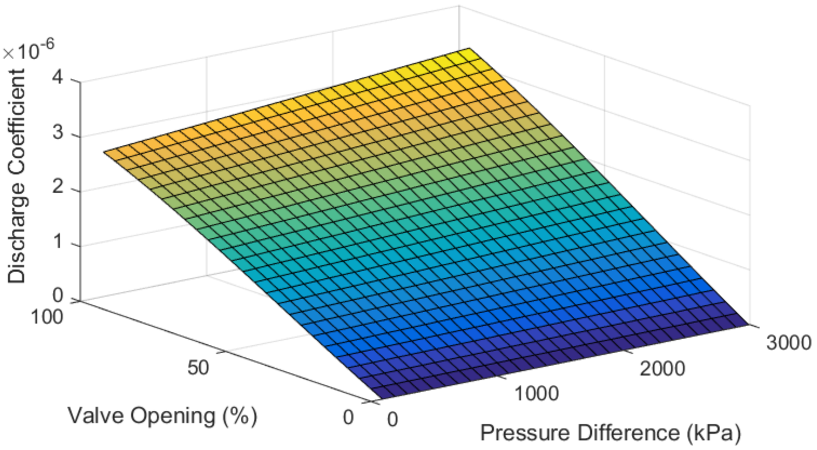

Figure 2-3 Discharge coefficient map.

Heat Exchangers

The FCV approach is widely used to model heat exchangers. A heat exchanger is discretized into n control volumes, and the k^{th} control volume has an internal surface area, $A_{i,k}$, an external surface area, $A_{o,k}$, and a volume, V_k. For a given set of parameters, there exists a minimum threshold for the number of control volumes required to accurately capture dynamics. Figure 2-4 and Figure 2-5 show the evaporator and condenser models, respectively. The evaporator has two-phase and super vapor zones. The condenser has super vapor, two-phase, and subcool liquid zones.

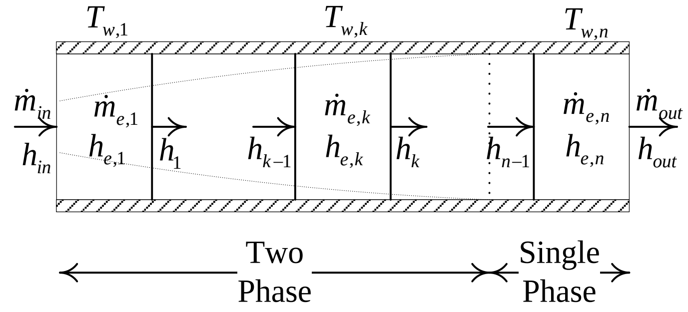

Figure 2-4 FCV model of an evaporator.

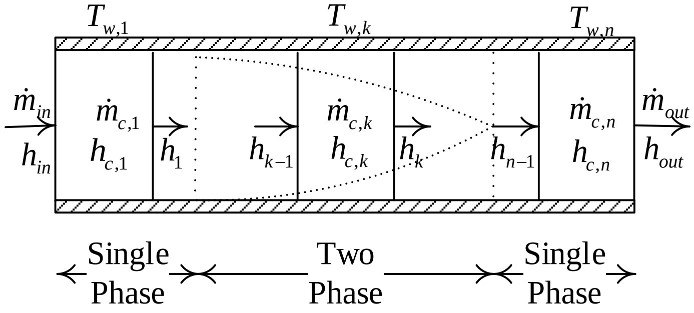

Figure 2-5 FCV model of a condenser.

Here are several modeling assumptions associated with the refrigerant flow in the heat exchanger:

- The heat exchanger is a long, thin, horizontal tube.
- The refrigerant flow through the heat exchanger is modeled as a one-dimensional fluid flow.
- Axial conduction of refrigerant is negligible.

- Pressure drop along the heat exchanger tube due to momentum change in refrigerant and viscous friction is negligible.

The conservation equations for refrigerant mass, refrigerant energy, and wall energy are applied to each control volume:

$$\begin{bmatrix} \dot{U}_1 \\ \vdots \\ \dot{U}_k \\ \vdots \\ \dot{U}_n \end{bmatrix} = \begin{bmatrix} \dot{m}_{in}h_{in} - \dot{m}_1 h_1 + \alpha_{i,1}A_{i,1}(T_{w,1} - T_{r,1}) \\ \vdots \\ \dot{m}_{k-1}h_{k-1} - \dot{m}_k h_k + \alpha_{i,k}A_{i,k}(T_{w,k} - T_{r,k}) \\ \vdots \\ \dot{m}_{n-1}h_{n-1} - \dot{m}_{out}h_n + \alpha_{i,n}A_{i,n}(T_{w,n} - T_{r,n}) \end{bmatrix} \tag{2.6}$$

$$\begin{bmatrix} \dot{m}_1 \\ \vdots \\ \dot{m}_k \\ \vdots \\ \dot{m}_n \end{bmatrix} = \begin{bmatrix} \dot{m}_{in} - \dot{m}_1 \\ \vdots \\ \dot{m}_{k-1} - \dot{m}_k \\ \vdots \\ \dot{m}_{n-1} - \dot{m}_{out} \end{bmatrix} \tag{2.7}$$

$$\begin{bmatrix} \dot{U}_{w,1} \\ \vdots \\ \dot{U}_{w,k} \\ \vdots \\ \dot{U}_{w,n} \end{bmatrix} = \begin{bmatrix} \alpha_{a,1}A_{a,1}(T_{a,1} - T_{w,1}) - \alpha_{r,1}A_{r,1}(T_{w,1} - T_{r,1}) \\ \vdots \\ \alpha_{a,k}A_{a,k}(T_{a,k} - T_{w,k}) - \alpha_{r,k}A_{r,k}(T_{w,k} - T_{r,k}) \\ \vdots \\ \alpha_{a,n}A_{a,n}(T_{a,n} - T_{w,n}) - \alpha_{r,n}A_{r,n}(T_{w,n} - T_{r,n}) \end{bmatrix} \tag{2.8}$$

The governing equations for the heat exchangers can be derived and then given in a state space model, shown in Equation (2.9):

$$Z(x,u)\begin{bmatrix} \dot{P} \\ \dot{h} \\ \dot{m} \\ \dot{T}_w \end{bmatrix} = f(x,u) \tag{2.9}$$

Heat transfer coefficients are calculated based on correlations. The heat transfer coefficient between the refrigerant and the heat exchanger depends on the refrigerant phase. Wattlet's and Chato's method [99] is used for two-phase flow in the evaporator, while the Dobson-Chato correlation [100] is used for two-phase flow in the condenser.

The Gnielinski correlation is used to calculate the heat transfer coefficient for single-phase flow [101]. The heat transfer coefficient between the air and the heat exchanger is calculated with the Colburn J-factor [102].

The pressure drop calculation for single-phase refrigerant flow through a pipe is calculated using the Darcy-Weishbach equation, shown in Equation (2.10), while the pressure drop for two-phase flow is calculated using Wattlet's and Chato's method [99], shown in Equation (2.11).

$$\Delta P = G^2 ff \frac{L}{2000 D\rho} \tag{2.10}$$

$$\mathit{\Delta} P = 2G^2 ff (1 - x_{ri})^2 \frac{L}{1000 D\rho} \mathit{\Phi}_l \tag{2.11}$$

Heat Exchanger with Condensation

When moist air passes through the evaporator, air temperature drops and relative humidity increases. When the air temperature reaches the dewpoint temperature, the relative humidity is 100%. Then, condensation will happen if the temperature of moist air continues decreasing [103]. A typical condensation process is shown in Figure 2-6.

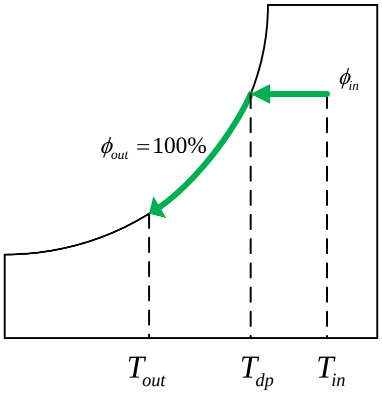

Figure 2-6 Condensation process on the psychrometric chart.

Conservation of mass can be divided into two parts: air and water vapor. Air mass flow rates at the inlet and outlet are always equal because condensation does not affect air balance.

$$\dot{m}_{air,in} = \dot{m}_{air,out} \tag{2.12}$$

Part of the water vapor becomes liquid and drops as condensation occurs. Water vapor mass at the inlet equals the sum of water vapor mass at the outlet and water mass dropping out.

$$\dot{m}_{w,in} = \dot{m}_{w,out} + \dot{m}_{cond} \tag{2.13}$$

Condensation rate can be given by Equation (2.14):

$$\dot{m}_{cond} = \dot{m}_{w,in} - \dot{m}_{w,out} = \dot{m}_{air}(w_{in} - w_{out}) \tag{2.14}$$

Conservation of energy can be expressed as:

$$\begin{aligned} &\dot{m}_{air,in}h_{air,in} + \dot{m}_{w,in}h_{w,in} - \dot{Q} \\ &\quad = \dot{m}_{air,out}h_{air,out} + \dot{m}_{w,out}h_{w,out} + \dot{m}_{cond}h_{l} \end{aligned} \tag{2.15}$$

A typical condensation process has three different conditions: dry, wet, and transitional. Dry means no condensation, and wet means condensation happens. The transitional condition is used to avoid jumps between dry and wet conditions. Table 2-1 lists the descriptions of the three conditions. $\Delta T_{transitional}$ is the temperature range of the transitional zone. When the wall temperature is equal to or higher than the sum of the dewpoint and the temperature difference of the transitional zone, the zone is defined as a dry zone. If the wall temperature is not higher than the dewpoint, the zone is a wet zone. Otherwise, the zone is a transitional zone.

Table 2-1 Condition description for heat exchanger with condensation.

Zone	Description
Dry	$T_{wall} \geq T_{dp} + \Delta T_{transitional}$
Transitional	$T_{dp} < T_{wall} < T_{dp} + \Delta T_{transitional}$
Wet	$T_{wall} \leq T_{dp}$

The dry condition model is developed based on the air side heat transfer coefficient under the dry condition, $\alpha_{\mathrm{air,dry}}$. Fin efficiency and number of heat transfer units (NTUs) are given by Equations (2.16) and (2.17), respectively [104].

$$\eta_{dry} = \frac{tanh\left(\beta_{Ad} L_{FIN\_A}\right)}{\beta_{Ad} L_{FIN\_A}} \tag{2.16}$$

$$NTU_{dry} = \frac{\eta_d \alpha_{air,dry} A_{air}}{\dot{m}_{out} C_p} \tag{2.17}$$

where $\beta_{Ad} = \sqrt{\frac{2\alpha_{air,dry}}{k_{wall} t_{fin}}}$.

Then, the outlet air temperature can be expressed as:

$$T_{ao} = T_{ai} + \frac{1 - exp(-NTU_{dry})}{T_{wall} - T_{ai}} \tag{2.18}$$

The relative humidity and absolute humidity at the outlet can be given by Equations (2.19) and (2.20), respectively.

$$RH_{out,dry} = \frac{101.3\, w_{in}}{(0.622 + w_{in})P_{vapor,dry}} \tag{2.19}$$

$$w_{out,dry} = \frac{0.622 RH_{out,dry}}{101.3 - P_{vapor,dry}} \tag{2.20}$$

Under the wet condition, the air side heat transfer coefficient, α_{ow}, is used to calculate fin efficiency and NTU:

$$\eta_{wet} = \frac{tanh(\beta_{Aw} L_{FIN\_A})}{\beta_{Aw} L_{FIN\_A}} \tag{2.21}$$

$$NTU_{wet} = \frac{\eta_{wet} \alpha_{air,wet} A_{air}}{\dot{m}_{out} C_p} \tag{2.22}$$

where $\beta_{Aw} = \sqrt{\frac{2\alpha_{air,wet}}{k_{wall} t_{fin}}}$.

The absolute humidity at the outlet of the evaporator can be expressed as:

$$w_{out,wet} = w_s + (w_{in} - w_s) exp(-NTU_w) \tag{2.23}$$

The relative humidity at the outlet equals 100%:

$$RH_{out,wet} = 100\% \tag{2.24}$$

The outlet air temperature is given by:

$$T_{ao} = \frac{h_{a\_in} + \left(1 - exp(-NTU_{wet})\right)\left(h_s - h_{a\_in}\right) - 2500.9\, w_{out}}{C_p} \tag{2.25}$$

Parameters for the transitional condition can be expressed as a function of dry and wet conditions. The relative humidity, absolute humidity, and air outlet temperature are given by Equations (2.26), (2.27), and (2.28), respectively.

$$RH_{out,tran} = \frac{T_{wall} - T_{dp}}{\Delta T_{tran}} RH_{out,dry} + \left(1 - \frac{T - T_{dp}}{\Delta T_{tran}}\right) RH_{out,wet} \tag{2.26}$$

$$w_{out,tran} = \frac{T_{wall} - T_{dp}}{\Delta T_{tran}} w_{out,dry} + \left(1 - \frac{T - T_{dp}}{\Delta T T_{tran}}\right) w_{out,wet} \tag{2.27}$$

$$T_{ao,tran} = \frac{T_{wall} - T_{dp}}{\Delta T} T_{ao,dry} + \left(1 - \frac{T - T_{dp}}{\Delta T}\right) T_{ao,wet} \tag{2.28}$$

Heat Exchanger with Accumulator

The accumulator works as a reservoir to prevent liquid from entering into the compressor. Conservation of energy and mass is shown in Equations (2.29) and (2.30), respectively:

$$\dot{U}_{acc} = \dot{m}_{in} h_{acc,in} - \dot{m}_{out} h_{acc,out} - UA_{acc}(T_{acc} - T_{amb}) \tag{2.29}$$

$$\dot{m}_{acc} = \dot{m}_{in} - \dot{m}_{out} \tag{2.30}$$

Usually the accumulator model is lumped with the heat exchanger model. The modified-state space model is shown in Equation (2.31).

$$Z(x,u)\begin{bmatrix} \dot{P} \\ \dot{h} \\ \dot{m} \\ \dot{T}_w \\ \dot{m}_{acc} \end{bmatrix} = f(x,u) \tag{2.31}$$

Charge Compensator

Charge compensators are used to adjust the total amount of refrigerant in heat pump cycles. In cooling mode, refrigerant in charge compensators absorbs heat and pressure becomes higher than liquid line pressure. Then, the refrigerant flows out of the charge compensators. In heating mode, refrigerant in charge compensators loses heat and pressure becomes lower than liquid line pressure. Then, refrigerant flows into the charge compensator. The net effect is that the system uses less charge in heating mode and the whole refrigerant charge in cooling mode.

The refrigerant mass flow rate is assumed to be proportional to the pressure difference between the charge compensator and the liquid line. The governing equations for the charge compensator model are given by:

$$\dot{m}_{cc,in\,/out} = k_{cc} * (P_{cc} - P_{liquidline}) \tag{2.32}$$

$$\frac{d(m_{cc}u_{cc})}{dt} = \dot{m}_{cc,in/out}h_{cc,in/out} - UA_{ex}(T_{cc} - T_{amb}) - UA_{in}(T_{cc} - T_w) \tag{2.33}$$

The state space model is given by Equation (2.34). The elements of matrix $Z(x,u)$ are given in Equation (2.35) for the two-phase condition and (2.36) for a single phase. The elements of matrix $f(x,u)$ are given in Equation (2.37).

$$Z(x,u)\begin{bmatrix}\dot{P}_{cc}\\ \dot{m}_{cc}\end{bmatrix} = f(x,u) \tag{2.34}$$

$$\begin{aligned} Z(x,u) = \Bigg[&\frac{d\rho_g}{dP_c}V_g u_g + \frac{d\rho_f}{dP_f}V_f u_f + \frac{du_g}{dP_c}m_g + \frac{du_f}{dP_c}m_f \\ &- \left(\frac{\rho_g u_g - \rho_f u_f}{\rho_g - \rho_f}\right)\left(\frac{d\rho_g}{dP_c}V_g + \frac{d\rho_f}{dP_c}V_f\right) \qquad \frac{\rho_g u_g - \rho_f u_f}{\rho_g - \rho_f}\Bigg] \end{aligned} \tag{2.35}$$

$$Z(x,u) = \left[\frac{\partial u_{cc}}{\partial P} \bigg|_{\rho} m_{cc} \quad \frac{\partial u_{cc}}{\partial \rho} \bigg|_{P} \rho + u_{cc} \right] \tag{2.36}$$

$$f(x,u) = \begin{bmatrix} \dot{m}_{cc,in/out} h_{cc,in/out} - UA_{ex}(T_{cc} - T_{amb}) - UA_{in}(T_{cc} - T_w) \\ \dot{m}_{cc,in/out} \end{bmatrix} \tag{2.37}$$

Fans

The fan model includes fan power and air flow rate calculations. Two modeling assumptions are (1) the fan follows the Affinity law and (2) fan efficiency is a constant. The fan power is a function of voltage, current, and power factor:

$$P_{fan} = U * I * PF \tag{2.38}$$

The volumetric flow rate is a function of the fan power, rated flow rate, and rated fan power:

$$\dot{V}_{air} = \dot{V}_{air,rated} * \left(\frac{P_{fan}}{P_{fan,rated}} \right)^{\frac{1}{2.5}} \tag{2.39}$$

The mass flow rate is given by Equation (2.40).

$$\dot{m}_{air} = \rho_{air} * \dot{V}_{air} \tag{2.40}$$

Pipes

The pipe model includes pressure drop, parasitic heat gain, and transport delay calculations. Assumptions of the pipe model include the following:

- The pipes are assumed to be long, thin, horizontal tubes.
- The refrigerant flow is considered as one-dimensional flow.
- Axial conduction is negligible.

The pressure drop correlations used in the FCV heat exchanger model are also used for the pipe model. The parasitic heat gain or loss of the pipe is proportional to the temperature difference and the UA value. The heat gain (loss) and the outlet enthalpy are given by:

$$\dot{Q}_{pipe} = (UA)_{pipe}\,(T_{amb} - T_r) \tag{2.41}$$

$$h_{out,pipe} = h_{in,pipe} + \frac{\dot{Q}_{pipe}}{\dot{m}_r} \tag{2.42}$$

Transport delay happens when the refrigerant flows from the inlet to the outlet. The parameter is used to indicate the delay of the calculated outlet enthalpy. The transport delay is given by:

$$\tau = \frac{\rho_r L A_{cs}}{\dot{m}_r} \tag{2.43}$$

Heat Pump Systems

The heat pump cycle can be built based on the above component models. Figure 2-7 shows the parameter transportation among the components. ID and OD air flow rates are given by the ID blower and OD fan model, respectively. With the air side and refrigerant side conditions, the evaporator and the condenser pressures can be obtained based on the heat exchanger models. Then, the refrigerant mass flow rates are calculated with the compressor and expansion valve models once the evaporator and condenser pressures are specified. The outlet refrigerant enthalpy of each model is set as the inlet enthalpy of the next model. When refrigerant flows through pipes, pressure drop, heat gain (loss), and transport delay are calculated.

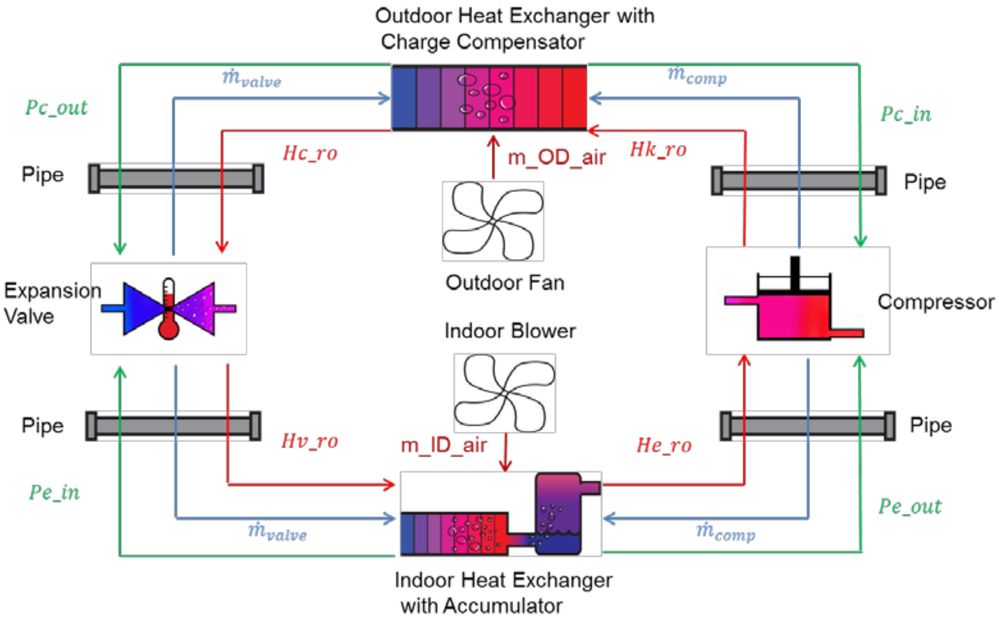

Figure 2-7 Heat pump model (cooling mode).

The refrigerant properties are generated based on REFPROP [105], R410A for example. Figure 2-8 and Figure 2-9 show the enthalpy of superheat vapor and subcool liquid, respectively. The enthalpy is plotted as a function of pressure and temperature.

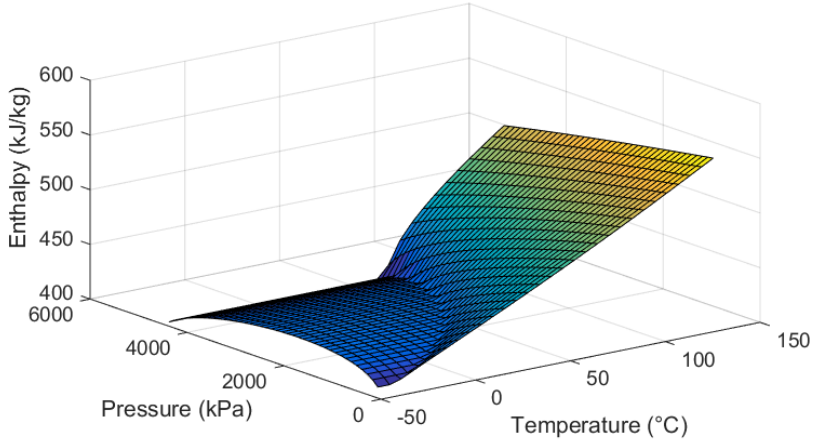

Figure 2-8 Enthalpy of superheat vapor.

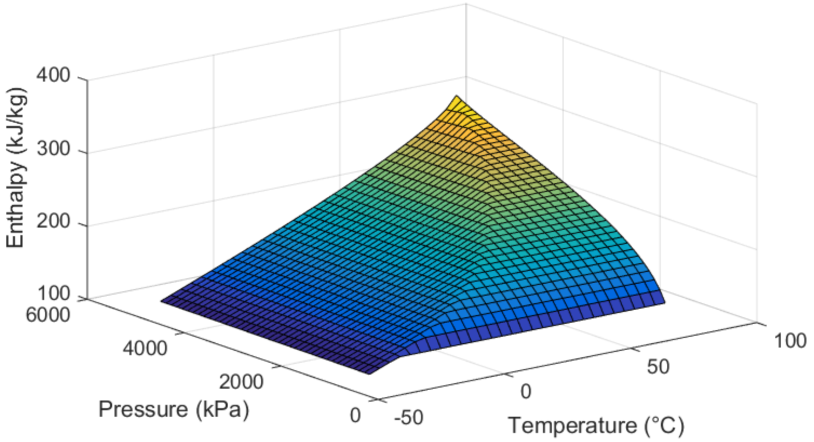

Figure 2-9 Enthalpy of subcool liquid.

Simulation Verification

To illustrate the capabilities of the heat pump model, several dynamic simulation studies are presented. The following verification results are based on a heat pump running in heating mode.

Step Response of the Compressor Speed

Figure 2-10 through Figure 2-13 illustrate the response to the step change in the compressor speed. When compressor speed increases from 1,800 to 2,100 rpm, the operating conditions change until the system reaches a new steady state. Higher compressor speed leads to higher discharge pressure but lower suction pressure, that is, larger pressure difference. The refrigerant mass flow rate through the compressor has a sudden jump and then drops, while the refrigerant mass flow rate through the valve rises. Finally, the two refrigerant mass flow rates equalize. Higher compressor speed also indicates higher superheat.

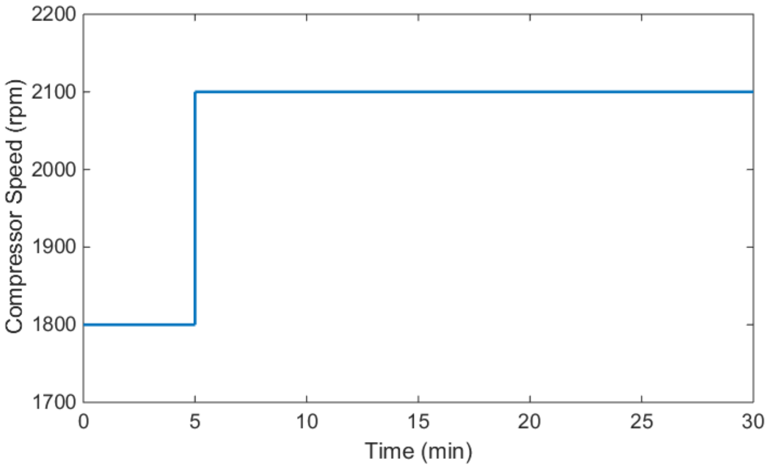

Figure 2-10 Step change of the compressor speed.

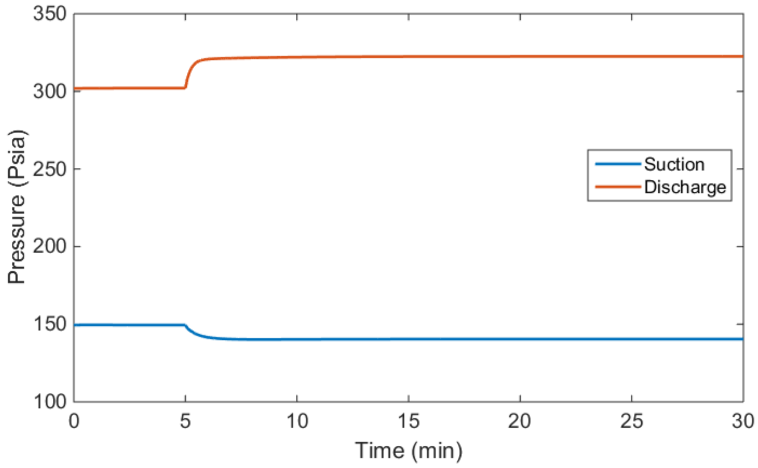

Figure 2-11 Suction and discharge pressure.

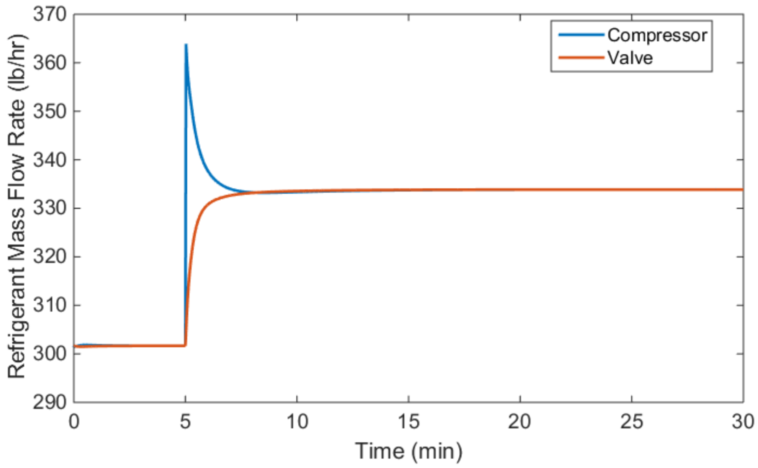

Figure 2-12 Refrigerant mass flow rate.

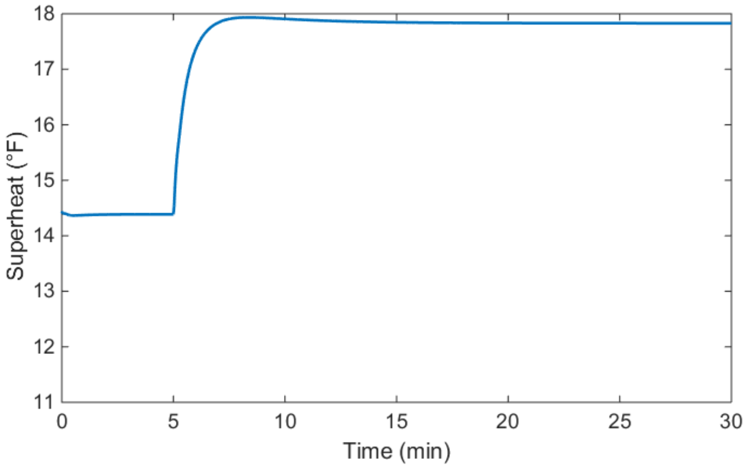

Figure 2-13 Superheat.

Step Response of the EXV Opening

Figure 2-14 through Figure 2-17 show the response to the step change in the EXV opening. When the valve opening increases from 35.6% to 40.6%, the discharge pressure drops while the suction pressure increases. Meanwhile, the refrigerant mass flow rate through the valve has a sudden jump and then drops slowly. The refrigerant mass flow rate through the compressor increases until the two refrigerant mass flow rates equalize. A larger valve opening also leads to smaller superheat.

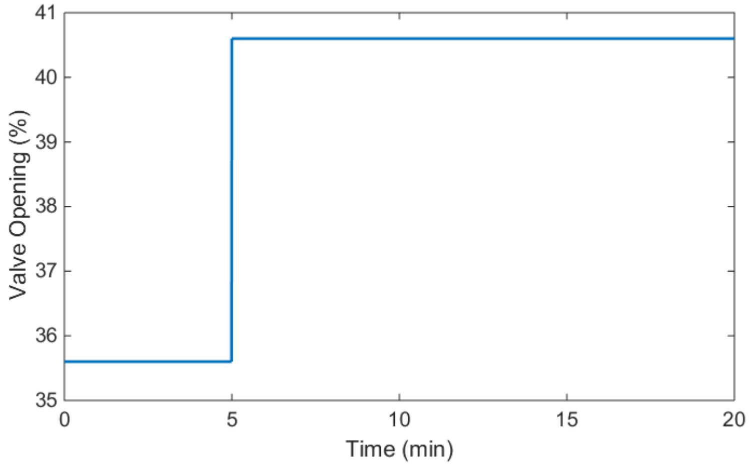

.

Figure 2-14 Step change of the valve opening.

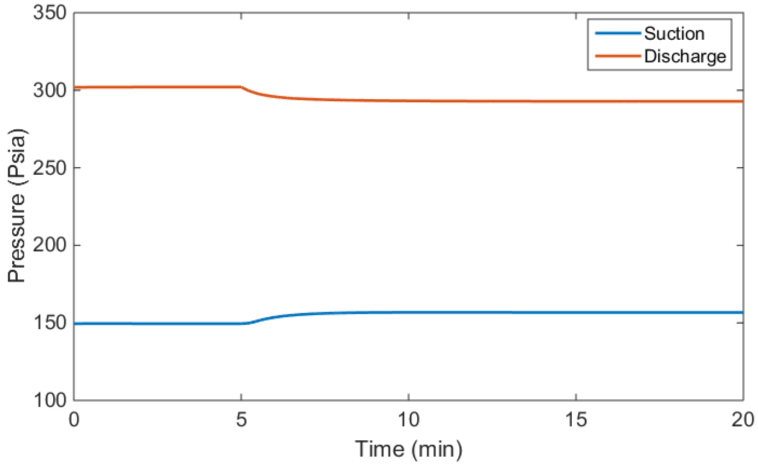

Figure 2-15 Suction and discharge pressure.

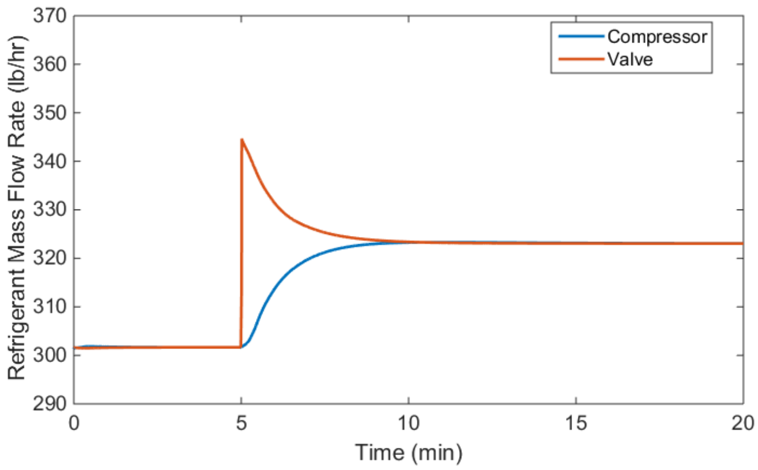

Figure 2-16 Refrigerant mass flow rate.

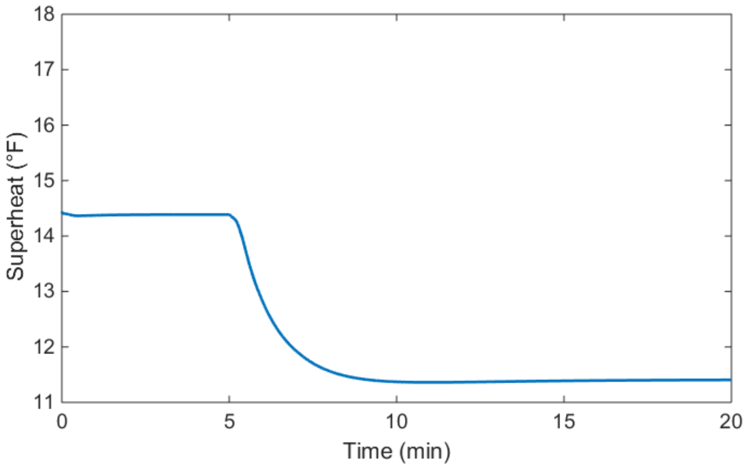

Figure 2-17 Superheat.

Step Response of Air Flow Rate

Figure 2-18 through Figure 2-20 show the step response of the ID air flow rate. Here, the ID heat exchanger works as a condenser. A higher condenser air flow rate leads to a decrease in discharge pressure. The effects of the ID air flow rate on the suction pressure and refrigerant mass flow rate are not significant.

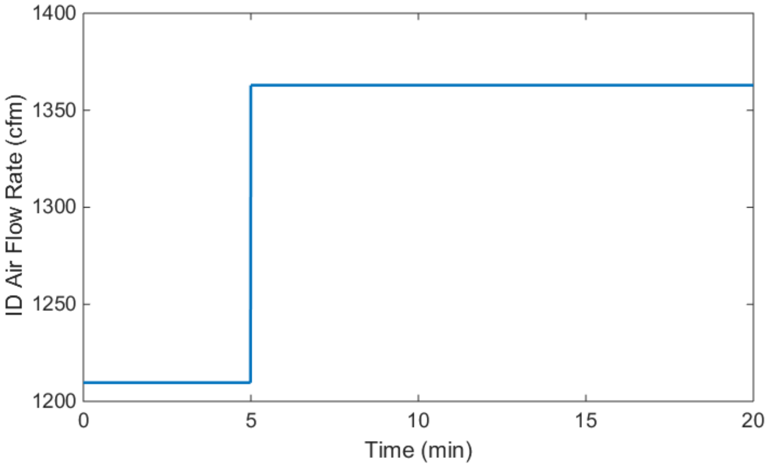

Figure 2-18 Step change of the ID air flow rate.

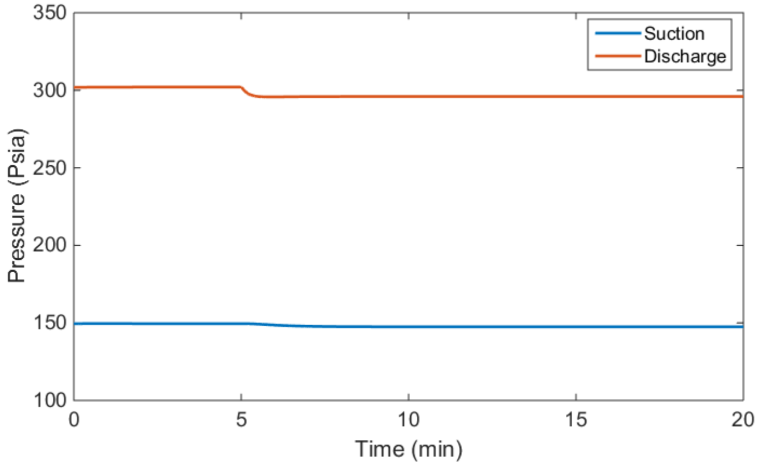

Figure 2-19 Suction and discharge pressure.

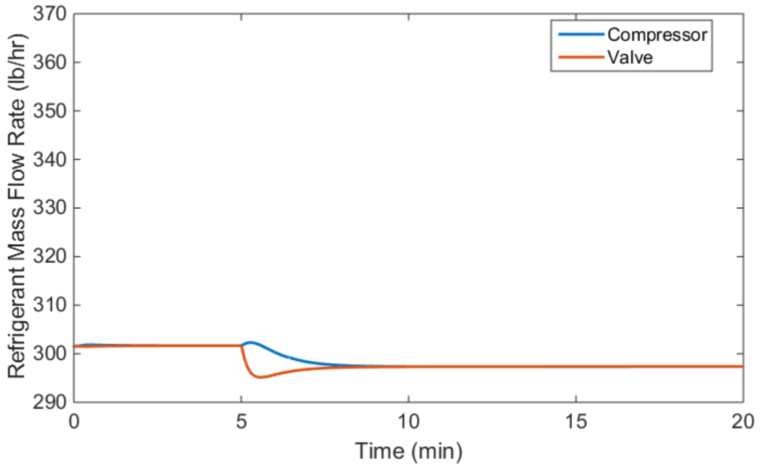

Figure 2-20 Refrigerant mass flow rate.

Step Response of the Inlet Air Temperature

Figure 2-21 through Figure 2-23 illustrate the response to the step change in the ID inlet air temperature. Higher ID inlet air temperature leads to higher discharge pressure because the ID heat exchanger works as a condenser during heating mode. Changing the ID air inlet temperature has minor effects on the suction pressure. When the inlet air temperature increases from 70.9°F to 74.5°F, the refrigerant mass flow rate increases by 8 lb/hr.

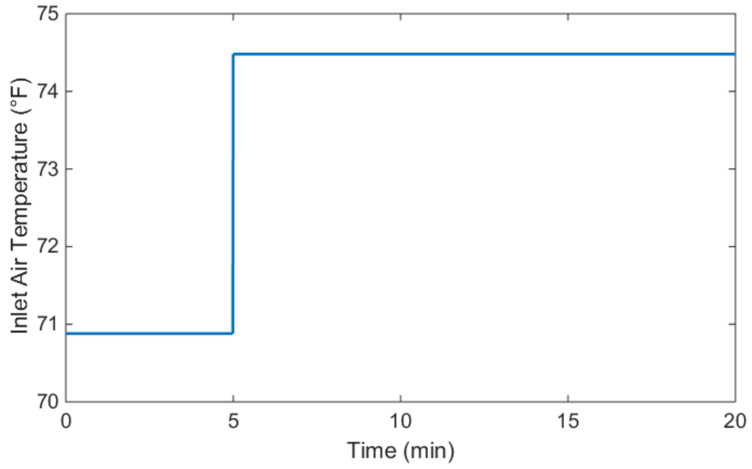

Figure 2-21 Step change of the inlet air temperature.

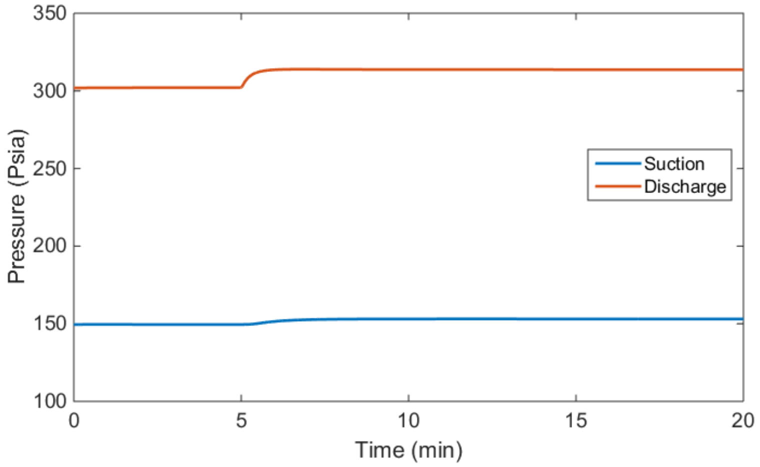

Figure 2-22 Suction and discharge pressure.

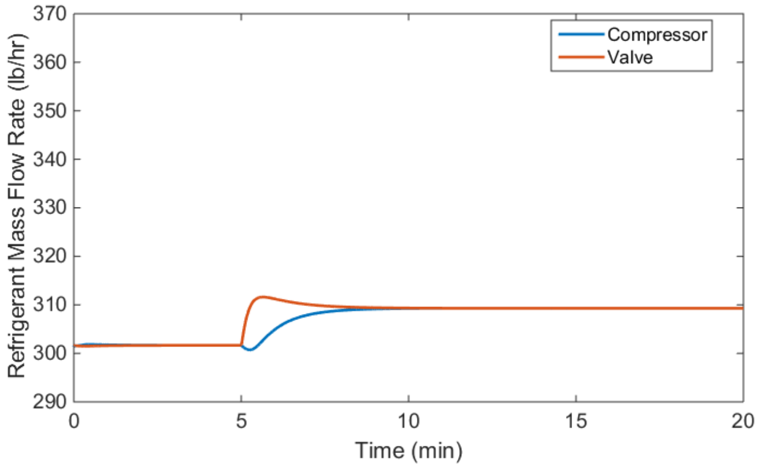

Figure 2-23 Refrigerant mass flow rate.

Start-Up and Shut-Down

During the shut-down process, the compressor is turned off while both the ID blower and OD fan are always on. The expansion valve can be open or closed. Here, simulation results for the two cases are presented.

Case 1: Expansion valve is closed during shut-down

Figure 2-24 and Figure 2-25 show the step changes of compressor and valve opening, respectively. The system is shut down at 500 seconds and restarted at 1,000 seconds. During the shut-down, the EXV opening is set at zero, but the fans keep running. The refrigerant temperature in the ID heat exchanger decreases until it equals the room temperature, while the refrigerant temperature in the OD heat exchanger rises to the ambient temperature. The changes in the refrigerant temperature lead to a drop in discharge pressure and an increase in suction pressure (Figure 2-26). The refrigerant mass flow rates through the compressor and the valve drop to zero, as shown in Figure 2-27.

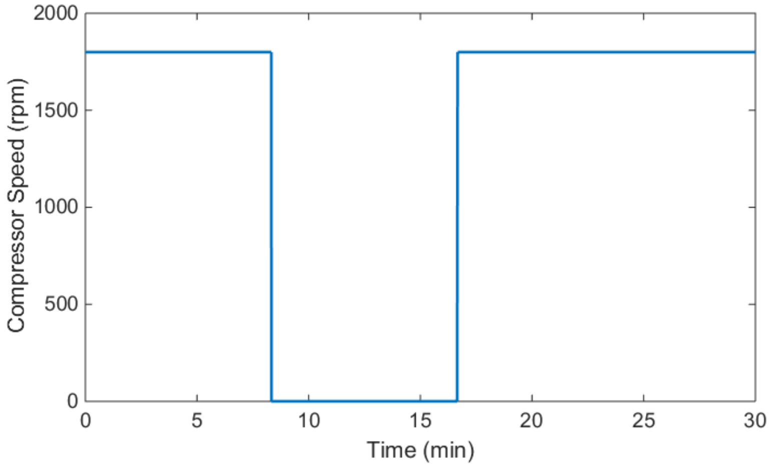

Figure 2-24 Compressor speed during start-up and shut-down.

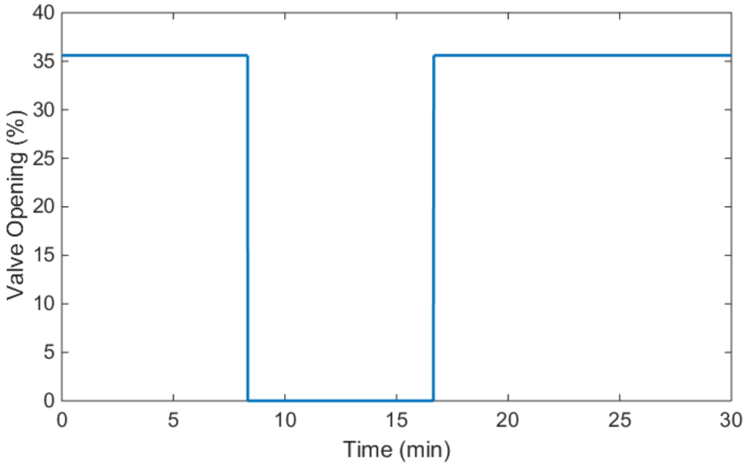

Figure 2-25 Valve opening during start-up and shut-down.

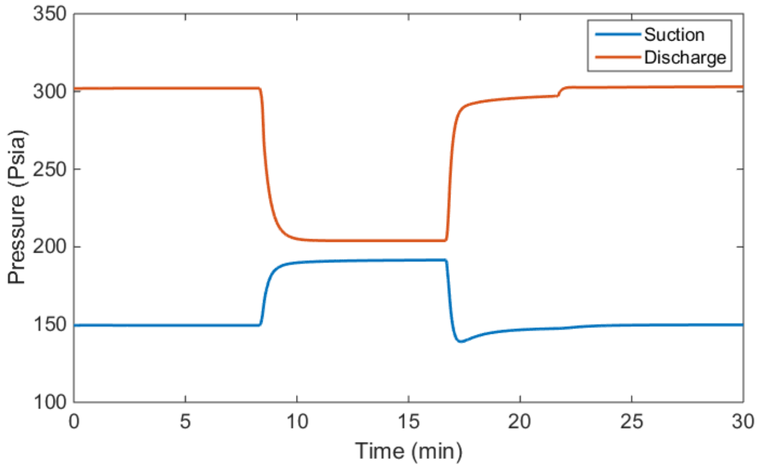

Figure 2-26 Pressure during start-up and shut-down.

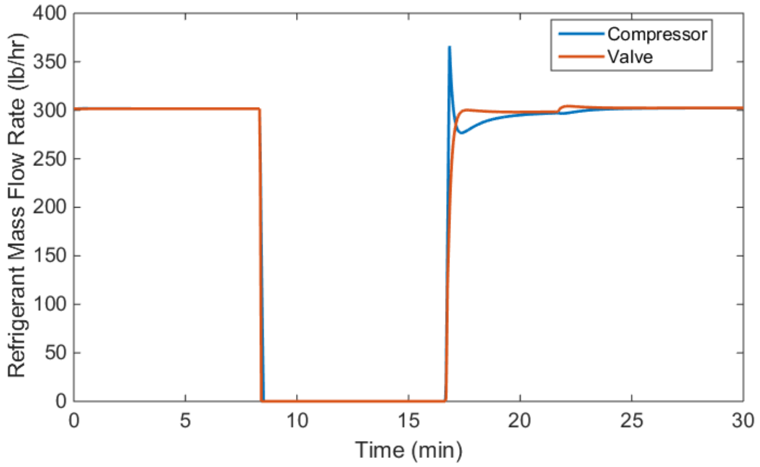

Figure 2-27 Refrigerant mass flow rate during start-up and shut-down.

Case 2: Valve is open during shut-down

The system shuts down at 500 seconds and restarts at 1,000 seconds. During the shut-down period, the EXV stays open (Figure 2-28). The refrigerant flow rate through the compressor drops to zero when the system shuts down. The refrigerant flow rate through the valve decreases slowly because the pressure difference decreases gradually. When the system is restarted, the refrigerant flow rate through the compressor has a big jump and then drops gradually until it equals the refrigerant mass flow rate through the valve.

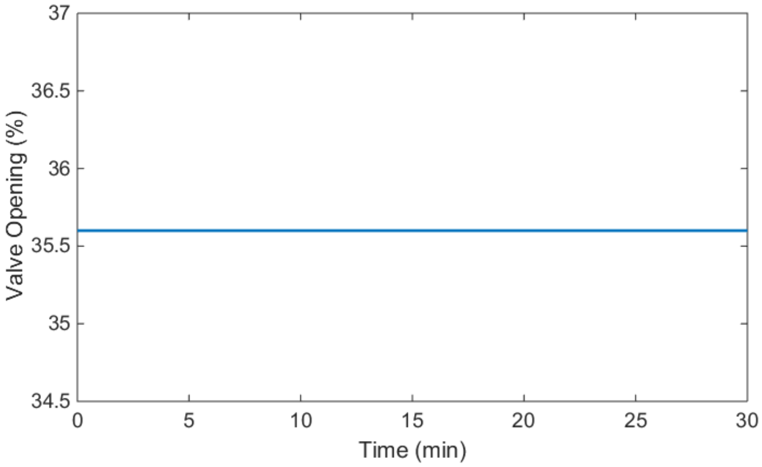

Figure 2-28 Valve opening during start-up and shut-down.

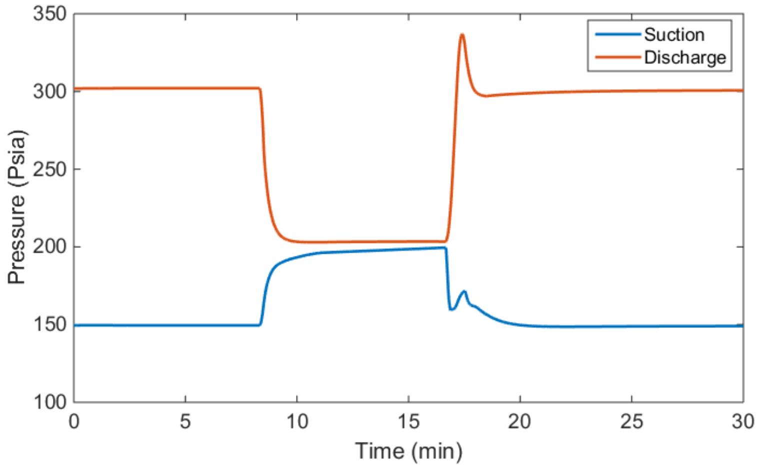

Figure 2-29 Pressure during start-up and shut-down.

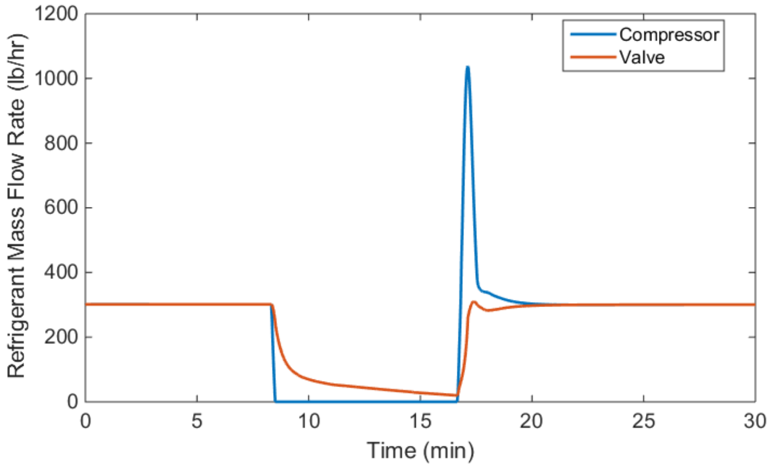

Figure 2-30 Refrigerant mass flow rates during start-up and shut-down.

Defrosting Model

A defrosting cycle can be divided into four stages: frost growth, switching, frost melting, and switching back. During the frost growth stage, the ID heat exchanger works as a condenser and the OD heat exchanger works as an evaporator. As frost accumulates, the OD heat exchanger surface temperature decreases. When the temperature difference between the frost sensor and the ambient is lower than a specified value, the frost melting stage is triggered. Switching from the frost growth to the frost melting stages happens instantly. For the frost melting stage, the ID heat exchanger works as an evaporator while the OD heat exchanger works as a condenser. A TXV is used to adjust the refrigerant flow rate. When the temperature difference between the frost sensor and the ambient is higher than the set value, the frost melting stage ends and the system switches back to the frost growth stage.

The following assumptions are made:

- Heat exchanger is modeled for mature frost growth. The crystal growth period is not included.
- Frost formation process is assumed to be quasi-steady-state.
- Frost is uniformly distributed on the heat exchanger surface and is characterized by average properties.
- The heat capacity of the frost layer is lumped to the OD heat exchanger.
- Heat and mass transfer over the heat exchanger is one-dimensional.
- Heat transfer by radiation between moisture air and frost layer is neglected.
- The effect of surface roughness of frost is neglected.
- Total heat transfer area of the OD heat exchanger is not affected by fin efficiency.
- There is no refrigerant flow through the TXV during the frost growth stage or through the EXV during the frost melting stage.
- To avoid singularity, the initial values for frost density and thickness are set as $30\ \mathrm{kg/m^3}$ and 2×10^{-5} m, respectively.
- The frost density is constant during the frost melting stage.

1) Frost Growth

The frost accumulation rate on the OD heat exchanger surface can be expressed as a loss of absolute humidity in the air:

$$\dot{m}_{fr} = \dot{m}_a(\omega_i - \omega_o) \tag{2.44}$$

And the total frost accumulation can be expressed as:

$$m_{fr} = m_{fr\_ini} + \int_0^t \dot{m}_{fr}\, dt \tag{2.45}$$

The total frost accumulation can be divided into two parts: one part increases the frost density and the rest increases the frost thickness.

$$\dot{m}_{fr} = \dot{m}_{\rho} + \dot{m}_{\delta} \tag{2.46}$$

O'Neal [106] used the following equation to calculate the mass of water vapor diffusing through the frost layer:

$$\dot{m}_{\rho} = A_o D_s \left[\frac{\left(1 - \rho_{fr}/\rho_{ice}\right)}{\left(1 + \rho_{fr}/\rho_{ice}\right)^{0.5}} \right] \frac{d\rho_V}{dx} \tag{2.47}$$

where D_s is the molecular diffusivity evaluated by an empirical equation by Eckert et al. [107]:

$$D_s = 2.302(0.98 \times 10^5/P)(T_w/256)^{1.81} \times 10^{-5} \tag{2.48}$$

The total energy transferred to the frost surface includes sensible heat caused by temperature difference and latent heat of solidification:

$$\dot{Q}_{fr} = A_o k_{fr} \frac{dT}{dx} + \dot{m}_{\rho} h_{sb} \tag{2.49}$$

Yonko et al. [108] suggested the following correlation for frost thermal conductivity:

$$k_{fr} = (0.02422 + 7.214 * 10^{-4} \cdot \rho_f + 1.1797 * 10^{-6} \cdot {\rho_f}^2)/1000 \tag{2.50}$$

The frost density rate can be expressed as:

$$\dot{m}_{\rho} = \frac{\dot{Q}_{fr}}{h_{sb}} + \frac{\lambda_{fr} R T_{fr} (v_V - v_{ice})}{D_s [h_{sb} - p_V (v_V - v_{ice})] \left(1 - \rho_{fr}/\rho_{ice}\right) / \left[1 + \left(\rho_{fr}/\rho_{ice}\right)^{0.5}\right]} \tag{2.51}$$

Both frost density and frost thickness are functions of time and are determined by:

$$\rho_{fr}(t) = \rho_{fr,ini} + \int_0^t \frac{\dot{m}_{\rho}}{A_o \delta_{fr}} dt \tag{2.52}$$

$$\delta_{fr}(t) = \delta_{fr,ini} + \int_0^t \frac{\dot{m}_{\delta}}{A_o \rho_{fr}} dt \tag{2.53}$$

Frost accumulation on the OD heat exchanger surfaces leads to higher air side pressure drop and a drop in the air flow rate. The air side pressure drop is calculated with Equation (2.54) [102].

$$\Delta P = \frac{G^2 v_i}{2} \left[(1 + \sigma^2) \left(\frac{\rho_i}{\rho_o} - 1 \right) + f \frac{A_o v_m}{A_{min} v_i} \right] \tag{2.54}$$

The empirical fan parameter solution method is proposed to calculate variable air flow rate [109]. The four coefficients can be determined experimentally.

$$\dot{V}_{air} = a_0 + a_1 * \Delta P + a_2 * \Delta P^2 + a_3 * \Delta P^3 \tag{2.55}$$

2) Switching

When defrosting is triggered, refrigerant flows through a bypass tube in the compressor so that the ID and OD heat exchangers and the accumulator can instantly reach a new balance state with the same pressure. Applying both mass and energy balance yields:

$$m_{total} = m_{ID1} + m_{OD1} + m_{acc1} = m_{ID2} + m_{OD2} + m_{acc2} \tag{2.56}$$

$$U_{total} = U_{ID1} + U_{OD1} + U_{acc1} = U_{ID2} + U_{OD2} + U_{acc2} \tag{2.57}$$

It is assumed that refrigerants in the accumulator and heat exchangers have the same quality. After switching, refrigerant mass and internal energy in each component are given by:

$$m_{ID2} = \frac{V_{ID}}{V_{ID} + V_{OD} + V_{acc}} m_{total} \tag{2.58}$$

$$m_{OD2} = \frac{V_{OD}}{V_{ID} + V_{OD} + V_{acc}} m_{total} \tag{2.59}$$

$$m_{acc2} = \frac{V_{acc}}{V_{ID} + V_{OD} + V_{acc}} m_{total} \tag{2.60}$$

$$U_{ID2} = \frac{V_{ID}}{V_{ID} + V_{OD} + V_{acc}} U_{total} \tag{2.61}$$

$$U_{OD2} = \frac{V_{OD}}{V_{ID} + V_{OD} + V_{acc}} U_{total} \tag{2.62}$$

$$U_{acc2} = \frac{V_{acc}}{V_{ID} + V_{OD} + V_{acc}} U_{total} \tag{2.63}$$

3) Frost Melting

The frost melting process can be subdivided into four steps: preheating, melting, water vaporizing, and dry heating. The stage of each control volume can be determined by the flow chart shown in Figure 2-31.

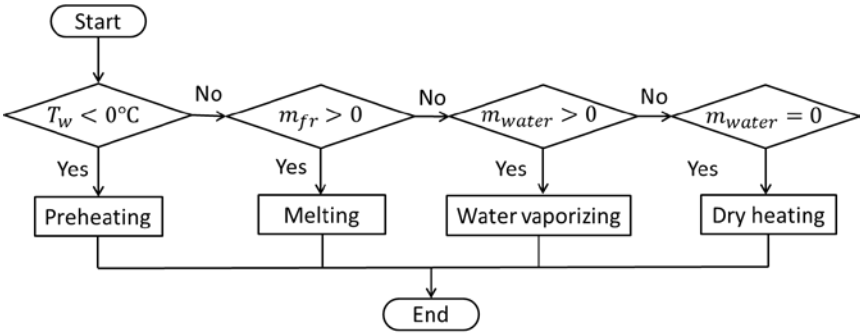

Figure 2-31 Flow chart of the frost melting process.

Stage 1: Preheating

The OD heat exchanger surface is heated from the initial temperature (the temperature of the OD heat exchanger at the end of the frost growth stage) to the melting point of ice (0^{o}C). There is no frost melting or water evaporating during the preheating stage. The heat transfer of the frost side is represented by:

$$\dot{\mathrm{Q}}_{\mathrm{stage1}} = \alpha_{stage1} A_o (T_w - T_a) \tag{2.64}$$

Stage 2: Melting

As the wall temperature reaches 0^{o}C, the frost begins to melt and a water film appears between the wall and the frost. The heat transfer process is given by:

$$\dot{Q}_{stage2} = \alpha_{stage2} A_o \left(T_{ice\_melting} - T_w\right) \tag{2.65}$$

The frost melting rate is given by:

$$\dot{m}_{fr} = \dot{Q}_{stage2} / l_{fr\_melting} \tag{2.66}$$

Stage 3: Water vaporizing

Surface water is evaporated during the water vaporizing stage. The vaporization rate and the mass of the remaining water are given by [37]:

$$\dot{m}_{water} = C_{sv} A_o \left(m_{water} / m_{water\_max}\right)^n (\rho_{vs} - \rho_{va}) \tag{2.67}$$

$$m_{water} = m_{water\_max} - \int_0^t \dot{m}_{water}\, dt \tag{2.68}$$

Heat transfer is given by:

$$\dot{Q}_{stage3} = L_{\mathrm{v\_}water}\dot{m}_{water} + \alpha_{\mathrm{stage3}} A_o (T_w - T_{air}) \tag{2.69}$$

Stage 4: Dry heating

The hot refrigerant continues to heat the dry wall surface during the dry heating stage. The heat transfer is represented by:

$$\dot{Q}_{stage4} = \alpha_{stage4} A_o (T_w - T_{air}) \tag{2.70}$$

4) Switching Back

The switching back process is similar to the switching process.

Simulation Results

The ID and OD air side operating conditions are listed in Table 2-2. The compressor speed is shown in Figure 2-32. During the frost growth stage, the compressor speed is 3,500 rpm. Before the system switches between the frost growth stage and the frost melting stage is triggered, the compressor speed decreases to 2,600 rpm for 15 seconds. During the frost melting stage and the next frost growth stage, the compressor runs at the maximum speed of cooling mode, 4,550 rpm.

Table 2-2 Air side operating conditions of defrosting cycles.

Room temperature	21℃
Ambient temperature	1.5℃
Room relative humidity	50%
Ambient relative humidity	80%
ID air volumetric flow rate	1,254 cfm
OD air volumetric flow rate	2,100 cfm

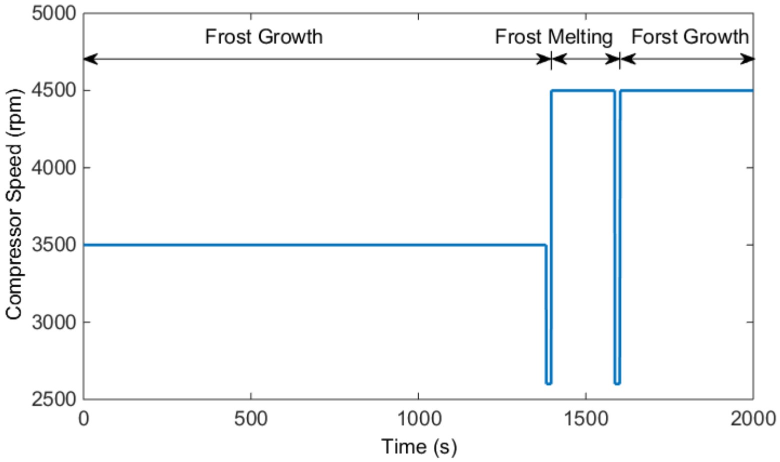

Figure 2-32 Compressor speed during defrosting cycles.

The simulation results include frost properties, effects of frost, and system characteristics during defrosting cycles. Figure 2-33 shows the frost density. During the frost growth stage, the density increases from the initial value, $30\ \mathrm{kg/m^3}$. The growth rate becomes slower as more frost forms on the OD heat exchanger surface. During the frost melting stage, the frost density is assumed constant, equaling the density at the end of the frost growth stage, $133\ \mathrm{kg/m^3}$. At the beginning of a new frost growth stage, the frost density equals the initial value because there is no frost formation.

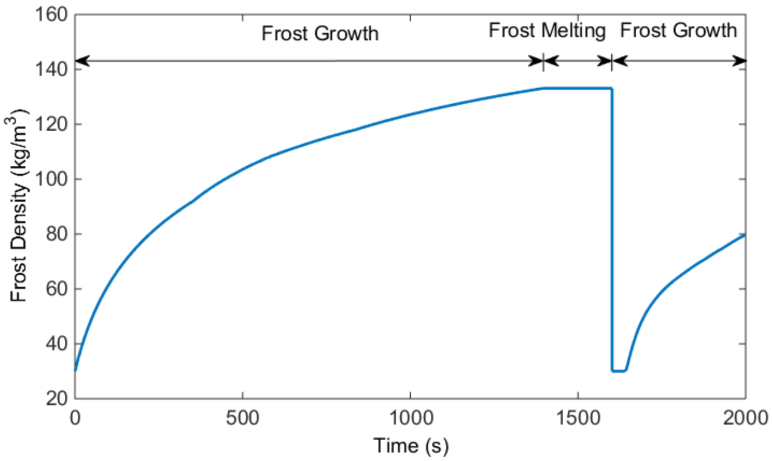

Figure 2-33 Frost density during defrosting cycles.

Figure 2-34 shows the frost thickness during defrosting cycles. The frost thickness starts to increase from the initial value, 2×10^{-5} m to 15.73×10^{-5} m. Then the thickness drops to zero during the frost melting stage. The melting rate is much faster than the growth rate. During the first 30 seconds of the next frost growth stage, the thickness equals the initial valve because there is no frost formation.

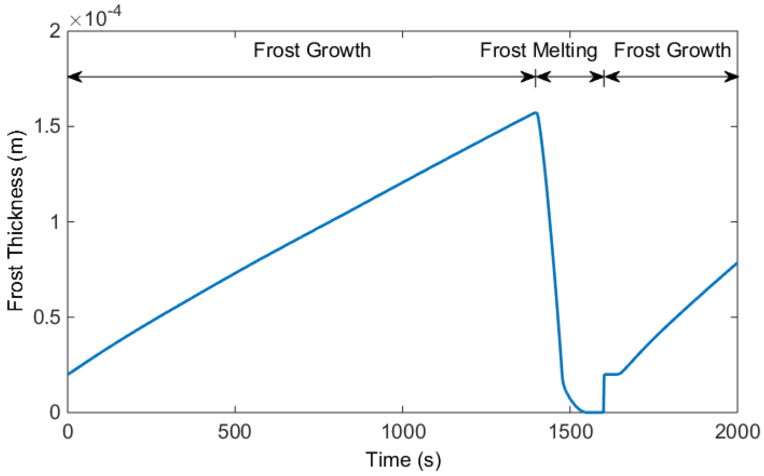

Figure 2-34 Frost thickness during defrosting cycles.

Figure 2-35 shows the total mass during defrosting cycles. The initial value of the frost mass is calculated based on the initial frost thickness and intial frost density, as well as total surface of the OD heat exchanger. During the frost growth stage, the total frost mass increases from 0.047 kg to 1.657 kg. During the frost melting stage, the total mass drops to zero. When the next frost growth stage begins, the total frost mass does not change during the first 30 seconds because there is no frost formation.

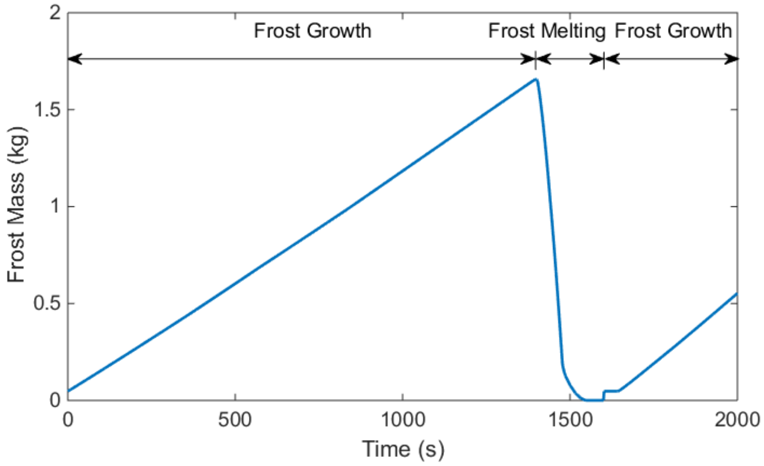

Figure 2-35 Frost mass during defrosting cycles.

Figure 2-36 and Figure 2-37 show the impacts of frost formation on air side pressure drop and air mass flow rate, respectively. During the frost growth stage, the air side pressure drop rises and the actual air mass flow rate descends. When the OD fan is turned off during the frost melting stage, there is no air flow and no pressure drop. At the beginning of the next frost growth stage, the hot OD heat exchanger leads to high outlet air temperature and low density. Thus the air pressure drop jumps to 1.1×10^{-3} kPa. As the outlet air temperature drops during the first 30 seconds, the air pressure drop decreases to 0.8×10^{-3} kPa. Then the pressure drop continues increasing because of the frost accumulation on the OD heat exchanger surface.

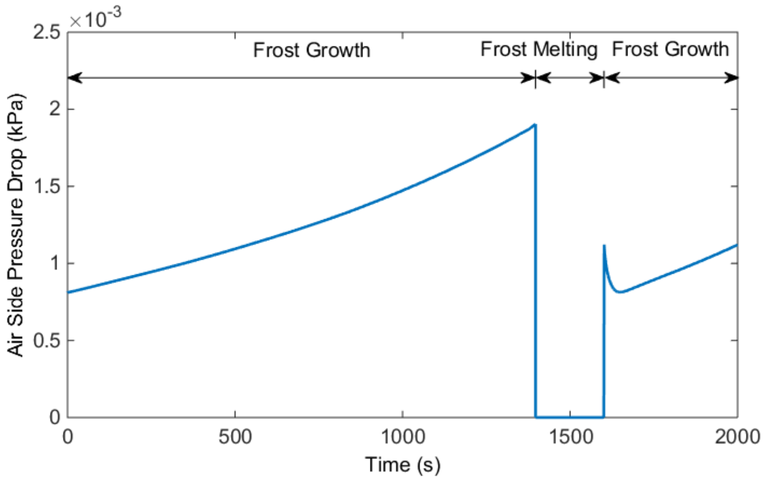

Figure 2-36 Air side pressure drop.

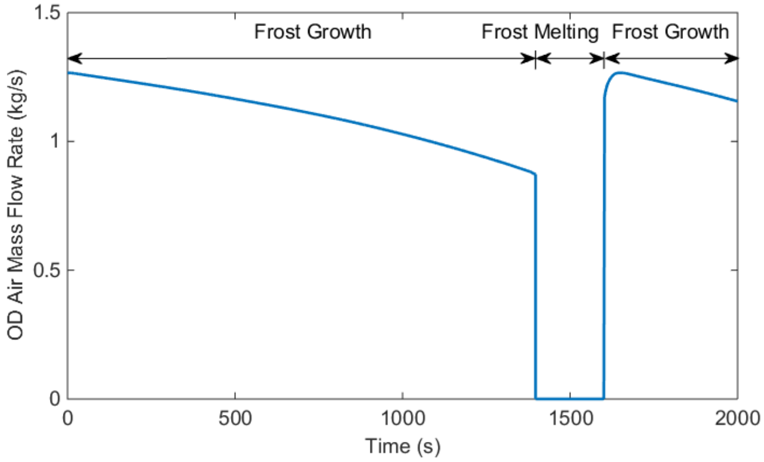

Figure 2-37 Air mass flow rate.

Figure 2-38 shows the suction and discharge pressure during defrosting cycles. During the frost growth stage, both the suction and discharge pressure drop gradually.

When the system switches between the frost growth and frost melting stages, suction and discharge pressures are very close. During the defrosting stage, the discharge pressure increases to 2,300 kPa while the suction pressure drops to 800 kPa.

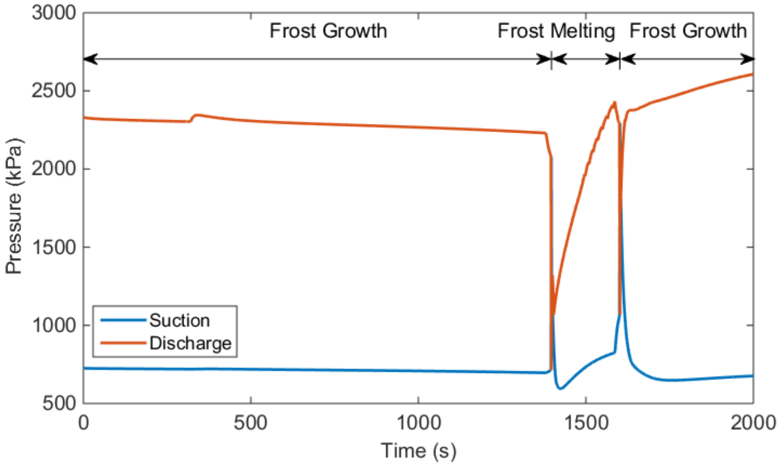

Figure 2-38 Suction and discharge pressure.

The defrost sensor temperature is measured by a temperature sensor attached to the OD heat exchanger surface. Usually, temperature is used as one of the criteria for switching and switching back. The temperature goes down slowly during the frost growth stage. Because the OD heat exchanger works as a condenser during the defrosting stage, the defrost sensor temperature rises rapidly, as shown in Figure 2-39.

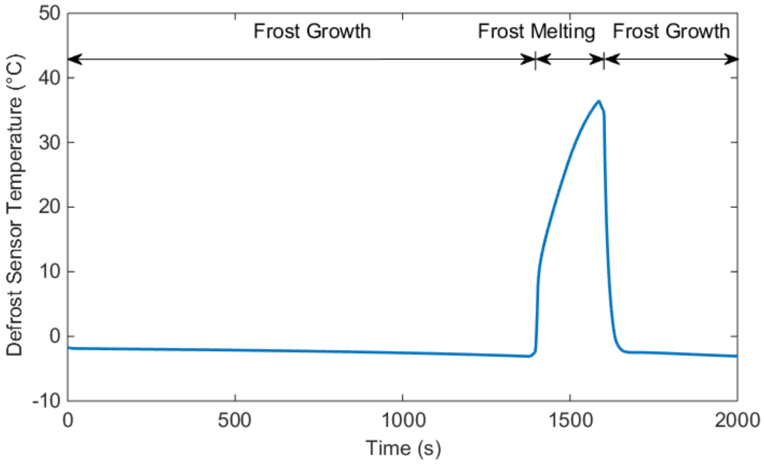

Figure 2-39 Defrost sensor temperature.

3. GRAPHICAL USER INTERFACE DEVELOPMENT

This chapter presents the GUI development for heat pump systems. The GUI allows users to interact with heat pump dynamic models. The first part introduces functionalities and layouts of the GUI. The main interface, configuration interface, and inputs/outputs interface are presented. The second part shows the generation of steady-state operating conditions. Examples are presented for both dynamic modeling and steady-state performance analysis.

Functionalities and Layouts

The main functionalities include:

- Accepting, saving, and loading system parameters.
- Handling heating, cooling, and defrosting modes, English/SI units, and different kinds of refrigerants.
- Analyzing system performance under steady states.
- Generating initialization condition for dynamic simulation.
- Selecting controllers and tuning control gains.
- Recording and displaying results.

Main Interface

Figure 3-1 shows the main interfaces of the GUI, including the basic settings panel, the scheme of heat pump systems panel, and the control panel. The basic settings panel allows users to choose the unit, refrigerant, type, and mode. The control panel allows users to load a saved GUI, initialize, save, and reset the GUI, and exit from the GUI.

The GUI has two unit systems, SI and English units. Changing the unit setup will reset all coefficients except the coefficients of the TXV and EXV. The nine refrigerants are ammonia, propane, R1234yf, R134A, R22, R32, R407C, R404A, and R410A. The type module contains dynamic model and steady-state tests. The option *Dynamic Model* allows users to run a dynamic model. The GUI calls a dynamic model automatically after all operation conditions are generated. The second option, *Steady State Tests*, allows users to do parameter analysis. For example, users can choose one or two independent variables and study the system performance. The mode module contains cooling, heating, and defrosting modes.

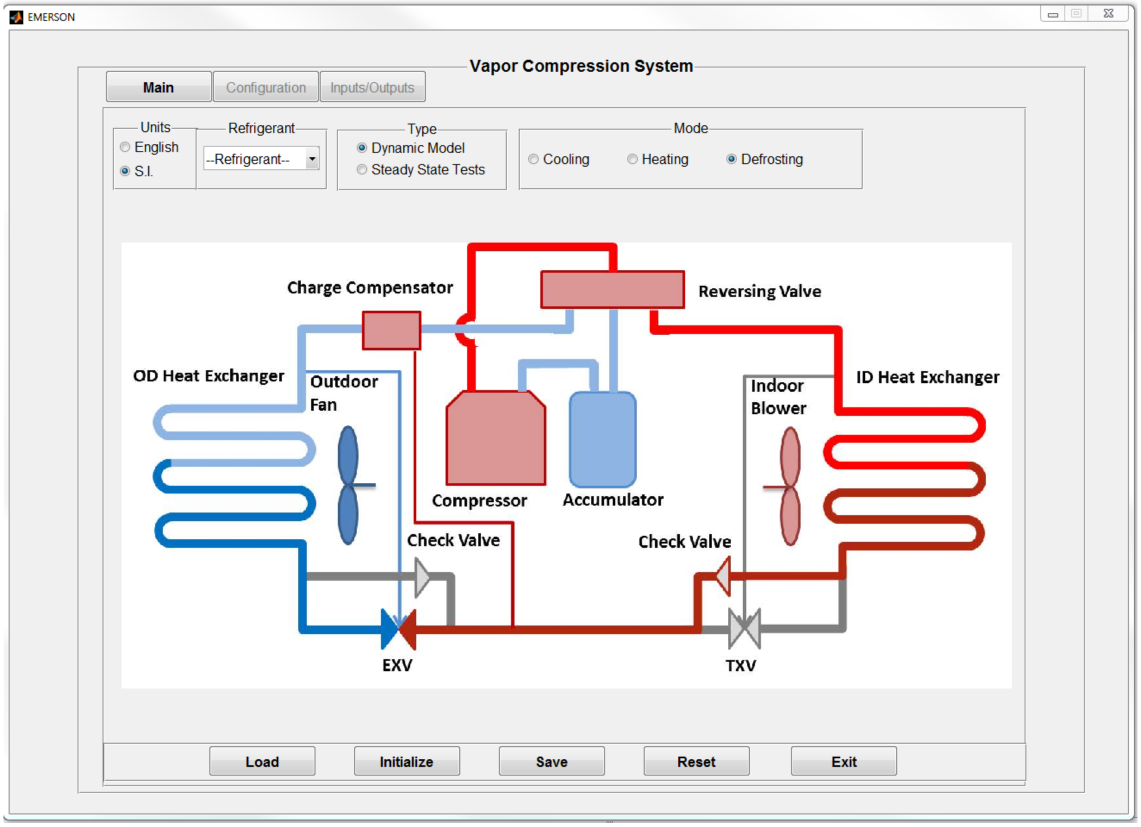

Units
○ English
● S.I.

Refrigerant
--Refrigerant--

Type
● Dynamic Model
○ Steady State Tests

Mode
○ Cooling ○ Heating ● Defrosting

Figure 3-1 Main interface.

Configuration Interface

The configuration interface allows users to input parameters of the components of typical heat pump systems. The components include compressor, ID heat exchanger, OD heat exchanger, valves, fans, pipes, and vessels.

Figure 3-2 shows the parameters of the compressor. Users need to specify the limits of the compressor speed, the rising and falling slew rates of the compressor speed, area, volume, efficiency map, etc.

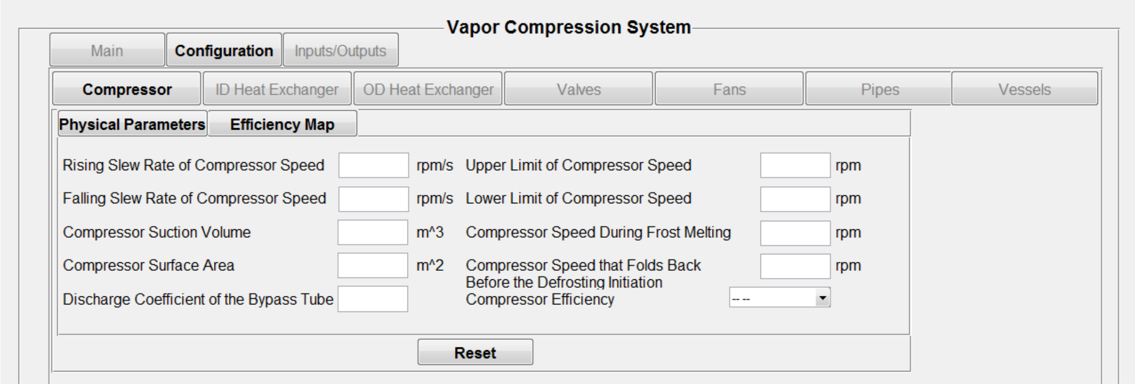

Figure 3-2 Configuration interface—compressor.

Figure 3-3 is the sub-GUI used to calculate volumetric efficiency and adiabatic efficiency. To get the efficiency maps, refrigerant mass flow rate and power consumption are needed. For fixed compressor speed, refrigerant mass flow rate and power consumption are estimated based on the saturated suction and discharge temperatures. The polynomials are given by Equations (3.1) and (3.2).

$$\dot{m}_{ref} = a_0 + a_1 T_e + a_2 T_c + a_3 T_e T_c + a_4 T_e^2 + a_5 T_c^2 + a_6 T_e T_c^2 + a_7 T_c T_e^2 + a_8 T_e^3 + a_9 T_c^3 \tag{3.1}$$

$$P_{comp} = b_0 + b_1 T_e + b_2 T_c + b_3 T_e T_c + b_4 T_e^2 + b_5 T_c^2 + b_6 T_e T_c^2 + b_7 T_c T_e^2 + b_8 T_e^3 + b_9 T_c^3 \tag{3.2}$$

For a variable-speed compressor, refrigerant mass flow rate and power consumption are estimated based on the saturated suction and discharge temperatures and compressor speed. The polynomials are given by Equations (3.3) and (3.4).

$$\dot{m}_{ref} = a_0 + a_1 T_e + a_2 T_c + a_3 T_e T_c + a_4 T_e^2 + a_5 T_c^2 + a_6 T_e T_c^2 + a_7 T_c T_e^2 + a_8 T_e^3 + a_9 T_c^3 + a_{10}\omega + a_{11} T_e \omega + a_{12} T_c \omega + a_{13}\omega^2 + a_{14} T_e T_c \omega + a_{15} T_e^2 \omega + a_{16} T_c^2 \omega + a_{17} T_e \omega^2 + a_{18} T_c \omega^2 + a_{19}\omega^3 \tag{3.3}$$

$$P_{comp} = b_0 + b_1T_e + b_2T_c + b_3T_eT_c + b_4T_e^2 + b_5T_c^2 + b_6T_eT_c^2 + b_7T_cT_e^2 + b_8T_e^3 + b_9T_c^3 + b_{10}\omega + b_{11}T_e\omega + b_{12}T_c\omega + b_{13}\omega^2 + b_{14}T_eT_c\omega + b_{15}T_e^2\omega + b_{16}T_c^2\omega + b_{17}T_e\omega^2 + b_{18}T_c\omega^2 + b_{19}\omega^3 \quad (3.4)$$

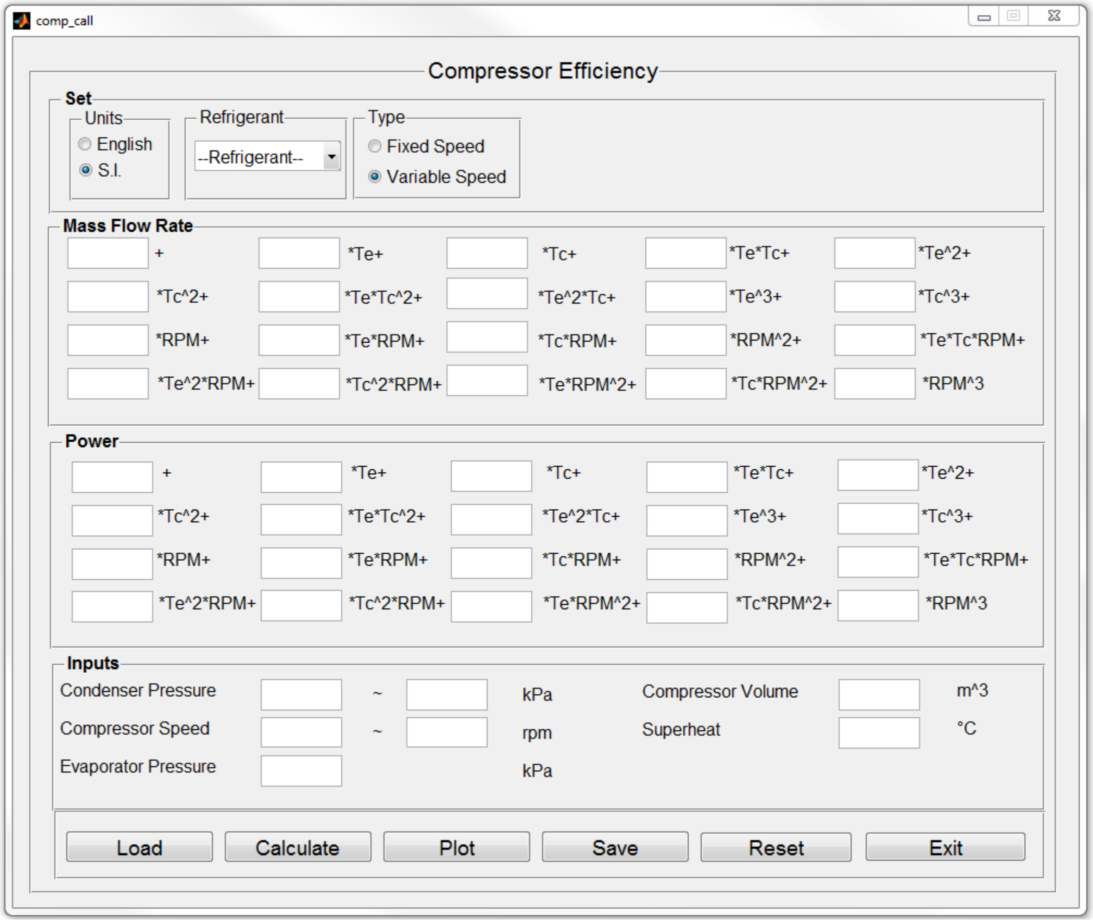

Units: ○ English ● S.I.

Type: ○ Fixed Speed ● Variable Speed

Figure 3-3 GUI compressor efficiency.

Figure 3-4 shows the interface for the ID heat exchanger. Inputs include heat exchanger type, fan, and tube parameters. The GUI calculates the outputs based on the above parameters. The configuration interface for the OD heat exchanger has the same function.

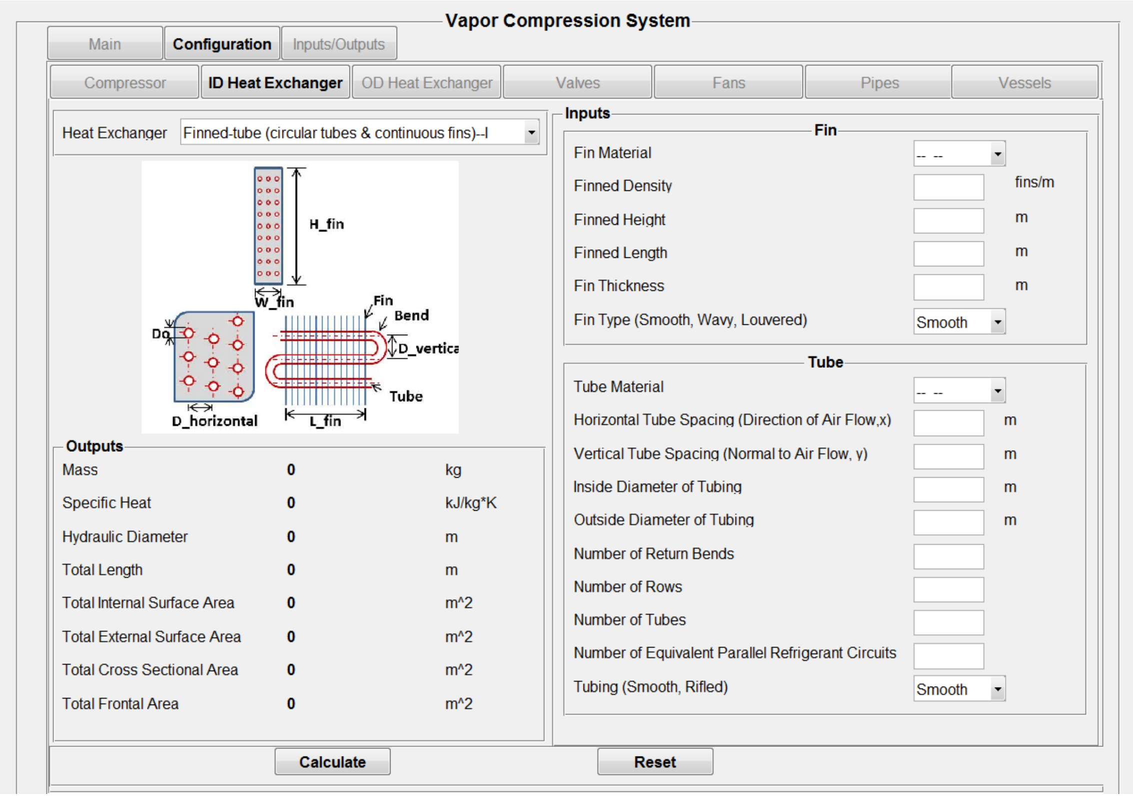

Heat Exchanger: Finned-tube (circular tubes & continuous fins)--I

Outputs

Mass	**0**	kg
Specific Heat	**0**	kJ/kg*K
Hydraulic Diameter	**0**	m
Total Length	**0**	m
Total Internal Surface Area	**0**	m^2
Total External Surface Area	**0**	m^2
Total Cross Sectional Area	**0**	m^2
Total Frontal Area	**0**	m^2

Inputs

Fin

Fin Material	-- --	
Finned Density		fins/m
Finned Height		m
Finned Length		m
Fin Thickness		m
Fin Type (Smooth, Wavy, Louvered)	Smooth	

Tube

Tube Material	-- --	
Horizontal Tube Spacing (Direction of Air Flow,x)		m
Vertical Tube Spacing (Normal to Air Flow, y)		m
Inside Diameter of Tubing		m
Outside Diameter of Tubing		m
Number of Return Bends		
Number of Rows		
Number of Tubes		
Number of Equivalent Parallel Refrigerant Circuits		
Tubing (Smooth, Rifled)	Smooth	

Figure 3-4 Configuration interface—ID heat exchanger.

Figure 3-5 shows the parameters for the TXV and EXV. The parameters for the TXV include two constants and the bulb time constant. For the EXV, users need to specify the maximum and minimum valve opening, rising and falling slew rates, time delay, and discharge coefficient map.

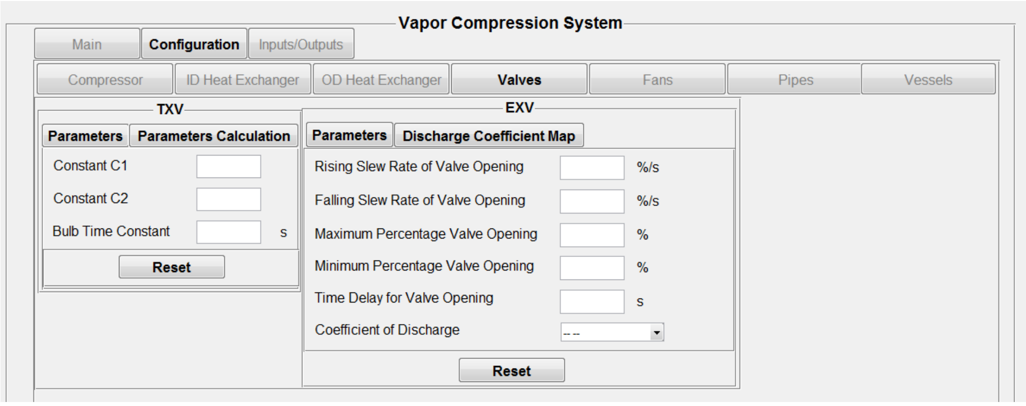

Figure 3-5 Configuration interface—expansion valves.

The sub-GUI shown in Figure 3-6 is used to generate the parameters of the TXV. To calculate the two constants, users need to specify the refrigerant mass flow rate, high and low pressure, and bulb temperature under two different operating conditions.

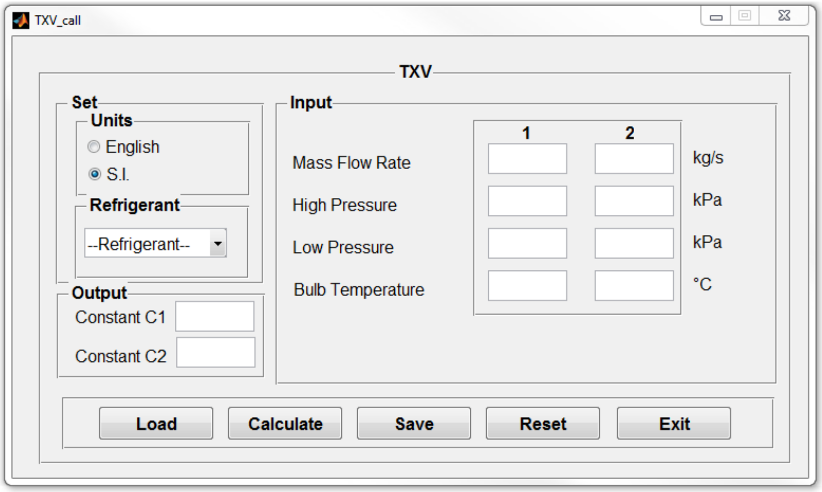

Figure 3-6 Sub-GUI for parameter generation for the TXV model.

The sub-GUI shown in Figure 3-7 is used to generate the discharge coefficient map for the EXV. The refrigerant mass flow rate is estimated based on the pressure difference and valve opening. The polynomial is given by Equation (3.5).

$$\dot{m}_{ref} = a_0 + a_1\Delta P + a_2 v + a_3 v\Delta P + a_4 v^2 + a_5 \Delta P^2 + a_6 v\Delta P^2 + a_7 \Delta P v^2 + a_8 v^3 + a_9 \Delta P^3 \tag{3.5}$$

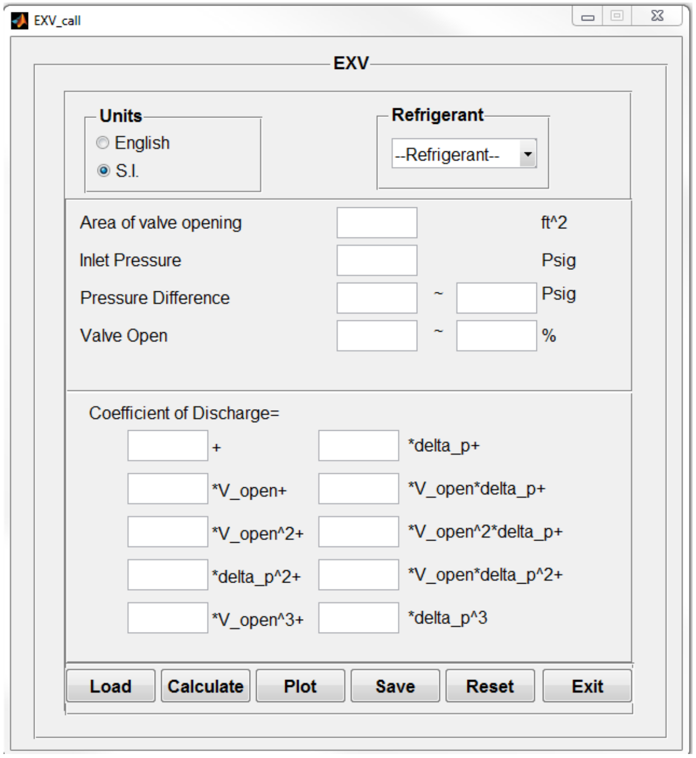

Units
○ English
● S.I.

Figure 3-7 Sub-GUI for discharge coefficient map generation.

Figure 3-8 shows the fan interface. Parameters include power factor, suction air pressure, rated power, rated cfm, and voltage. The OD fan volumetric flow rate–pressure correlation is only used in the defrosting model. This correlation can be obtained based on experimental data.

$$\dot{V}_{air} = a_0 + a_1\Delta P + a_2\Delta P^2 + a_3\Delta P^3 \quad (3.6)$$

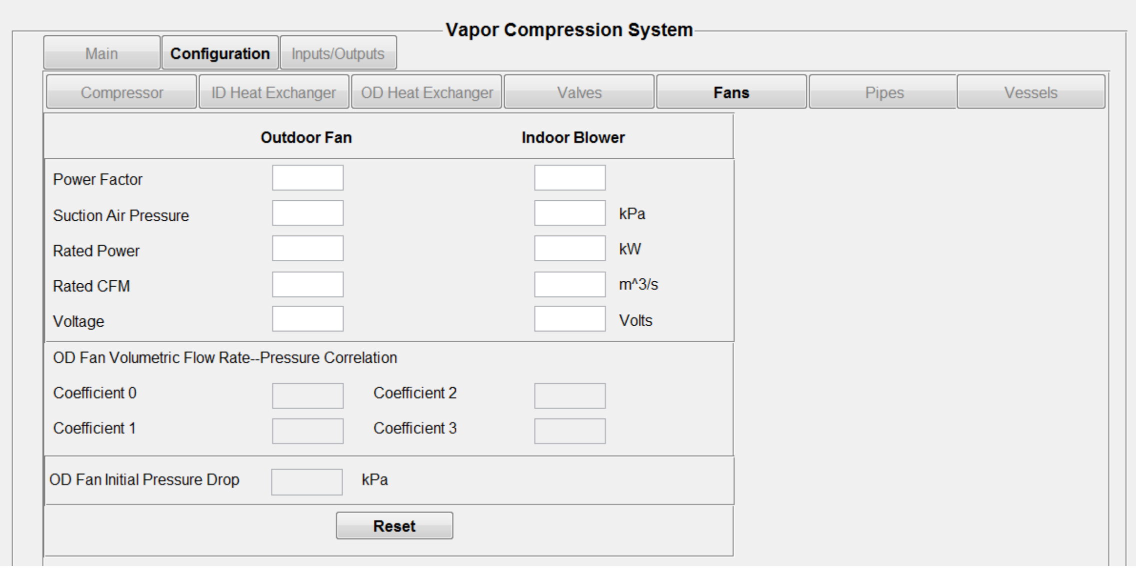

Figure 3-8 Configuration interface—fans.

Figure 3-9 shows the pipe interface. For each pipe, UA value, inside diameter, length, and roughness need to be specified. The five pipes are:

- Comp—OD HX: pipe connecting the compressor and OD heat exchanger
- Comp—ID HX: pipe connecting the compressor and ID heat exchanger
- EXV—OD HX: pipe connecting the OD heat exchanger and EXV
- TXV—ID HX: pipe connecting the TXV and ID heat exchanger
- Liquid Line: liquid line pipe

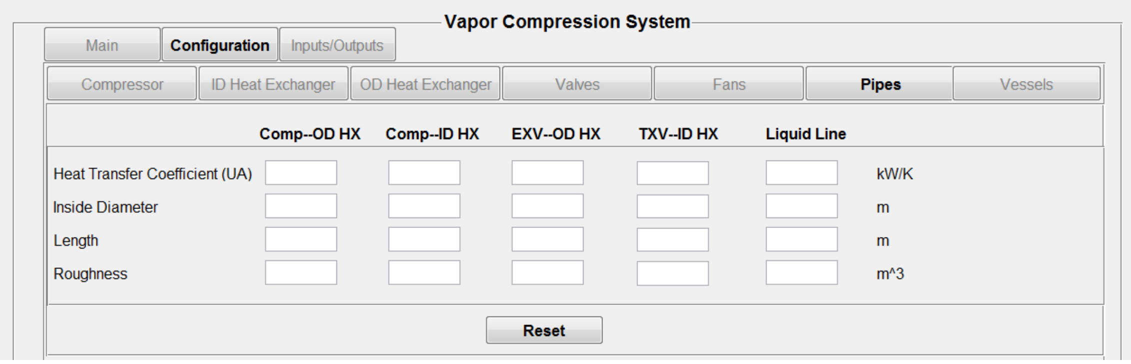

Figure 3-9 Configuration interface—pipes.

Figure 3-10 shows the interface for vessels. Parameters of the accumulator include ambient temperature, initial mass of refrigerant, UA value, and volume. Parameters of the charge compensator include discharge coefficient, external and internal UA values, and volume.

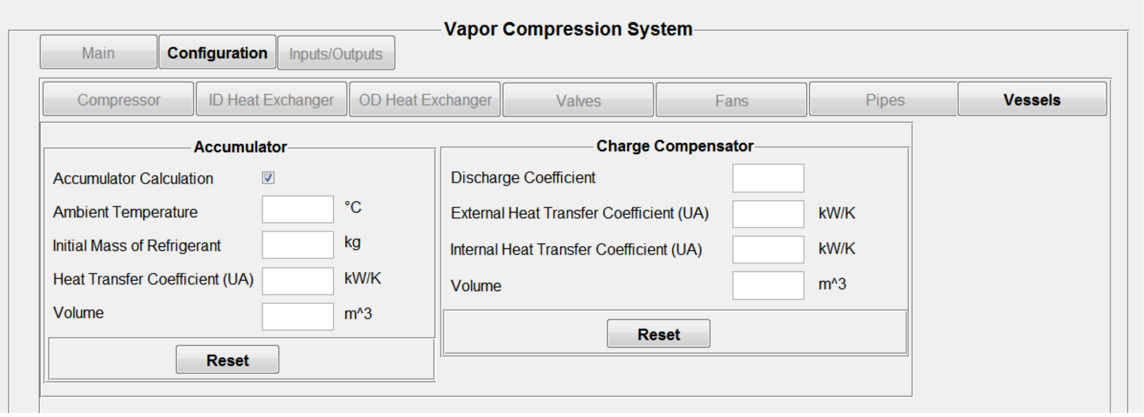

Accumulator Calculation ☑

Figure 3-10 Configuration interface—vessels.

Inputs/Outputs Interface

The inputs interface allows users to specify the inputs, including compressor speed, fan current, superheat or subcool or valve opening (for an EXV), air temperature, and relative humidity, as shown in Figure 3-11. For heating mode, users can only select one parameter among *Superheat*, *Subcool*, and *Valve Opening (EXV)*. For cooling mode, users need to choose between *Superheat* and *Subcool*.

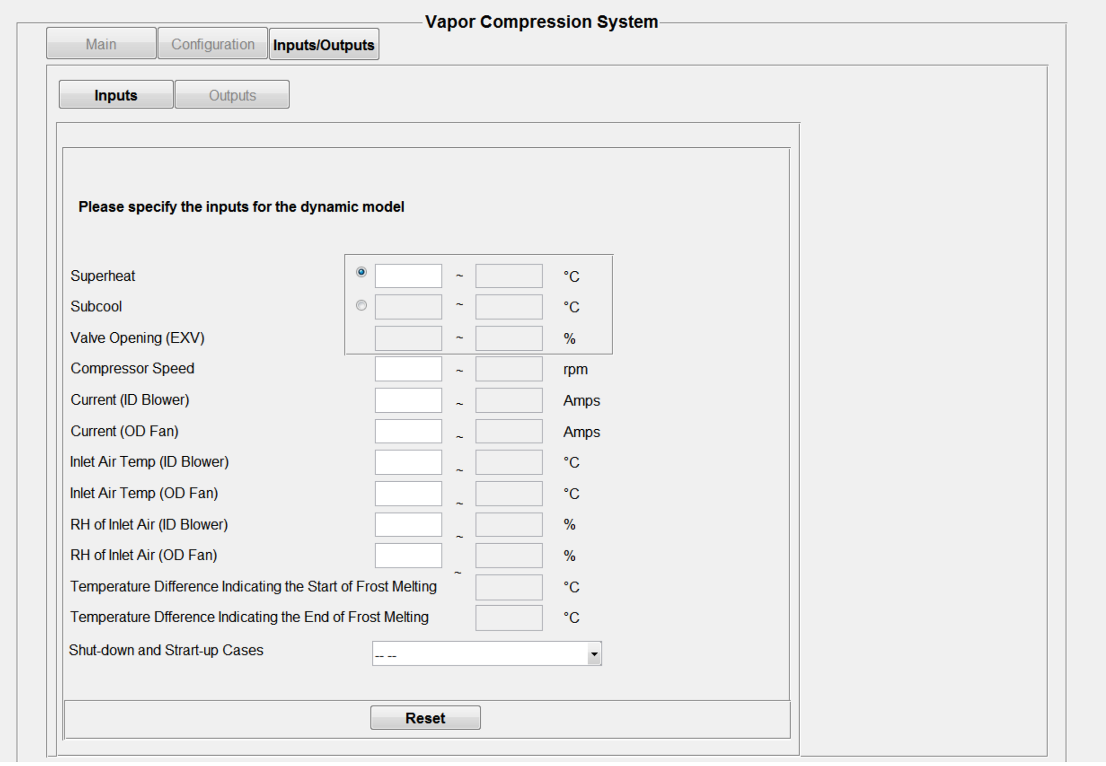

Figure 3-11 Inputs interface.

Figure 3-12 shows the outputs panel. Parameters of the system level include cooling power, heating power, COP, refrigerant charge, and refrigerant mass flow rate. For the components level, parameters include ID/OD air volumetric flow rate, discharge and suction pressure, superheat, and subcool. The outputs can be shown in tables and figures. The *Value* button shows users the values of objective functions. For a successful optimization problem, the function value should be less than 0.1. The *Export* button allows users to export all data to Microsoft Excel® spreadsheets.

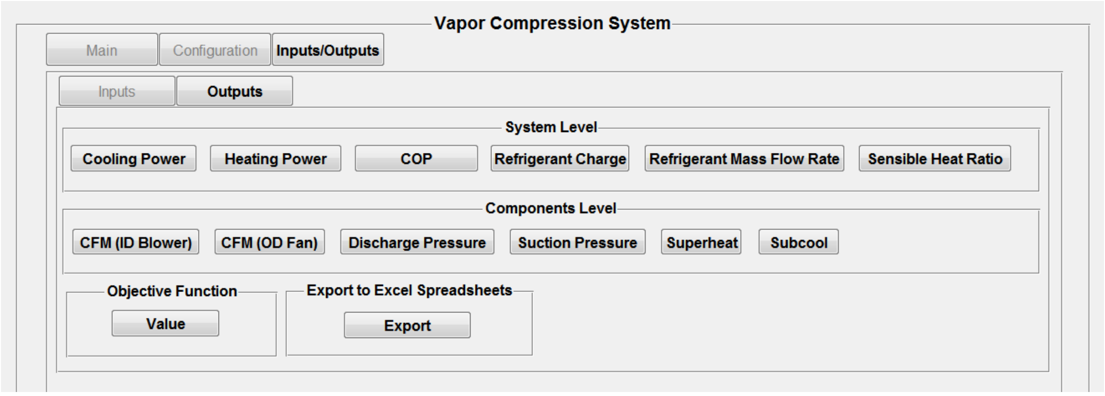

Figure 3-12 Outputs interface.

Generation of Steady-State Operating Conditions

Steady-state operating conditions are necessary for both the dynamic model and steady-state performance analysis. The operating conditions can be generated by solving an optimization problem with given parameters and inputs. Four guess parameters of the optimization problem are suction pressure, discharge pressure, pressure at the inlet of the evaporator, and suction temperature. The objective function is based on the mode and inputs. Five cases are presented here.

1) Heating mode with specified expansion valve opening

For steady state, the refrigerant mass flow rate through the compressor and the expansion valve should be the same. The optimized suction pressure and suction enthalpy should be the same as the initial suction pressure and initial suction enthalpy, respectively. The objective function is given by:

$$f = \left\| \frac{m_{comp} - m_{valve}}{m_{comp}} \right\| + \left\| \frac{H_{suc} - H_{suc\_initial}}{H_{suc}} \right\| + \left\| \frac{P_{suc} - P_{suc\_initial}}{P_{suc}} \right\| \quad (3.7)$$

Here, the parameters with the subscript $initial$ indicate that the values are obtained from the initial guess.

2) Heating mode with specified subcool

For a given subcool, the four terms are refrigerant mass flow rate, suction enthalpy, enthalpy at the outlet of the condenser, and subcool. The objective function can be described as:

$$\begin{aligned} f = &\left\| \frac{m_{comp} - m_{valve}}{m_{comp}} \right\| + \left\| \frac{H_{suc} - H_{suc\_initial}}{H_{suc}} \right\| \\ &+ \left\| \frac{Ho_{cond} - Ho_{cond\_initial}}{Ho_{cond}} \right\| + \left\| \frac{T_{sc} - T_{sc\_initial}}{T_{sc}} \right\| \end{aligned} \quad (3.8)$$

3) Heating mode with specified superheat

For specified superheat, the four terms of the objective function include refrigerant mass flow rate, suction enthalpy, enthalpy at the outlet of the condenser, and superheat. The objective function is:

$$\begin{aligned} f = &\left\| \frac{m_{comp} - m_{valve}}{m_{comp}} \right\| + \left\| \frac{H_{suc} - H_{suc\_ini}}{H_{suc}} \right\| + \left\| \frac{Ho_{cond} - Ho_{cond\_initial}}{Ho_{cond}} \right\| \\ &+ \left\| \frac{T_{sh} - T_{sh\_initial}}{T_{sh}} \right\| \end{aligned} \quad (3.9)$$

4) Cooling mode with specified subcool

For cooling mode with specified subcool, the objective function includes refrigerant mass flow rate, suction enthalpy, suction pressure, and subcool.

$$f = \left\| \frac{m_{comp} - m_{valve}}{m_{comp}} \right\| + \left\| \frac{H_{suc} - H_{suc\_initial}}{H_{suc}} \right\| + \left\| \frac{P_{suc} - P_{suc\_initial}}{P_{suc}} \right\| + \left\| \frac{T_{sc} - T_{sc\_initial}}{T_{sc}} \right\| \tag{3.10}$$

5) Cooling mode with specified superheat

Similarly, when the superheat is specified, the objective function includes refrigerant mass flow rate, suction enthalpy, suction pressure, and superheat. The function is presented as:

$$f = \left\| \frac{m_{comp} - m_{valve}}{m_{comp}} \right\| + \left\| \frac{Ho_{cond} - Ho_{cond\_initial}}{Ho_{cond}} \right\| + \left\| \frac{P_{suc} - P_{suc\_initial}}{P_{suc}} \right\| + \left\| \frac{T_{sh} - T_{sh\_initial}}{T_{sh}} \right\| \tag{3.11}$$

Generation of Operating Conditions for Dynamic Models

This section shows an example of generation of steady-state operating conditions for the dynamic model running in heating mode. The value of the objective function is shown in Figure 3-13. A smaller final value indicates better optimization.

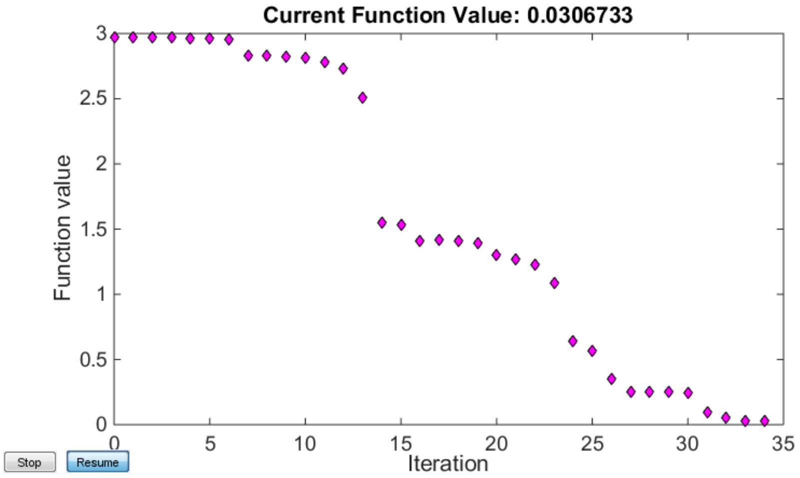

Figure 3-13 Function value during the optimization process.

The heat pump model is run with the operating conditions generated by the GUI. The simulation results are shown in Figure 3-14 and Figure 3-15. Both suction and discharge are almost steady, while the refrigerant mass flow rate through the compressor and the expansion valve are transient at 70 seconds. The difference between the operating conditions generated by the GUI and the steady-state operating conditions given by the dynamic model are caused by two reasons: (1) compared with the dynamic model, the GUI uses a simplified model to find the steady-state operating conditions and (2) the optimization process may not be accurate enough.

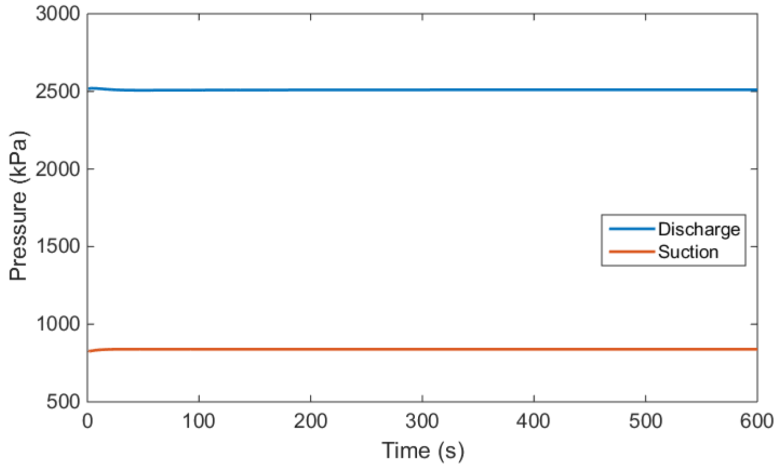

Figure 3-14 Suction and discharge pressure.

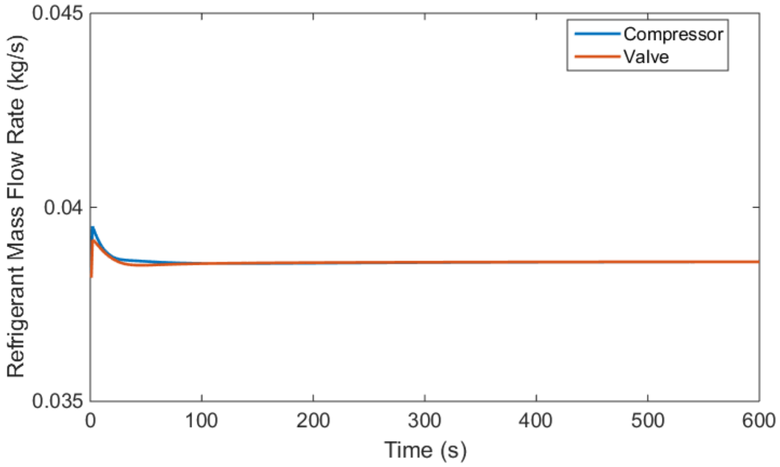

Figure 3-15 Refrigerant mass flow rate.

Generation of Operating Conditions for Steady-State Analysis

One function of the GUI is analyzing system performance for steady-state tests. An example is shown in Figure 3-16. Here, the compressor speed is the first independent variable and the valve opening is the second independent variable. Both have three cases. The compressor speeds for the three cases are 1,800 rpm, 2,150 rpm, and 2,500 rpm. The valve openings for the three cases are 15%, 20%, and 25%. Other inputs remain unchanged for the above nine cases.

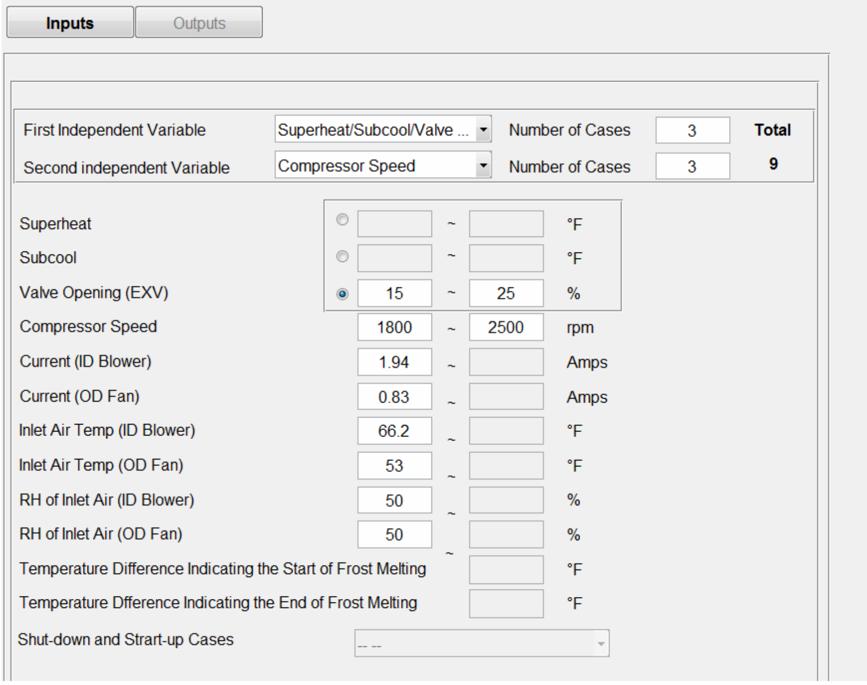

First Independent Variable: Superheat/Subcool/Valve ... — Number of Cases: 3 — **Total**
Second independent Variable: Compressor Speed — Number of Cases: 3 — **9**

○ Superheat ~ °F
○ Subcool ~ °F
● Valve Opening (EXV): 15 ~ 25 %
Compressor Speed: 1800 ~ 2500 rpm
Current (ID Blower): 1.94 ~ Amps
Current (OD Fan): 0.83 ~ Amps
Inlet Air Temp (ID Blower): 66.2 ~ °F
Inlet Air Temp (OD Fan): 53 ~ °F
RH of Inlet Air (ID Blower): 50 ~ %
RH of Inlet Air (OD Fan): 50 ~ %
Temperature Difference Indicating the Start of Frost Melting ~ °F
Temperature Dfference Indicating the End of Frost Melting °F
Shut-down and Strart-up Cases: -- --

Figure 3-16 Inputs for performance analysis for steady-state tests.

Figure 3-17 and Figure 3-18 show discharge pressure and suction pressure, respectively. When the compressor speed increases from 1,800 rpm to 2,500 rpm, the discharge pressure increases while the suction pressure decreases. A smaller valve opening also indicates higher discharge pressure. The effect of the valve opening on the suction pressure, however, is not significant.

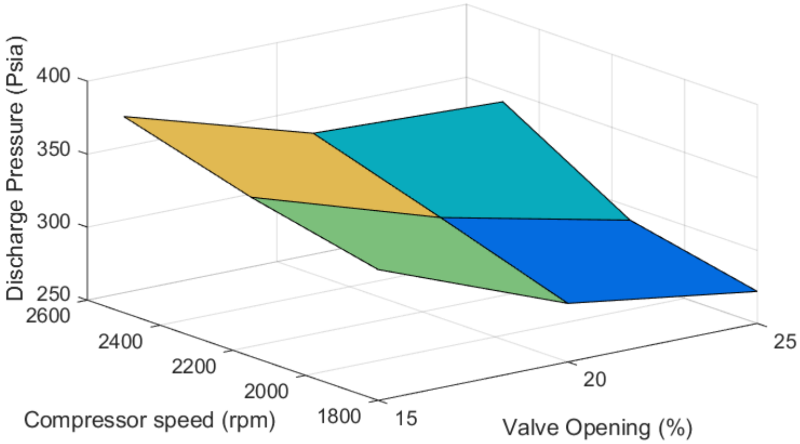

Figure 3-17 Discharge pressure.

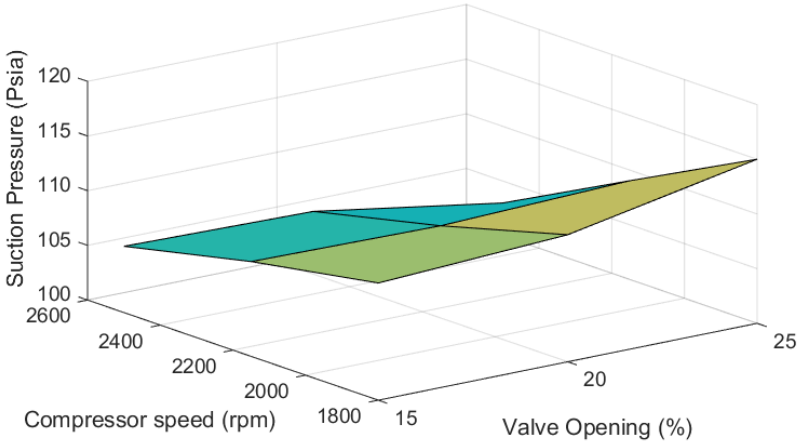

Figure 3-18 Suction pressure.

Figure 3-19 shows the refrigerant mass flow rate for the nine cases. When the compressor speed increases or the valve opening becomes larger, the refrigerant mass flow rises. Higher refrigerant mass flow rate means higher heating capacity (Figure 3-20).

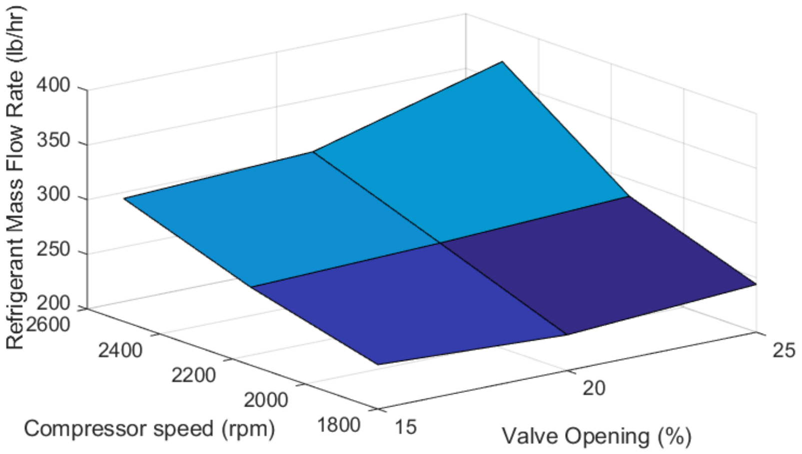

Figure 3-19 Refrigerant mass flow rate.

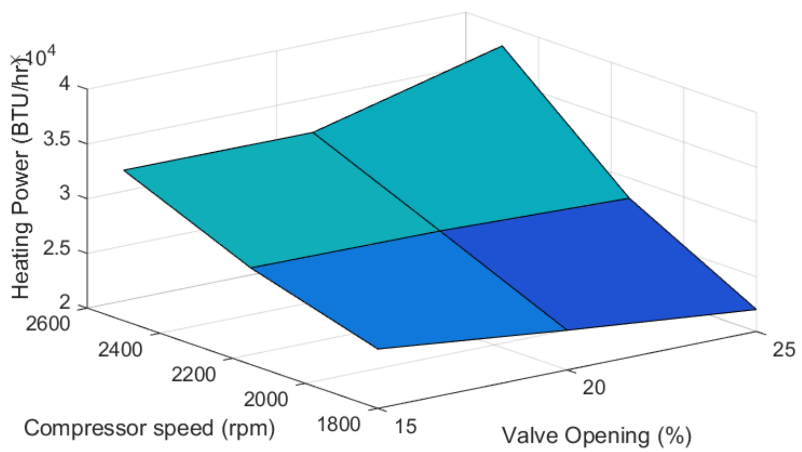

Figure 3-20 Heating capacity.

COP is shown in Figure 3-21. For a fixed valve opening, higher compressor speed indicates lower COP. When the valve opening is 20%, COP drops from 5.2 to 4.6 when the compressor speed changes from 1,800 to 2,500 rpm. For a given compressor speed, COP also drops as the valve opening decreases from 25% to 15%.

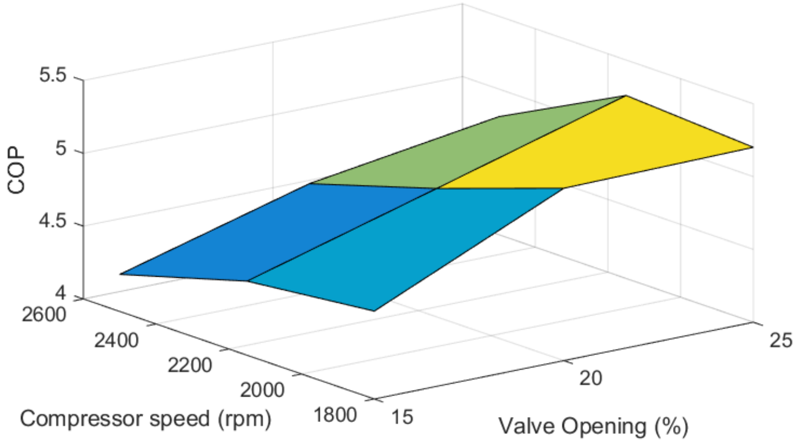

Figure 3-21 COP.

4. EXPERIMENTAL SYSTEM FOR CONTROL VALIDATION

This chapter describes the experimental setup for control design and validation. First, the chapter gives an overview of a 3-ton heat pump system. The ambient control and moisture generation systems for defrosting tests are also introduced. Then the details of the system components, sensors, and data acquisition (DAQ) system are presented.

System Description

Figure 4-1 shows a 3-ton heat pump with a DAQ system used for control validation. The schematic of the heat pump system is shown in Figure 4-2. The ID unit includes an ID heat exchanger, an ID blower, and a TXV. The OD unit includes a scroll compressor, an OD heat exchanger, an OD fan, an EXV, a reversing valve, and two charge compensators. The DAQ system contains a laptop, National Instruments (NI) modules, and a control box. Experimental data measured by NI modules are sent to the laptop. Control signals generated based on the control algorithm are sent to the control box and finally to the actuators (compressor, valves, and fans).

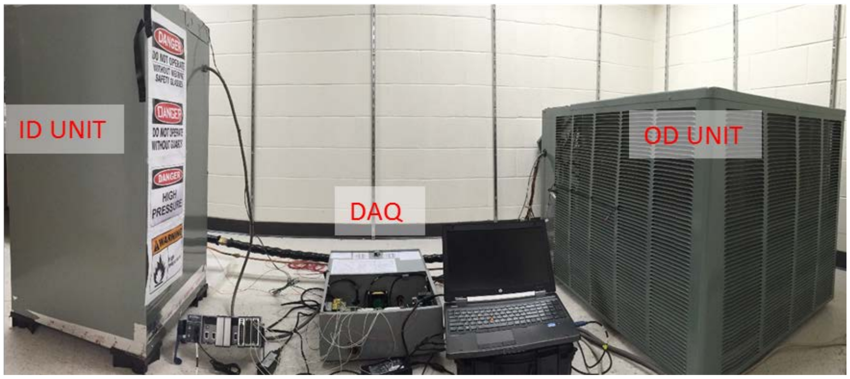

Figure 4-1 Experimental setup.

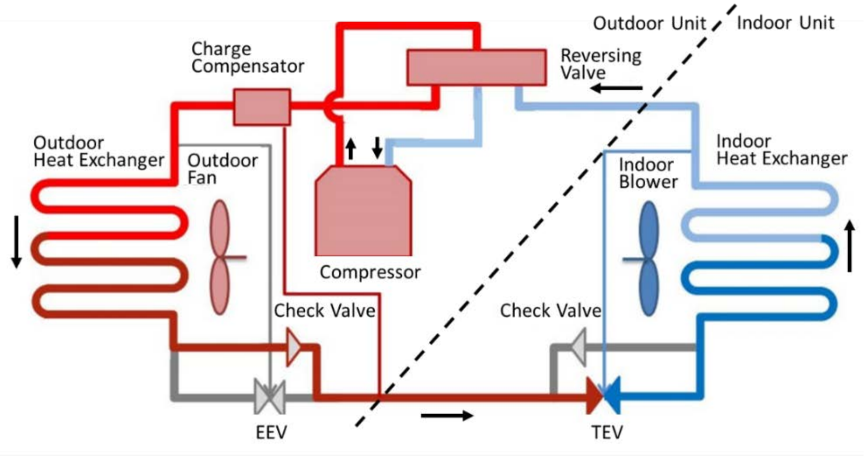

Figure 4-2 Schematic of the 3-ton heat pump system.

For heating tests, an insulation chamber is built to ensure that the ambient temperature will not be above 47°F, as shown in Figure 4-3. Holes are used to adjust the ambient temperature.

Figure 4-3 Insulation chamber for heating tests.

Ambient Control and Moisture Generation Systems

An ambient control loop and moisture generation system are built for defrosting tests, as shown in Figure 4-4 and Figure 4-5. The ambient temperature loop is used to maintain constant ambient temperature during the frost growth stage. The moisture generation system is used to provide constant moisture rate during the frost growth stage.

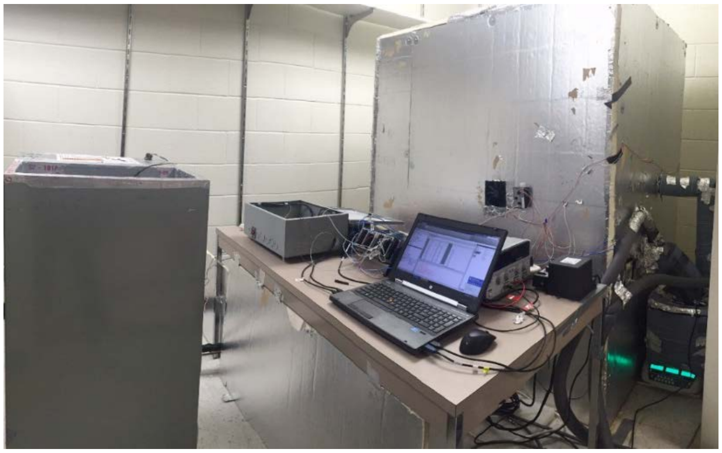

Figure 4-4 Experimental setup for defrosting tests.

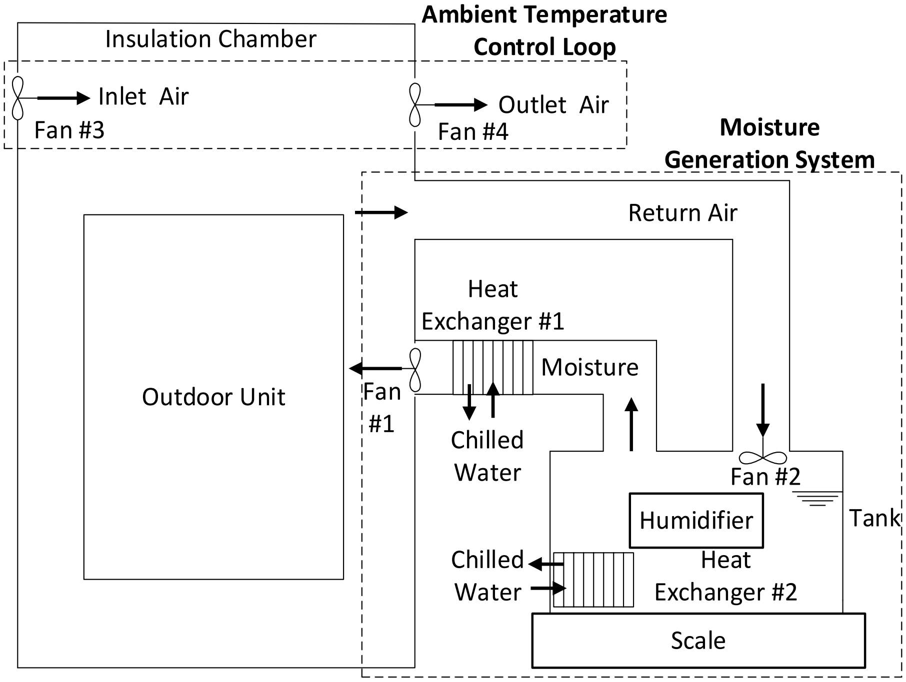

Figure 4-5 Schematic of the moisture generation system and ambient temperature control loop.

The ambient temperature control system includes a pair of case fans (Figure 4-6). The fan speed can be adjusted to maintain constant ambient temperature inside the chamber during the frost growth stage. The inlet air is around 75°F, and the outlet air temperature equals the ambient temperature inside the chamber. Figure 4-7 shows the PI control loop. The ambient temperature is used as the feedback signal. The control signal generated by the PI controller is converted to an analog voltage signal (0 to +12 VDC) by a pulse width modulation (PWM) driver (Figure 4-8).

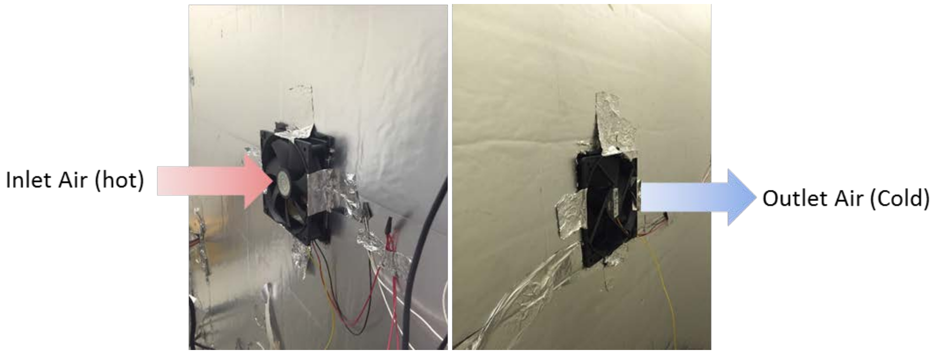

Figure 4-6 Case fans.

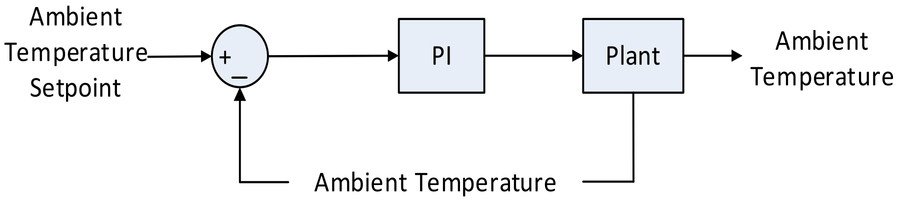

Figure 4-7 Ambient temperature control.

Figure 4-8 PWM controller.

Figure 4-9 shows the moisture generation system. The system includes a water tank, a humidifier, two case fans, two heat exchangers, return air and moisture pipes, and a digital scale. The humidifier is in the water tank and can provide moisture rate (Figure 4-10). The moisture rate can be adjusted and is measured with the digital scale (Model: CTS-300000). The capacity of the scale is 30 kg with a division of 0.5 g. During the defrosting stage, frost melts, becomes liquid, and is stored in the catch pan (Figure 4-11). Heat exchanger #1 is inside the moisture pipe, and heat exchanger #2 is inside the water tank. Both water and moisture are cooled down by the chilled water system.

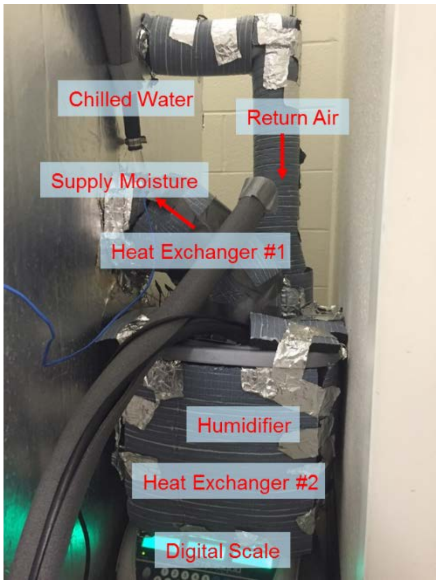

Figure 4-9 Moisture generation system.

Figure 4-10 Humidifier.

Figure 4-11 Catch pan.

System Components

Compressor

The compressor is a Copeland ZPV36K1 scroll compressor. The refrigerant is R410A, and the nominal capacity is 3 tons. The speed range is 1,800 to 4,500 rpm under cooling mode and 1,800 to 7,000 rpm under heating mode. The maximum defrost speed is 4,500 rpm. The displacement is 1.31 in^3/rev.

Figure 4-12 Variable-speed scroll compressor.

Heat Exchangers

Both the ID and OD heat exchangers are finned-tube heat exchangers. The fin type of the OD heat exchanger is smooth wavy (Figure 4-13). The ID heat exchanger is an N type heat exchanger with smooth fins, as shown in Figure 4-14. Table 4-1 lists the parameters of the two heat exchangers.

Figure 4-13 OD heat exchanger and fins.

Figure 4-14 ID heat exchanger and fins.

Table 4-1 Parameters of the ID and OD heat exchangers.

Parameter (Unit)	OD	ID
Frontal area (ft^2)	22.22	5.75
Number of rows	2	2
Total number of circuits	3	6
Tubes per circuit	22 (Circuits 1 & 2) 20 (Circuit 3)	20
Number of equivalent circuits	3	6
Horizontal tube spacing (in)	0.863	0.7875
Vertical tube spacing (in)	1.04	0.74
Number of return bends	58	114
Outside diameter of tubing (in)	0.375	0.3125
Inside diameter of tubing (in)	0.311	0.2485
Finned length (in)	100	17.25
Finned height (in)	32	48
Fin density (fins/in)	22	17
Fin thickness (in)	0.004	0.004
Fin pattern	Smooth wavy	Smooth
Fin material	Aluminum	Aluminum
Refrigerant flow	Cross-parallel flow	Cross-parallel flow

Expansion Valves

Both the EXV and TXV are used to control the refrigerant flowing into the evaporator. The EXV works under heating mode while the TXV works under cooling mode. The EXV (Model: EXM-125) has 250 steps and is controlled by a stepper motor, as shown in Figure 4-15. The supply voltage is +12 VDC.

Figure 4-15 EXV.

Figure 4-16 shows the TXV. The valve opening depends on the difference between inlet and outlet pressure. Inlet pressure is the saturated pressure corresponding to the refrigerant temperature at the outlet of the ID heat exchanger. Outlet pressure is the sum of the ID heat exchanger pressure and the spring force. A sensor bulb is located at the outlet of the ID heat exchanger to measure refrigerant temperature. Higher superheat means larger pressure difference and larger valve opening.

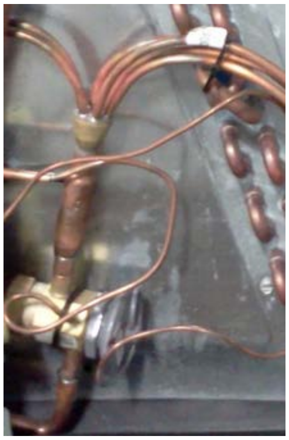

Figure 4-16 TXV.

Fans

The system has two fans: an ID blower (Figure 4-17) and an OD fan (Figure 4-18). The ID blower has three stages: low (400 cfm), medium (500 cfm), and high (800 cfm). The OD fan is a variable-speed fan (Model: PROTECH 70-21858-17). The range of the OD air flow rate is 0 to 3,300 cfm.

Figure 4-17 ID blower.

Figure 4-18 OD fan.

Reversing Valve

The reversing valve is used to control the direction of refrigerant flow. The supply voltage is 0 or 24 VAC. When the supply voltage is zero, the valve is relaxed and the system runs in cooling mode. When the voltage is 24 VAC, the valve is energized and the system runs in heating mode.

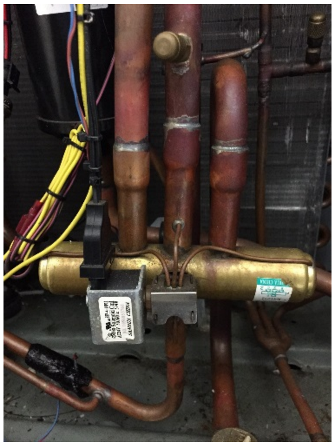

Figure 4-19 Reversing valve.

Sensors

Measured data include pressure, temperature, and relative humidity. Table 4-2 details the location of all sensors.

Table 4-2 Sensors for the 3-ton heat pump system.

Parameter	Location
Refrigerant pressure	Suction line
	Discharge line
Refrigerant temperature	Suction line
	Discharge line
Air pressure drop	Outlet of the OD fan
Air temperature	ID heat exchanger inlet
	ID heat exchanger outlet
	OD heat exchanger inlet
	OD heat exchanger outlet
Air relative humidity	ID heat exchanger inlet
	ID heat exchanger outlet
	OD heat exchanger inlet
Defrost sensor temperature	OD heat exchanger surface

Refrigerant pressure is measured with the sensor 2CP5-47-1 manufactured by Sensata Technologies (Figure 4-20). The sensor has a range of 0 to 500 psi and an accuracy of $\pm 1.2\%$. The supply voltage is 5 VDC, and the output voltage is 0.5 to 4.5 VDC. The operating temperature is -40 to 135℃. Two pressures sensors are installed at the inlet and outlet of the compressor to measure the suction and discharge pressure.

Figure 4-20 Pressure sensor.

Thermistors and thermocouples are used for temperature measurement (Figure 4-21 and Figure 4-22). Four thermistors are located at the inlet and outlet of the ID unit, the suction line, and the surface of the OD heat exchanger. The model number is USP 10973, US sensor. The maximum temperature rating is 105℃ (221°F). A thermocouple is used to measure ambient temperature. The model number is EXTT-T-24. The maximum temperature is 100℃ (212°F).

Figure 4-21 Thermistor.

Figure 4-22 Thermocouple.

TDK Corporation's CHS series humidity sensors are used to measure relative humidity (Figure 4-23). Three sensors are used to measure relative humidity at the inlet of the OD heat exchanger and at the inlet and outlet of the ID unit. The supply voltage is

+5 VDC and the output is 0 to 5 VDC. The accuracy is ±5% and the response time is 1 minute. The operating temperature is 0 to 50℃.

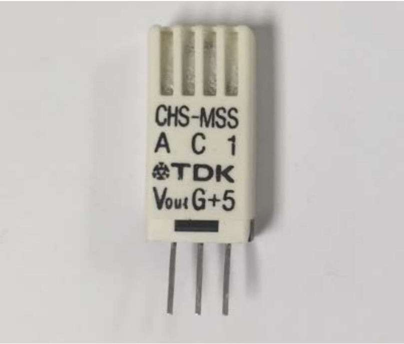

Figure 4-23 Relative humidity sensor.

DAQ and Control System

The DAQ and control system include a laptop, NI modules, and a control box, as shown in Figure 4-24. The sample rate of the DAQ system is 2 seconds. NI modules include NI 9213, NI 9264, NI 9220, and NI USB-6008 (two) (Figure 4-25). NI 9213 is a thermocouple model with 16 channels. The module supports J, K, T, E N, B, R, and S thermocouple types. NI 9220 is a 16-channel simultaneous analog input module. NI 9264 is a 16-channel simultaneous analog output module. The output range of these two analog modules is ±10 V. The operating temperature for the above three types of modules is −40 to 70℃. NI USB-6008 has eight analog inputs, two static analog outputs, and 12 digital inputs (outputs). The range for analog inputs is ±10 V and for analog outputs is 0 to 5 V. The operating temperature is 0 to 70℃.

Figure 4-24 DAQ system.

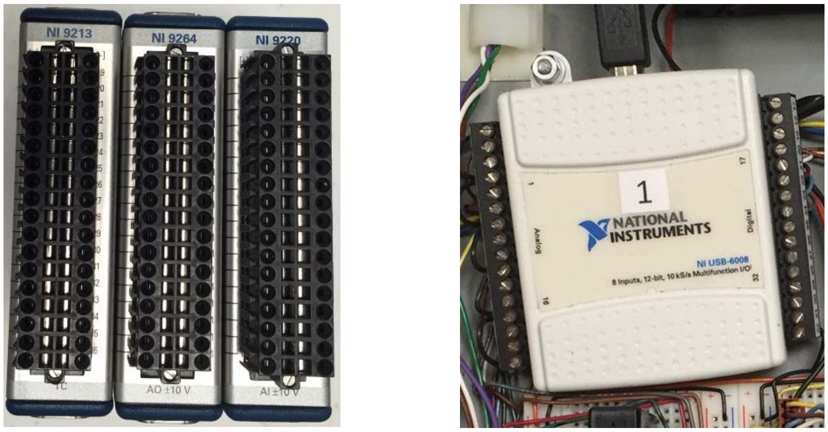

Figure 4-25 NI 9213, NI 9264, NI9220, and NI USB 6008.

The control box has a transformer, an Arduino, and five terminals (Figure 4-26). Terminal 1 provides control voltages to drive the EXV and OD fan. Terminals 2 and 3 provide +5-VDC signal conditioning circuits for temperature, pressure, and humidity sensors. Terminals 4 and 5 provide +24-VAC voltage to drive the ID blower, compressor contactor, and reversing valve.

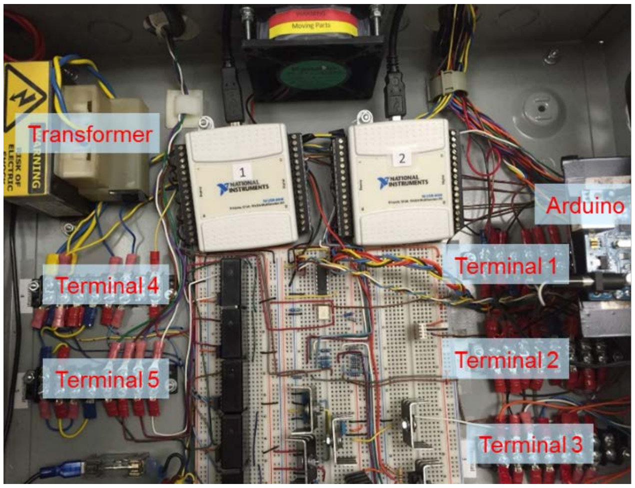

Figure 4-26 Control box.

5. MODEL VALIDATION

This chapter briefly introduces model validation results finished by Shuangshuang Liang [23]. A wavelet-based parameter tuning and validation method is developed and applied to heat pump systems. Validation results shown in this chapter are based on experimental data of a Rheem 5-ton heat pump system, which is very close to the Rheem 3-ton system described in Chapter 4. The first part introduces the validation results based on pseudo-steady data. Then, the simultaneous tuning results, based on both pseudo-steady-state and transient data, are presented.

Validation Results Using Pseudo-Steady-State Data

Expansion Valve Parameters

The tuned parameters of the TXV model are the two coefficients shown in Equation (2.4). The validation result is shown in Figure 5-1. For most cases, the error between the predicted refrigerant mass flow rate and the experimental data is less than 10%. The tuned parameters of the EXV model are the discharge coefficient map and valve area. The error between the predicted and the experimental data is less than 10% (Figure 5-2).

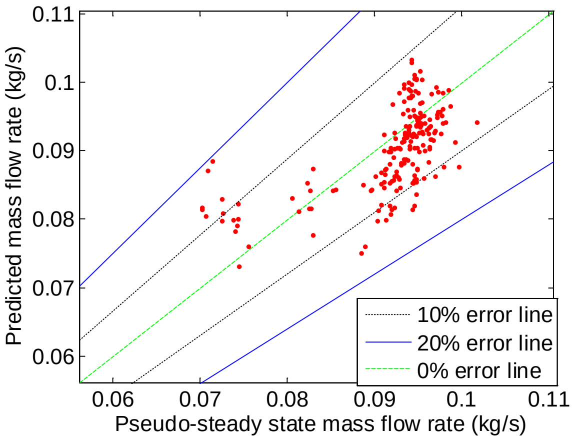

Figure 5-1 Refrigerant mass flow rate through the TXV.

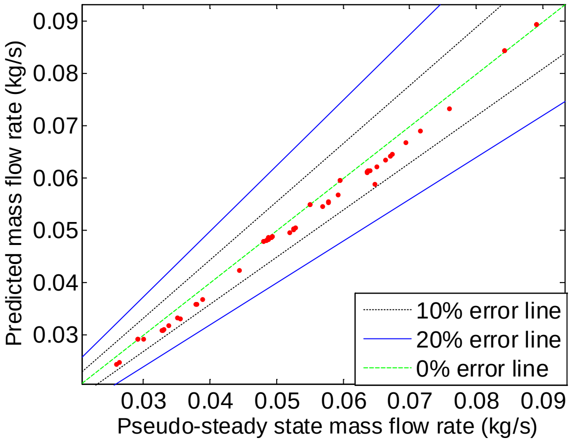

Figure 5-2 Refrigerant mass flow rate through the EXV.

Compressor Parameters

Both the volumetric efficiency and adiabatic efficiency maps are tuned based on pseudo-steady state data. Tuned refrigerant mass flow rate and pressure consumption are shown in Figure 5-3 and Figure 5-4. Results indicate that the model can give good predictions for mass flow rate and compressor power.

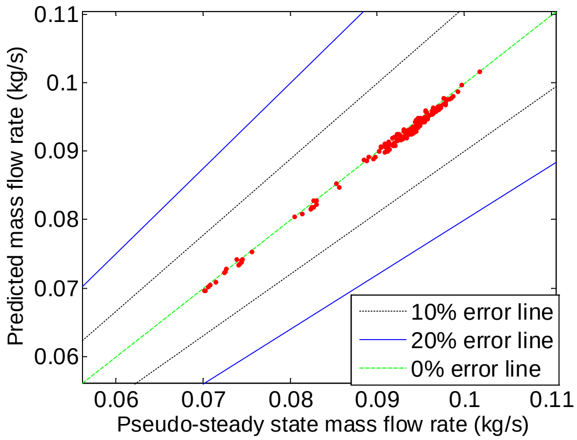

Figure 5-3 Refrigerant mass flow rate through the compressor.

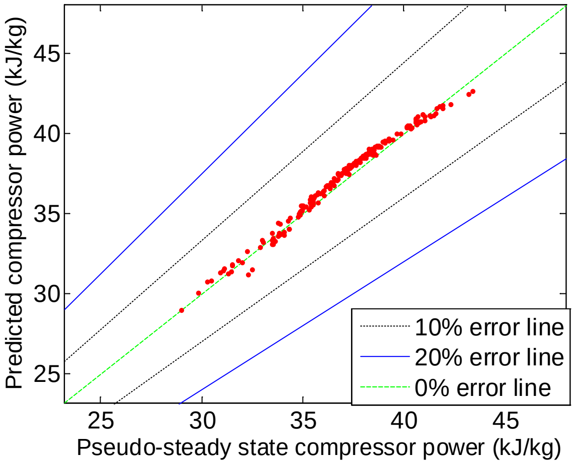

Figure 5-4 Power consumption.

FCV Heat Exchanger

The tuning parameters for the heat exchanger model include the cross-section area of the tube, internal and external surface area, and tube length and diameter. The above parameters are tuned simultaneously. The predicted parameters include pressure, outlet enthalpy, and outlet temperature. Figure 5-5 and Figure 5-6 show validation results for the evaporator and condenser models. The averaged errors of the predicted parameters are less than 10%.

Heat Pump System

The heat pump model is validated based on pseudo-steady heating and cooling data. Tuning parameters include ID and OD heat exchanger parameters (tube length, tube diameter, tube cross-section area, internal and external surface area, and heat transfer coefficient) and pipe parameters (heat transfer coefficient, diameter, and length). Validation results are shown in Figure 5-7 and Figure 5-8. The average relative errors of all the outputs are 13.8% under heating mode and 5.53% under cooling mode.

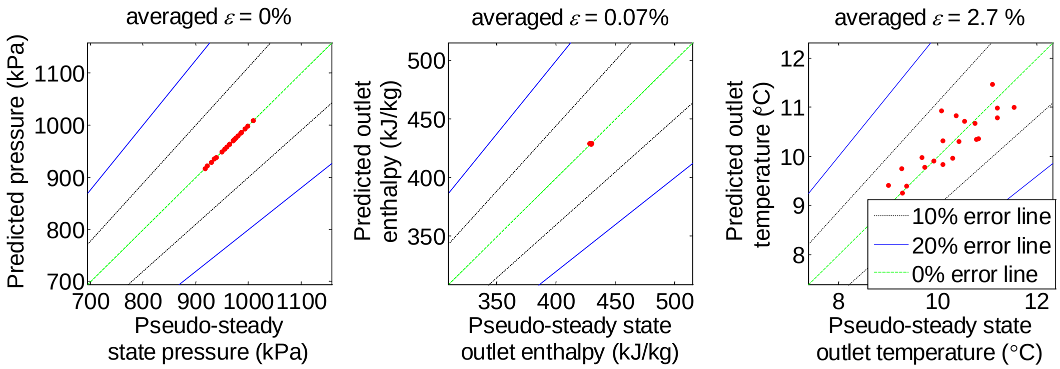

Figure 5-5 Evaporator model validation using Rheem 5-ton pseudo-steady state cooling data.

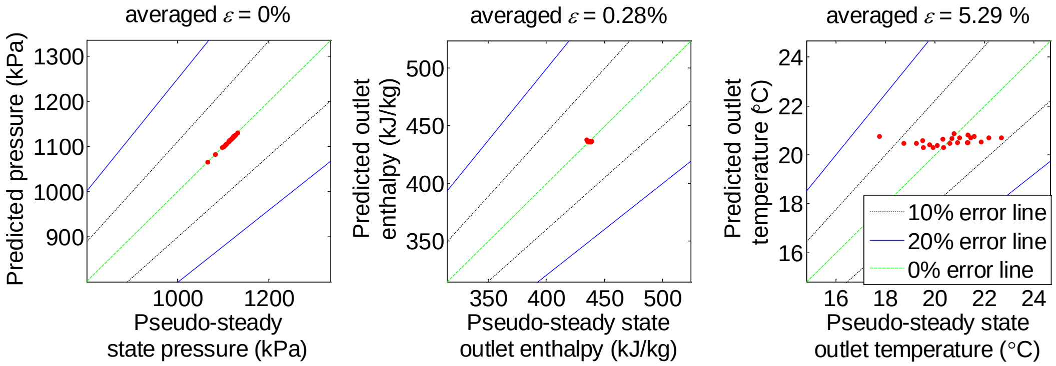

Figure 5-6 Condenser model validation using Rheem 5-ton pseudo-steady state cooling data.

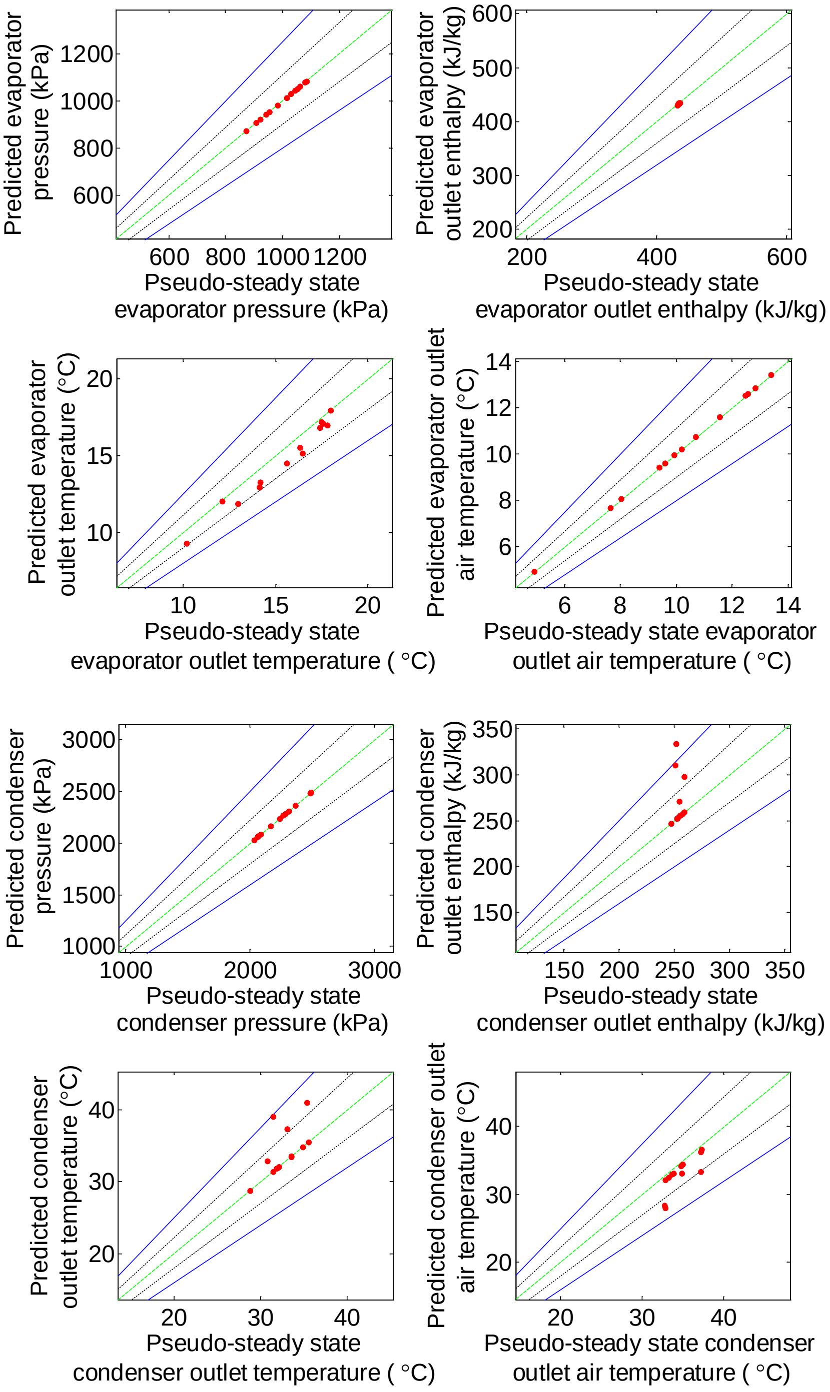

Figure 5-7 Heat pump model validation using pseudo-steady state heating data.

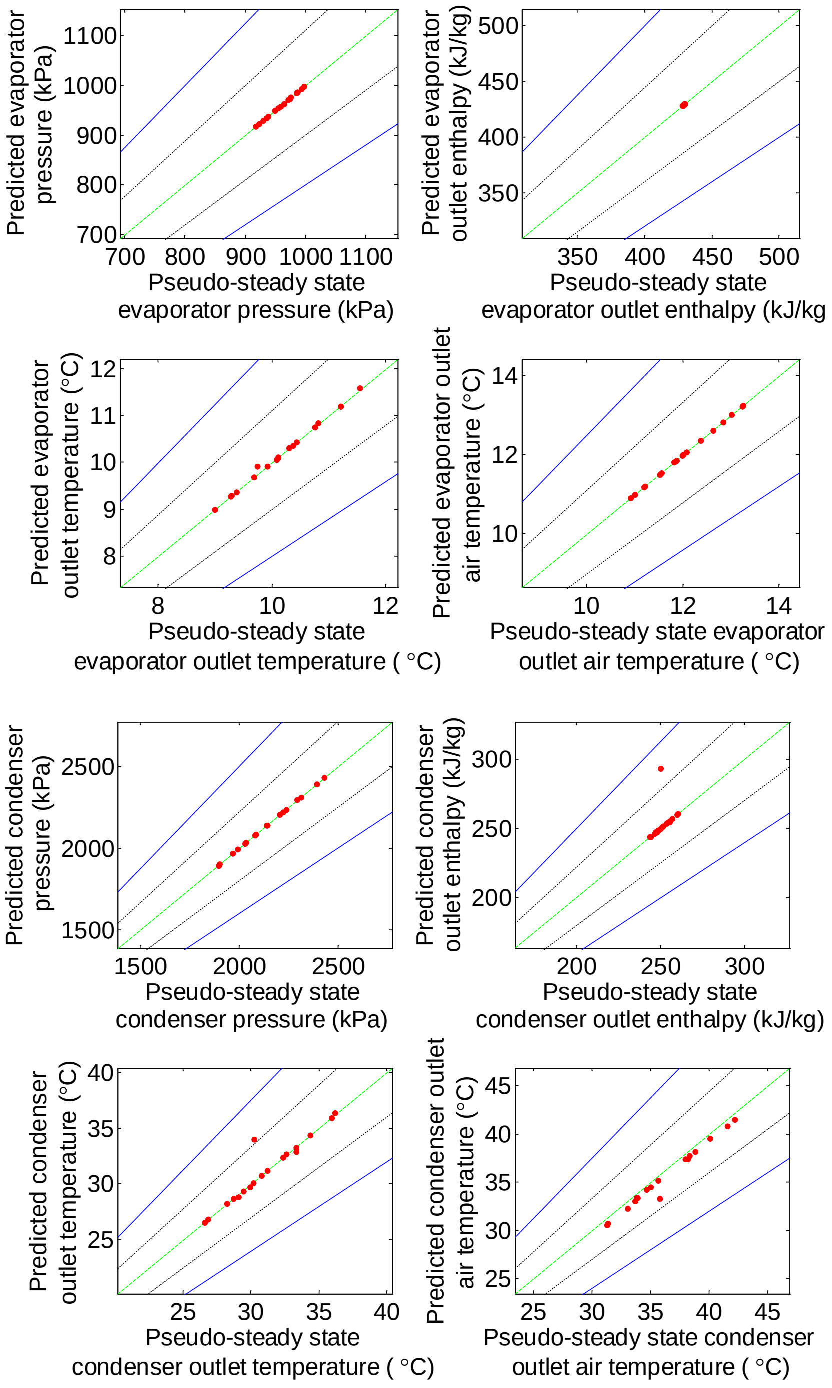

Figure 5-8 Heat pump model validation using pseudo-steady state cooling data.

Validation Results Using Both Pseudo-Steady State and Transient Data

FCV Heat Exchanger

Using the cooling mode as an example, the tuning parameters include the internal and cross area of the tube, diameter and length of the heat exchanger, and TXV and compressor map coefficients. The outputs used in the objective function include refrigerant pressure, outlet enthalpy, and outlet temperature. Validation results for the evaporator model and condenser model are shown in Figure 5-9 and Figure 5-10, respectively. The black lines represent the nominal predicted outputs of the evaporator model, while the blue lines show the final tuned outputs obtained from the proposed parameter tuning method. The good match indicates that simultaneous tuning works for the heat exchanger model.

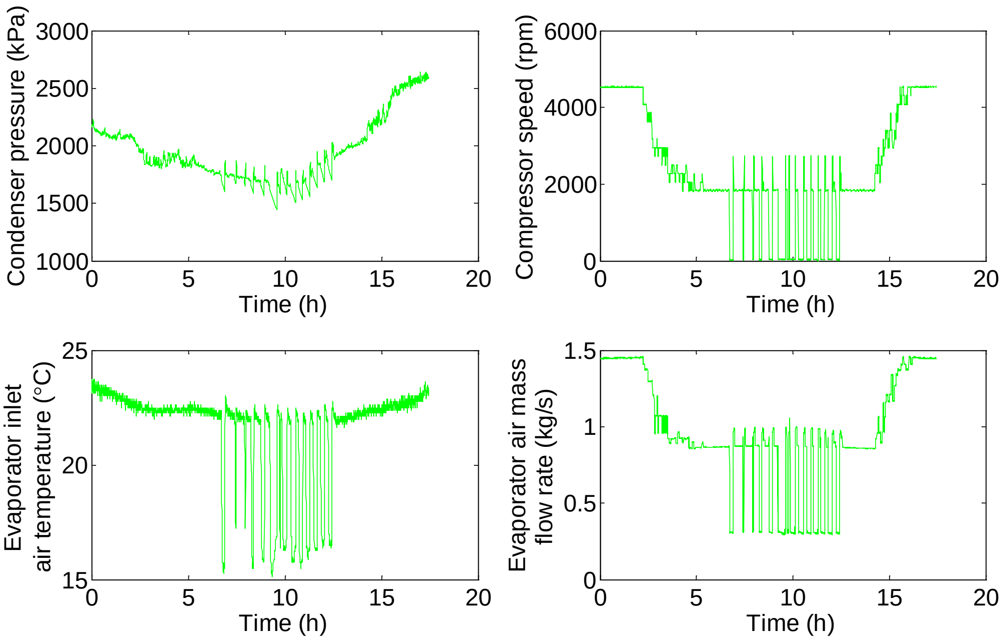

(a) Inputs

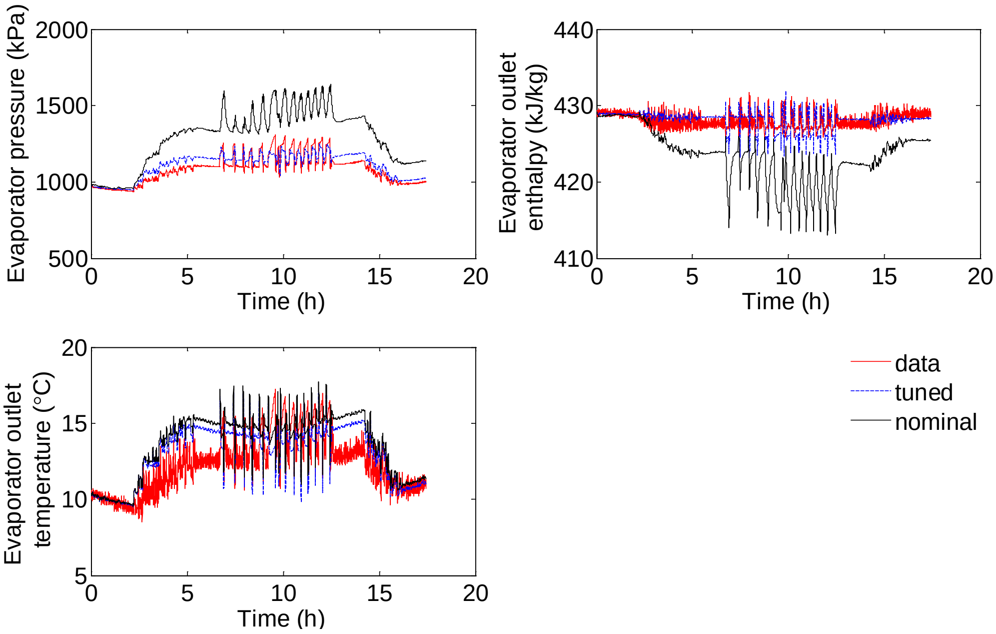

(b) Outputs

Figure 5-9 Evaporator model validation using Rheem 5-ton field cooling data, 05/30/2011.

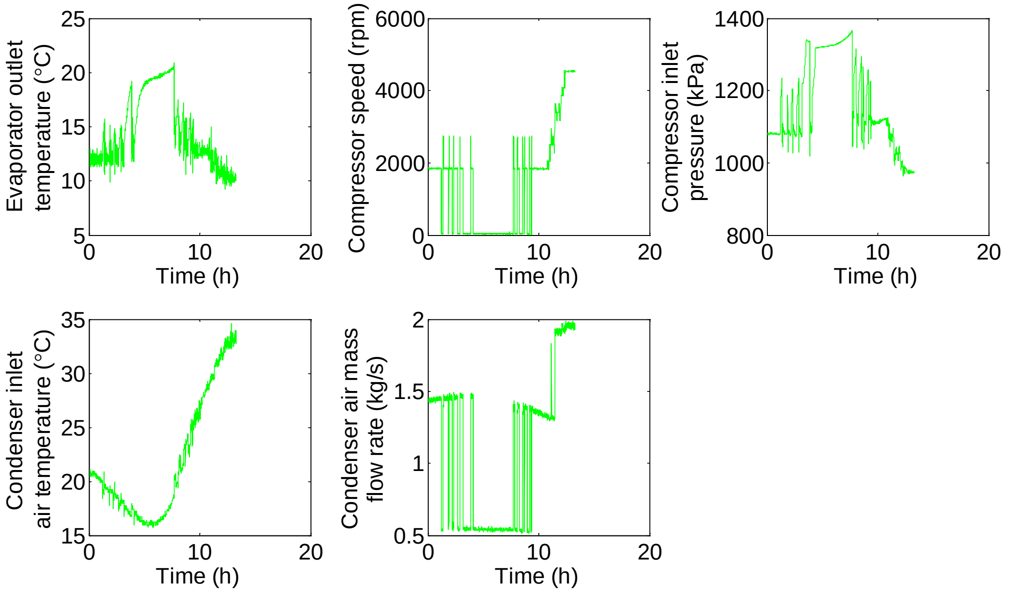

(a) Inputs

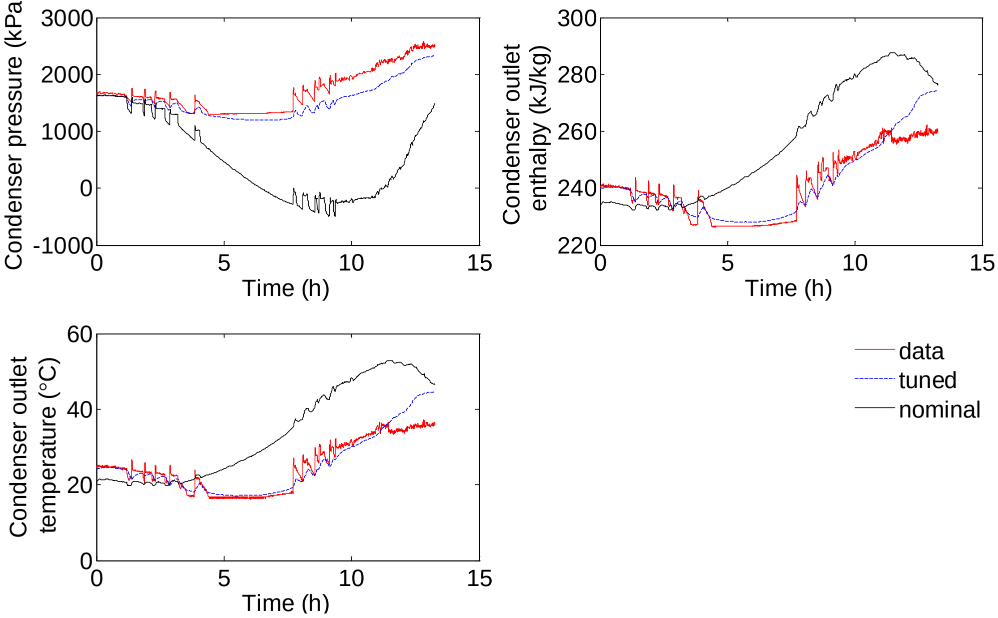

(b) Outputs

Figure 5-10 Condenser model validation using Rheem 5-ton field cooling data, 06/06/2011.

Heat Pump System

Tuning parameters for the heat pump model include TXV coefficients, compressor map coefficients and cross area of the tube, internal area, diameter, and length of the heat exchanger. The outputs used in the objective function include evaporator pressure, evaporator refrigerant outlet temperature, condenser pressure, and condenser refrigerant outlet temperature. Validation results are shown in Figure 5-11. The black lines represent the nominal predicted outputs, while the blue lines indicate the final tuned outputs with the proposed parameter tuning method. Relative error of the complete heat pump model is around 12.7%. The matches of both steady-state and transient data indicate that simultaneous tuning is feasible for the complete heat pump model.

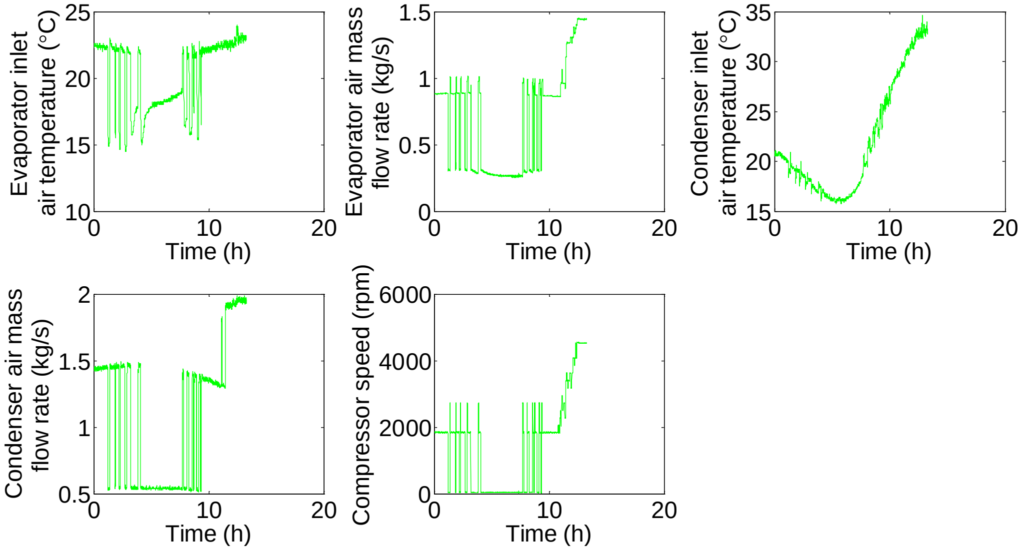

(a) Inputs

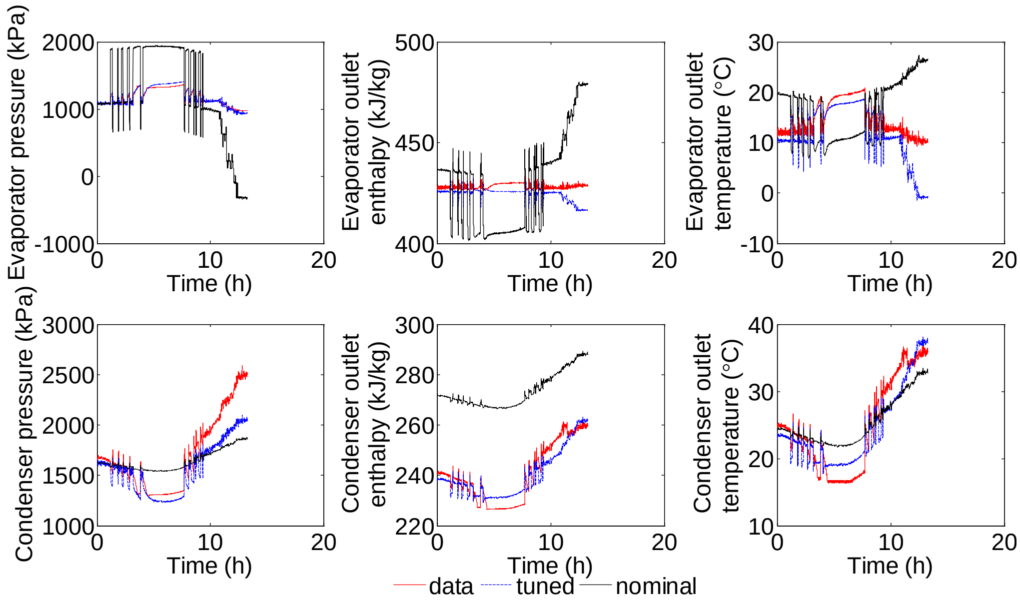

(b) Outputs

Figure 5-11 Complete heat pump model validation using Rheem 5-ton field cooling data, 06/06/2011.

6. DYNAMIC MODEL WITH CONTROL

This chapter describes energy optimal control design based on heat pump dynamic models. Three control strategies described in this chapter are SISO control with fan scheduling, multi-SISO control, and MIMO control. The first step is to generate the optimal fan and pressure scheduling using pseudo-steady state data. The schedulings provide fan speed and pressure setpoints for controllers. The above three control algorithms are then validated using simulated data from the heat pump dynamic models.

Control Architectures

In order to compare the influences of SISO control and MIMO control on heat pump systems, three control strategies are proposed.

1) SISO control with fan scheduling (FS)

This control strategy is designed to test optimal fan speed scheduling on system performance. As shown in Figure 6-1, the strategy uses optimal fan speed scheduling and two SISO control loops for cooling (heating) capacity and superheat. Here, optimal fan speed scheduling is the speed that maximizes COP for given cooling or heating capacity setpoints. Both fan speeds use open loop control. The disadvantage is that changes of system characteristics, like heat exchanger fouling, can lead to deviations from the best COP because there is no feedback for the fan speed control.

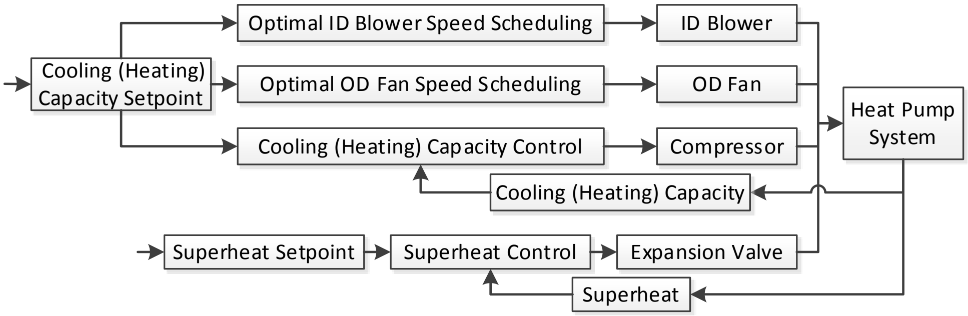

Figure 6-1 Flow chart of SISO control with fan scheduling for cooling (heating) tests.

2) Multi-SISO control

Multi-SISO control is proposed to overcome the lack of fan speed control in the first scenario. Discharge and suction pressure control are added, as shown in Figure 6-2. Optimal pressure scheduling is used to provide the setpoint for the pressure control. The multi-SISO control includes four loops: discharge pressure control, suction pressure control, cooling (heating) capacity control, and superheat control. Possible conflicts among these SISO controls become more critical.

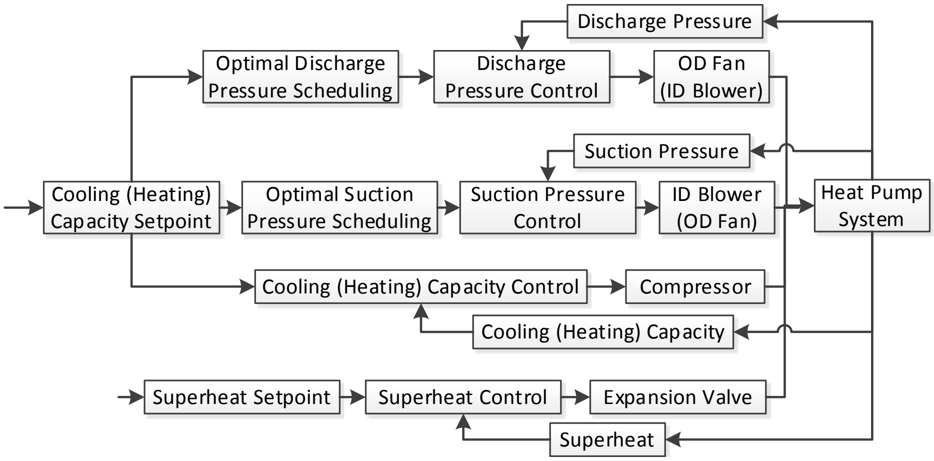

Figure 6-2 Flow chart of multi-SISO control for cooling (heating) tests.

3) MIMO control

MIMO control is designed to eliminate the possible conflicts in SISO control. Figure 6-3 shows a four-input, four-output control for heat pump systems. The controller generates control signals by comparing the setpoints and measured parameters. The parameters are cooling (heating) capacity, discharge and suction pressure, and superheat. The optimal discharge pressure and suction pressure schedulings are used to provide the pressure setpoints.

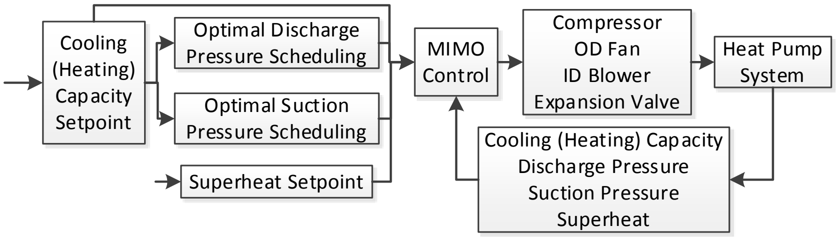

Figure 6-3 Flow chart of MIMO control for cooling (heating) tests.

Based on above descriptions the advantages and disadvantages of the three proposed control architectures are summarized in Table 6-1.

Table 6-1 Advantages and disadvantages of three control strategies.

Control Strategy	Advantage	Disadvantage
SISO control with fan scheduling	Low complexity: fewer feedback controllers. High feasibility: easy controller tuning and simple implementation.	Suboptimal COP as ambient conditions change.
Multi-SISO control	Improved robustness: feedback on all actuators maximizes COP for changing conditions.	Possible conflicts among SISO controllers.
MIMO control	Better tracking performance: smaller deviation and less rising time	High complexity: requires a dynamic model, experienced control designer.

Optimal Fan Speed and Pressure Scheduling

COP is defined as the ratio of cooling (heating) capacity and total power consumption. When the system runs in steady state, COP can be expressed as a function of cooling (heating) capacity and suction and discharge pressure. COP can also be defined as a function of cooling (heating) capacity and ID and OD fan speeds. Pressure curve and fan speed curve are defined as:

$$COP_{fan} = a_0 + a_1 * P_e + a_2 * P_c + a_3 * Q + a_4 * P_e * P_c + a_5 * P_e * Q + a_6 * P_c * Q + a_7 * P_e^2 + a_8 * P_c^2 + a_9 * Q^2 \tag{6.1}$$

$$COP_{pressure} = b_0 + b_1 * \dot{V}_{ID} + b_2 * \dot{V}_{OD} + b_3 * Q + b_4 * \dot{V}_{ID} * \dot{V}_{OD} + b_5 * \dot{V}_{ID} * Q + b_6 * \dot{V}_{OD} * Q + b_7 * \dot{V}_{ID}^2 + b_8 * \dot{V}_{OD}^2 + b_9 * Q^2 \tag{6.2}$$

Cooling Mode

To ensure the system is running in a pseudo-steady state, nine groups of tests are carried out. For each group, the compressor speed and ID blower speed stay unchanged, while the OD fan speed increases slowly at a rate of 1 $\mathrm{cfm/s}$. Control signals are shown in Figure 6-4 and Figure 6-5.

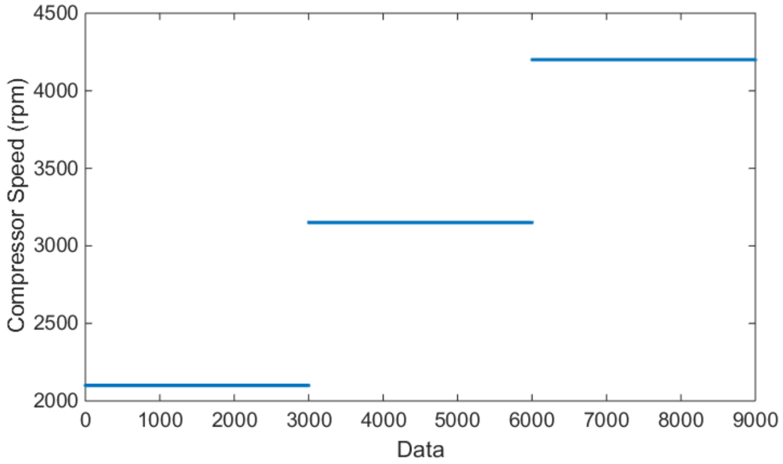

Figure 6-4 Compressor speed.

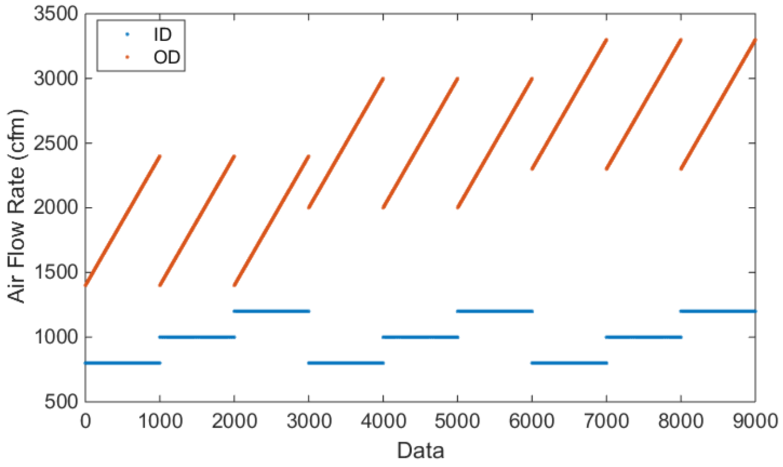

Figure 6-5 Air flow rate.

Pressure is shown in Figure 6-6. For each group, when the OD fan speed increases, the discharge pressure decreases while the suction pressure is almost constant. High compressor speed indicates high discharge pressure and low suction pressure. High ID blower means high suction pressure. However, the effect of the ID blower speed on discharge pressure is negligible.

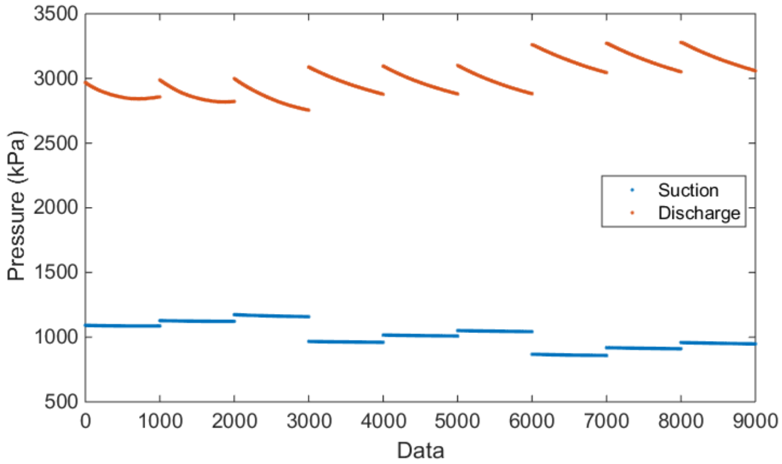

Figure 6-6 Suction and discharge pressure.

Cooling capacity is shown in Figure 6-7. For a given compressor speed and ID blower speed, the heating capacity is almost constant. High compressor speed indicates high cooling capacity. For a given compressor speed, cooling capacity goes up when the ID blower speed increases from 800 to 1,200 cfm.

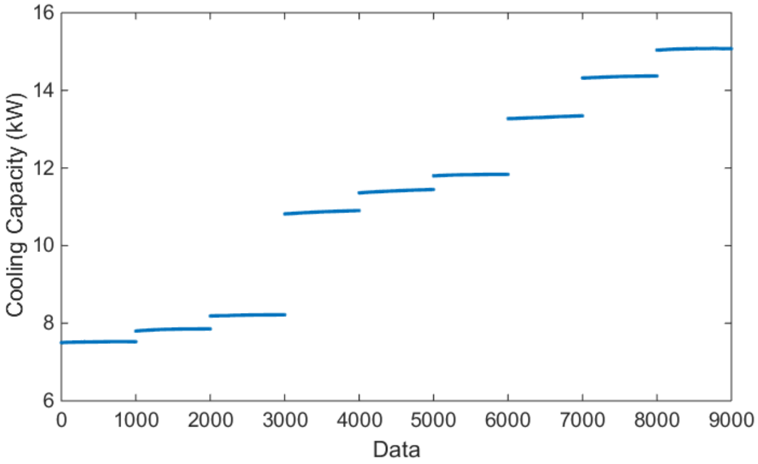

Figure 6-7 Cooling capacity.

COP is shown in Figure 6-8. For each case, COP first increases and then drops when the OD fan speed increases. There exists a maximum COP for each case. For a given compressor speed, higher ID blower speed indicates higher COP. For a given ID blower, higher compressor speed leads to lower COP.

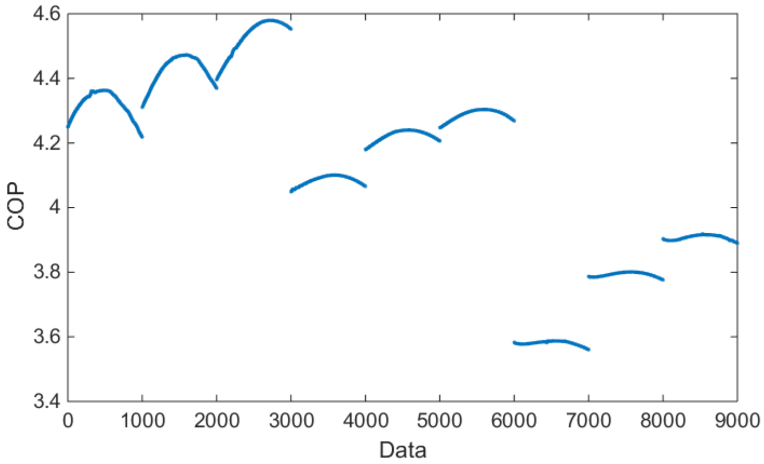

Figure 6-8 COP.

The fan speed curve and pressure curve are obtained by:

$$COP_{pressure} = -22.0187 + 0.0222 * P_e + 0.0102 * P_c - 0.2332 * Q - 0.0001 * P_e * Q + 0.0002 * P_c * Q - 0.0137 * Q^2 \tag{6.3}$$

$$COP_{fan} = 3.0085 + 0.0020 * \dot{V}_{ID} + 0.0005 * \dot{V}_{OD} - 0.0459 * Q + 0.0002 * \dot{V}_{ID} * Q - 0.0148 * Q^2 \tag{6.4}$$

Comparison between COP from the dynamic model and COP generated by the curves are shown in Figure 6-9 and Figure 6-10. The error is less than 10%.

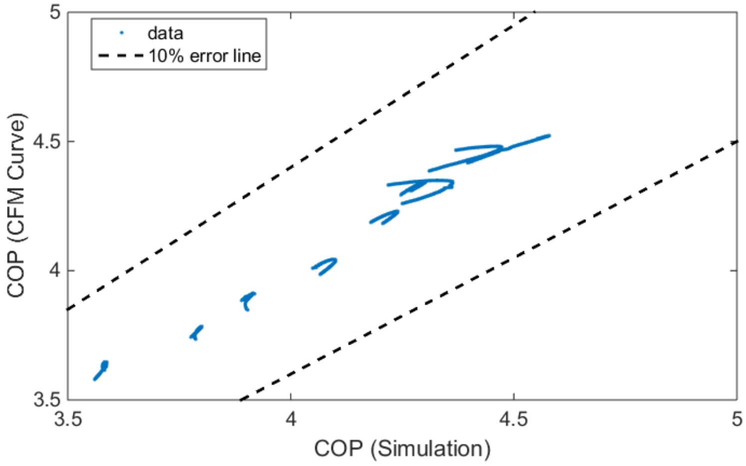

Figure 6-9 COP from the dynamic model and fan speed curve.

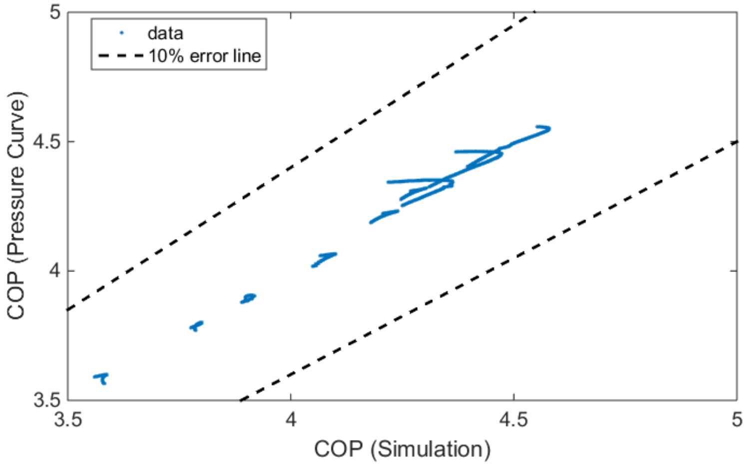

Figure 6-10 COP from the dynamic model and pressure curve.

Fan speed scheduling is shown in Figure 6-11. When the cooling capacity setpoint changes from 8 to 16 kW, the OD air flow rate increases from 2,100 to 3,000 cfm. Meanwhile, the ID blower speed changes from 1,180 to 1,200 cfm.

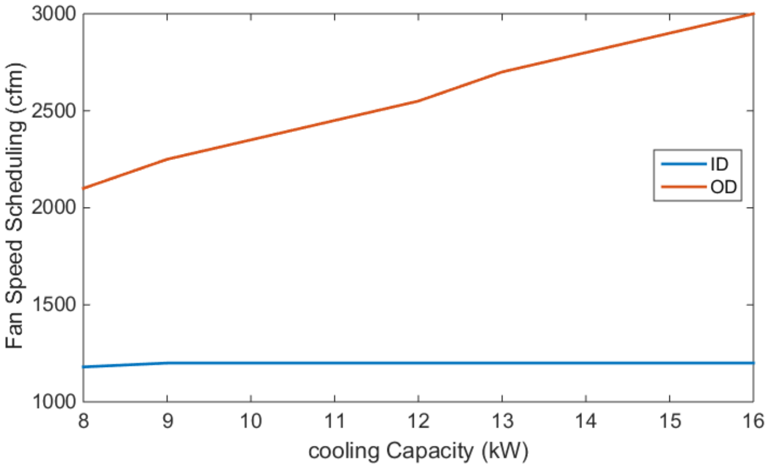

Figure 6-11 Optimal fan speed scheduling for cooling tests.

Pressure scheduling is shown in Figure 6-12. Higher cooling capacity setpoint indicates higher discharge pressure but lower suction pressure. When the setpoint increases from 8 to 16 kW, the discharge pressure setpoint increases from 2,765 to 3,445 kPa, while the suction pressure setpoint drops from 1,110 to 790 kPa.

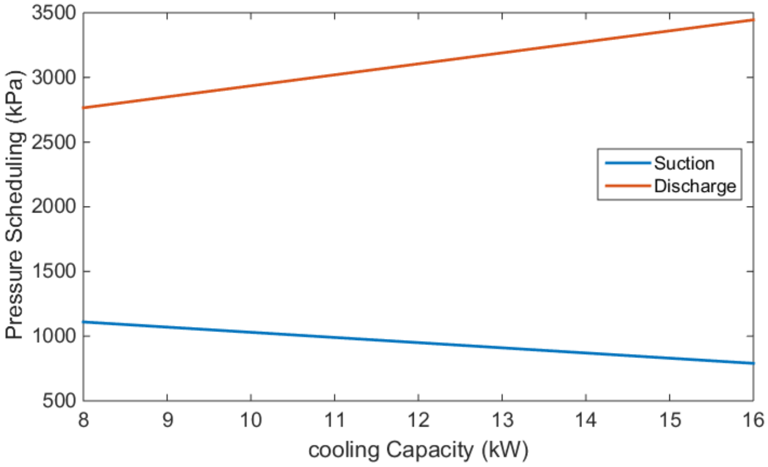

Figure 6-12 Optimal pressure scheduling for cooling tests.

Heading Mode

For heating mode, the control signals for the pseudo-steady state data generation are shown in Figure 6-13 and Figure 6-14. There are 12 test groups. For each group, the compressor speed and ID blower speed stay constant, while the OD fan speed increases slowly. In the first group as an example, the compressor speed is 1,800 rpm, and the ID blower speed is 600 cfm. The OD fan speed increases from 1,200 to 2,500 cfm with a rate of 1 cfm/s.

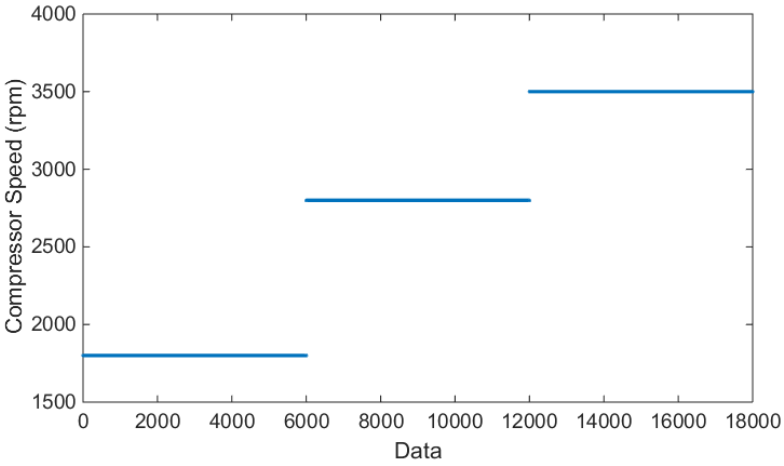

Figure 6-13 Compressor speed.

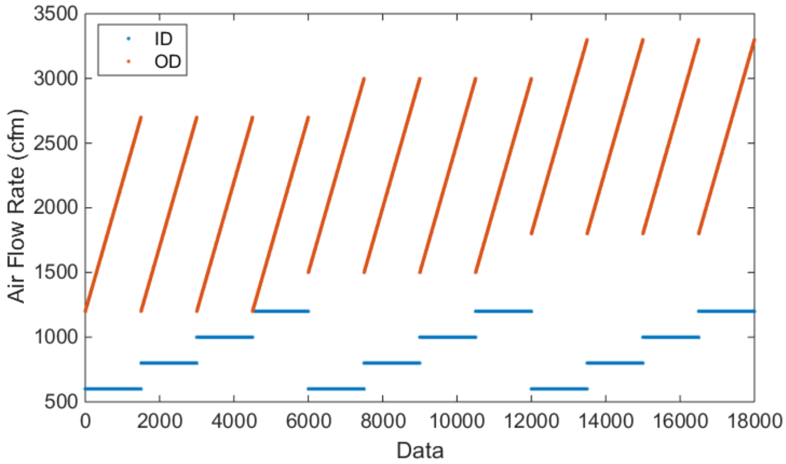

Figure 6-14 ID and OD air flow rates.

The pseudo-steady state data are shown in Figure 6-15 through Figure 6-17. Both discharge pressure and heating capacity are significantly affected by the compressor speed. Higher compressor speed indicates larger discharge pressure and higher heating capacity. For a given compressor speed and ID blower speed, COP first increases and then decreases when the OD fan speed increases.

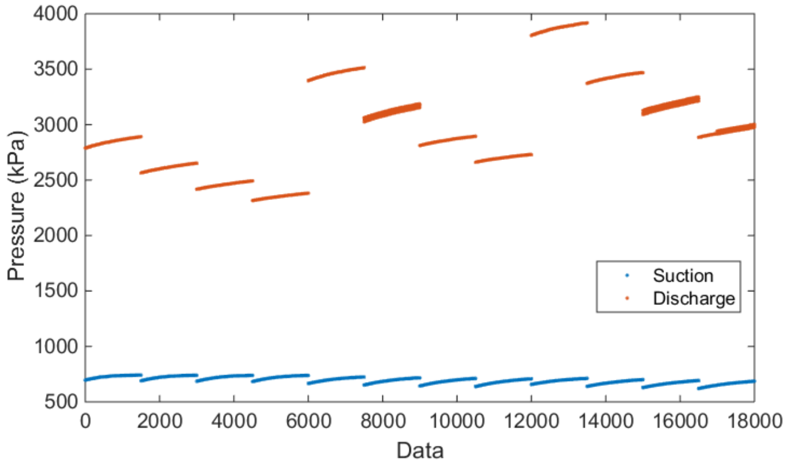

Figure 6-15 Suction and discharge pressure.

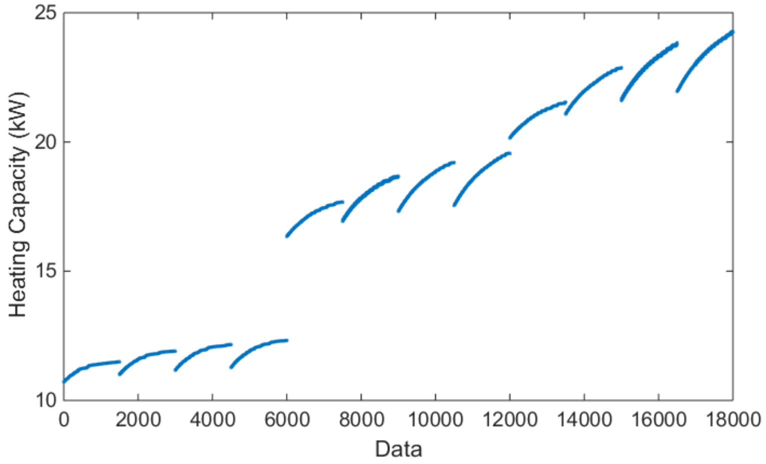

Figure 6-16 Heating capacity.

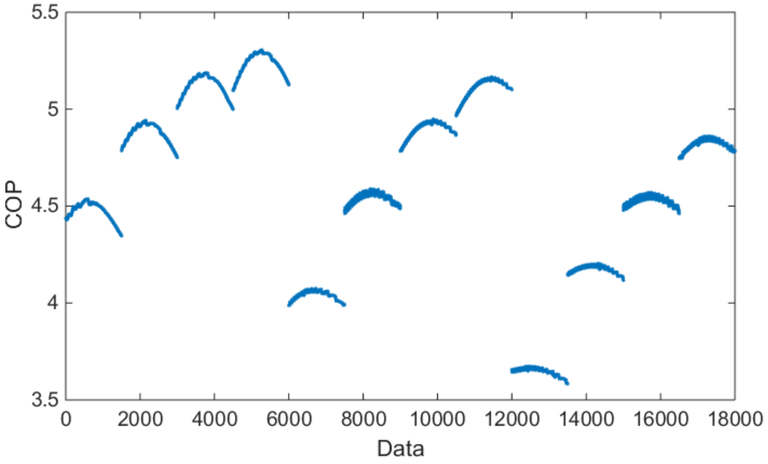

Figure 6-17 COP.

Fan speed curve and pressure curve are estimated based on the above pseudo-steady state data.

$$COP_{pressure} = -27.6591 + 0.0932 * P_e - 0.0026 * P_c + 0.5844 * Q - 0.0005 * P_e Q - 0.0001 * P_e^2 - 0.0057 * Q^2 \tag{6.5}$$

$$COP_{fan} = 2.6656 + 0.0041 * \dot{V}_{ID} + 0.0005 * \dot{V}_{OD} - 0.0672 * Q + 0.0001 * \dot{V}_{ID} * Q - 0.0053 * Q^2 \tag{6.6}$$

A comparison between COP from the dynamic model and COP generated by the curves is shown in Figure 6-18 and Figure 6-19. The error is less than 10%.

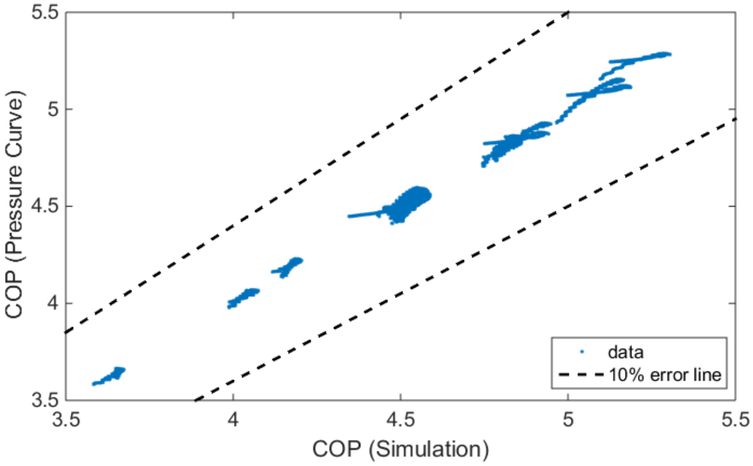

Figure 6-18 COP based on the dynamic model and pressure curve.

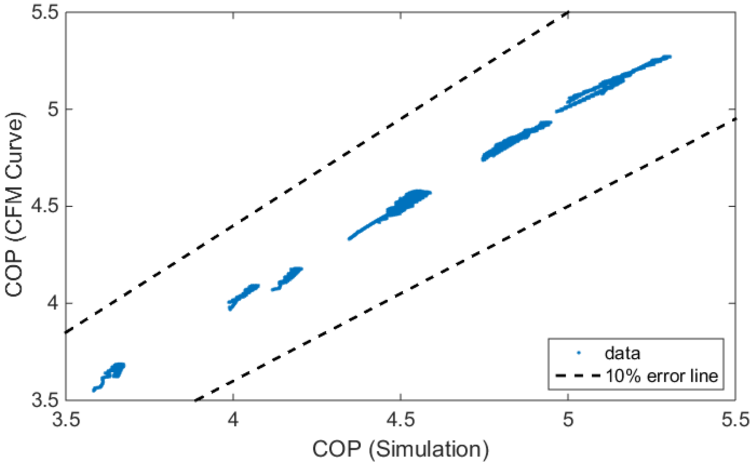

Figure 6-19 COP based on the dynamic model and fan speed curve.

Optimal pressure scheduling is shown in Figure 6-20. Higher heating capacity indicates higher discharge pressure and lower suction pressure. Optimal fan speed scheduling is shown in Figure 6-21. The ID blower speed always runs at its maximum speed, while the OD fan speed goes up as the heating capacity setpoint increases.

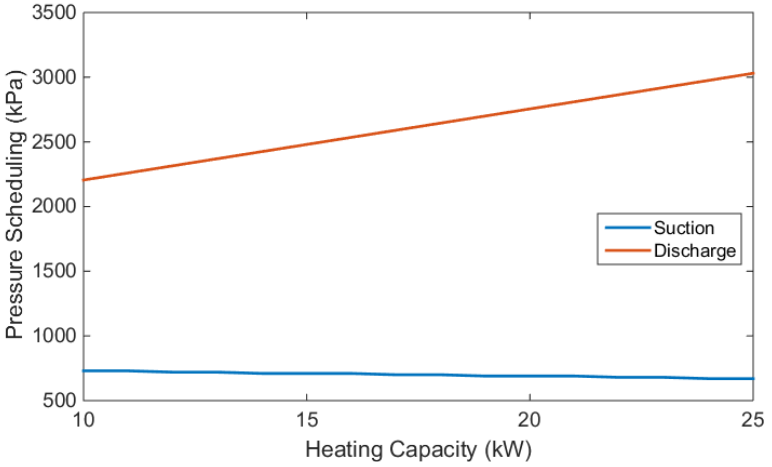

Figure 6-20 Pressure scheduling for heating tests.

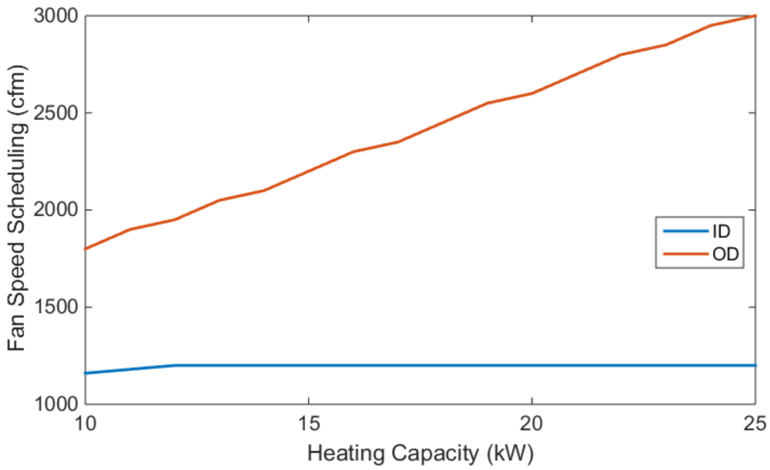

Figure 6-21 Fan speed scheduling for cooling tests.

SISO Control with Fan Scheduling

The control loops include the optimal fan speed scheduling and SISO control. Both the ID blower and OD fan use the optimal fan speed scheduling (Figure 6-22 and Figure 6-23). PID control is applied for both cooling (heating) capacity control (Figure 6-24) and superheat control (Figure 6-25).

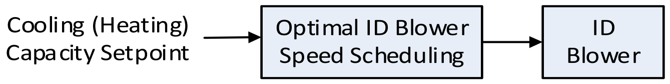

Figure 6-22 ID blower speed control loop.

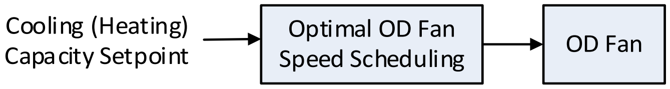

Figure 6-23 OD fan speed control loop.

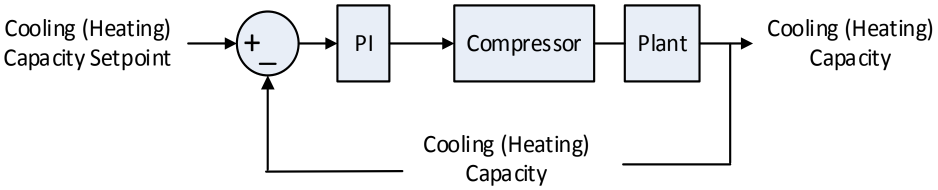

Figure 6-24 Cooling (heating) capacity control loop.

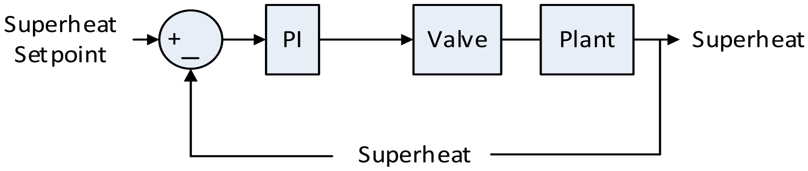

Figure 6-25 Superheat control loop.

Multi-SISO Control

The control algorithm has multi-SISO controllers and ID blower speed scheduling. Based on the fan speed scheduling, the maximum COP for the specified cooling (heating) capacity is obtained when the ID blower runs at its highest speed. Here, the optimal fan speed scheduling is used to control the blower speed.

The cooling (heating) capacity control (Figure 6-24) and superheat control (Figure 6-25) are also used here. The OD fan speed control uses one PI controller with a fan speed lookup table, as shown in Figure 6-26. The control loop uses discharge pressure as the feedback signal during cooling mode and uses suction pressure as the feedback signal during heating mode. With fan speed scheduling, the OD fan speed can reach the desired values quickly when the cooling capacity setpoint changes.

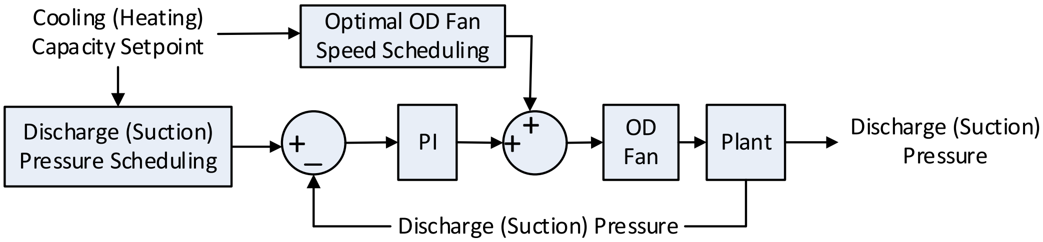

Figure 6-26 Discharge (suction) pressure control loop under cooling (heating) mode.

MIMO Control

LQG is used to design the MIMO control. The control loop is shown in Figure 6-27. For cooling tests, the control signals include compressor speed and OD fan speed. The feedback signals are cooling capacity and discharge pressure. For heating tests, the feedback signals are heating capacity, suction pressure, and superheat. The three control signals generated by the controller are compressor speed, OD fan speed, and valve opening. The optimal fan speed scheduling is also used to control the ID blower speed.

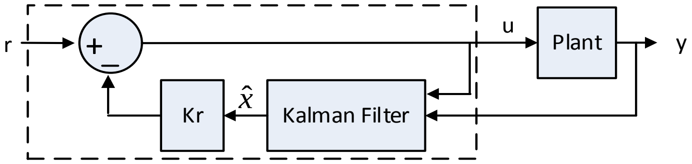

Figure 6-27 LQG controller.

The LQG controller minimizes the cost function:

$$J = E\left\{\lim_{\tau\to\infty}\frac{1}{\tau}\int_0^{\tau}\left([x^T, u^T]Q_{xu}\begin{bmatrix}x\\u\end{bmatrix} + x_i^T Q_i x_i\right)dt\right\} \tag{6.7}$$

A state space model is needed for LQG controller design. The discrete-time state-space model is given by:

$$x[k+1] = Ax[k] + Bu[k] \tag{6.8}$$

$$y[k] = Cx[k] + Du[k] \tag{6.9}$$

For cooling tests, the system can be considered as a two-input (compressor speed and OD fan speed), two-output (cooling capacity and discharge pressure) system. For heating tests, the heat pump can be described as a three-input, three-output system. The inputs are compressor speed, OD fan speed, and valve opening. The outputs are heating capacity, suction pressure, and superheat. Matrices A, B, C, and D are estimated based on experimental data.

Generation of State Space Model for Cooling Tests

The control signals used for the state space model are shown in Figure 6-28 and Figure 6-29. The range of the compressor speed is 1,750 to 4,500 rpm, and the range of OD fan speed is 1,000 to 3,300 cfm. Simulation results are shown in Figure 6-30 and Figure 6-31. The cooling capacity changes from 7 to 14 kW, and the discharge pressure changes from 2,900 to 3,700 kPa. When the compressor speed increases, both the heating capacity and discharge pressure go up. Higher OD air flow rate leads to lower discharge pressure.

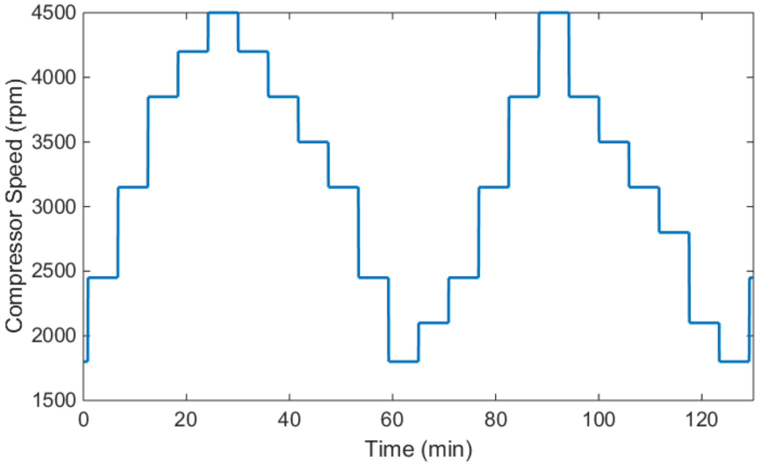

Figure 6-28 Compressor speed.

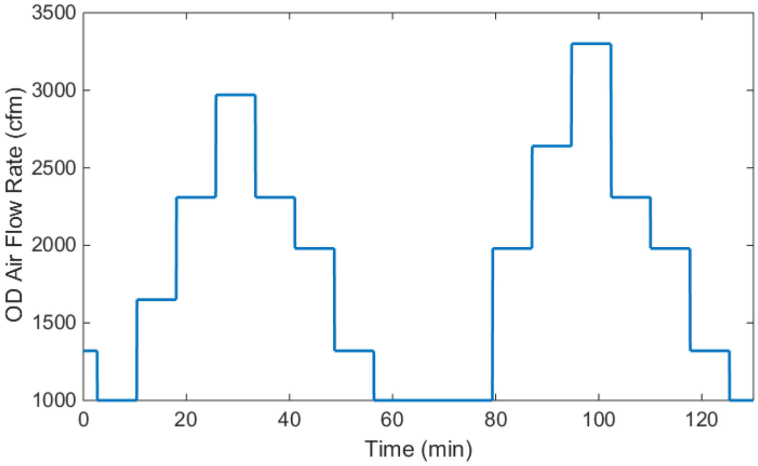

Figure 6-29 OD air flow rate.

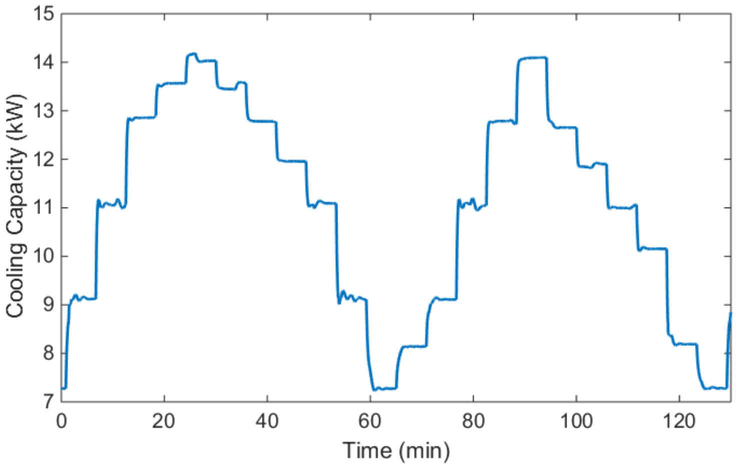

Figure 6-30 Cooling capacity.

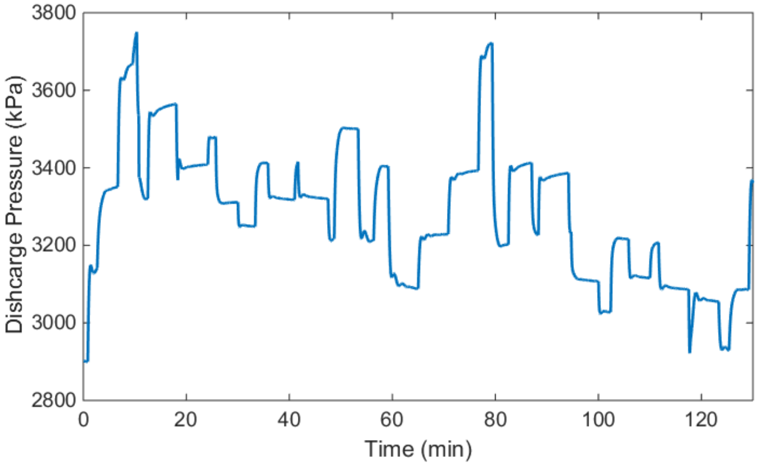

Figure 6-31 Discharge pressure.

The state space model is obtained with the System Identification Toolbox (Figure 6-32). The state space value is specified as 4. The selected model is *Discrete Time*. The estimation method is *Prediction Error Minimization (PEM)*.

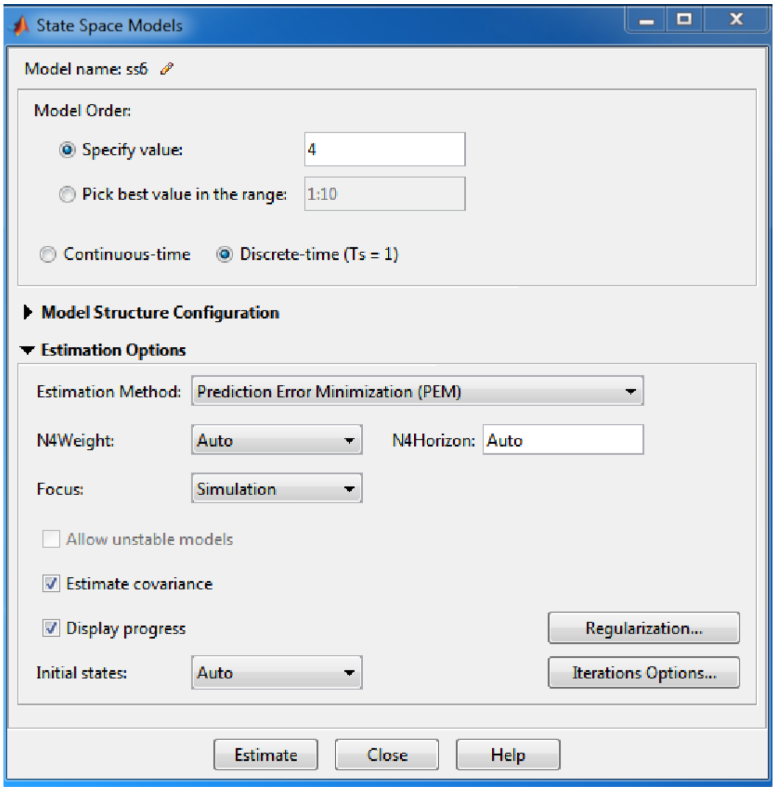

State Space Models

Model name: ss6

Model Order:

● Specify value: 4

○ Pick best value in the range: 1:10

○ Continuous-time ● Discrete-time (Ts = 1)

Model Structure Configuration

Estimation Options

Estimation Method: Prediction Error Minimization (PEM)

N4Weight: Auto N4Horizon: Auto

Focus: Simulation

☐ Allow unstable models

☑ Estimate covariance

☑ Display progress

Initial states: Auto

Figure 6-32 State space model generation.

The system is identified as a discrete model with four states. The four matrices are:

$$A = \begin{bmatrix} 0.9192 & -0.0318 & -0.0558 & -0.0131 \\ 0.0092 & 0.8773 & 0.0721 & 0.0772 \\ -0.0934 & -0.1022 & 0.0373 & -0.3870 \\ -0.0584 & 0.3004 & -0.7032 & 0.4432 \end{bmatrix}$$

$$B = \begin{bmatrix} -0.0000 & 0.0001 \\ 0.0001 & -0.0001 \\ -0.0006 & 0.0014 \\ -0.0006 & 0.0012 \end{bmatrix}$$

$$C = 10^3 \times \begin{bmatrix} 0.0105 & 0.0011 & -0.0007 & -0.0003 \\ 1.6310 & -1.7415 & -0.1125 & -0.1701 \end{bmatrix}$$

$$D = \begin{bmatrix} 0 & 0 \\ 0 & 0 \end{bmatrix}$$

Figure 6-33 and Figure 6-34 show the measured and simulated data of cooling capacity and discharge pressure, respectively. The fit of the cooling capacity is 90.6%, and the fit of the discharge pressure is 53.19%.

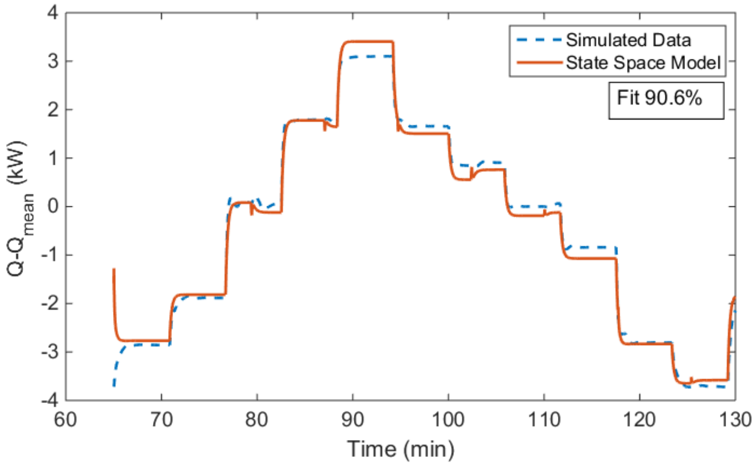

Figure 6-33 Cooling capacity generated by the dynamic model and the state space model.

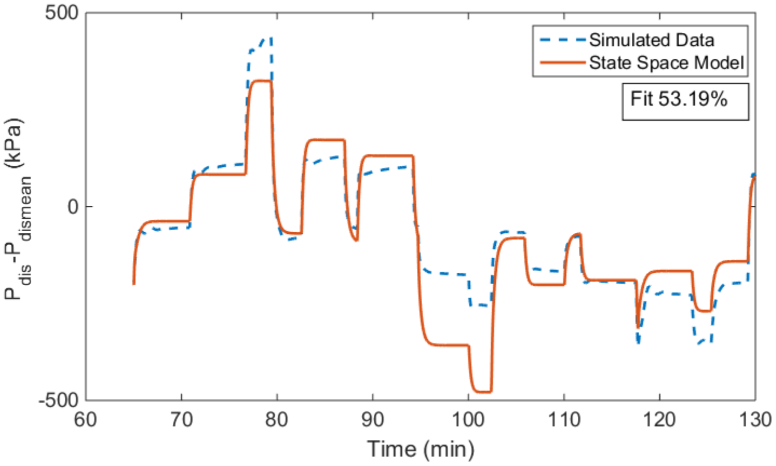

Figure 6-34 Discharge pressure generated by the dynamic model and the state space model.

Generation of State Space Model for Heating Tests

The control signals for heating tests include compressor speed, OD fan speed, and expansion valve opening. Steps for changes of the above three control signals are shown in Figure 6-35, Figure 6-36, and Figure 6-37.

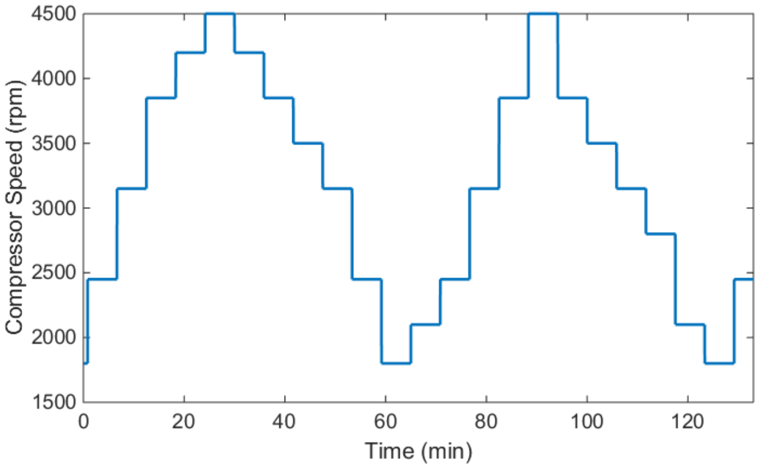

Figure 6-35 Compressor speed.

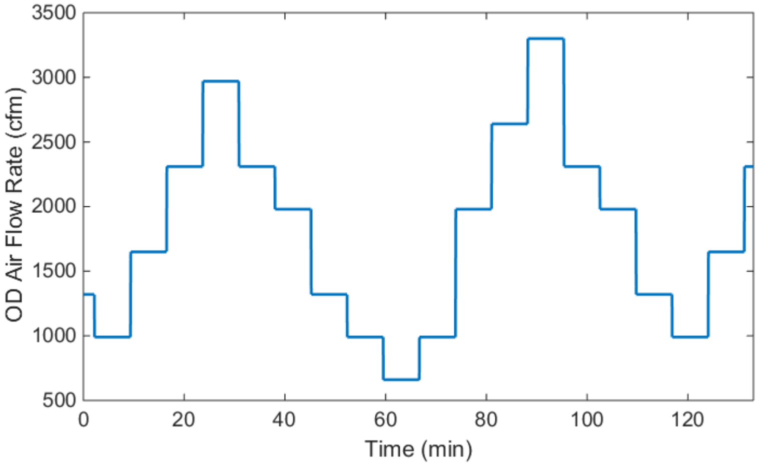

Figure 6-36 OD air flow rate.

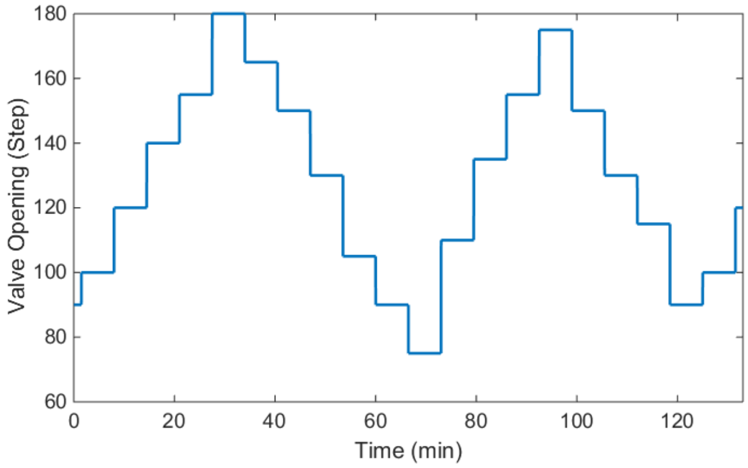

Figure 6-37 Expansion valve opening.

Simulation results are shown in Figure 6-38, Figure 6-39, and Figure 6-40. Heating capacity is highly affected by compressor speed. Higher compressor speed leads to high heating capacity. Meanwhile, high compressor speed causes lower suction pressure. The OD air flow rate also affects suction pressure. Lower OD air flow rate indicates lower suction pressure. Among all control signals, the expansion valve opening has the most significant effect on superheat. Larger valve opening indicates smaller superheat.

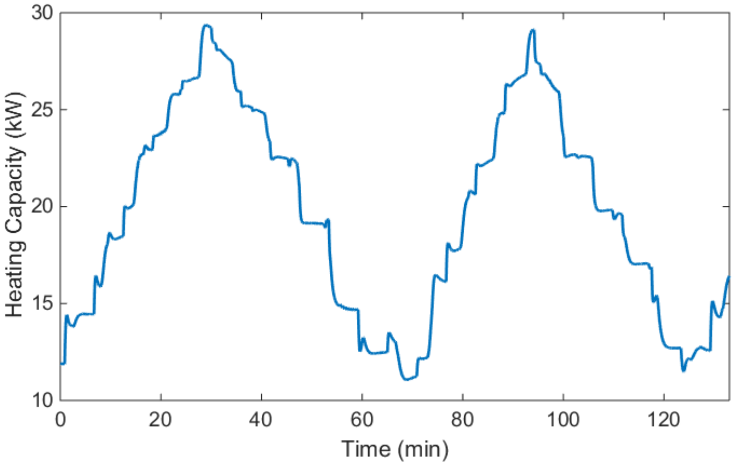

Figure 6-38 Heating capacity.

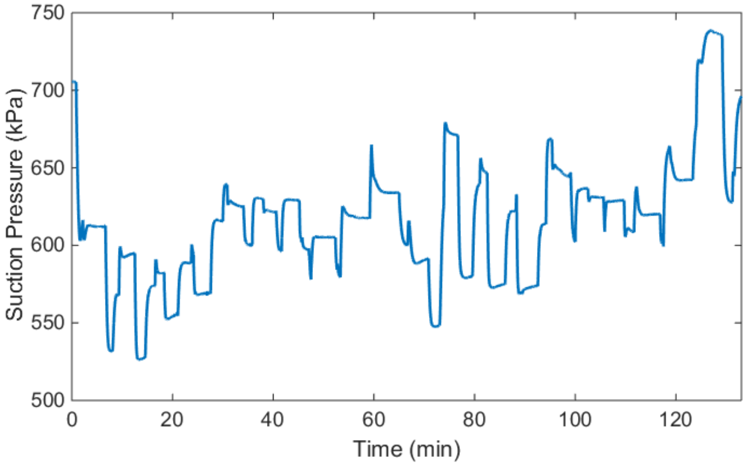

Figure 6-39 Suction pressure.

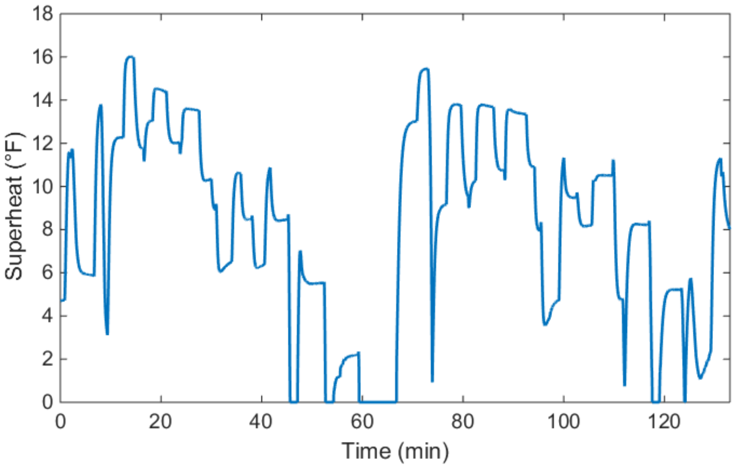

Figure 6-40 Superheat.

The system is estimated as a discrete model with five states. The four matrices are given by:

$$A = \begin{bmatrix} 0.9260 & -0.0286 & -0.0223 & 0.0265 & -0.0414 \\ -0.0408 & 0.9476 & -0.0061 & 0.0082 & 0.0362 \\ -0.0581 & -0.0862 & 0.9220 & 0.0466 & 0.0195 \\ -0.1283 & 0.0377 & 0.1208 & 0.9306 & 0.0650 \\ -0.0153 & -0.0758 & -0.0563 & 0.0380 & 1.0066 \end{bmatrix}$$

$$B = \begin{bmatrix} -0.0139 & 0.0226 & -0.0537 \\ -0.0085 & 0.0041 & -0.1329 \\ -0.0112 & 0.0303 & -0.1896 \\ -0.0294 & -0.0331 & 0.1517 \\ -0.0027 & 0.0212 & -0.2047 \end{bmatrix}$$

$$C = \begin{bmatrix} -8.9217 & -26.5787 & 9.7490 & 0.2345 & 5.0165 \\ 488.8235 & -351.1188 & 95.6421 & 58.2190 & -93.4573 \\ -27.9635 & 69.4271 & 15.7139 & -22.2313 & -27.8830 \end{bmatrix}$$

$$D = \begin{bmatrix} 0 & 0 & 0 \\ 0 & 0 & 0 \\ 0 & 0 & 0 \end{bmatrix}$$

Comparisons between the dynamic model and the state space model are shown in Figure 6-41, Figure 6-42, and Figure 6-43. The fit for suction pressure, heating capacity, and superheat are 64.78%, 84.21%, and 47.51%, respectively.

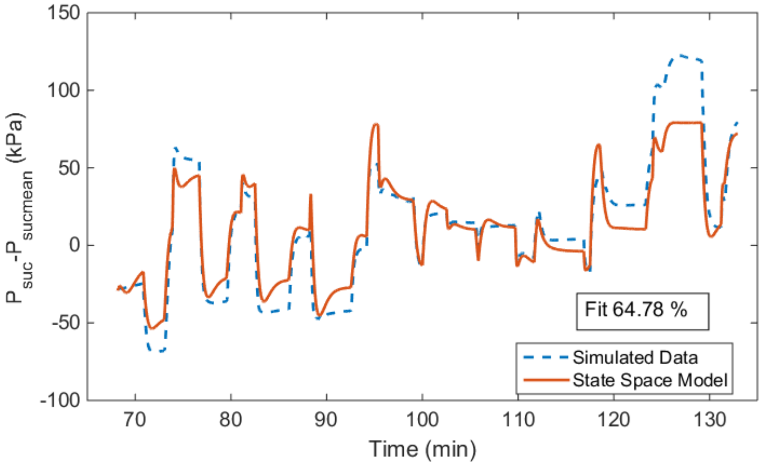

Figure 6-41 Suction pressure obtained from the dynamic model and predicted by the state space model.

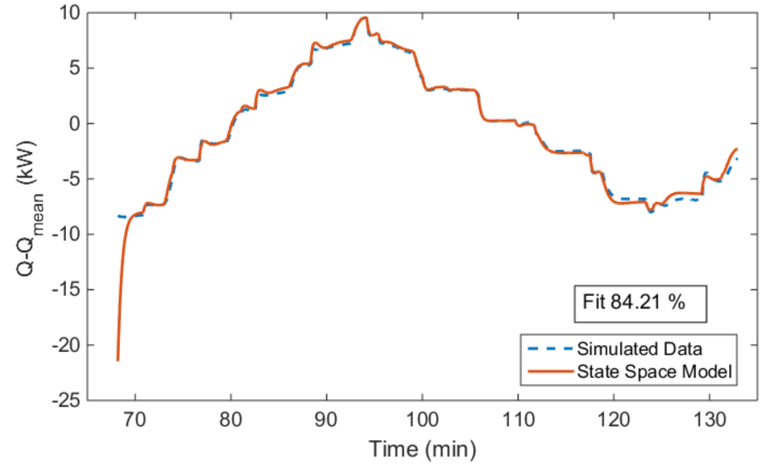

Figure 6-42 Heating capacity obtained from the dynamic model and predicted by the state space model.

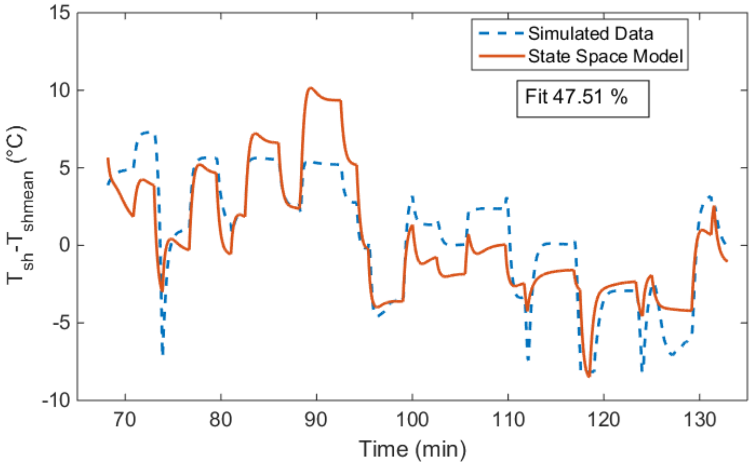

Figure 6-43 Superheat obtained from the dynamic model and predicted by the state space model.

Tuning Results

Cooling Mode

The tuning results for cooling mode are shown in Figure 6-44 and Figure 6-45. The cooling capacity tracking performance under the three scenarios are pretty close. The setting time is around 3 minutes. The MIMO control, however, gives better discharge pressure tracking than the multi-SISO control. The overshoot of the pressure tracking under the MIMO control is smaller and the setting time is shorter.

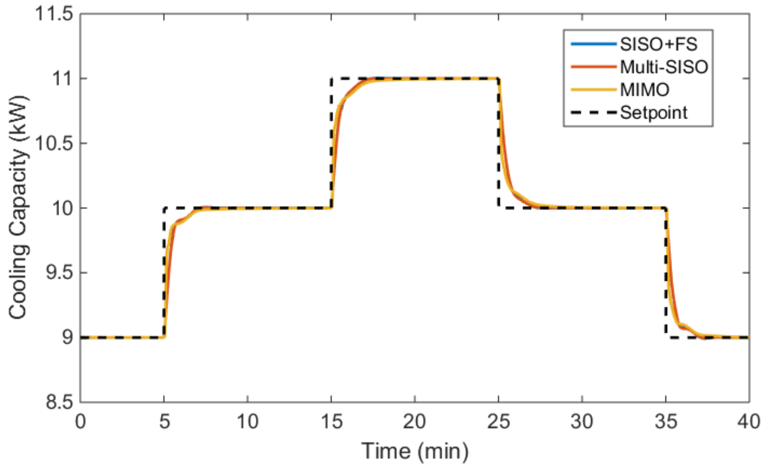

Figure 6-44 Cooling capacity.

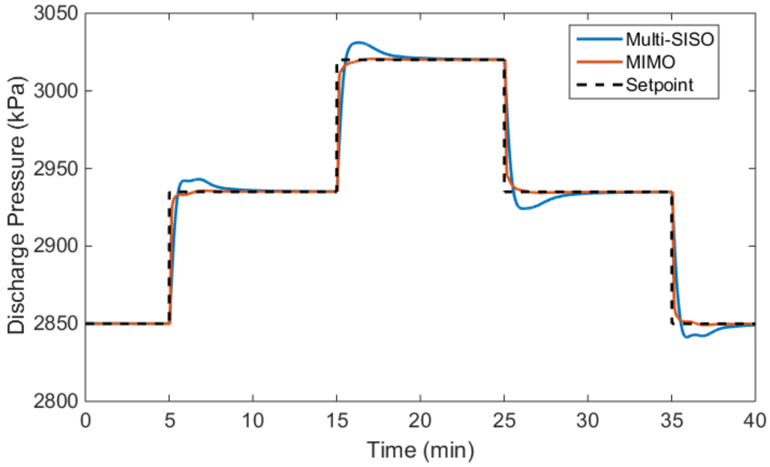

Figure 6-45 Discharge pressure.

The corresponding control signals are shown in Figure 6-46 and Figure 6-47. Higher cooling capacity setpoint indicates higher compressor speed and higher OD air flow rate. The control signals of the MIMO control are more aggressive.

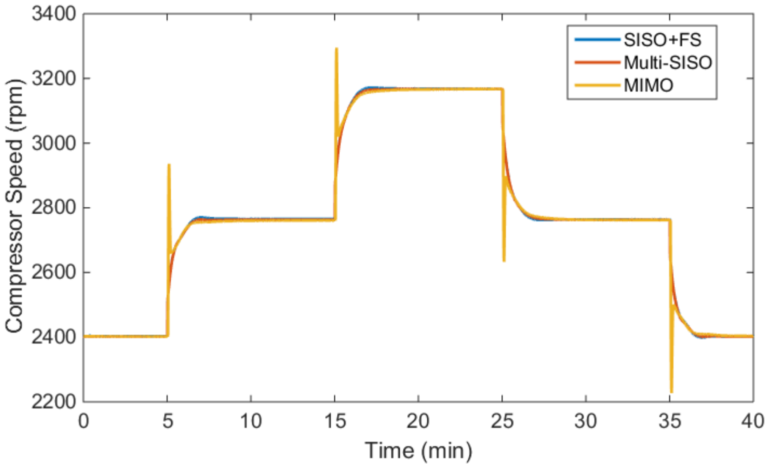

Figure 6-46 Compressor speed.

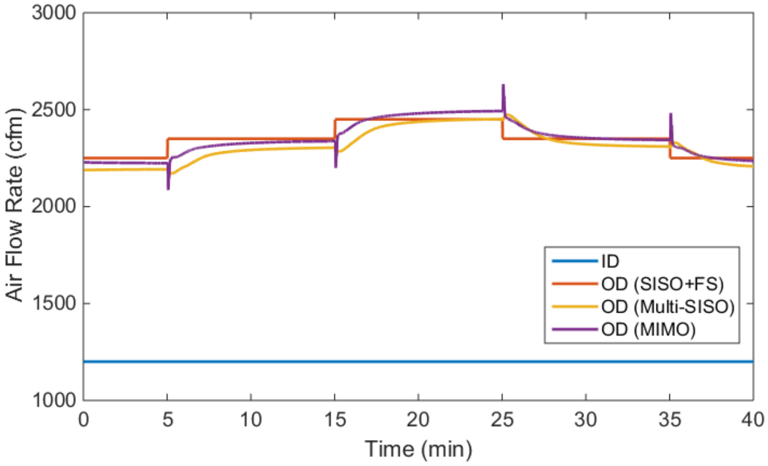

Figure 6-47 Air flow rate.

Heating Mode

The tuning results for heating mode are shown in Figure 6-48 through Figure 6-50. Heating tracking performance of the three control strategies are pretty close. When the heating capacity setpoint changes by 2 kW, the setting time is around 10 minutes.

The MIMO control shows better suction pressure tracking performance and superheat tracking performance than SISO control.

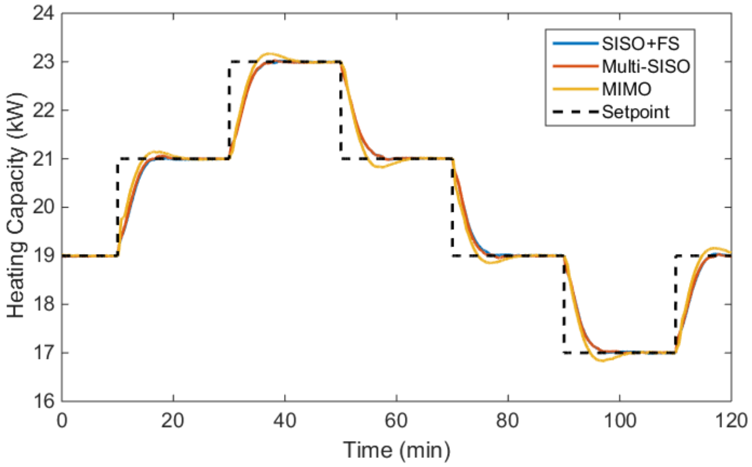

Figure 6-48 Heating capacity tracking.

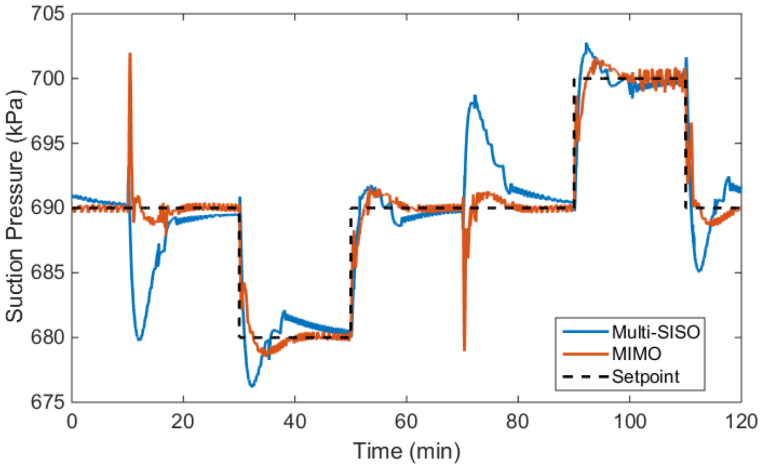

Figure 6-49 Suction pressure tracking.

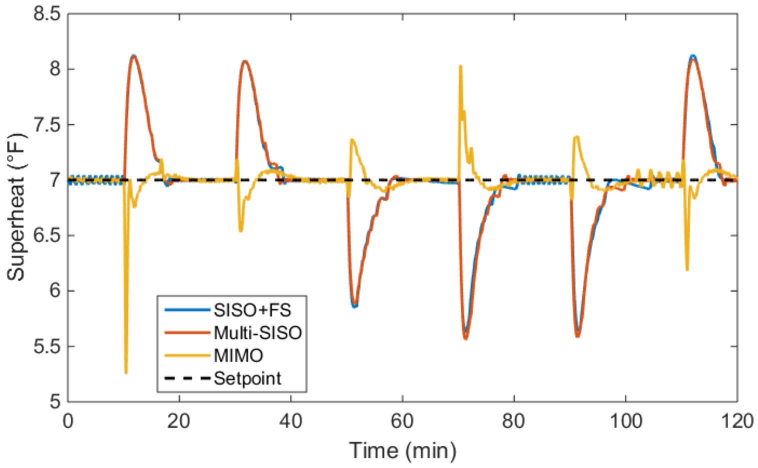

Figure 6-50 Superheat tracking.

The corresponding compressor speed, OD fan speed, and expansion valve are shown in Figure 6-51, Figure 6-52, and Figure 6-53, respectively. High heating capacity setpoint needs high compressor speed and high OD air flow rate. To maintain a constant superheat setpoint, the expansion valve opening increases as the heating capacity setpoint increases. Control signals under MIMO control are more aggressive.

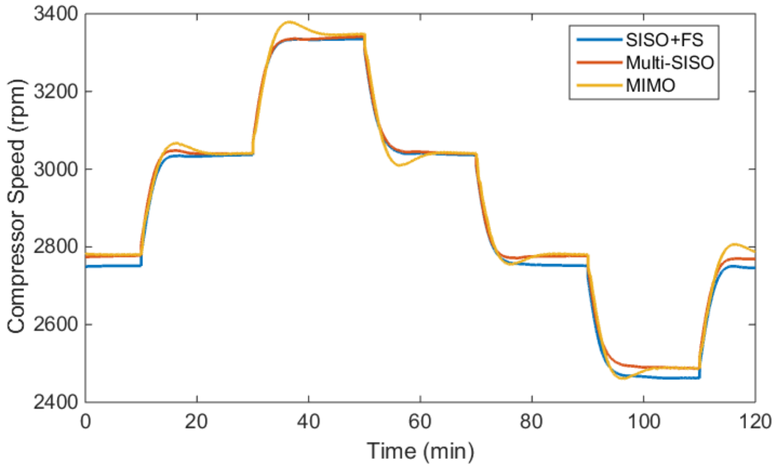

Figure 6-51 Compressor speed.

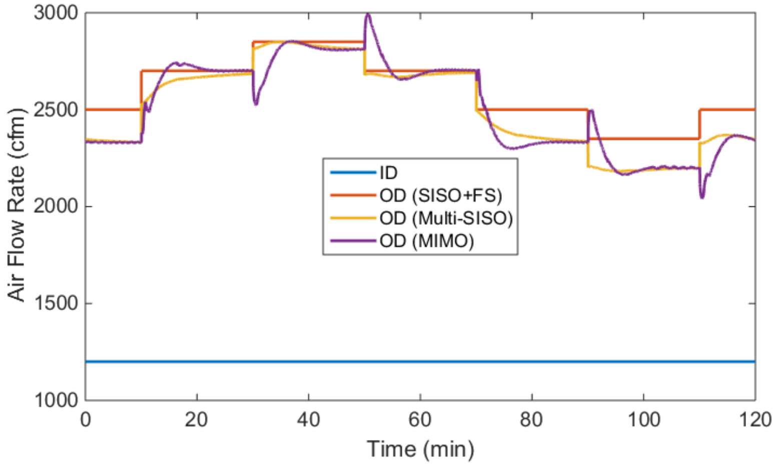

Figure 6-52 Air flow rate.

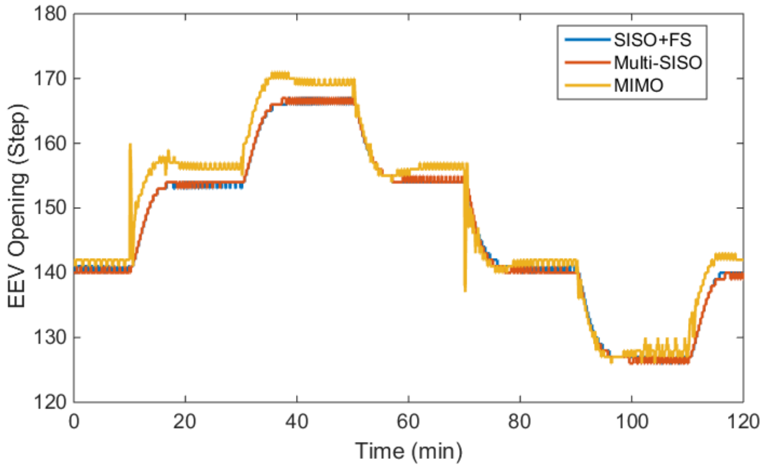

Figure 6-53 Expansion valve opening.

7. OPTIMAL EFFICIENCY CONTROL DESIGN AND VALIDATION

Both SISO and MIMO control have been verified as effective methods for heat pump dynamic models in Chapter 6. This chapter presents energy optimal control design and validation based on the experimental system shown in Chapter 4. The three energy-optimal control architectures are SISO control with fan scheduling, multi-SISO control, and MIMO control. First, the optimal fan and pressure scheduling are obtained based on pseudo-steady state data. The scheduling provides fan speed and pressure setpoint for controllers. Then, the above control algorithms are validated based on a 3-ton heat pump system.

Optimal Fan Speed and Pressure Scheduling

The optimal fan speed or pressure scheduling specifies the fan speed or pressure setpoints to maximize COP for given cooling or heating capacities. When the system runs in pseudo-steady state under constant ambient temperature, COP can be expressed as a function of the ID and OD air flow rates and cooling (heating) capacity. The polynomial is given by Equation (6.1). The COP can be maximized by optimizing the ID and OD air flow rates for a given cooling or heating capacity. Similarly, COP can also be described as a function of the discharge and suction pressure and cooling (heating) capacity. The polynomial is given by Equation (6.2). Again, the highest COP can be obtained by optimizing pressure for a specified cooling (heating) capacity. The two curves are obtained based on pseudo-steady state data.

Cooling Tests

The control signals (compressor speed and ID and OD air flow rates) for generating pseudo-steady state data are listed in Table 7-1. For each case, both the ID air flow rate and the compressor speed stay constant, while OD air flow rate increases slowly to ensure that each operating condition is pseudo-steady state.

Table 7-1 Control signals for cooing tests.

Case	ID Air Flow Rate (cfm)	Compressor Speed (rpm)	OD Air Flow Rate (cfm)
1	400 (Low)	1,750	1,320 to 2,640
2		2,450	1,320 to 2,640
3		3,150	1,650 to 2,970
4		3,850	1,650 to 2,970
5		4,550	1,980 to 3,300
6	500 (Medium)	1,750	1,320 to 2,640
7		2,450	1,320 to 2,640
8		3,150	1,650 to 2,970
9		3,850	1,650 to 2,970
10		4,550	1,980 to 3,300
11	800 (High)	1,750	1,320 to 2,640
12		2,450	1,320 to 2,640
13		3,150	1,650 to 2,970
14		3,850	1,650 to 2,970
15		4,550	1,980 to 3,300

For a given ID and OD air flow rate, higher compressor speed leads to larger pressure difference (Figure 7-1). For a given ID air flow rate and compressor speed, higher OD air flow rate indicates lower discharge pressure. The effect of the OD air flow rate on suction pressure can be neglected. The cooling capacity is proportional to the compressor speed. Also, higher ID air flow rate leads to larger cooling capacity (Figure 7-2). Changes in OD air flow rate has a negligible effect on cooling capacity. Figure 7-3 shows that COP drops as the compressor speed goes up. For a given ID air flow rate and compressor speed, there exists an optimal range for OD air flow rate.

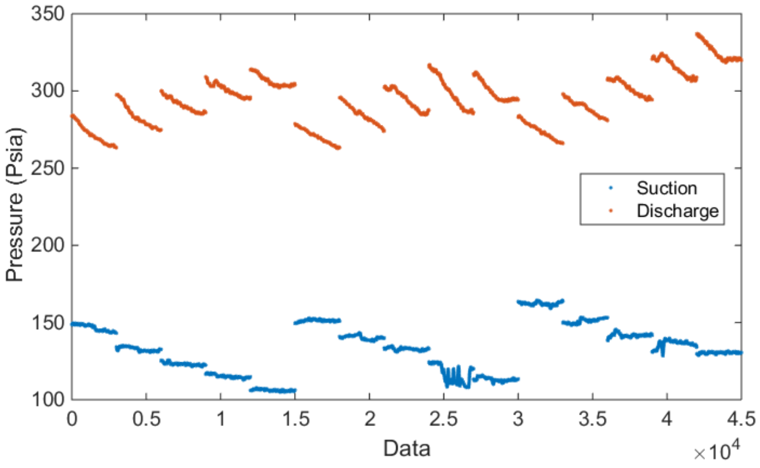

Figure 7-1 Suction and discharge pressure.

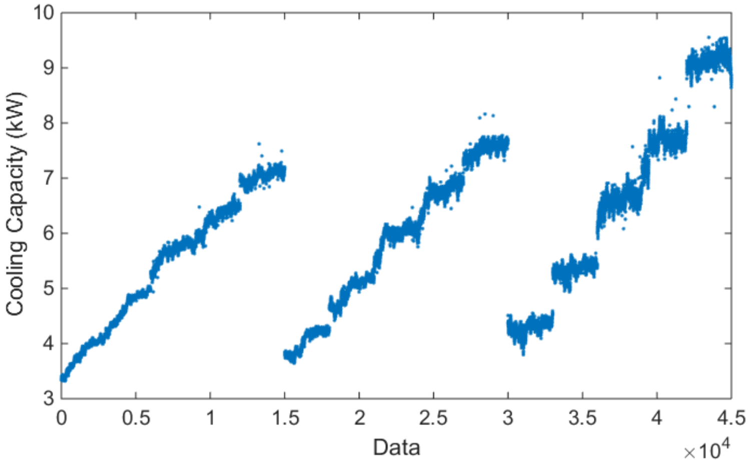

Figure 7-2 Cooling capacity.

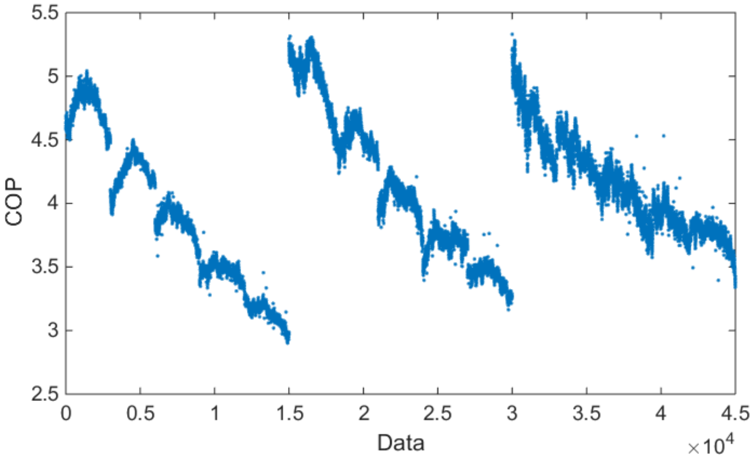

Figure 7-3 COP.

The fan speed curve and pressure curve are estimated based on the above pseudo-steady state data. The two polynomials are:

$$COP_{fan} = 3.0808 + 0.0114\dot{V}_{ID} + 0.0025\dot{V}_{OD} - 1.4336Q + 0.0009\dot{V}_{ID}Q + 0.0002\dot{V}_{OD}Q + 0.0069Q^2 \quad (7.1)$$

$$COP_{pressure} = -12.8402 + 0.0470P_{suc} + 0.1399P_{dis} - 2.4064Q \tag{7.2}$$
$$+ 0.0007P_{suc}P_{dis} - 0.0133P_{suc}Q + 0.0176P_{dis}Q$$
$$- 0.0006P_{suc}^2 - 0.0006P_{dis}^2 - 0.0973Q^2$$

Comparisons between the COP generated from the experimental data and the COP predicted by the fitted curves are shown in Figure 7-4 and Figure 7-5. In most cases, the error is less than 10%. A small error indicates that both curves have good predictions.

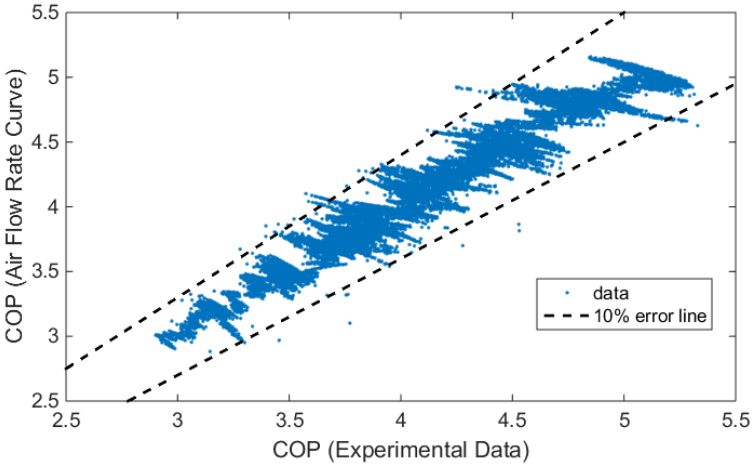

Figure 7-4 COP predicted by the fan speed curve and obtained from the experimental data.

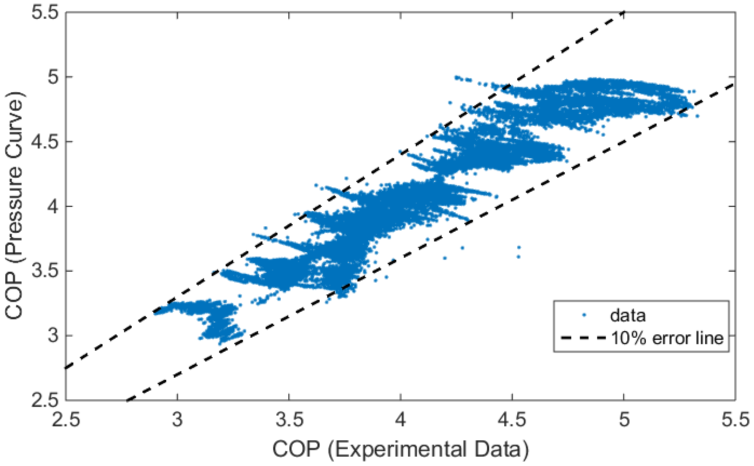

Figure 7-5 COP predicted by the pressure curve and obtained from the experimental data.

The inverse COP (ICOP) is defined as:

$$ICOP = 1/COP \tag{7.3}$$

ICOP is also a function of fan speeds or pressure for a specified cooling capacity. Figure 7-6 shows the ICOP changes with the ID and OD air flow rates under given cooling capacities. For each specified cooling capacity, there exists an optimal combination of ID and OD air flow rates that gives the lowest ICOP. The combination is used as the optimal fan speed scheduling. Figure 7-7 shows the ICOP changes with the suction and discharge pressure. Similarly, for each given cooling capacity, there also exists a minimum ICOP value. The pressure corresponding to the smallest ICOP is the optimal pressure schedule.

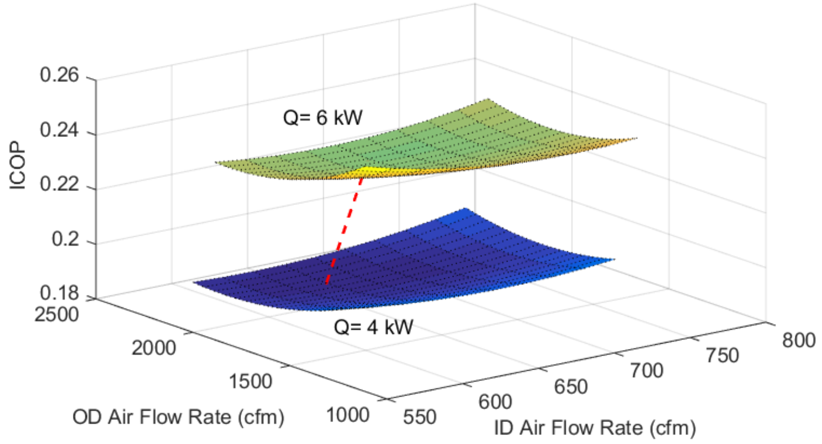

Figure 7-6 ICOP based on the ID and OD air flow rates.

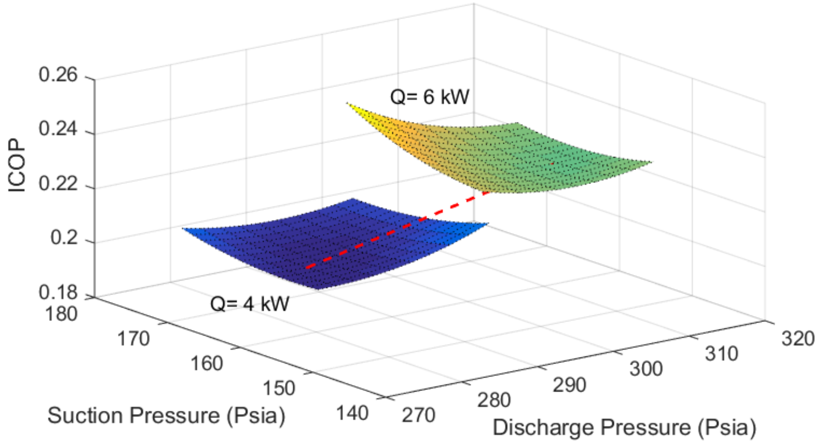

Figure 7-7 ICOP based on the suction and discharge pressure.

The optimal air flow rate scheduling is shown in Figure 7-8. Higher cooling capacity setpoint indicates both higher ID and OD air flow rates. The optimal pressure scheduling is shown in Figure 7-9. Higher cooling capacity setpoint indicates higher discharge pressure but lower suction pressure. In other words, higher cooling capacity means higher pressure difference.

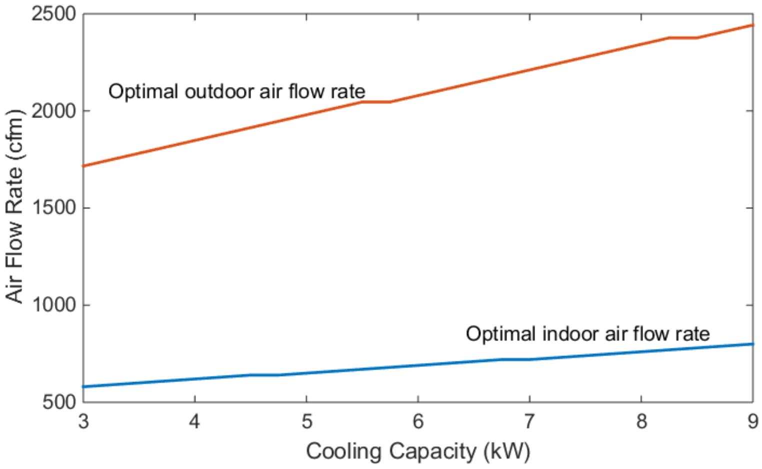

Figure 7-8 Optimal fan speed scheduling for cooling tests.

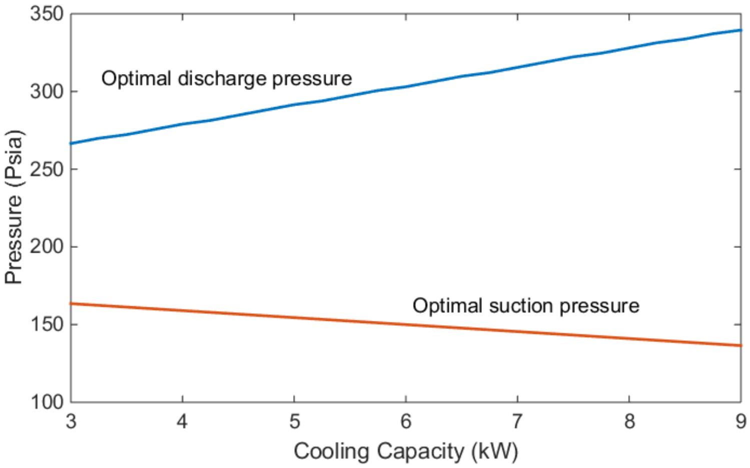

Figure 7-9 Optimal pressure scheduling for cooling tests.

Heating Tests

Control signals for heating tests are shown in Table 7-2. For each case, both ID air flow rate and compressor speed stay constant, while OD air flow rate increases slowly to get the pseudo-steady state data.

Table 7-2 Control signals for estimating optimal fan and pressure scheduling for heating tests.

Case	ID Air Flow Rate (cfm)	Compressor Speed (rpm)	OD Air Flow Rate (cfm)
1	800 (High)	1,750	825 to 1,320
2	800 (High)	2,450	990 to 1,485
3	800 (High)	3,150	1,156 to 1,650

Experimental results are shown in Figure 7-10, Figure 7-11, and Figure 7-12. Both discharge pressure and suction pressure drop as OD air flow rate increases. However, the change in discharge pressure is more significant, showing that OD air flow rate has a stronger effect on discharge pressure. Comparison between the three cases shows that higher compressor means higher heating capacity. When the compressor speed increases from 1,750 to 3,150 rpm, the heating capacity rises from 2.5 to 4.7 kW. But there is no significant increase in COP as the compressor speed increases.

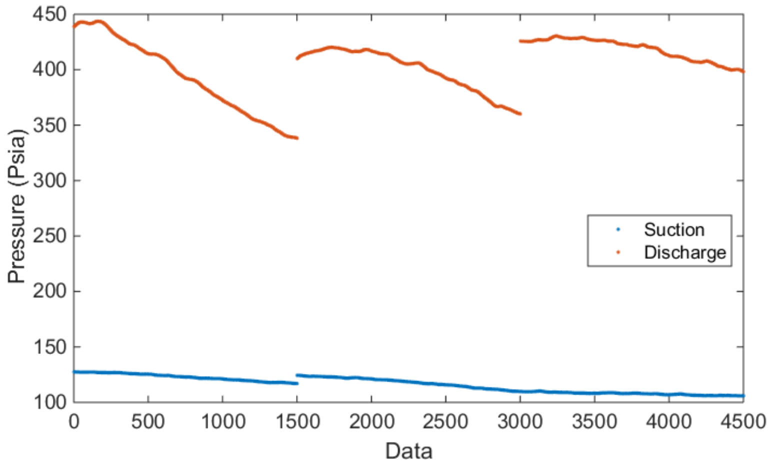

Figure 7-10 Suction and discharge pressure.

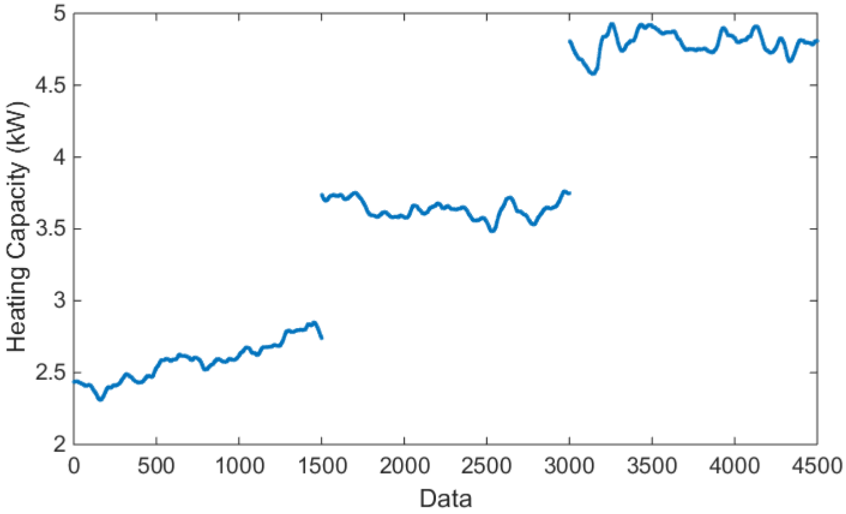

Figure 7-11 Heating capacity.

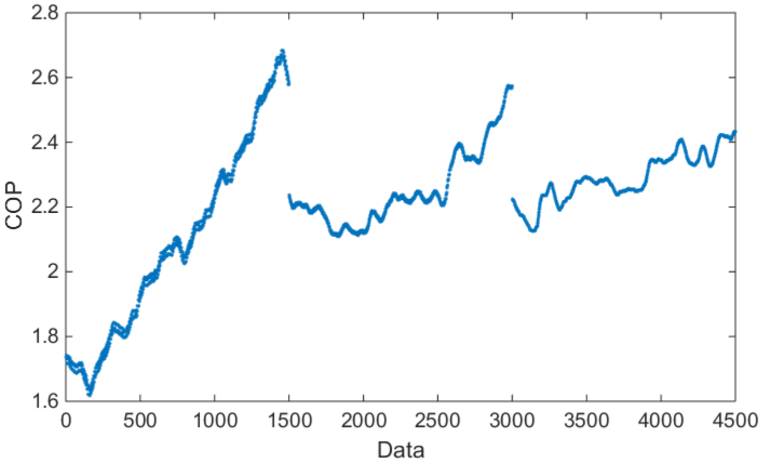

Figure 7-12 COP.

Fan curve and pressure curve are estimated as:

$$COP_{fan} = 0.0011\dot{V}_{ID}Q \ + 0.0001\dot{V}_{OD}Q - 0.1047Q^2 \qquad (7.4)$$

$$COP_{pressure} = -20.8857 + 0.4854P_{suc} - 0.0659P_{dis} + 4.3626Q + 0.0003P_{suc}P_{dis} - 0.0331P_{suc}Q + 0.0018P_{dis}Q - 0.0020P_{suc}^2 - 0.1149Q^2 \tag{7.5}$$

Figure 7-13 and Figure 7-14 show the comparison between experimental data and the fitted curves. Results show that the error between experimental data and the pressure curve is generally less than 10%.

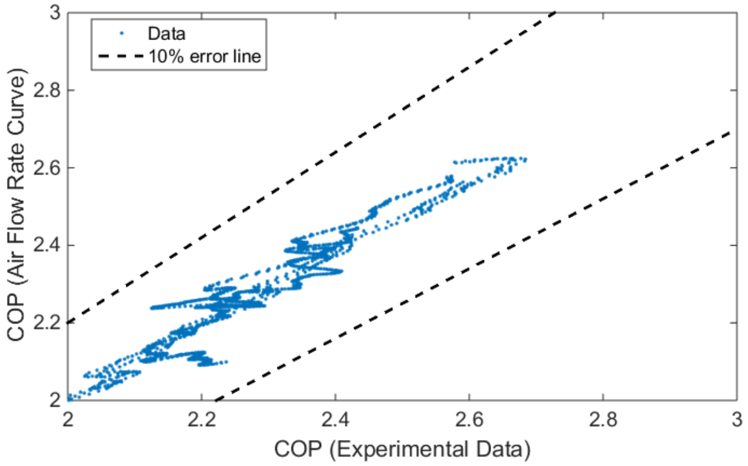

Figure 7-13 COP predicted by the fitted air flow rate curve and obtained from the experimental data.

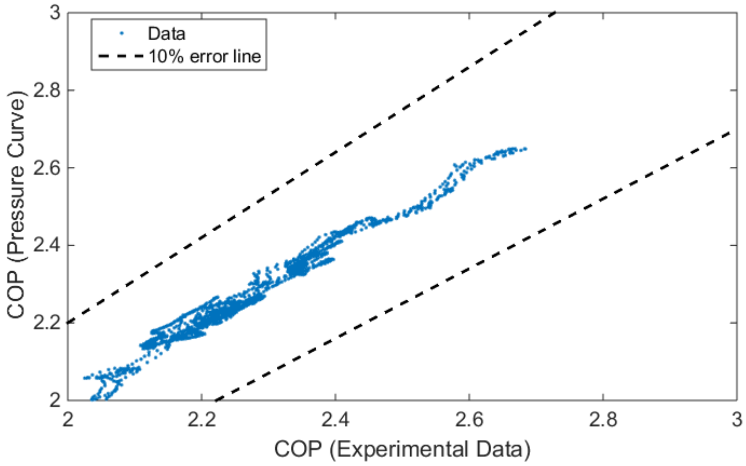

Figure 7-14 COP predicted by the fitted pressure curve and obtained from the experimental data.

The optimal air flow rate scheduling is shown in Figure 7-15. The optimal ID air flow rate is 800 cfm, which is the highest value of the ID blower. Higher heating capacity indicates higher OD air flow rates. The optimal discharge and suction pressure scheduling are shown in Figure 7-16. Higher heating capacity means higher discharge pressure but lower suction pressure.

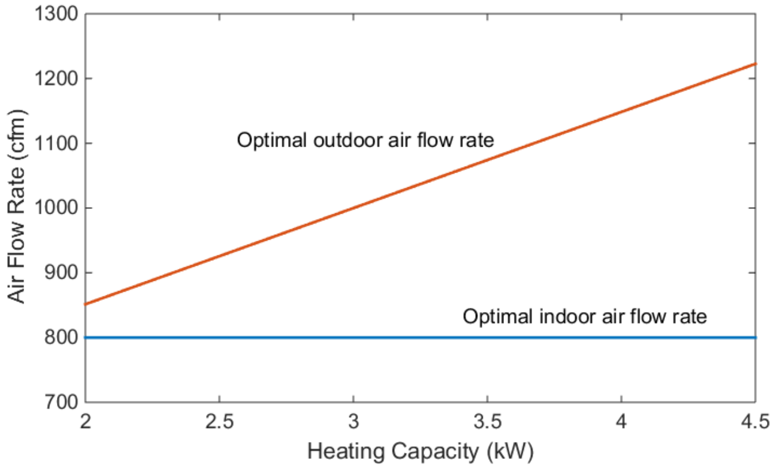

Figure 7-15 Optimal fan speed scheduling under heating mode.

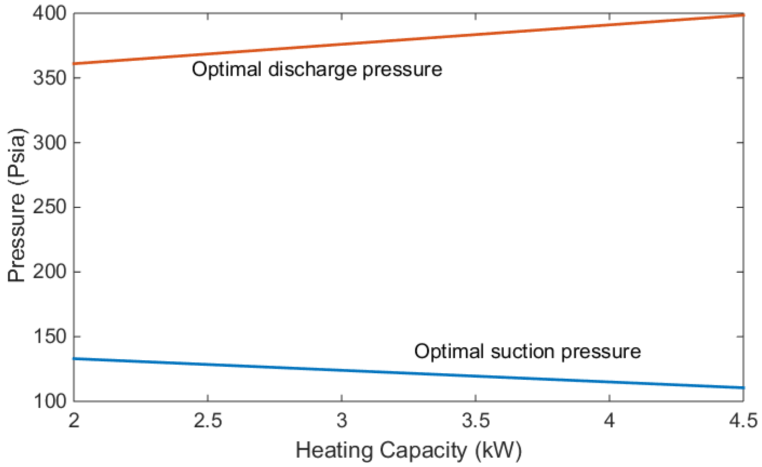

Figure 7-16 Optimal pressure scheduling under heating mode.

Fan Speed Scheduling with SISO Control

The control loops include the optimal fan speed scheduling and SISO control. Both the ID blower and OD fan use the optimal fan speed scheduling, as shown in Figure 6-22 and Figure 6-23. Cascaded PID control is applied for both cooling (heating) capacity control and superheat control, as shown in Figure 7-17 and Figure 7-18. Each control loop contains one inner loop and one outer loop. The inner loop uses proportional control to track the setpoint generated by the outer loop. For the cooling (heating) capacity control, the inner loop uses pressure difference as the feedback signal. For the superheat control, the inner loop uses suction pressure as the feedback signal.

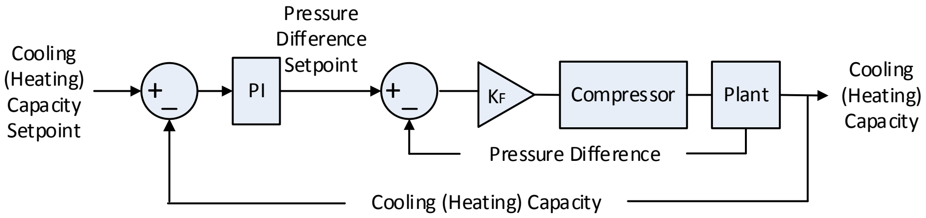

Figure 7-17 Cooling (heating) capacity control loop.

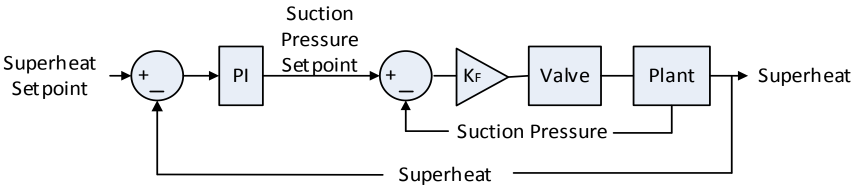

Figure 7-18 Superheat control loop.

Multi-SISO Control

The control algorithm has multi-SISO controllers and ID blower speed scheduling. Because the ID blower only has three stages, SISO control causes oscillations between two stages. Here, the optimal fan speed scheduling is used to control blower speed.

The cooling (heating) capacity control (Figure 7-17) and superheat control (Figure 7-18) are also used here. The OD fan speed control uses a PI controller with a fan speed lookup table, as shown in Figure 7-19. The control loop uses discharge pressure as the feedback signal during cooling mode and uses suction pressure as the feedback signal during heating mode. With the fan speed scheduling, the OD fan speed can reach the desired values quickly when the cooling capacity setpoint changes.

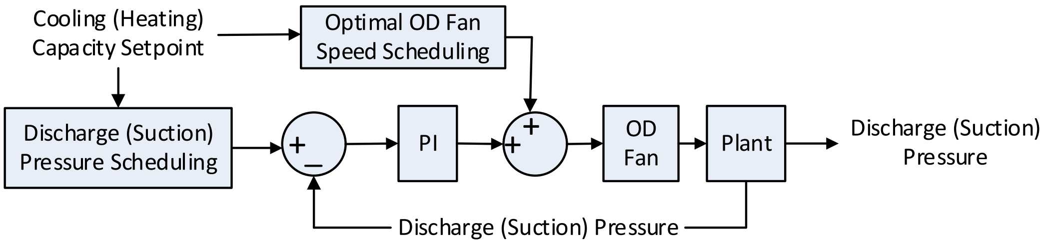

Figure 7-19 Discharge (suction) pressure control loop under cooling (heating) mode.

MIMO Control

MIMO controllers are designed with the LQG method. For cooling tests, the control signals include compressor speed and OD fan speed. The feedback signals include cooling capacity and discharge pressure. For heating tests, the control signals are compressor speed, OD fan speed, and valve opening. The feedback signals include heating capacity, suction pressure, and superheat. The optimal fan speed scheduling is used to control the blower speed.

A state space model is needed for LQG design. The discrete-time state-space model is given by:

$$x[k+1] = Ax[k] + Bu[k] \tag{7.6}$$

$$y[k] = Cx[k] + Du[k] \tag{7.7}$$

For cooling tests, the system can be considered as a two-input (compressor speed and OD fan speed), two-output (cooling capacity and discharge pressure) system. The superheat control is added for the heating tests. Then, the heat pump is described as a three-input, three-output system. The inputs are compressor speed, OD fan speed, and valve opening. The outputs are heating capacity, suction pressure, and superheat. Matrices A, B, C, and D are estimated based on experimental data.

State Space Model for Cooling Tests

The transient data can be obtained based on the OD air flow rate (Figure 7-20) and compressor speed (Figure 7-21). The compressor speeds are 1,750 rpm, 2,100 rpm, 2,450 rpm, 2,800 rpm, 3,150 rpm, 3,500 rpm, 3,850 rpm, 4,200 rpm, and 4,550 rpm. The range of the OD fan speed is 1,320 to 3,300 cfm.

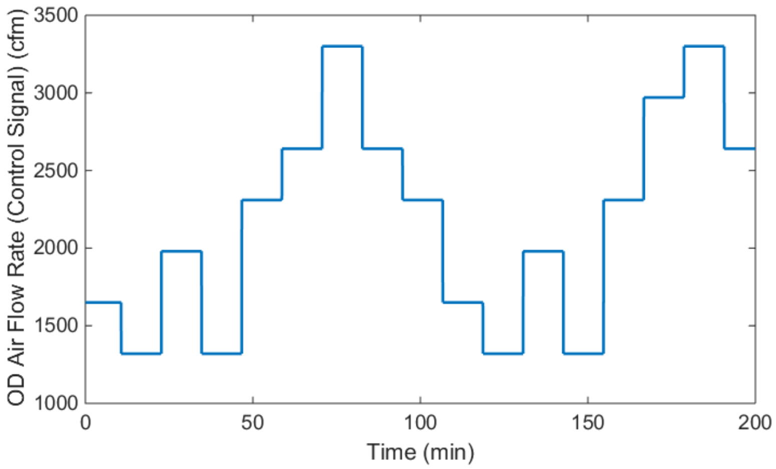

Figure 7-20 OD air flow rate for transient data generation.

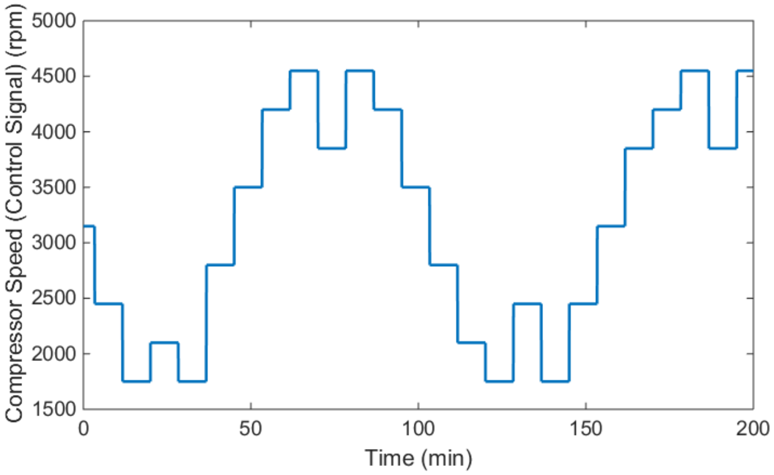

Figure 7-21 Compressor speed for transient data generation.

Discharge pressure is shown in Figure 7-22. Both the OD air flow rate and compressor speed affect the discharge pressure. High OD air flow rate leads to low discharge pressure, while high compressor speed indicates high discharge pressure. The cooling capacity is shown in Figure 7-23. Higher compressor speed indicates larger cooling capacity.

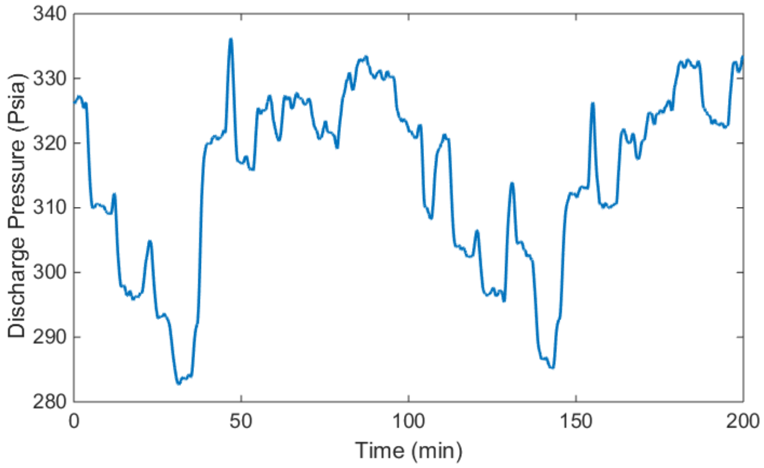

Figure 7-22 Discharge pressure.

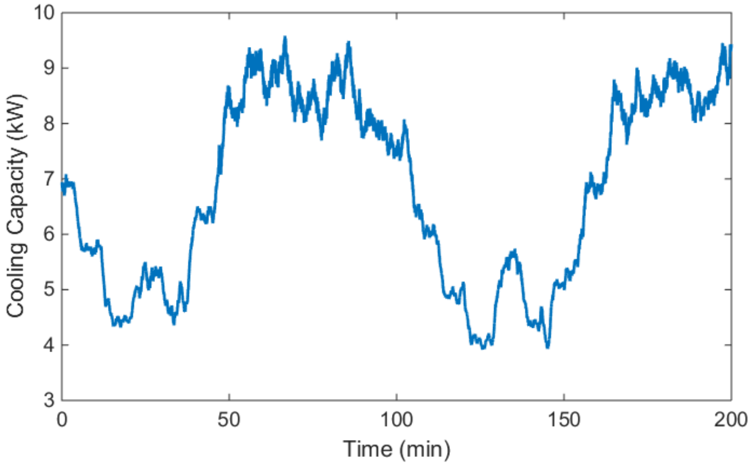

Figure 7-23 Cooling capacity.

The four matrices can be obtained with the System Identification Toolbox. The estimation method is *Prediction Error Minimization (PEM)*. The system is identified as a two-input, two-output discrete system with four states:

$$A = \begin{bmatrix} 0.9886 & -0.0298 & -0.0241 & -0.0161 \\ 0.0604 & 0.9648 & -0.0178 & 0.0085 \\ 0.0014 & 0.0258 & 0.9648 & -0.0026 \\ 0.0124 & -0.0818 & -0.0138 & 0.9680 \end{bmatrix}$$

$$B = 10^{-04} \times \begin{bmatrix} -0.0458 & 0.0427 \\ -0.0484 & 0.0502 \\ 0.0644 & -0.0178 \\ -0.1628 & 0.1075 \end{bmatrix}$$

$$C = \begin{bmatrix} 14.1283 & -0.1628 & 14.5017 & -0.5997 \\ 266.9416 & -31.8752 & -5.2620 & -55.7815 \end{bmatrix}$$

$$D = \begin{bmatrix} 0 & 0 \\ 0 & 0 \end{bmatrix}$$

Figure 7-24 and Figure 7-25 show the measured and simulated data of cooling capacity and discharge pressure, respectively. The fits are above 70%, indicating that the state space model gives good fits.

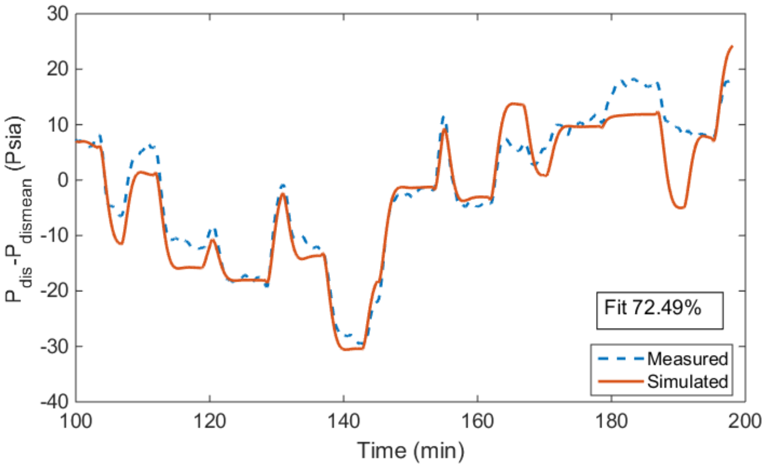

Figure 7-24 Discharge pressure predicted by the state space model and obtained from the measured data.

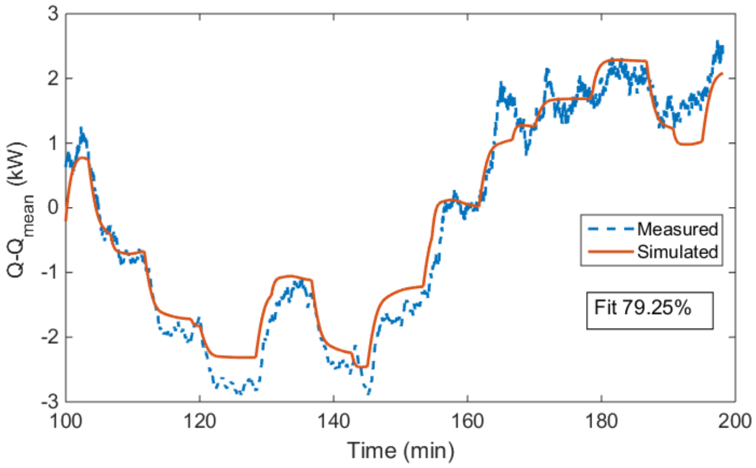

Figure 7-25 Cooling capacity predicted by the state space model and obtained from the measured data.

State Space Model for Heating Tests

Control signals for generating transient data include compressor speed (Figure 7-26), OD fan speed (Figure 7-27), and EXV opening (Figure 7-28). The compressor speeds are 1,750 rpm, 2,100 rpm, 2,450 rpm, 2,800 rpm, and 3,150 rpm. The range of the OD fan speed is 1,150 to 1,550 cfm. The step of the expansion valve changes from 47 to 56.

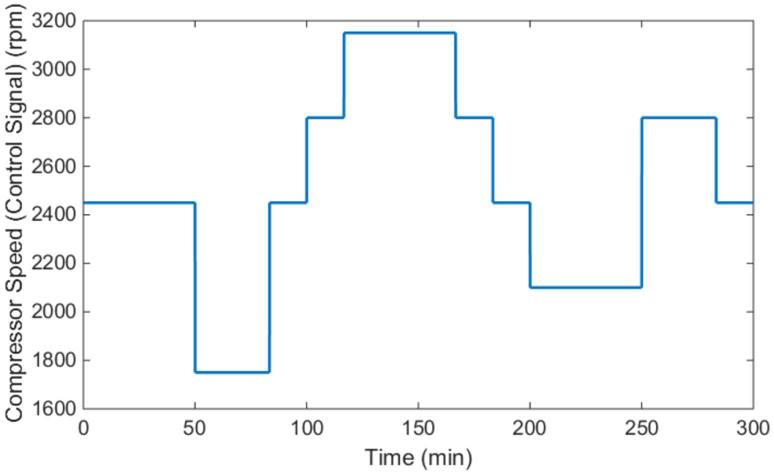

Figure 7-26 Compressor speed for transient data generation.

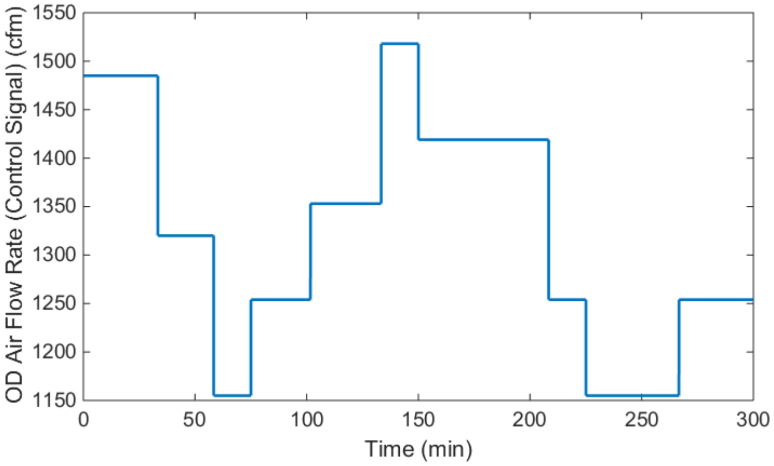

Figure 7-27 OD air flow rate for transient data generation.

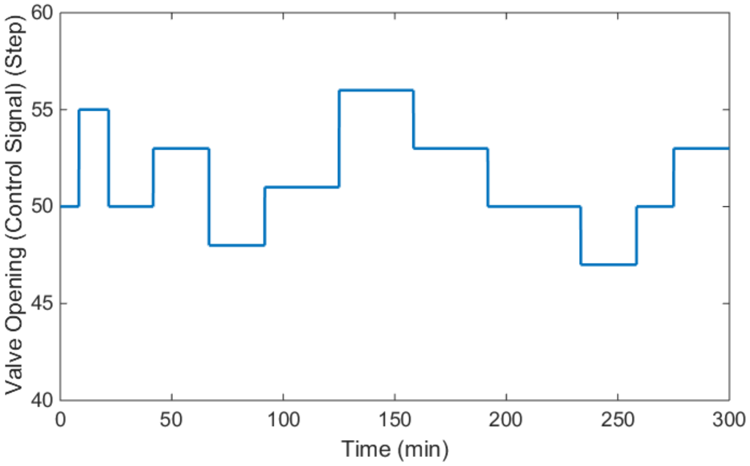

Figure 7-28 Valve opening for transient data generation.

Experimental results are shown in Figure 7-29, Figure 7-30, and Figure 7-31. Both compressor speed and OD fan speed affect the suction pressure. High compressor speed or high OD fan speed leads to low suction pressure. Heating capacity is mainly affected by compressor speed. Higher compressor speed results in higher heating capacity. The superheat is greatly affected by the valve opening. A smaller valve opening causes an increase in superheat. Compressor speed also affects superheat. High compressor speed results in high superheat.

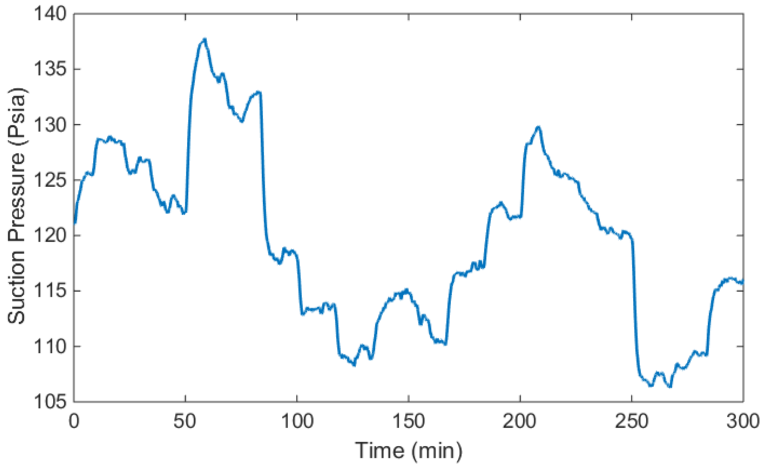

Figure 7-29 Suction pressure.

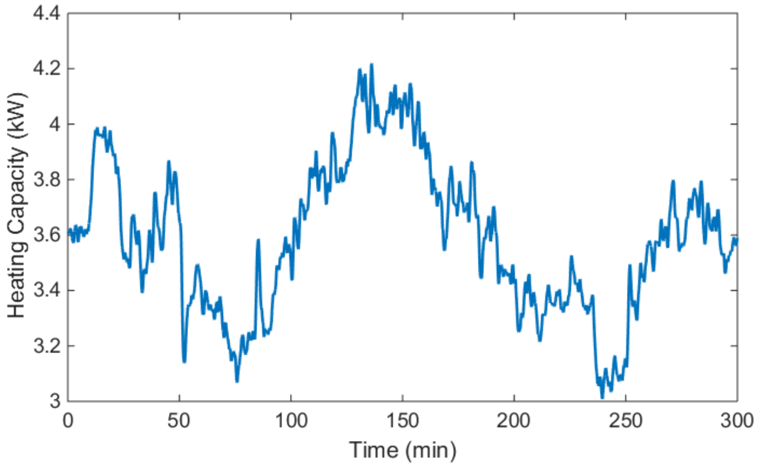

Figure 7-30 Heating capacity.

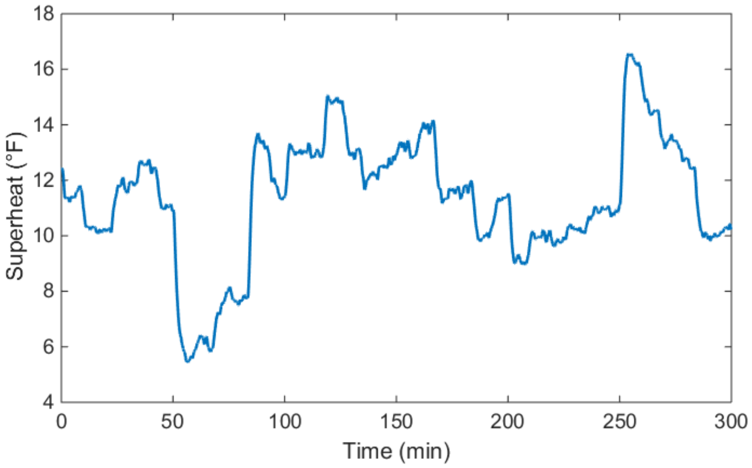

Figure 7-31 Superheat.

The four matrices can be obtained with the System Identification Toolbox. The estimation method is *Prediction Error Minimization (PEM)*. The heat pump is identified as a discrete model with five states:

$$A = \begin{bmatrix} 1.0117 & -0.0397 & 0.0237 & 0.0514 & 0.0060 \\ -0.0025 & 1.0044 & 0.0027 & -0.0095 & -0.0364 \\ 0.0053 & -0.0175 & 1.0353 & 0.0186 & -0.1485 \\ -0.0357 & 0.0593 & -0.0449 & 0.9209 & 0.0335 \\ 0.0018 & -0.0001 & 0.0243 & 0.0017 & 0.9219 \end{bmatrix}$$

$$B = 10^{-04} \times \begin{bmatrix} 0.0001 & 0.0008 & -0.0219 \\ 0.0019 & -0.0085 & 0.0485 \\ -0.0017 & 0.0097 & -0.0225 \\ 0.0244 & -0.0288 & -0.7551 \\ -0.0088 & 0.0010 & -0.5783 \end{bmatrix}$$

$$C = \begin{bmatrix} -0.8292 & 2.2019 & 6.3301 & 0.0252 & -0.2254 \\ -145.2502 & -57.6571 & 10.8444 & -0.8242 & 0.0077 \\ 54.2727 & -32.9037 & 7.0541 & 0.3791 & 0.0061 \end{bmatrix}$$

$$D = \begin{bmatrix} 0 & 0 & 0 \\ 0 & 0 & 0 \\ 0 & 0 & 0 \end{bmatrix}$$

Measured and simulated data of superheat, suction pressure, and heating capacity are shown in Figure 7-32, Figure 7-33, and Figure 7-34, respectively. The fits are above 60%, indicating that the state space model gives a good prediction.

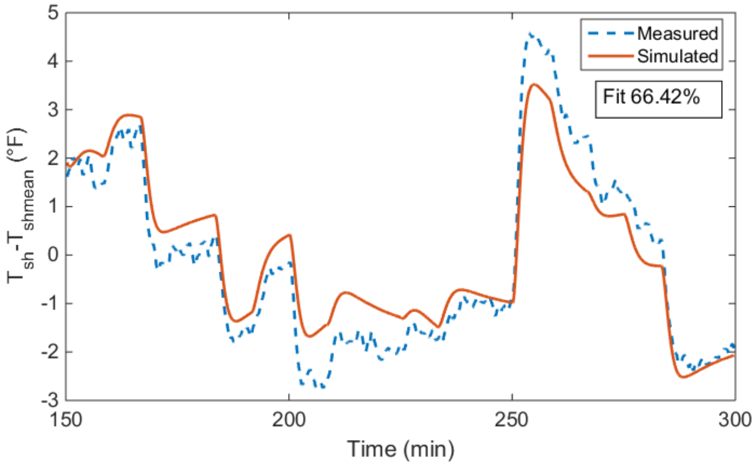

Figure 7-32 Superheat predicted by the state space model and obtained from the measured data.

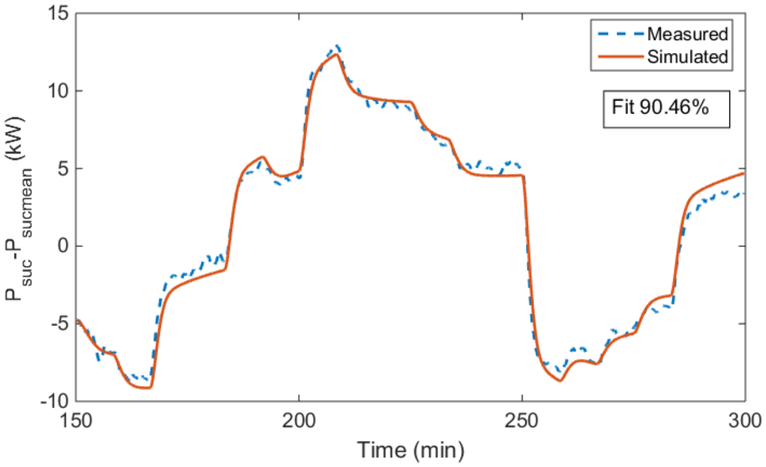

Figure 7-33 Suction pressure predicted by the state space model and obtained from the measured data.

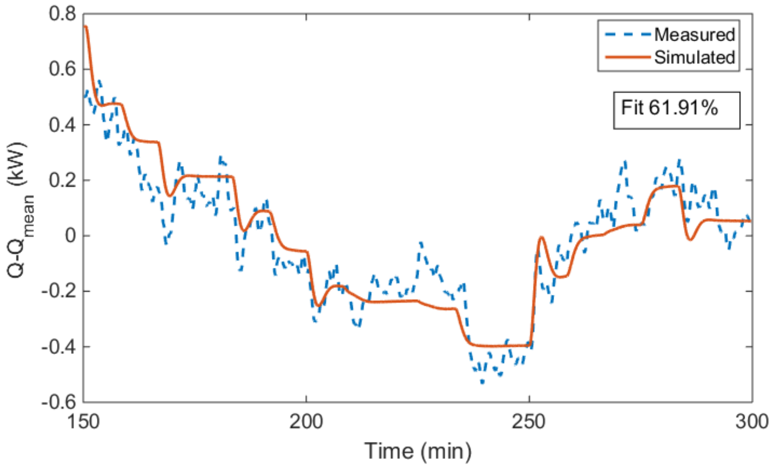

Figure 7-34 Heating capacity predicted by the state space model and obtained from the measured data.

Validation Results

Cooling Tests

Normally, the ambient temperature during the cooling tests is around 90°F. Tracking performances for cooling tests are shown in Figure 7-35 and Figure 7-36. The rising time of the cooling capacity control is around 3 minutes. And, normally, the maximum error between the cooling capacity and the setpoint is less than 0.3 kW. The discharge pressure control has a similar rising time. Normally, the error is less than 5 psi. Compared with SISO controllers, the MIMO controller has a smaller rising time and better tracking performance. The sudden changes in cooling capacity and discharge pressure at 30 and 100 minutes are caused by a change in ID blower speed from 500 to 800 cfm.

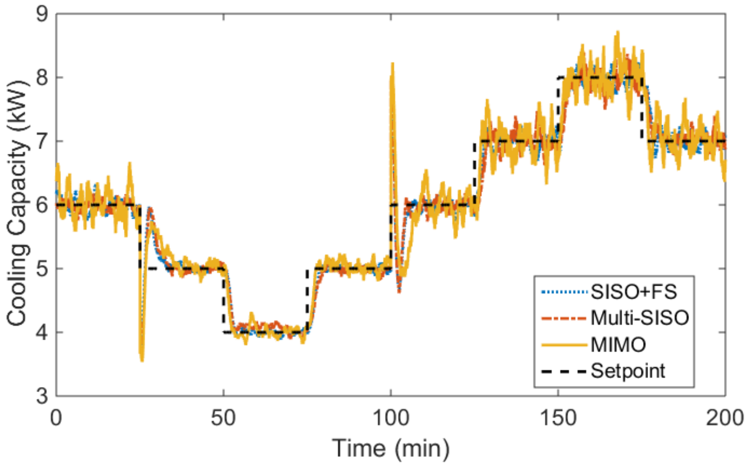

Figure 7-35 Cooling capacity tracking.

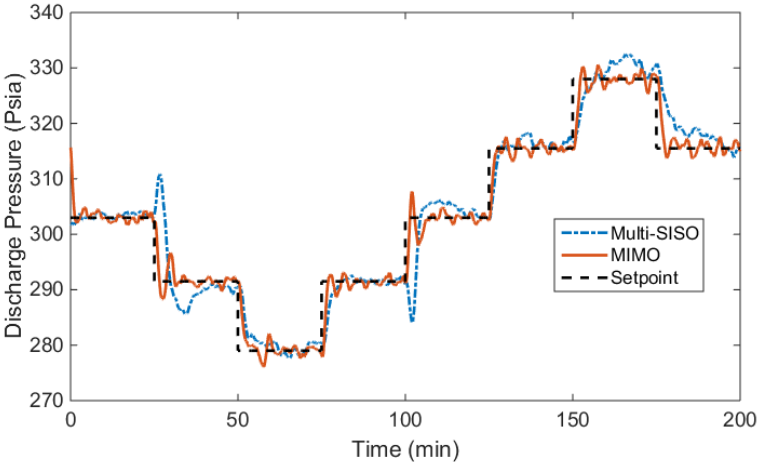

Figure 7-36 Discharge pressure tracking.

Control signals are shown in Figure 7-37 and Figure 7-38. Higher cooling capacity setpoint means higher compressor speed and ID blower speed. When the setpoint increases from 4 to 8 kW, the compressor speed rises from 1,750 to 4,300 rpm, and the ID blower speed rises from 500 to 800 cfm. For MIMO control, the sudden changes in OD fan speed at 30 and 100 minutes are also caused by the changes in ID blower speed.

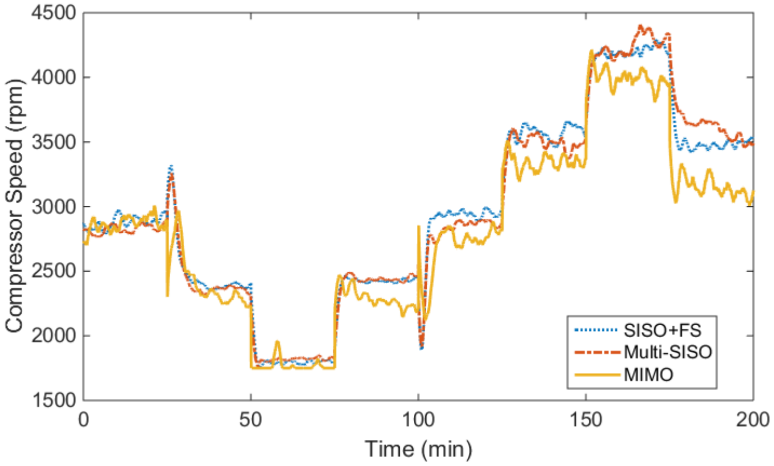

Figure 7-37 Compressor speed for cooling tests.

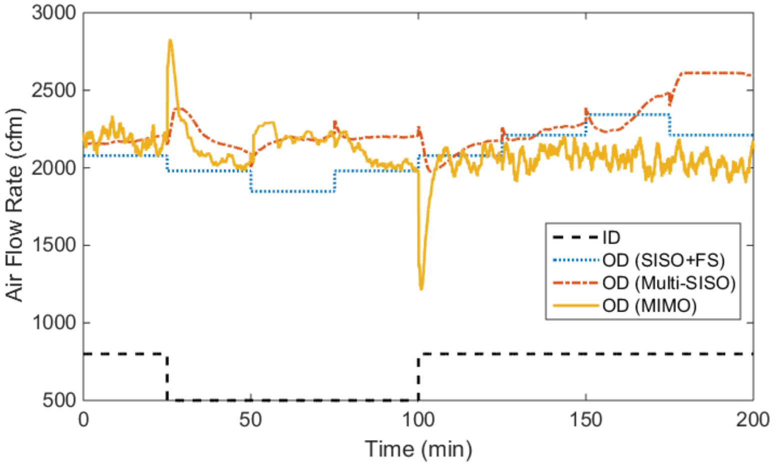

Figure 7-38 Air flow rate for cooling tests.

A control group is designed and used as the benchmark. The group has only compressor speed–cooling capacity control. Both the ID blower and OD fan speed run at their maximum speeds. Figure 7-39 shows that the average COP of the control group is 3.5. The average COP for SISO control with fan scheduling, multi-SISO control, and MIMO control are 4.2, 4.1, and 4.2, respectively. The energy optimal control strategies improve COP by around 20%.

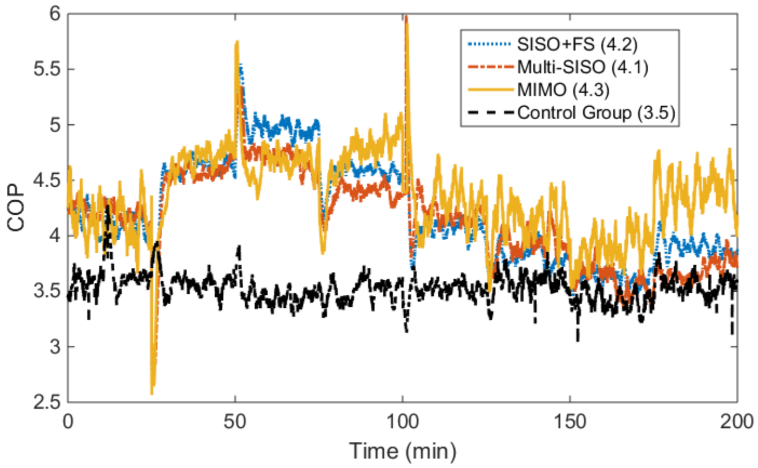

Figure 7-39 COP under different control strategies.

Heating Tests

For heating tests, the superheat setpoint is constant, but the heating capacity setpoint has step changes. Validation results are shown in Figure 7-40, Figure 7-41, and Figure 7-42. The rising time of the heating capacity control under the three scenarios are around 6 minutes. Superheat is affected by both compressor speed and valve opening. The maximum deviation from the setpoint is less than 3°F. For MIMO control, the rising time of the heating capacity control and suction pressure control is around 5 minutes.

The maximum deviation from setpoint is smaller than 2°F. Results show that MIMO control has better superheat and pressure tracking performances than SISO control.

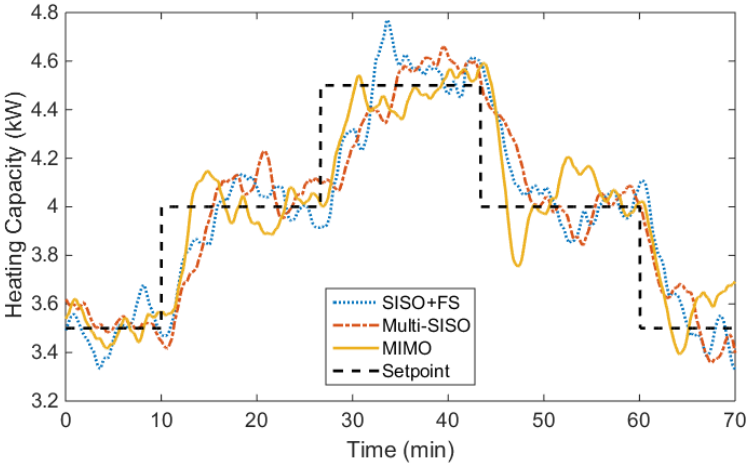

Figure 7-40 Heating capacity tracking.

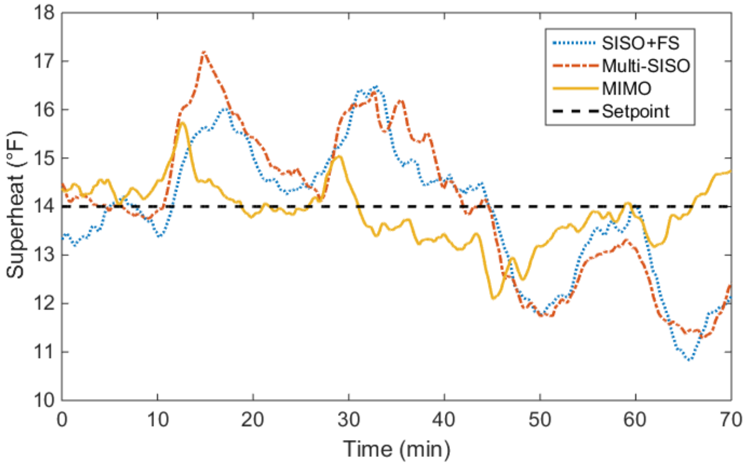

Figure 7-41 Superheat tracking.

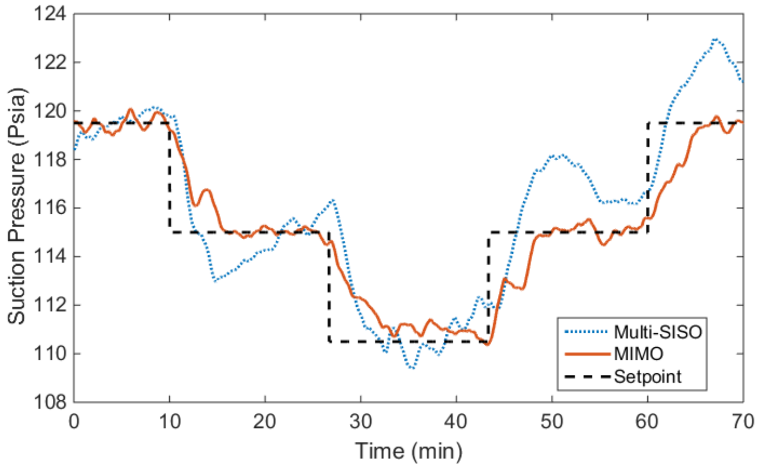

Figure 7-42 Suction pressure tracking.

Control signals include compressor speed, ID blower speed, OD fan speed, and EXV opening, as shown in Figure 7-43, Figure 7-44, and Figure 7-45. High heating capacity setpoint means high compressor speed and high OD air flow rate. As the compressor speed goes up, the valve opening also rises to compensate for the influence of the compressor speed on the superheat.

Control signals under MIMO control are more aggressive compared with those under the two SISO control scenarios. For example, when the heating capacity setpoint changes from 3.5 to 4.0 kW at 9 minutes, both the compressor speed and the OD fan speed jump instantaneously. The valve opening also has more step changes during the transient cases.

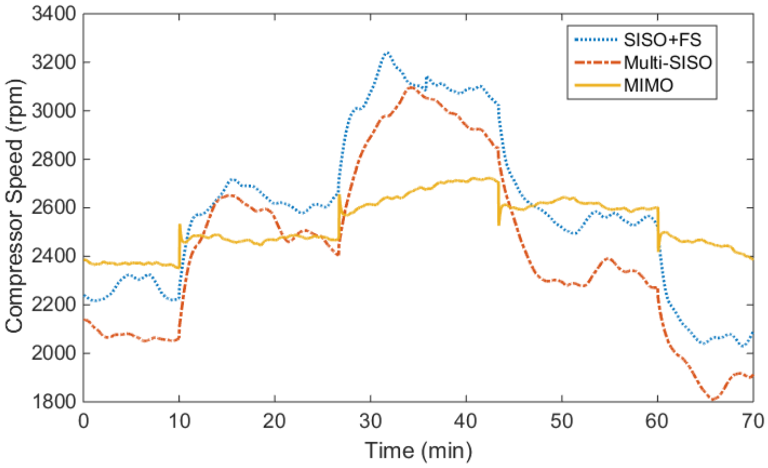

Figure 7-43 Compressor speed for heating tests.

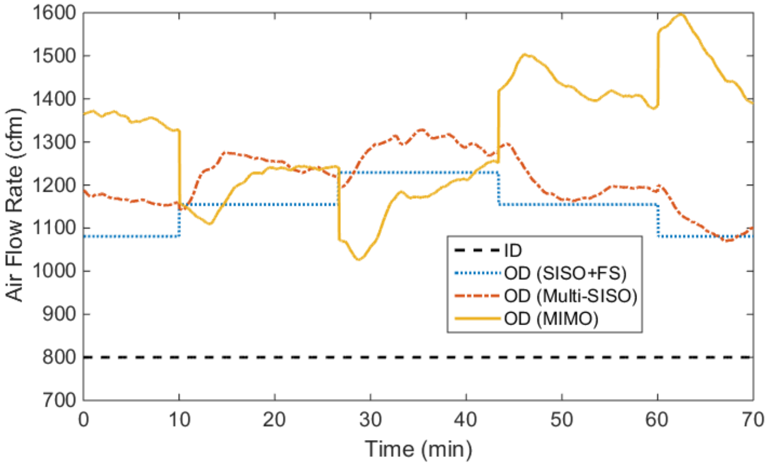

Figure 7-44 Air flow rate for heating tests.

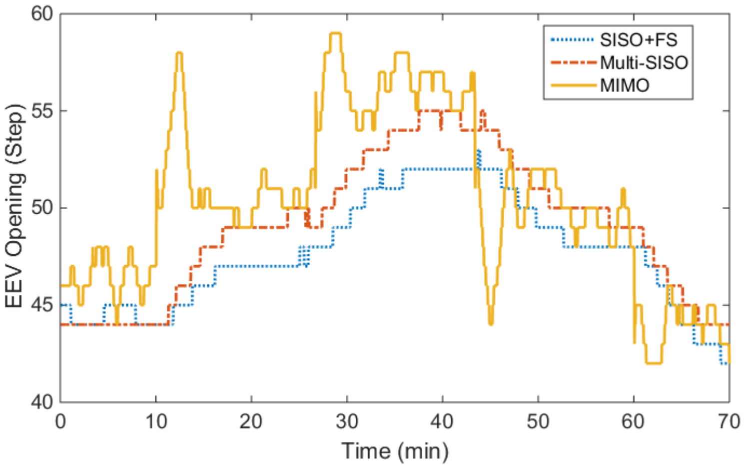

Figure 7-45 Valve opening for heating tests.

8. DEFROSTING CONTROL

The time and temperature control used in the HVAC industry may unnecessarily trigger defrosting and cause low efficiency and human discomfort. In this chapter, an intelligent defrosting control aimed at maximizing system efficiency and human comfort is proposed. First, experimental results of the time and temperature control are presented. Then, the intelligent defrost design is tested based on simulated data and experimental tests. Results shows that there exists an optimal combination of frost growth time and defrost termination temperature. The influences of compressor speed, moisture rate, and ambient temperature on the optimal frost growth time and optimal defrost termination temperature are investigated.

Time and Temperature Control

The time and temperature control is shown in Figure 8-1. Defrosting is triggered when the temperature difference (T_{fr}) between the ambient temperature (T_{amb}) and the defrost sensor (T_{dfr}) is not less than the predetermined maximum temperature differential $(\Delta T_{trigger})$ **AND** when the time of frost growth stage (t_{fr}) reaches the predetermined maximum time $(t_{trigger})$. Defrosting is terminated when the defrost sensor temperature (T_{dfr}) is not less than the predetermined maximum temperature $(T_{terminate})$ **OR** when the time of defrosting stage (t_{dfr}) reaches the predetermined maximum time $(t_{terminate})$.

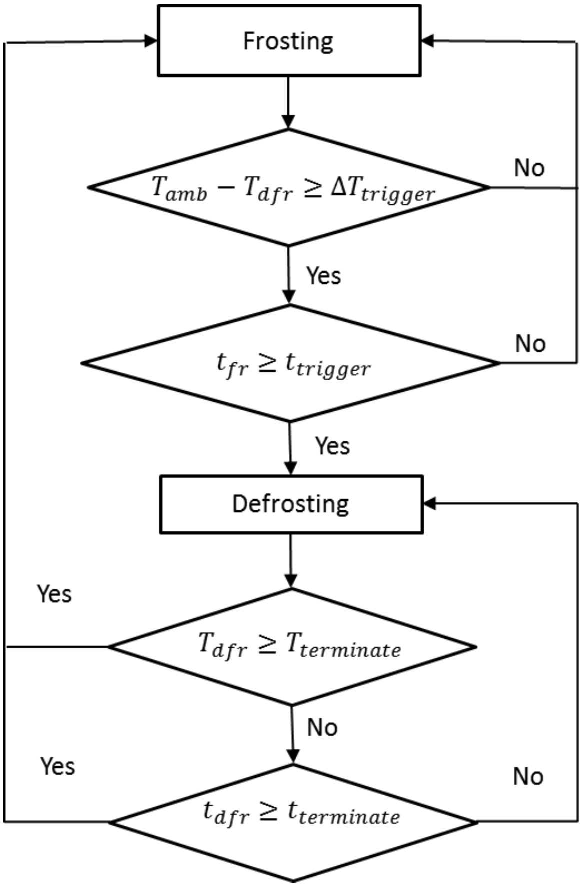

Figure 8-1 Time and temperature defrost control.

Operating conditions during a typical defrosting cycle are shown in Table 8-1. When the reversing valve is on, the system runs in heating mode. During the frost growth stage, the compressor speed, OD fan speed, and ID blower speed are constant. The superheat is controlled by the EXV. During the defrosting stage, the compressor runs at maximum speed in cooling mode, while the ID blower runs at minimum speed (400 cfm). The TXV controls superheat, while the EXV is fully open. The OD fan is off during the defrosting stage.

Table 8-1 Operating conditions.

Actuators	Frost Growth Stage	Defrosting Stage
Compressor	2,800 rpm	4,500 rpm (Maximum speed for cooling)
OD fan duty	40% (1,320 cfm)	0 (OFF)
ID blower	High (800 cfm)	Low (400 cfm)
EXV	Superheat control loop	250 (Fully open)
Reversing valve	ON	OFF
Humidifier	Moisture rate: 1.1 to 1.2 lb/hr	OFF

Here is a typical group of predetermined parameters: $\Delta T_{trigger} = 5°\mathrm{F}$, $T_{terminate} = 75°\mathrm{F}$, $t_{trigger} = 90$ minutes, $t_{terminate} = 10$ minutes. Experimental results are shown in Figure 8-2 through Figure 8-7. The frost growth stage ends when the frost growth time is not less than 60 minutes and the temperature difference is not less than 5°F. Then, the system switches to the defrosting stage. The defrosting stage ends when the defrost sensor temperature reaches 75°F, even if the defrost time is less than 10 minutes.

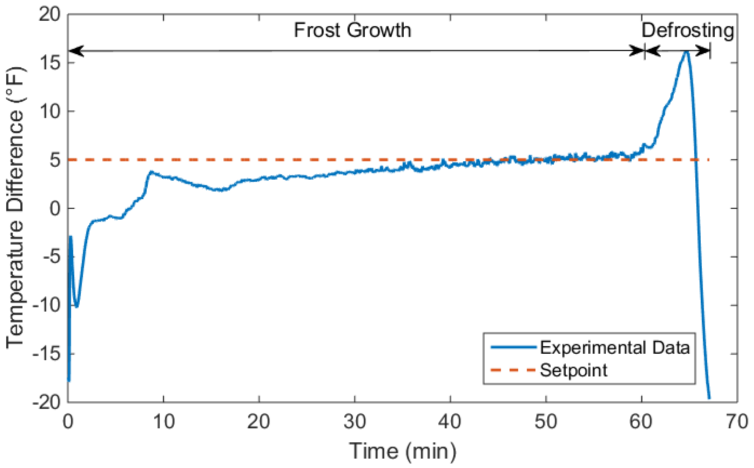

Figure 8-2 Temperature difference between the defrost sensor and the ambient.

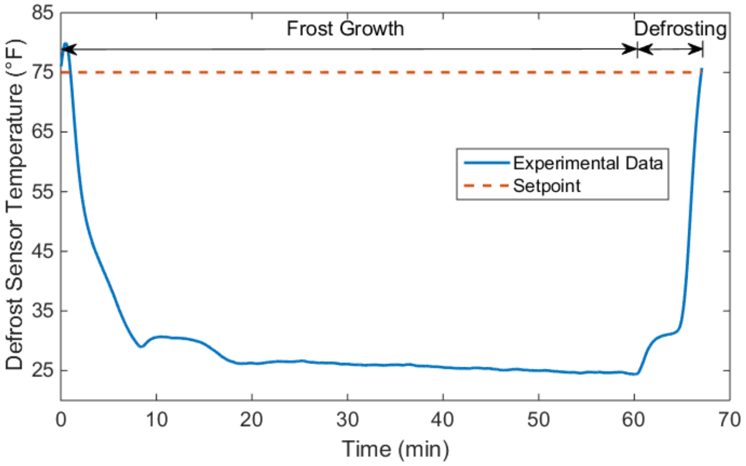

Figure 8-3 Defrost sensor temperature.

The ambient temperature during the frost growth stage is controlled by the ambient temperature controller and is maintained at 30°F (Figure 8-4). But during the defrosting stage, the system generates heat to remove frost, and the ambient temperature goes up.

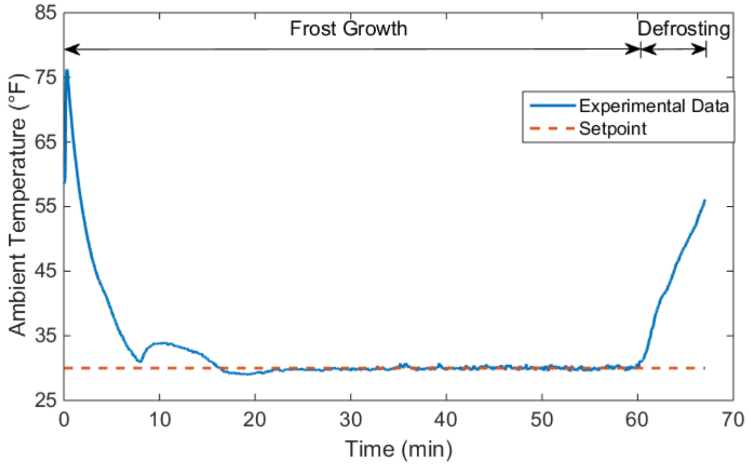

Figure 8-4 Ambient temperature.

Suction and discharge pressure are shown in Figure 8-5. Suction pressure drops slowly during the frost growth stage. When the system switches from the frost growth stage to the defrosting stage, discharge pressure drops quickly to 120 psia and then increases.

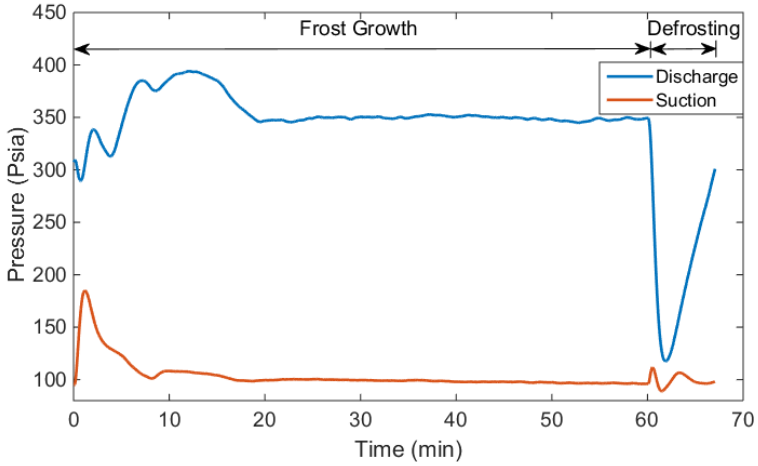

Figure 8-5 Suction and discharge pressure.

Power consumption is shown in Figure 8-6. Because the ID blower speed, OD fan speed, and compressor speed keep constant during the frost growth stage and the defrosting stage, total power consumption can be expressed as a function of discharge pressure and suction pressure. Hence, power consumption has a shape similar to that of discharge pressure.

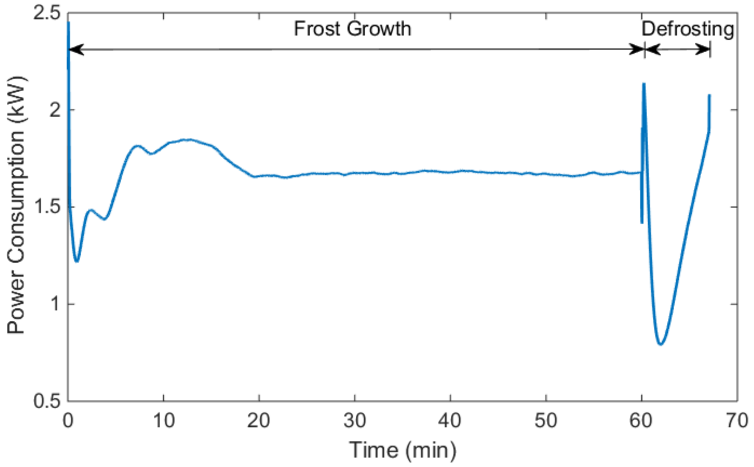

Figure 8-6 Power consumption.

Heating capacity is shown in Figure 8-7. As frost grows, heating capacity decreases from 4.5 kW to 3.9 kW during the frost growth stage. During the defrosting stage, the ID heat exchanger works as an evaporator. Here, negative values indicate that the system provides cooling capacity.

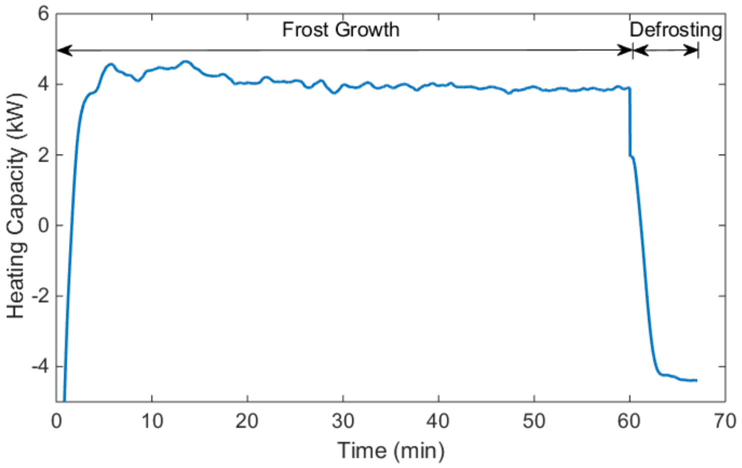

Figure 8-7 Heating capacity.

Intelligent Defrosting Control Design

Intelligent defrosting control is used to optimize system performance and human comfort. In order to evaluate system efficiency and human comfort during defrosting cycles, the inverse efficiency is defined as the ratio of total power consumption divided by the total heating power during defrosting cycles.

$$\eta = \frac{\int_{t_{fr}} W_{fr}\, dt + \int_{t_{dfr}} W_{dfr}\, dt}{\int_{t_{\mathrm{fr}}} Q_{fr}\, dt + \int_{t_{\mathrm{dfr}}} Q_{\mathrm{dfr}}\, dt} \tag{8.1}$$

Human discomfort depends on the temperature difference between the room and the setpoint. A larger temperature difference indicates higher human discomfort. The dimensionless parameter can be defined as:

$$\varepsilon = \frac{\int_{t_{fr}+t_{dfr}} \Delta\tilde{T} dt}{t_{fr} + t_{dfr}} \tag{8.2}$$

The objective function can be presented as a combination of the inverse efficiency and human discomfort:

$$J = \alpha * \eta + (1 - \alpha) * \varepsilon \tag{8.3}$$

The following presents a case study based on simulation results. During the frost growth stage, the heating capacity drops as frost forms on the surface of the OD heat exchanger. Decreasing heating capacity causes human discomfort. Heating capacity, power consumption, and human discomfort can be assumed to be given by Equations (8.4), (8.5), and (8.6), respectively.

$$Q_{fr} = 4 + 3 * tanh\left(\frac{120 - t_{fr}}{30}\right) \tag{8.4}$$

$$W_{fr} = 3 + tanh\left(\frac{t_{fr} - 120}{30}\right) + 3 * exp(-t_{dfr}) \tag{8.5}$$

$$\Delta\tilde{T} = \left(tanh\left(\frac{120 - t_{fr}}{30}\right) - 1\right) * \frac{5}{26} \tag{8.6}$$

Supposing both heating capacity and power consumption are constant during the defrosting stage, an electric heater is used to compensate the cooling capacity generated by the system during the defrosting stage. The total heating capacity and the power of the heater are given by Equation (8.7) and Equation (8.8):

$$Q_{dfr} = 0 \tag{8.7}$$

$$W_{dfr} = 4\, kW \tag{8.8}$$

Discomfort during the defrosting stage can be assumed as a function of the defrosting time and is given by:

$$\Delta\tilde{T} = \left(\exp\left(-\frac{t_{dfr}}{10}\right) - 1\right) * \frac{5}{26} \tag{8.9}$$

Figure 8-8, Figure 8-9, and Figure 8-10 show heating capacity, power consumption, and human discomfort during defrosting cycles, respectively. Heating capacity decreases continuously during the frost growth stage and drops to zero during the defrosting stage. Power consumption during the frost growth stage is almost constant. During the defrosting stage, heater power is added to total power consumption. Discomfort during the frost growth stage drops as the heating capacity decreases and is much higher during the frost growth stage because there is no heating capacity provided to the room.

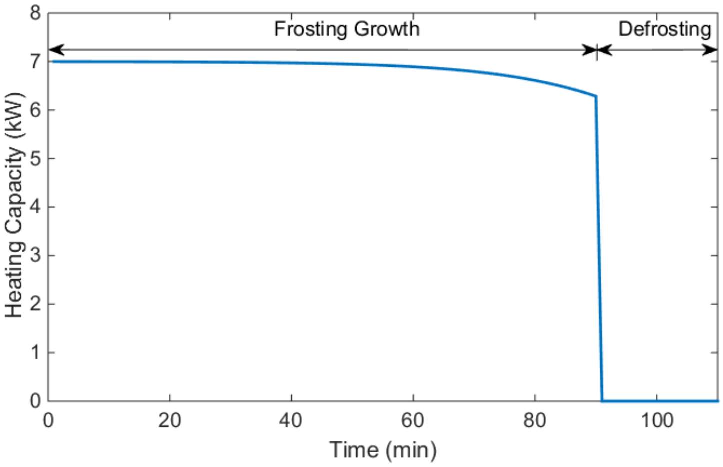

Figure 8-8 Heating capacity during defrosting cycles.

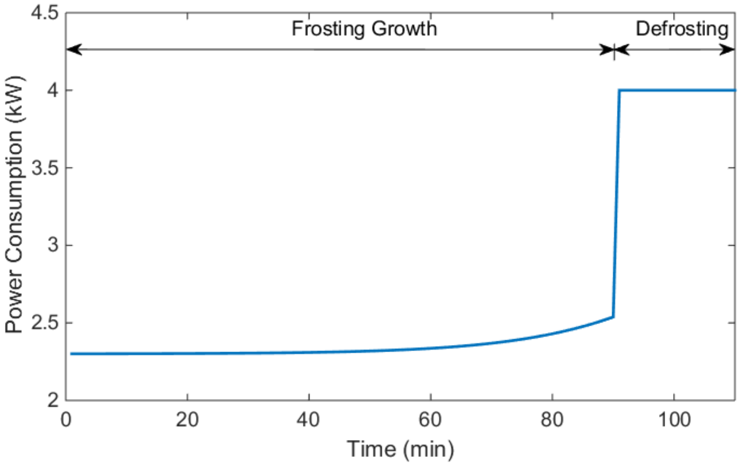

Figure 8-9 Power consumption during defrosting cycles.

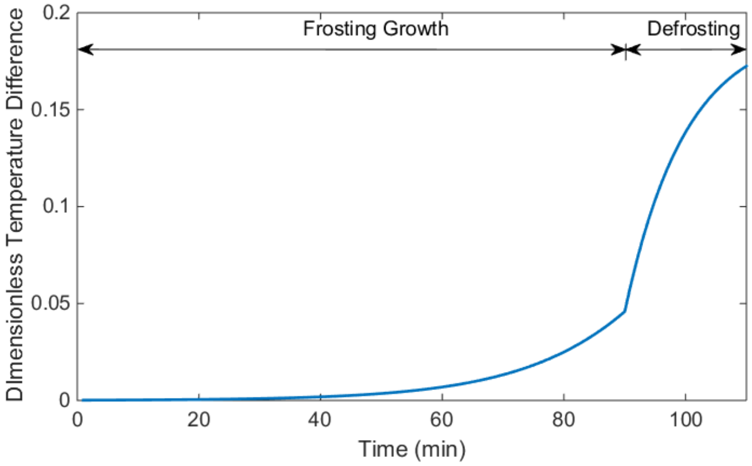

Figure 8-10 Discomfort during defrosting cycles.

Figure 8-11 shows that system efficiency and human discomfort can be minimized by setting optimal frost growth time and defrosting time. For $\alpha = 0.5$, the minimum value occurs when $t_{fr} = 72.00$ minutes and $t_{dfr} = 4.00$ minutes.

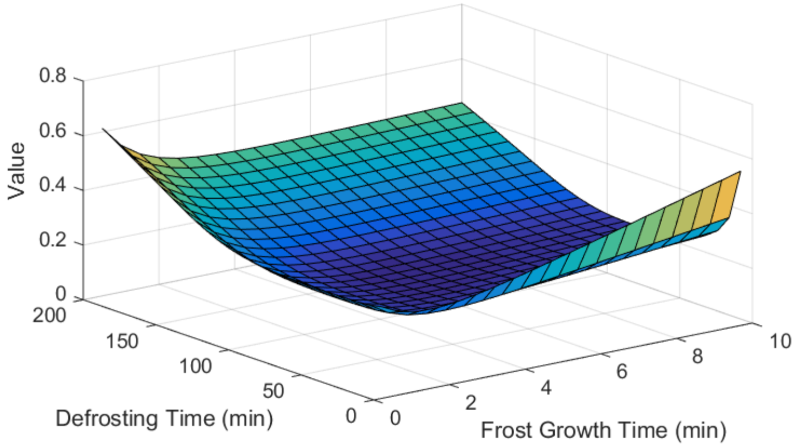

Figure 8-11 Objective value of the cost function.

Intelligent Defrost Control

The intelligent defrost control is used to maximize both system efficiency and human comfort by optimizing the frost growth time and defrost termination temperature. First, the effects of frost growth time and defrost termination temperature on system efficiency are investigated. Then, the effect of different operating conditions on optimal frost growth time and optimal defrost termination temperature is studied. Three parameters in Table 8-2 are moisture rate, compressor speed, and ambient temperature. Case A and Case B have the same compressor speed and the same ambient temperature but different moisture rates. Case A and Case C have the same moisture rate and ambient temperature but different compressor speeds. Case C and Case D have the same compressor speed and moisture rate but different ambient temperatures.

Table 8-2 Test cases.

Case	Ambient Temperature (°F)	Compressor Speed (rpm)	Moisture Rate (lb/hr)
A	30	2,800	0.5 to 0.6
B	30	2,800	1.1 to 1.2
C	30	3,500	0.5 to 0.6
D	25	3,500	0.5 to 0.6

Effects of Frost Growth Time and Defrost Termination Temperature

For Case A, the compressor speed is 2,800 rpm and the moisture rate is 0.5 to 0.6 lb/hr. Here, the effects of frost growth time and defrost termination temperature are studied for both the frost growth stage and the defrosting stage.

1) Frost Growth Stage

The frost growth stage is triggered when the defrost termination temperature reaches the predetermined setpoint. Three tests listed in Table 8-3 are used to study the effect of defrost termination temperature on system performance.

Table 8-3 Tests with different defrost termination temperatures.

Test	Defrost termination temperature (°F)	Frost growth time (min)
I	35	120
II	55	120
III	75	120

Experimental results are shown in Figure 8-12, Figure 8-13, and Figure 8-14. When the defrost termination temperature increases from 35°F to 75°F, the variations in heating capacity and power consumption can be neglected. The defrost sensor temperature in the above three cases are almost the same after 20 minutes. The effect of defrost termination temperature on system performance is negligible.

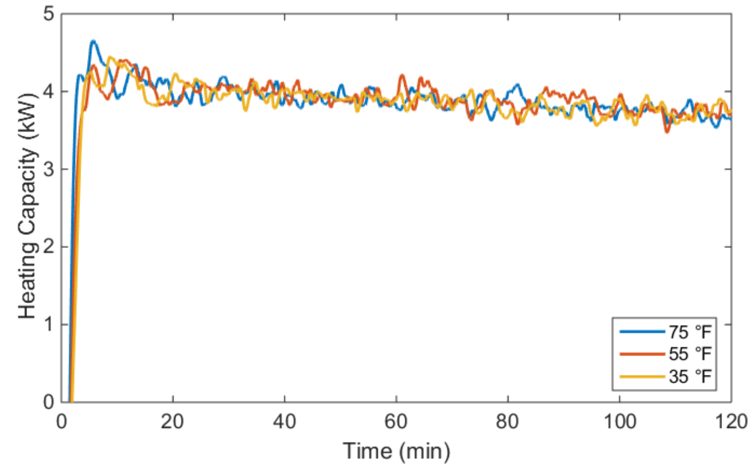

Figure 8-12 Heating capacity.

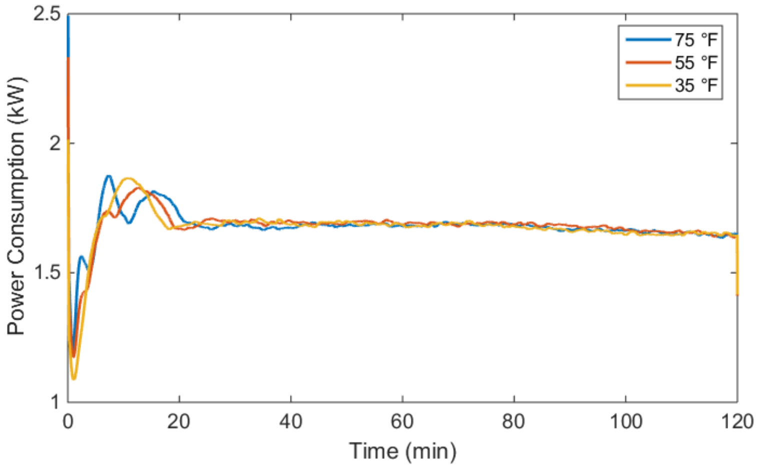

Figure 8-13 Power consumption.

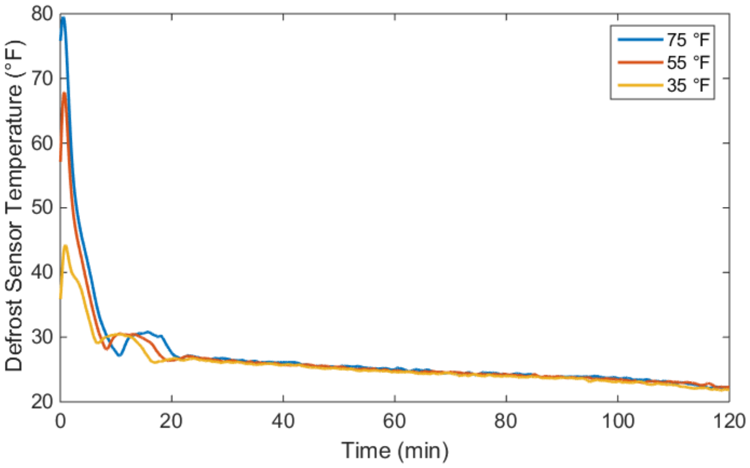

Figure 8-14 Defrost sensor temperature.

A 5-hour test is carried out to analyze the effects of frost growth time on system performance during the frost growth stage. As shown in Figure 8-15, the ambient temperature is around 30°F, except at the beginning of the frost growth stage. Hence, the effect of ambient temperature on system performance can be excluded.

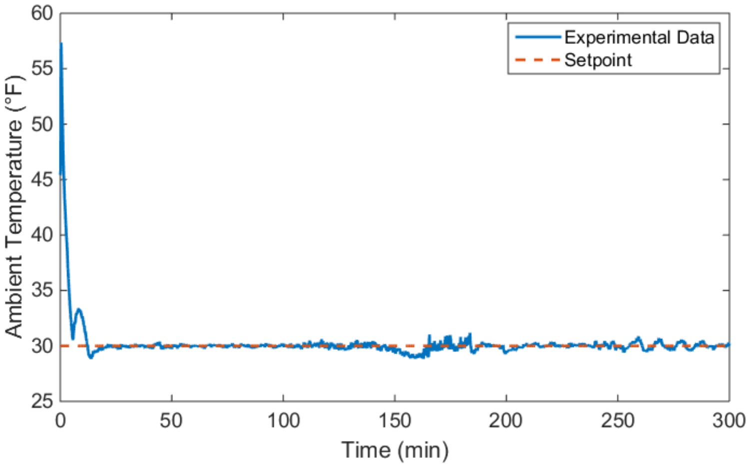

Figure 8-15 Ambient temperature.

Figure 8-16 shows discharge and suction pressure. Both discharge and suction pressures drop as frost grows. Meanwhile, discharge pressure is also affected by the valve opening. Because the valve opening decreases continuously, the discharge pressure begins to increase after 180 minutes.

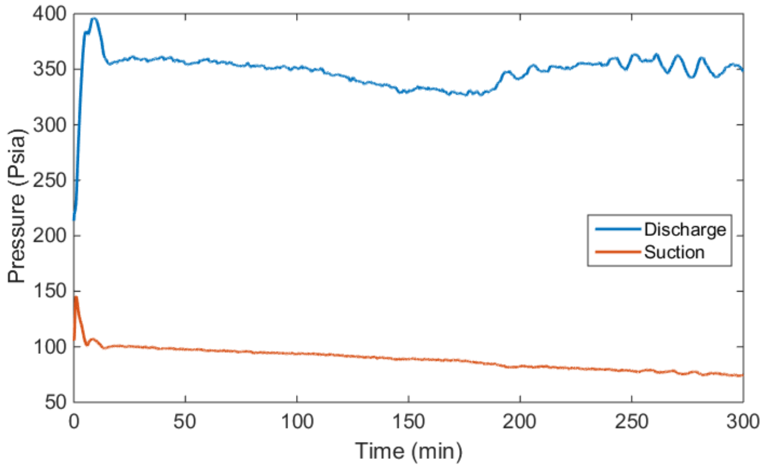

Figure 8-16 Suction and discharge pressure.

Superheat is shown in Figure 8-17. In order to track the setpoint (14°F), the valve opening decreases continuously. It can be seen that the tracking performance is good during the first 180 minutes. However, the superheat has significant oscillations after 180 minutes, even with one or two step changes of the valve opening.

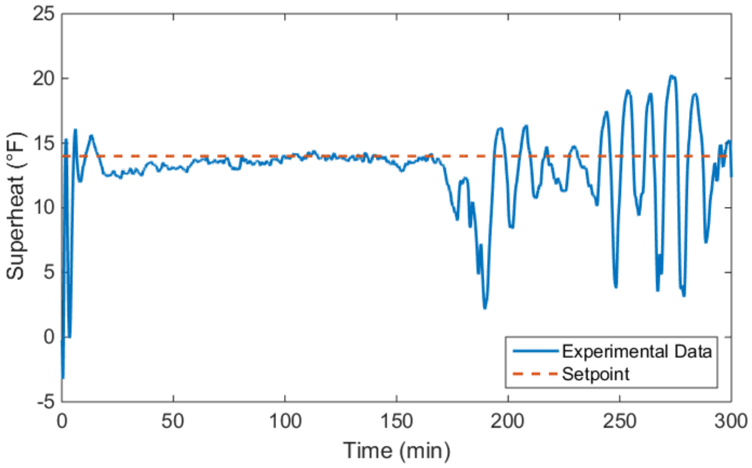

Figure 8-17 Superheat.

Air pressure drop is shown in Figure 8-18. The air pressure drops from 0.05 to 0.15 in H_2O in the first 150 minutes. Larger air pressure drop indicates frost formation on the surface of the OD heat exchanger. After 150 minutes, the air pressure drop becomes almost constant, indicating that the frost formation rate becomes slower.

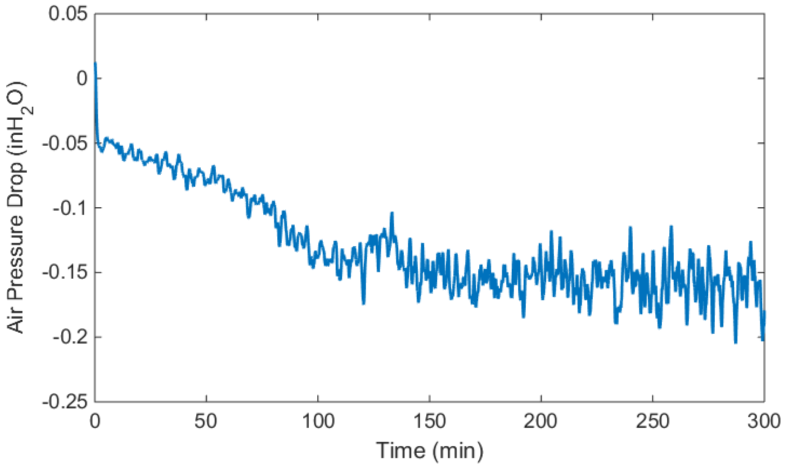

Figure 8-18 Air pressure drop.

Defrost sensor temperature is shown in Figure 8-19. Frost formation on the surface of the OD heat exchanger leads to low heat transfer between the heat exchanger and the ambient. The sensor temperature drops to 13°F after 5 hours.

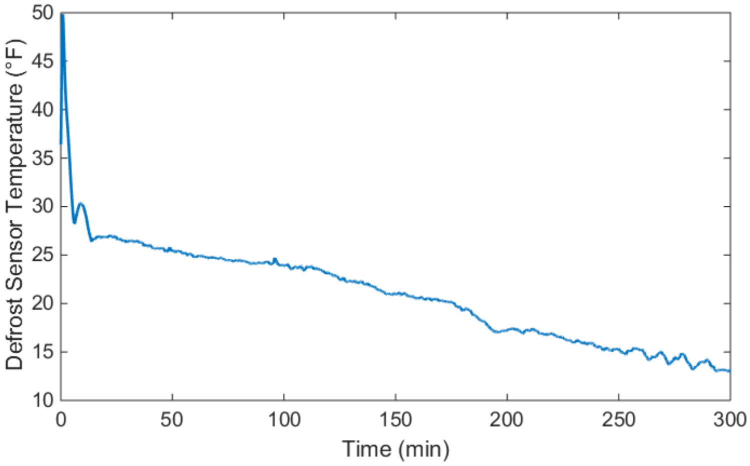

Figure 8-19 Defrost sensor temperature.

Power consumption is shown in Figure 8-20 and can be expressed as a function of the frost growth time. The fitted curve is given by:

$$P_{fr} = 0.60e^{-\frac{t_{fr}}{507.62}} - 1.67e^{-\frac{t_{fr}}{160.56}} + 1.68 - 0.00t_{fr} \tag{8.10}$$

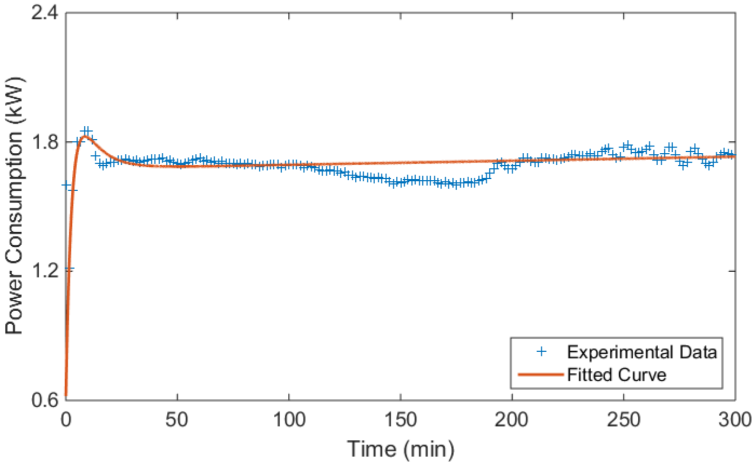

Figure 8-20 Power consumption.

Heating capacity is shown in Figure 8-21. Frost accumulation on the surface of the heat exchanger causes a decrease in heating capacity during the frost growth stage. The heating capacity decreases from 4.5 to 3.3 kW in 5 hours. The fitted curve is given by:

$$Q_{fr} = 1.74e^{-\frac{t_{fr}}{15138.02}} - 5.15e^{-\frac{t_{fr}}{34.06}} + 2.66 - 0.00t_{fr} \tag{8.11}$$

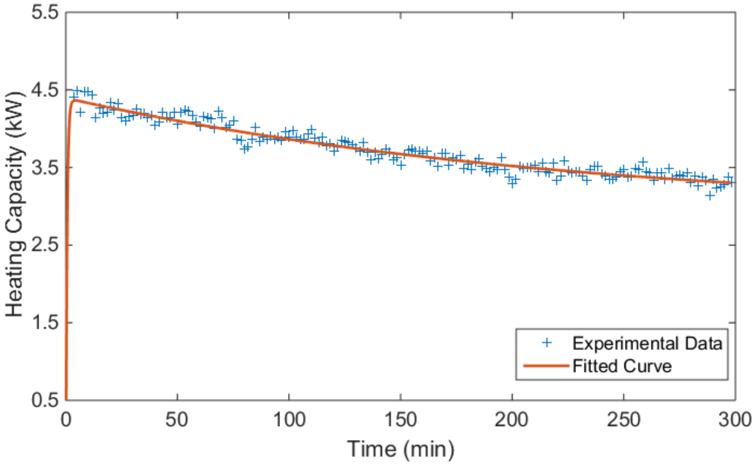

Figure 8-21 Heating capacity.

2) Defrosting Stage

Three tests listed in Table 8-4 are used to show the effect of frost growth time and defrost termination temperature on system performance during the defrosting stage. The predetermined defrost termination temperature stays unchanged.

Table 8-4 Tests with different frost growth times.

Test	Frost growth time (min)	Defrost termination temperature (°F)
I	60	75
II	180	75
III	300	75

The defrost sensor temperature is shown in Figure 8-22. Based on the defrost sensor temperature, the defrosting stage can be divided into three steps:

$T_{dfr} < 32$°F, preheating

$T_{dfr} = 32$°F, frost melting

$T_{dfr} > 32$°F, coil heating

The defrost time is determined by both the frost growth time and the defrost termination temperature. Longer frost growth time and higher predetermined defrost sensor temperature indicate longer defrost time.

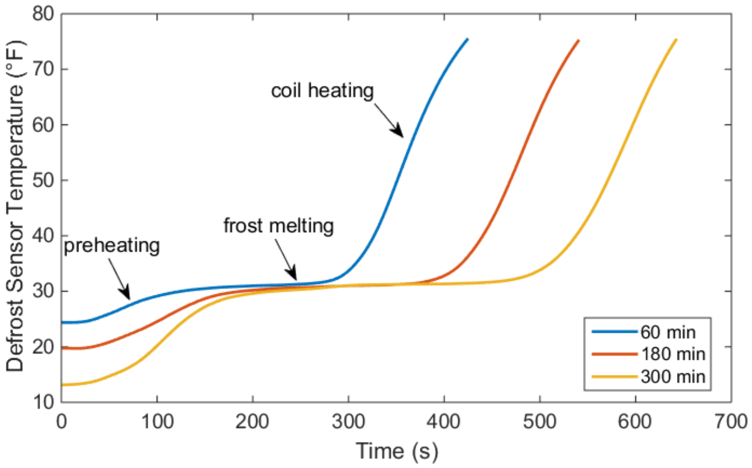

Figure 8-22 Defrost sensor temperature.

Figure 8-23 shows that the power consumption drops from 2.2 kW to around 0.8 kW during the first 120 seconds and then increases at a slower rate. Power consumption can be estimated as a function of both frost growth time and defrost time. The fitted curve is given by:

$$P_{dfr} = A_1 e^{A_2 t_{dfr}} + \ A_3 e^{A_4 t_{dfr}} \tag{8.12}$$

where $A_1 = 0.0004 * t_{fr} + 1.7065,$

$A_2 = 0.0000 * t_{fr} - 0.0193,$

$A_3 = -0.0003 * t_{fr} + 0.5219,$

$A_4 = -0.0000 * t_{fr} + 0.0034,$

t_{dfr} is the total defrost time, which can be expressed as a function of both frost growth time and the defrost termination temperature:

$$t_{dfr} = 276.4067 + 0.7667 * t_{fr} \ + \left(T_{dfr} - 32\right) * 2.7533 \tag{8.13}$$

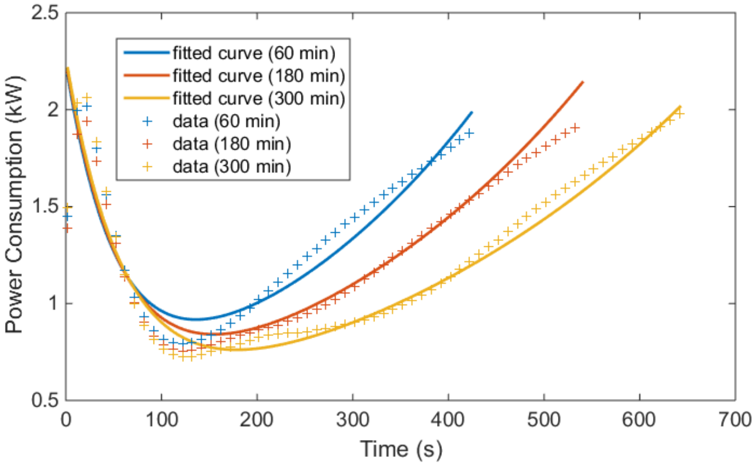

Figure 8-23 Power consumption.

Figure 8-24 shows that heating capacity drops from 2 kW to −4 kW in the first 3 minutes and then becomes almost constant. A negative value means that the system is providing cooling instead of heating to the room during the defrosting stage.

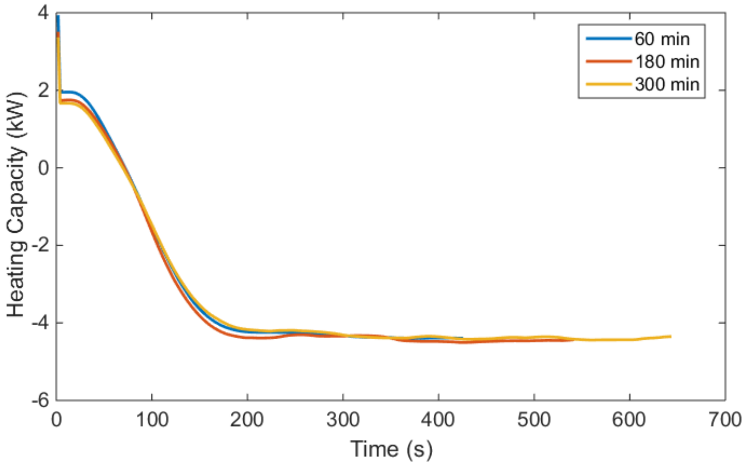

Figure 8-24 Heating capacity.

3) Optimization

Here, two scenarios are provided. The first scenario considers only the system efficiency. The second one includes human comfort. If only system efficiency is considered, the cost function can be defined as:

$$J = \frac{\int_{t_{fr}} W_{fr}\, dt + \int_{t_{dfr}} W_{dfr}\, dt}{\int_{t_{fr}} Q_{fr}\, dt} \tag{8.14}$$

The second case considers both system efficiency and human comfort. Supposing there is no human discomfort caused by defrosting, a heater is needed to not only compensate the cooling capacity, but also to generate the same heating capacity as that occurring during the frost growth stage. The normal heating capacity during the frost growth stage is around 3.5 kW, and the cooling capacity during the defrosting stage is 4.5 kW. Then, the power of the heater Q_{heater} is estimated as 8.0 kW. The cost function can be expressed as:

$$J = \frac{\int_{t_{fr}} W_{fr}\, dt + \int_{t_{dfr}} W_{dfr}\, dt + \int_{t_{dfr}} Q_{heater}\, dt}{\int_{t_{fr}} Q_{fr}\, dt} \tag{8.15}$$

where Q_{heater} is the power of the heater.

Results are shown in Figure 8-25 and Figure 8-26. The optimal defrost termination temperature is 32°F for both cases. When both system efficiency and human comfort are considered, the optimal defrost termination temperature increases from 70 to 210 minutes.

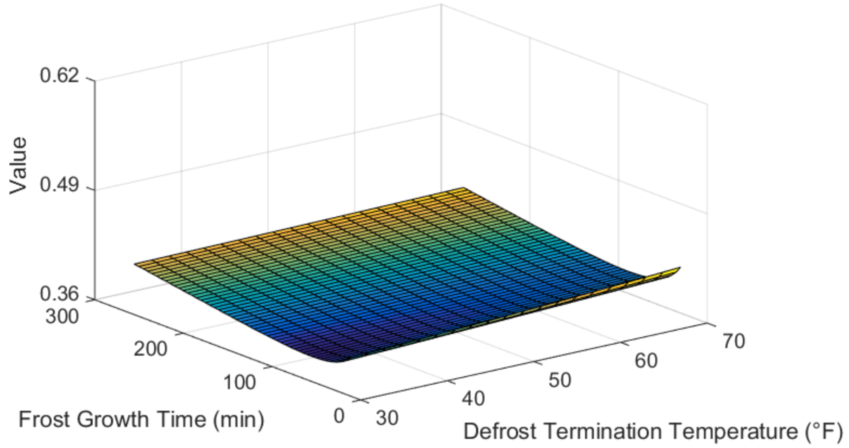

Figure 8-25 Value of the cost function without heat compensation.

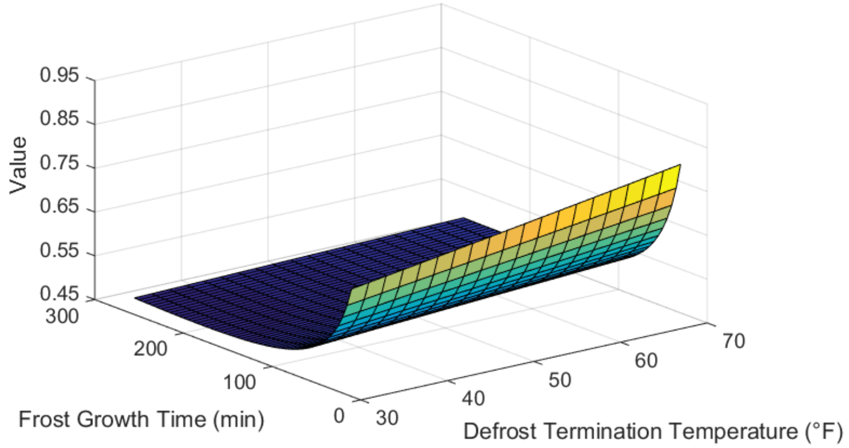

Figure 8-26 Value of the cost function with heat compensation.

Effects of Moisture Rate on System Performance

The effects of moisture rate can be obtained by comparing the results of Case A and Case B. The heating capacities of the two cases are shown in Figure 8-27. During the first 100 minutes, the difference is pretty small and can be neglected. After that, the heating capacity drops faster under a high moisture rate. At the end of the 5-hour test, the heating capacity drops to 3.3 kW with a low moisture rate and to 2.6 kW with a high moisture rate. It can be concluded that a higher moisture rate indicates a more significant decrease in heating capacity. Meanwhile, the power consumptions of the two cases shown in Figure 8-28 are pretty close. Hence, the effect of moisture rate on power consumption can be neglected. Figure 8-29 shows that the defrost sensor temperature drops faster with a higher moisture rate.

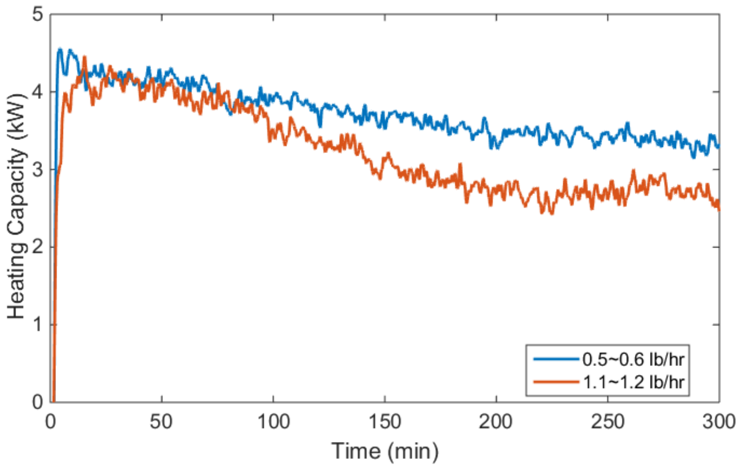

Figure 8-27 Heating capacity during the frost growth stage.

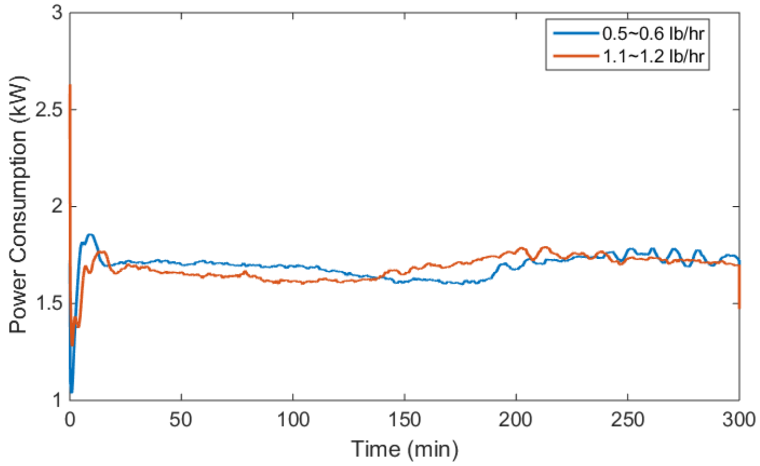

Figure 8-28 Power consumption during the frost growth stage.

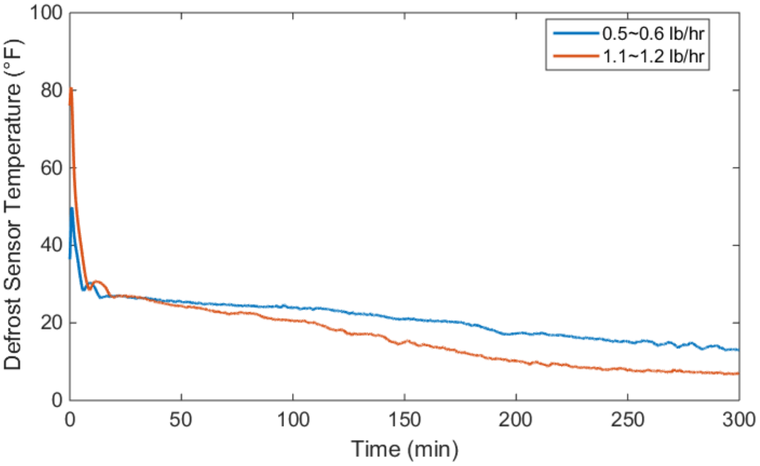

Figure 8-29 Defrost sensor temperature during the frost growth stage.

System performances during the defrosting stage are shown in Figure 8-30, Figure 8-31, and Figure 8-32. Compared with Case A, the defrost time under a higher moisture rate becomes longer. The defrost sensor temperature, power consumption, and heating capacity have similar tendencies to those of Case A.

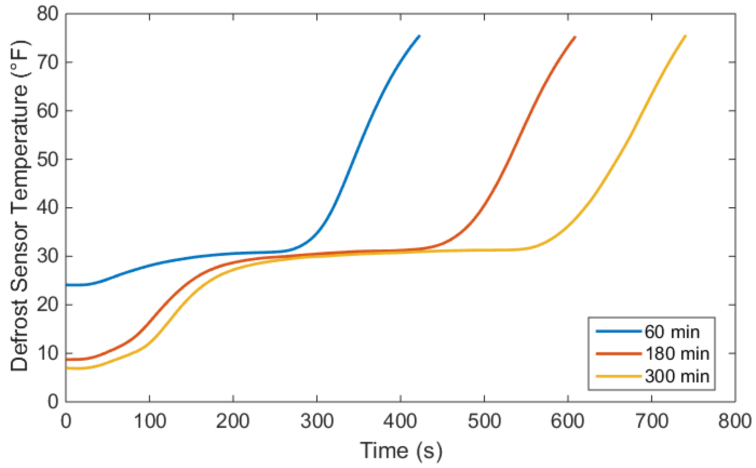

Figure 8-30 Defrost sensor temperature.

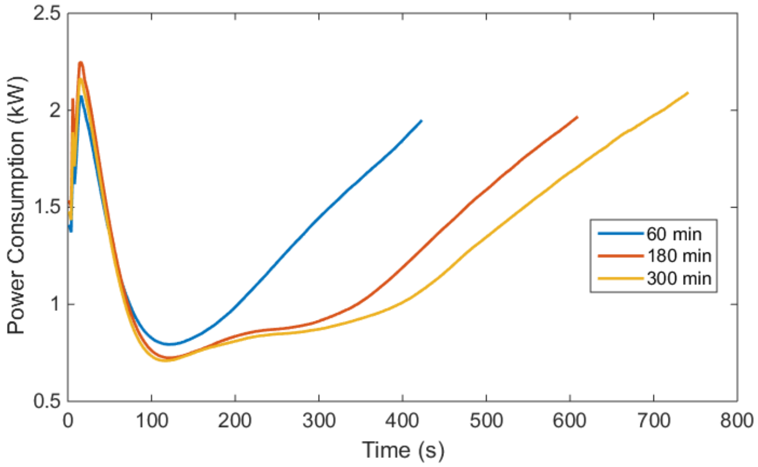

Figure 8-31 Power consumption during the defrosting stage.

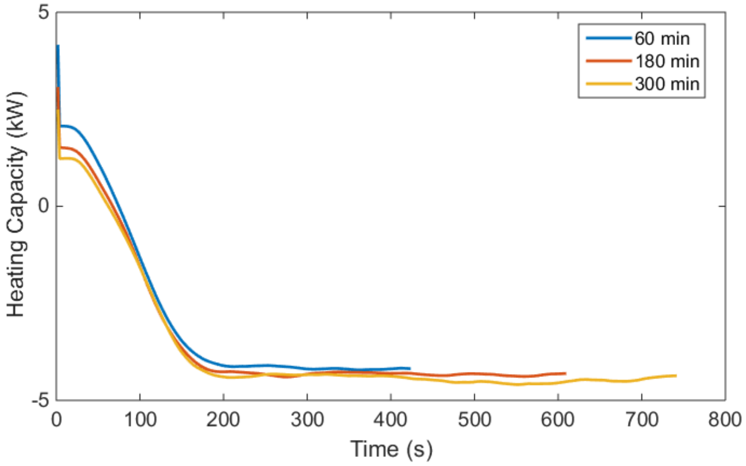

Figure 8-32 Heating capacity during the defrosting stage.

The heating capacity curve and power consumption curve during the frost growth stage are given by Equation (8.16) and Equation (8.17), respectively.

$$P_{fr} = 0.35e^{-\frac{t_{fr}}{1302.58}} - 0.75e^{-\frac{t_{fr}}{322.00}} + 1.59 - 0.00t_{fr} \tag{8.16}$$

$$Q_{fr} = 3.99e^{-\frac{t_{fr}}{998.87}} - 2.39e^{-\frac{t_{fr}}{498.07}} + 0.92 - 0.00t_{fr} \tag{8.17}$$

The fitted curve for power consumption during the defrosting stage is given by:

$$P_{dfr} = A_1e^{A_2t_{dfr}} + \ A_3e^{A_4t_{dfr}} \tag{8.18}$$

where $A_1 = 0.0005 * t_{fr} + 1.75,$

$A_2 = 0.0000 * t_{fr} - 0.0196,$

$A_3 = -0.0003 * t_{fr} + 0.5219,$

$A_4 = -0.0000 * t_{fr} + 0.0041,$

$t_{dfr} = 244.3000 + 1.175 * t_{fr} \ + \left(T_{dfr} - 32\right) * 3.06667$

Optimized results are shown in Figure 8-33 and Figure 8-34. Again, the optimal defrost termination temperature is 32°F. Higher moisture rate indicates smaller optimal frost growth time. The optimal frost growth time drops from 70 to 60 minutes if only system efficiency is considered and drops from 210 to 105 minutes when both system efficiency and human comfort are considered. The slopes of these two curves are higher than those under Case A. The optimal frost growth time is more sensitive when the moisture rate becomes higher.

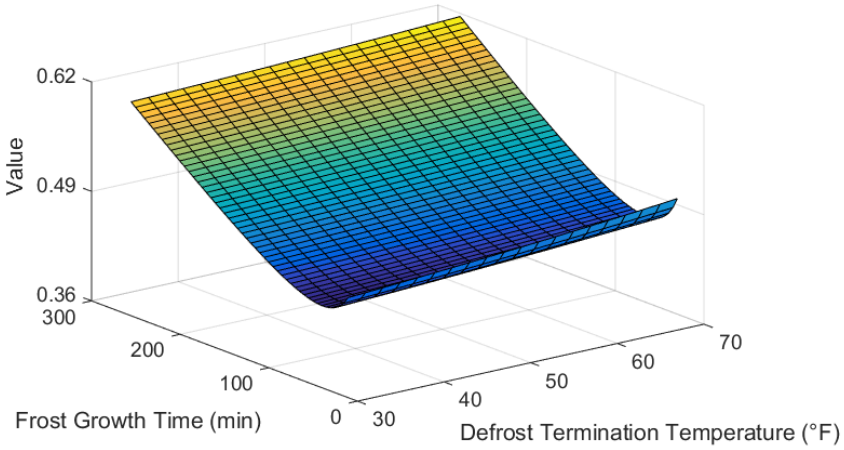

Figure 8-33 Value of the cost function without heat compensation.

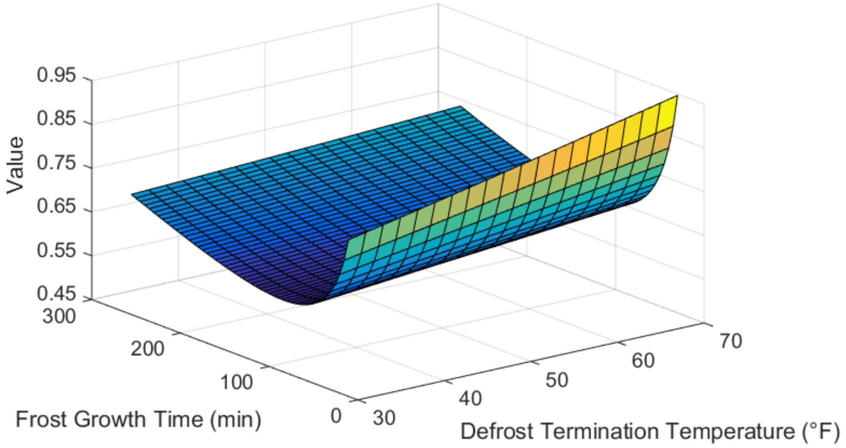

Figure 8-34 Value of the cost function with heat compensation.

Effects of Compressor Speed on System Performance

The effects of compressor speed can be obtained by comparing Case A and Case C. The heating capacities of the two cases are shown in Figure 8-35. Higher capacity is caused by higher compressor speed. The drop in the heating capacity of the two cases is around 0.8 kW. The power consumptions of the two cases are shown in Figure 8-36. Higher compressor speed leads to higher power consumption.

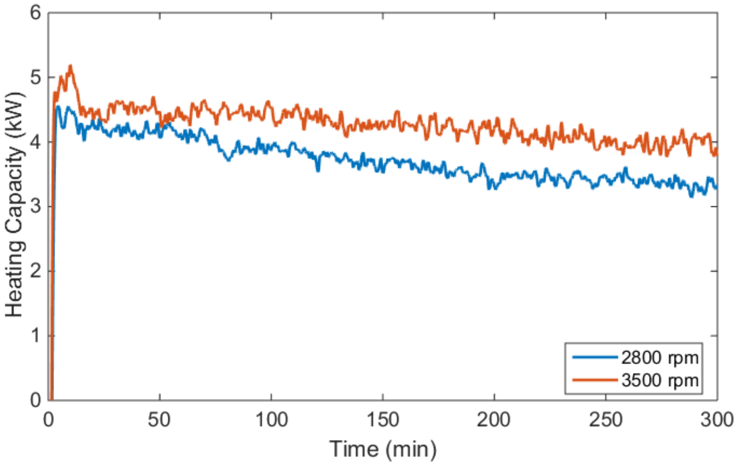

Figure 8-35 Heating capacity.

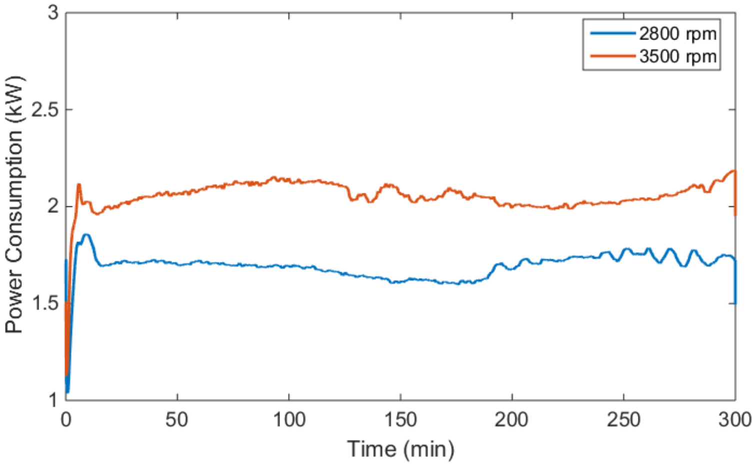

Figure 8-36 Power consumption.

The heating capacity curve and power consumption curve during the frost growth stage are given by Equation (8.19) and Equation (8.20), respectively.

$$P_{fr} = 0.29e^{-t_{fr}/997.78} - 1.08e^{-\frac{t_{fr}}{60.57}} + 2.10 - 0.00t_{fr} \tag{8.19}$$

$$Q_{fr} = 7.30e^{-t_{fr}/188.92} - 8.57e^{-\frac{t_{fr}}{148.12}} + 4.61 - 0.00t_{fr} \tag{8.20}$$

The fitted curve for power consumption during the defrosting stage is given by:

$$P_{dfr} = A_1 e^{A_2 t_{dfr}} + A_3 e^{A_4 t_{dfr}} \tag{8.21}$$

where $A_1 = 0.0005 * t_{fr} + 2.1384,$

$A_2 = 0.0000 * t_{fr} - 0.0212,$

$A_3 = -0.0001 * t_{fr} + 0.5067,$

$A_4 = -0.0000 * t_{fr} + 0.0033,$

$t_{dfr} = 257.96 + 0.7667 * t_{fr} + \left(T_{dfr} - 32\right) * 3.347$

System performances during the defrosting stage are shown in Figure 8-37, Figure 8-38, and Figure 8-39. The defrost sensor temperature, power consumption, and heating capacity have similar tendencies to those of Case A and Case B.

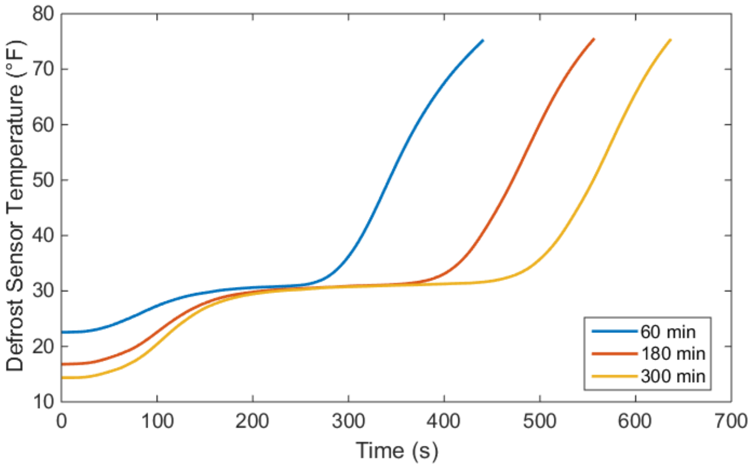

Figure 8-37 Defrost sensor temperature.

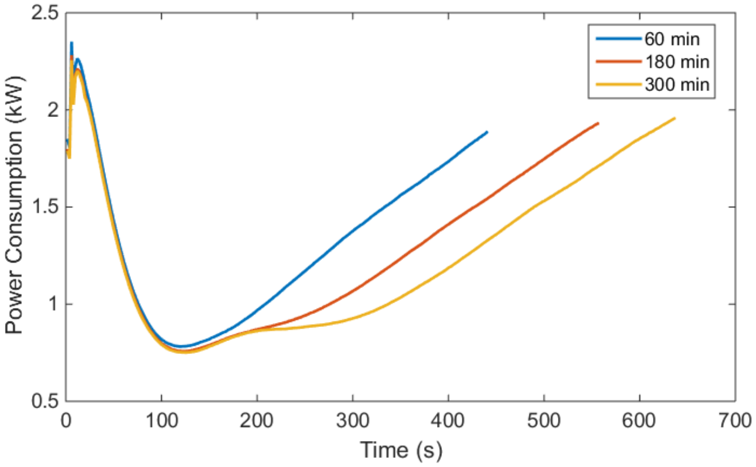

Figure 8-38 Power consumption.

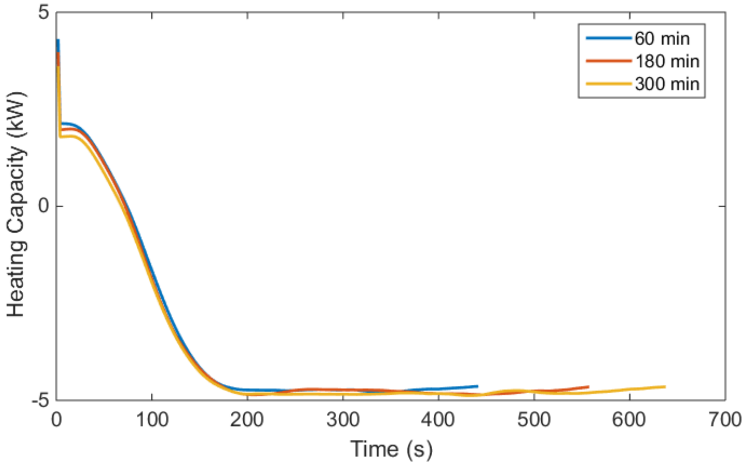

Figure 8-39 Heating capacity.

Optimized results are shown in Figure 8-40 and Figure 8-41. When only system efficiency is considered, the minimum value occurs when t_{fr} is around 35 to 40 minutes and T_{dfr} is around 32°F. When both system efficiency and human comfort are considered, the minimum value is obtained when t_{fr} is around 275 minutes and T_{dfr} is around 32°F.

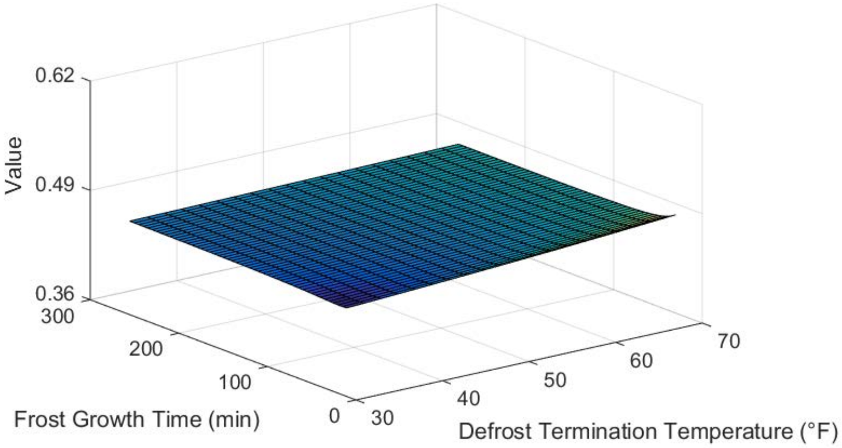

Figure 8-40 Value of the cost function without heat compensation.

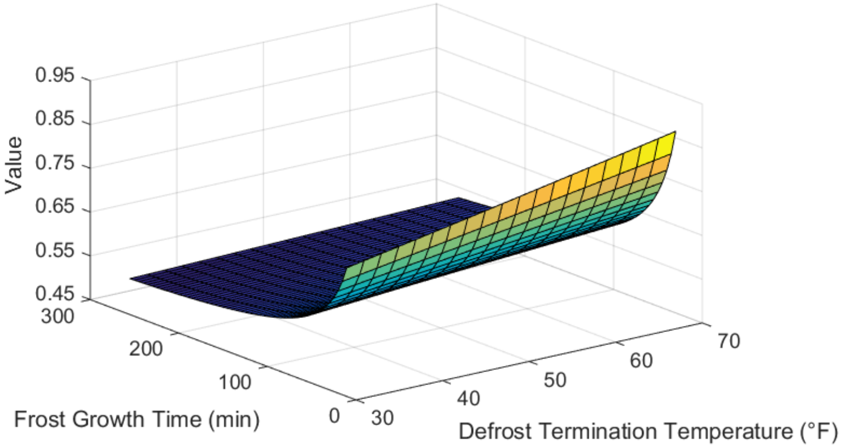

Figure 8-41 Value of the cost function with heat compensation.

Effects of Ambient Temperature on System Performance

The effects of ambient temperature can be obtained by comparing Case C and Case D. The heating capacities of the two cases are shown in Figure 8-42. It is obvious that higher ambient temperature indicates higher heating capacity. The power consumptions of the two cases shown in Figure 8-43 are similar. Hence, the effect of ambient temperature on power consumption can be neglected.

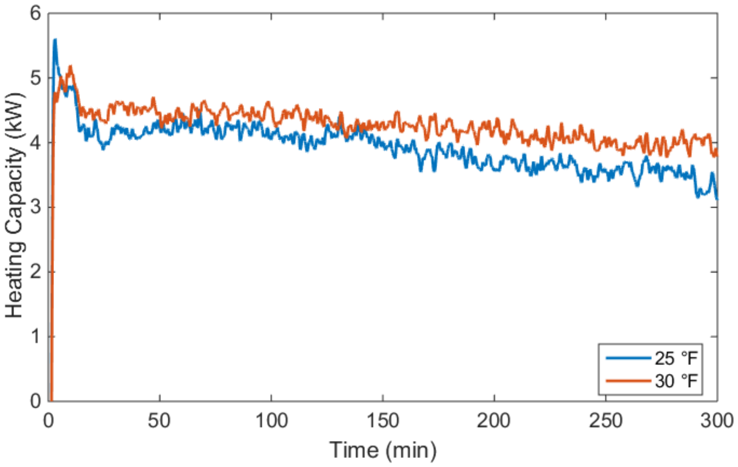

Figure 8-42 Heating capacity under different ambient temperatures.

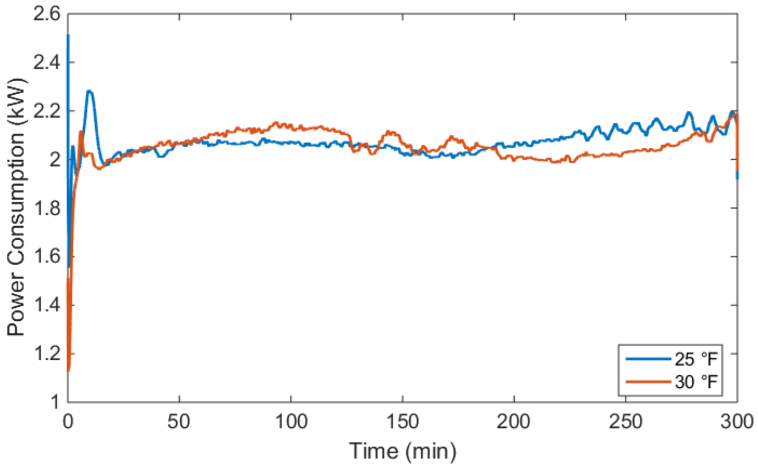

Figure 8-43 Power consumption under different ambient temperatures.

The heating capacity curve and power consumption curve during the frost growth stage are given by Equation (8.22) and Equation (8.23), respectively.

$$P_{fr} = 3.48e^{-t_{fr}/238.02} - 3.96e^{-\frac{t_{fr}}{209.32}} + 2.02 - 0.00t_{fr} \tag{8.22}$$

$$Q_{fr} = 1.63e^{-t_{fr}/231.47} - 4.39e^{-\frac{t_{fr}}{22.51}} + 4.41 - 0.00t_{fr} \tag{8.23}$$

The fitted curve for power consumption during the defrosting stage is given by:

$$P_{dfr} = A_1 e^{A_2 t_{dfr}} + A_3 e^{A_4 t_{dfr}} \tag{8.24}$$

where $A_1 = 0.0004 * t_{fr} + 2.043,$

$A_2 = 0.0000 * t_{fr} - 0.0211,$

$A_3 = -0.0002 * t_{fr} + 0.5065,$

$A_4 = -0.0000 * t_{fr} + 0.0031,$

$t_{dfr} = 278.8867 + 0.7417 * t_{fr} + (T_{dfr} - 32) * 3.4267$

System performances during the defrosting stage are shown in Figure 8-44, Figure 8-45, and Figure 8-46. The defrost sensor temperature, power consumption, and heating capacity have similar tendencies to those of other cases.

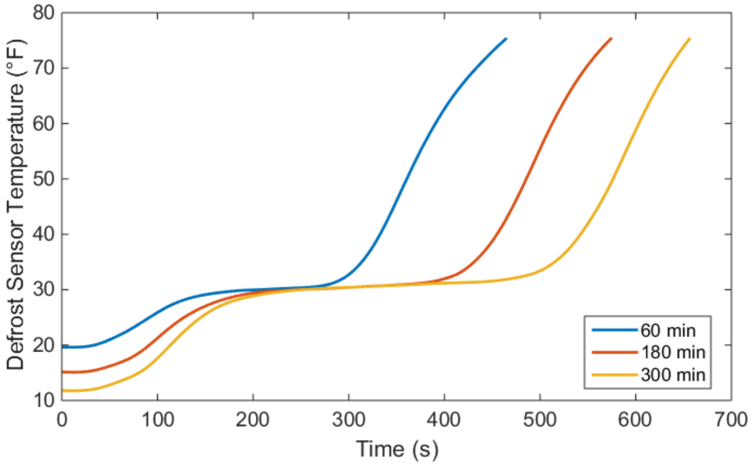

Figure 8-44 Defrost sensor temperature.

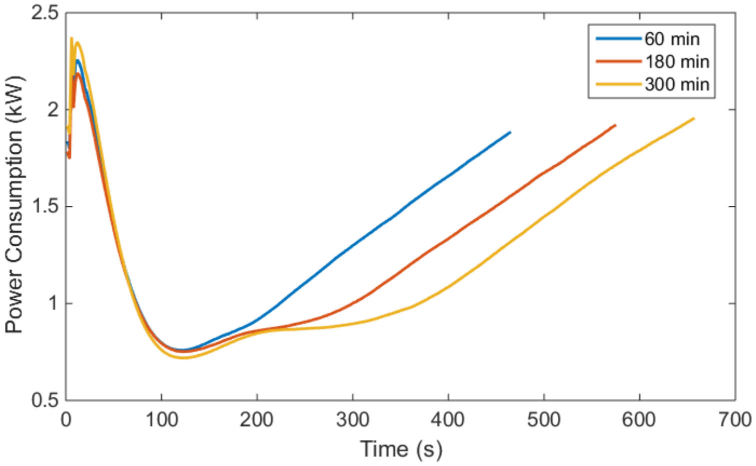

Figure 8-45 Power consumption.

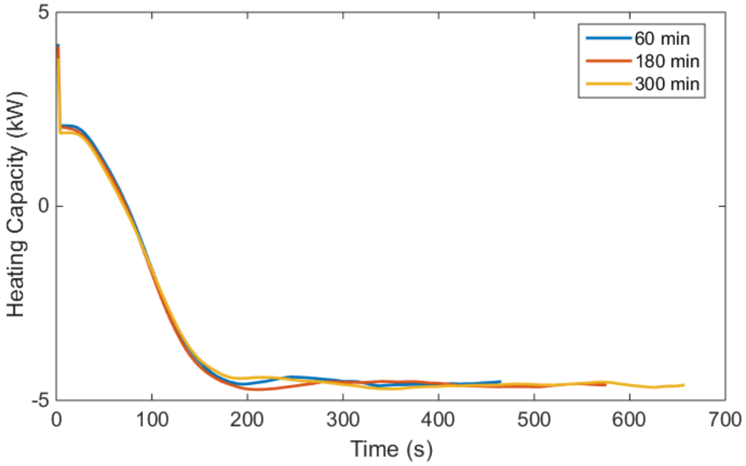

Figure 8-46 Heating capacity.

Optimized results are shown in Figure 8-47 and Figure 8-48. When only system efficiency is considered, the cost function reaches the minimum value when t_{fr} is around 45 minutes and T_{dfr} is around 32°F. When both system efficiency and human comfort are considered, the cost function reaches the minimum value when t_{fr} is around 145 to 150 minutes and T_{dfr} is around 32°F.

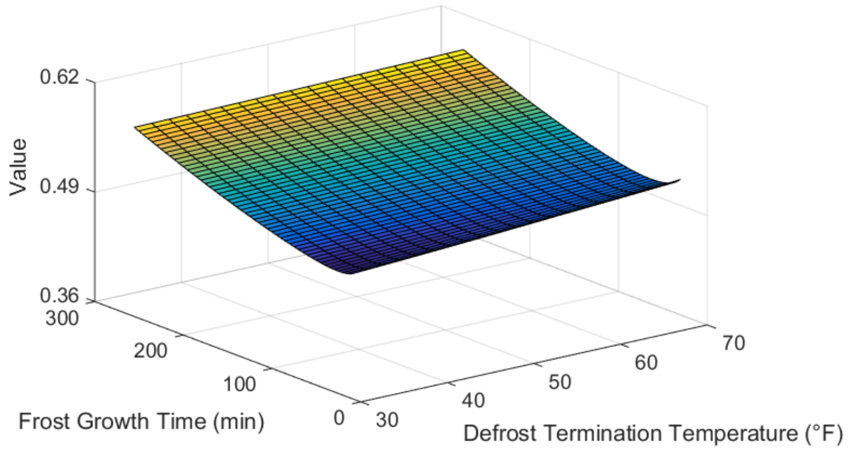

Figure 8-47 Value of the cost function without heat compensation.

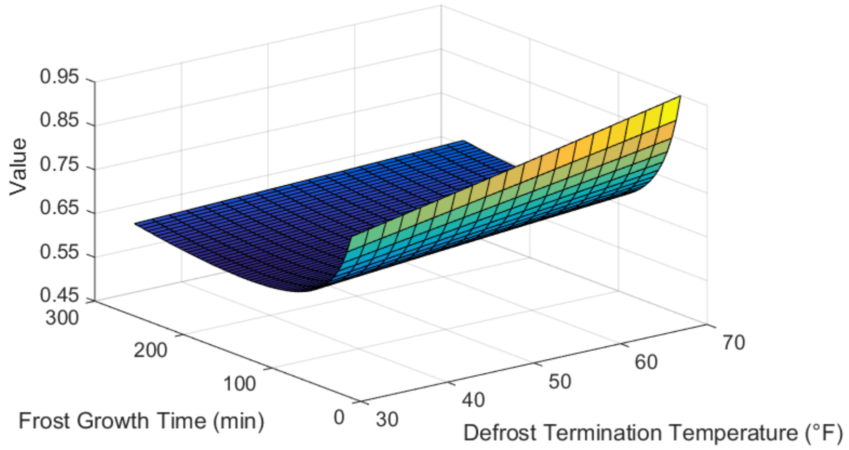

Figure 8-48 Value of the cost function with heat compensation.

9. CONCLUSIONS AND FUTURE WORK

Summary of Research Contributions

This dissertation presents dynamic modeling, control design, and validation for heat pump systems. The primary contributions include (1) the development of control-oriented heat pump model in cooling, heating, and defrosting modes; (2) control algorithm design and validation for heat pump systems; (3) intelligent defrosting control for maximizing both system performance and human comfort during defrosting cycles.

1) Dynamic modeling for heat pump systems

Heat pump systems include compressors, expansion valves, heat exchangers, fans, pipes, and vessels. A dynamic model is developed by combining the above component models. Step responses of compressor speed, valve opening, air temperature, and air flow rate show the system verification.

A defrost model is developed to study the dynamics during defrosting cycles. A complete defrost cycle is divided into four steps: frost growth stage, switching, defrosting stage, and switching back. A submodel of each stage is developed based on energy and mass conservation. Simulation results show that frost growth leads to higher pressure drop and less air flow rate. Both pressure difference and defrost sensor temperature decrease slowly during the frost growth stage. During the defrosting stage, defrost sensor temperature increases quickly.

A GUI is developed for parameter specification, system configuration, and outputs visualization. The GUI can generate steady-state operating conditions by solving an optimization problem based on user inputs. The operating conditions can be used for both steady state performance analysis and dynamic modeling.

2) Control algorithm design and validation

Energy optimal efficiency control is designed and validated based on a 3-ton heat pump system. Pseudo-steady state data show that COP can be maximized by optimizing fan speed or pressure for a given cooling or heating capacity. The optimal fan speed schedule and optimal pressure schedule are used to provide the optimal setpoints for controllers. Three different algorithms are SISO control with fan scheduling, multi-SISO control, and MIMO control. Validation results show that both SISO and MIMO control are effective for heat pump systems.

3) Intelligent defrost control

Intelligent defrost control is used to maximize both system efficiency and human comfort during defrosting cycles. Experimental tests are carried out based on a 3-ton heat pump system with an ambient temperature control and moisture generation system. The effects of frost growth time and defrost termination temperature on system performance are studied. During the frost growth stage, heating capacity drops gradually because of frost accumulation on the surface of the OD unit. During the defrosting stage, the system provides cooling capacity and, thus, causes significant human discomfort. A higher defrost termination temperature does not bring extra benefits during the frost growth stage. Experimental results show that there exists an optimal combination of frost growth time and defrost termination temperature. The optimal combination is affected by operating conditions, including moisture rate and ambient temperature. Higher moisture rate or lower ambient temperature indicates that the optimal frost growth time is more sensitive.

Future Research

Defrosting Model Modification and Defrost Control Design

Switching between heating and cooling modes is a big challenge for dynamic modeling. The switching model assumes that the refrigerant quality after switching is uniform in heat exchangers. A more accurate switching model focusing on dynamics in each control volume can be developed.

Experimental results have proved that there exists an optimal combination of frost growth time and defrost termination temperature. There are two possible ways to design the controller. One is to find the relationship between the optimal combination and the ambient temperature, relative humidity, and heating capacity setpoint based on more experimental data. The relationship can be used as the optimal scheduling for frost growth time and defrost termination temperature. The other is to find one parameter that corresponds to the optimal combination of frost growth time and defrost termination temperature. Iterative learning control could be used to design the defrost controller.

Integration of Heat Pump Systems and House Models

The heat pump model with control algorithm has been developed and validated. The heat pump model can be integrated with a house model. The first step is to develop a dynamic model including both the heat pump model and the house model. One potential problem could be the different time scales because the time scale of the heat pump model is much smaller than that of the house model. The second step is control design and validation for a real house with heat pump systems. Room temperature and humidity control are used as supervisory controls and provide setpoints for the local control developed in this dissertation.

REFERENCES

[1] U.S. Energy Information Administration, "Annual Energy Outlook 2014," 2014.

[2] Eisenhower, B. and Runolfsson, T., "System level modeling of a transcritical vapor compression system for bistability analysis," *Nonlinear Dynamics,* vol. 55, pp. 13-30, 2009.

[3] Eldredge, B. D., Rasmussen, B. P., and Alleyne, A. G., "Moving-boundary heat exchanger models with variable outlet phase," *Journal of Dynamic Systems, Measurement, and Control,* vol. 130, pp. 061003–061012, 2008.

[4] Higuchi, K. and Hayano, M., "Dynamic characteristics of thermostatic expansion valves," *International Journal of Refrigeration,* vol. 5, pp. 216-220, 1982.

[5] Yasuda, H., Touber, S., and Machielsen, C. H. M., "Simulation model of a vapor compression refrigeration system," *ASHRAE Transactions,* vol. 89, pp. 408–425, 1983.

[6] Mulay, V., A. Kulkarni, Agonafer, D., and Schmidt, R., "Effect of the location and the properties of thermostatic expansion valve sensor bulb on the stability of a refrigeration system," *Journal of Heat Transfer,* vol. 127, pp. 85-94, 2005.

[7] Rasmussen, B. P., "Dynamic modeling for vapor compression systems—Part I: Literature review," *HVAC&R Research,* vol. 18, pp. 934–955, 2012.

[8] Rasmussen, B. P. and Shenoy, B., "Dynamic modeling for vapor compression systems—Part II: Simulation tutorial," *HVAC&R Research,* vol. 18, pp. 956-973, 2012.

[9] McKinley, T. L. and Alleyne, A. G., "An advanced nonlinear switched heat exchangermodel for vapor compression cycles using the moving-boundary method," *International Journal of Refrigeration,* vol. 31, pp. 1253-1264, 2008.

[10] Zhang, W.-J. and Zhang, C.-L., "A generalized movingboundary model for transient simulation of dry-expansion evaporators under larger disturbances," *International Journal of Refrigeration,* vol. 29, pp. 1119-1127, 2006.

[11] Kumar, M., Kar, I. N., and Ray, A., "State space based modeling and performance evaluation of an air-conditioning system," *HVAC&R Research,* vol. 14, pp. 797-816, 2008.

[12] Rasmussen, B. P. and Alleyne, A., "Control-oriented modeling of transcritical vapor compression systems," *ASME Journal of Dynamic Systems, Measurement, and Control,* vol. 126, pp. 54-64, 2004.

[13] Jensen, J. M. and Tummescheit, H., "Moving boundary models for dynamic simulations of two-phase flows," in *Proceedings of the Second International Modelica Conference*, ed. Oberpfaffenhofen, Germany, 2002, pp. 235-244.

[14] Grald, E. W. and MacArthur, J. W., "A Moving-Boundary Formulation for Modeling Time-Dependent Two-Phase Flows," *International Journal of Heat & Fluid Flow,* vol. 13, pp. 266-272, 1992.

[15] Li, B. and Alleyne, A. G., "A dynamic model of a vapor compression cycle with shut-down and start-up operations," *International Journal of Refrigeration,* vol. 33, pp. 538-552, 2010.

[16] Bendapudia, S., Braunb, J. E., and Grollb, E. A., "A comparison of moving-boundary and finite-volume formulations for transients in centrifugal chillers," *international Journal of Refrigeration*, vol. 31, pp. 1437-1452, 2008.

[17] Mithraratne, P. and Wijeysundera, N. E., "An experimental and numerical study of the dynamic behaviour of a counter-flow evaporator," *International Journal of Refrigeration*, vol. 24, pp. 554-565, 2001.

[18] Koury, R. N. N., Machado, L., and Ismail, K. A. R., "Numerical simulation of a variable speed refrigeration system," *International Journal of Refrigeration*, vol. 24, pp. 192-200, 2001.

[19] Kim, M., Kim, M. S., and Chung, J. D., "Transient thermal behavior of a water heater system driven by a heat pump," *International Journal of Refrigeration*, vol. 27, pp. 415-421, 2004.

[20] Tso, C. P., Cheng, Y. C., and Lai, A. C. K., "Dynamic behavior of a direct expansion evaporator under frosting condition. PartI. Distributed model," *International Journal of Refrigeration*, vol. 29, pp. 611-623, 2006a.

[21] Tso, C. P., Cheng, Y. C., and Lai, A. C. K., "Dynamic behavior of a direct expansion evaporator under frosting condition. Part II. Field investigation on a shipping container," *International Journal of Refrigeration*, vol. 29, pp. 624-631, 2006b.

[22] Zhou, X., "Dynamic Modeling of Chilled Water Cooling Coils," PhD, Department of Mechanical Engineering, Purdue University, 2005.

[23] Liang, S., "Dynamic Modeling and Wavelet-Based Multi-Parametric Tuning and Validation for HVAC Systems," Ph.D., Mechanical Engineering, Texas A&M University, 2014.

[24] Wang, Y.-W., Cai, W.-J., Soh, Y.-C., Li, S.-J., Lu, L., and Xie, L., "A simplified modeling of cooling coils for control and optimization of HVAC systems," *Energy Conversion and Management,* vol. 45, pp. 2915-2930, 2004.

[25] Byun, J.-S., Lee, J., and Jeon, C.-D., "Frost retardation of an air-source heat pump by the hot gas bypass method," *international Journal of Refrigeration,* vol. 31, pp. 328-334, 2008.

[26] Guo, X.-M., Chen, Y.-G., Wang, W.-H., and Chen, C.-Z., "Experimental study on frost growth and dynamic performance of air source heat pump system," *Applied Thermal Engineering,* vol. 28, pp. 2267-2278, 2008.

[27] Kondepudi, S. N. and O'Neal, D. L., "Frosting performance of tube fin heat exchangers with wavy and corrugated fins," *Experimental Thermal and Fluid Science,* vol. 4, pp. 613-618, 1991.

[28] Vocale, P., Morini, G. L., and Spig, M., "Influence of outdoor air conditions on the air source heat pumps performance," *Energy Procedia,* vol. 45, pp. 653 – 662, 2014.

[29] Sami, S. M. and Duong, T., "Mass and heat transfer during frost growth," *ASHRAE Transactions* vol. 95, pp. 158-65, 1989.

[30] Sherif, S. A., Raju, S. P., Padki, M. M., and Chan, A. B., "A semi-empirical transient method for modelling frost formation on a flat plate," *International Journal of Refrigeration,* vol. 16, pp. 321-29, 1993.

[31] Kondepudi, S. N. and O'Neal, D. L., "Performance of fin-tube heat exchangers under frosting condition (part I): simulation model," *International Journal of Refrigeration,* vol. 16, pp. 175-180, 1993.

[32] Yao, Y., Jiang, Y. Q., Deng, S. M., and Ma, Z. L., "A study on the performance of the airside heat exchanger under frosting in an air source heat pump water heater/chiller unit," *International Journal of Heat and Mass Transfer,* vol. 47, p. 12, 2004.

[33] Seker, D., Karatasa, H., and Egricanb, N., "Frost formation on fin-and-tube heat exchangers. Part I—Modeling of frost formation on fin-and-tube heat exchangers," *International Journal of Refrigeration,* vol. 27, pp. 367-74, 2004.

[34] Chen, H., Thomas, L., and Besant, R. W., "Modeling frost characteristics on heat exchanger fins: Part I, numerical model," *ASHRAE Transactions,* vol. 106, pp. 357-67, 2000.

[35] Tso, C. P., Cheng, Y. C., and Lai, A. C. K., "An improved model for predicting performance of finned tube heat exchanger under frosting condition,with frost thickness variation along fin," *Applied Thermal Engineering,* vol. 26, pp. 111-20, 2006.

[36] Padhmanabhan, S. K., Fisher, D. E., Cremaschi, L., and Moallem, E., "Modeling non-uniform frost growth on a fin-and-tube heat exchanger," *International Journal of Refrigeration,* vol. 34, pp. 2018-30, 2011.

[37] Krakow, K. I., Yan, L., and Lin, S., "A model of hot gas defrosting of evaporators--Part 1: heat and mass transfer theory," *ASHRAE Transactions,* vol. 98, pp. 3585-461, 1992.

[38] Dopazo, J. A., Fernandez-Seara, J., Uhı´a, F. J., and Diz, R., "Modeling and experimental validation of the hot-gas defrost process of an air-cooled evaporator," *International Journal of Refrigeration,* vol. 33, pp. 829-839, 2010.

[39] Qu, M., Pan, D., Xia, L., Deng, S., and Jiang, Y., "A study of the reverse cycle defrosting performance on a multi-circuit outdoor coil unit in an air source heat pump – Part II: Modeling analysis," *Applied Energy,* vol. 91, pp. 274–280, 2012.

[40] Hoffenbecker, N., Klein, S. A., and Reindl, D. T., "Hot gas defrost model development and validation," *International Journal of Refrigeration,* vol. 28, pp. 605-615, 2005.

[41] Rasmussen, B. P., "Dynamic Modeling and Advanced Control of Air Conditioning and Refrigeration Systems," Phd, Dept. of Mechanical Engineering, University of Illinois at Urbana-Champaign, 2005.

[42] Keir, M. C., "Dynamic modeling, control, and fault detection in vapor compression systems," MS thesis, University of Illinois at Urbana-Champaign, USA, 2006.

[43] Lin, J.-L. and Yeh, T.-J., "Modeling, identification and control of air-conditioning systems," *International Journal of Refrigeration,* vol. 30, pp. 209-220, 2007.

[44] Shah, R., Rasmussen, B. P., and Alleyne, A. G., "Application of a multivariable adaptive control strategy to automotive air conditioning systems," *International Journal of Adaptive Control and Signal Process,* vol. 18, pp. 199-221, 2004.

[45] Yeh, T.-J., Chen, Y.-J., Hwang, W.-Y., and Lin, J.-L., "Incorporating fan control into air-conditioning systems to improve energy efficiency and transient response," *Applied Thermal Engineering,* vol. 29, pp. 1955–1964, 2009.

[46] He, X., Liu, S., and Asada, H., "Modeling of Vapor Compression Cycles for Advanced Controls in HVAC systems," *Journal of Dynamic Systems, Measurement, and Control,* vol. 119, pp. 183-191, 1997.

[47] Outtagarts, A., Haberschill, P., and Lallemand, M., "Transient Response of an Evaporator Fed Through an Electronic Expansion Valve," *International Journal of Energy Research,* vol. 21, pp. 793-807, 1997.

[48] Finn, D. P. and Doyle, C. J., "Control and Optimization Issues Associated with Algorithm-Controlled Refrigerant Throttling Devices," *ASHRAE Transactions,* vol. 106, pp. 524-533, 2000.

[49] Elliott, M., Bolding, B., Walton, Z., and Rasmussen, B. P., "Superheat Control: A Hybrid Approach," *HVAC&R Research,* vol. 15, pp. 1021-1044, Nov. 2009 2009.

[50] Elliott, M. S. and Rasmussen, B. P., "On reducing evaporator superheat nonlinearity with control architecture," *International Journal of Refrigeration,* vol. 33, pp. 607–614, 2010.

[51] Leducq, D., Guilpart, J., and Trystam, G., "Non-linear predictive control of a vapour compression cycle," *International Journal of Refrigeration,* vol. 29, pp. 761-772, 2006.

[52] Beghi, A. and Cecchinato, L., "A simulation environment for dry-expansion evaporators with application to the design of autotuning control algorithms for electronic expansion valves," *International Journal of Refrigeration,* vol. 32, pp. 1765-1775, 2009.

[53] Fallahsohi, H., Changenet, C., Place, S., Ligeret, C., and Lin-Shi, X., "Predictive functional control of an expansion valve for minimizing the superheat of an evaporator," *International Journal of Refrigeration,* vol. 33, pp. 409-418, March 2010.

[54] Elliott, M. S., Estrada, C., and Rasmussen, B. P., "Cascaded superheat control with a multiple evaporator refrigeration system," in *American Control Conference*, San Francisco, CA, 2011.

[55] Keir, M. C. and Alleyne, A. G., "Feedback Structures for Vapor Compression Cycle Systems " in *American Control Conference*, New York City, USA, 2007, pp. 5052-5058.

[56] Jain, N. and Alleyne, A. G., "Comparison of SISO and MIMO Control Techniques for a Diagonally Dominant Vapor Compression System," presented

at the American Control Conference, Hyatt Regency Riverfront, St. Louis, MO, USA, 2009.

[57] Jain, N., Li, B., Keir, M., Hencey, B., and Alleyne, A., "Decentralized Feedback Structures of a Vapor Compression Cycle System," *IEEE TRANSACTIONS ON CONTROL SYSTEMS TECHNOLOGY*, vol. 18, pp. 185-193, 2010.

[58] Qureshi, T. Q. and Tassou, S. A., "Variable-Speed Capacity Control in Refrigeration Systems," *Applied Thermal Engineering*, vol. 16, pp. 103-13, 1996.

[59] Choi, J., Kim, Y., and Ha, J., "Experimental study on superheat control of a variable speed heat pump," *Korean Journal of Air-Conditioning and Refrigeration Engineering*, vol. 16, pp. 167-174, 2001.

[60] Larsen, L. S. and Thybo, C., "Potential energy savings in refrigeration systems using optimal set-points," in *IEEE International Conference on Control Applications*, 2004, pp. 701-704.

[61] Qi, Q. and Deng, S., "Multivariable control-oriented modeling of a direct expansion (DX) air conditioning (A/C) system," *International Journal of Refrigeration*, vol. 31, pp. 841-849, 2008.

[62] Elliott, M. S. and Rasmussen, B. P., "Decentralized Model Predictive Control of a Multi-Evaporator Air Conditioning System," *Control Engineering Practice*, vol. 21, pp. 1665-1667, 2013.

[63] Rasmussen, B. P., "Dynamic Modeling and Advanced Control of Air Conditioning and Refrigeration Systems," Ph.D., Dept. of Mechanical Engineering, University of Illinois at Urbana-Champaign, 2005.

[64] Anderson, M., Buehner, M., Young, P., Hittle, D., Anderson, C., Tu, J., *et al.*, "MIMO robust control for hvac systems," *IEEE Transactions on Control Systems Technology,* vol. 16, pp. 475-483, 2008.

[65] Elliott, M. S. and Rasmussen, B. P., "Decentralized Model Predictive Control of a Multi-Evaporator Air Conditioning System," *Control Engineering Practice,* vol. 21, pp. 1665-1667, 2013.

[66] Elliott, M. S., "Distributed control of HVAC&R networks," Ph.D., Texas A&M University, 2013.

[67] He, X.-D., Liu, S., Asada, H. H., and Itoh, H., "Multivariable Control of Vapor Compression Systems," *HVAC&R RESEARCH*, vol. 4, pp. 205-230, 1998.

[68] Schurt, L. C., Hermes, C. J. L., and Neto, A. T., "A model-driven multivariable controller for vapor compression refrigeration systems," *international Journal of Refrigeration,* vol. 32, pp. 1672-1682, 2009.

[69] Qi, Q. and Deng, S., "Multivariable control-oriented modeling of a direct expansion (DX) air conditioning (A/C) system," *International Journal of Refrigeration,* vol. 31, pp. 841-849, 2008.

[70] Song, M. J., Deng, S. M., Pan, D. M., and Mao, N., "An experimental study on the effects of downwards flowing of melted frost over a vertical multi-circuit outdoor coil in an air source heat pump on defrosting performance during reverse cycle defrosting," *Applied Thermal Engineering,* vol. 67, pp. 258-265, 2014.

[71] Song, M., Chen, A., and Mao, N., "An experimental study on defrosting performance of an air source heat pump unit with a multi-circuit outdoor coil at

different frosting evenness values," *Applied Thermal Engineering,* vol. 94, pp. 331–340, 2016.

[72] Ding, Y., Ma, G., Chai, Q., and Jiang, Y., "Experiment investigation of reverse cycle defrosting methods on air source heat pump with TXV as the throttle regulator," *International Journal of Refrigeration*, vol. 27, pp. 671-678, 2004.

[73] Qu, M., Xia, L., Deng, S., and Jiang, Y., "A study of the reverse cycle defrosting performance on a multi-circuit outdoor coil unit in an air source heat pump – Part I: Experiments," *Applied Energy* vol. 91, pp. 122-129, 2012.

[74] Krakow, K. I., Yan, L., and Lin, S., "Model of hot-gas defrosting of evaporators-Part 1: heat and mass transfer theory," *ASHRAE Trans*, vol. 98, pp. 451-461, 1991.

[75] Bansal, P., Fothergill, D., and Fernandes, R., "Thermal analysis of the defrost cycle in a domestic freezer," *international Journal of Refrigeration,* pp. 589-599, 2010.

[76] Melo, C., Knabben, F. T., and Pereira, P. V., "An experimental study on defrost heaters applied to frost-free household refrigerators," *Applied Thermal Engineering,* pp. 239-245, 2013.

[77] Yin, H. J., Yang, Z., Chen, A. Q., and Zhang, N., "Experimental research on a novel cold storage defrost method based on air bypass circulation and electric heater," *Energy,* vol. 37, pp. 623-631, 2012.

[78] Liang, C.-H., Zhang, X.-S., Li, X.-W., and Chen, Z.-Q., "Control strategy and experimental study on a novel defrosting method for air-source heat pump," *Applied Thermal Engineering* vol. 30, pp. 892–899, 2010.

[79] Ameen, F. R., Coney, J. E. R., and Sheppard, C. G. W., "Experimental study of warm-air defrosting of heat-pump evaporators," *International Journal of Refrigeration,* vol. 16, pp. 13-18, 1993.

[80] Steiner, A. and Rieberer, R., "Simulation based identification of the ideal defrost start time for a heat pump system for electric vehicles," *international Journal of Refrigeration,* vol. 57, pp. 87-93, 2015.

[81] Zakrzewski, B., "Optimal defrost cycle for the air cooler," *International Journal of Refrigeration,* vol. 7, pp. 41-45, 1984.

[82] Fanger, P. O., *Thermal comfort*: Copenhagen: Danish Technical Press, 1970.

[83] Fanger, P. O., *Thermal comfort*. Malabar, FL.: Robert E. Krieger Publishing Company, 1982.

[84] Qu, M., Xia, L., Deng, S., and Jiang, Y., "Improved indoor thermal comfort during defrost with a novel reverse-cycle defrosting method for air source heat pumps," *Building and Environment,* vol. 11, pp. 2354-2361, 2010.

[85] Yao, Y., Jiang, Y., Deng, S., and Ma, Z., "A study on the performance of the airside heat exchanger under frosting in an air source heat pump water heater/chiller unit," *International Journal of Heat and Mass Transfer,* vol. 47, pp. 3745-3756, 2004.

[86] Vocale, P., Morini, G. L., and Spiga, M., "Influence of Outdoor Air Conditions on the Air Source Heat Pumps Performance," *Energy Procedia,* vol. 45, pp. 653-662, 2014.

[87] Muller, E. D., "A new concept for defrosting refrigeration plants," *Kalte,* vol. 28, pp. 52-54, 1975.

[88] Jiang, Y., Dong, J., Qu, M., Deng, S., and Yao, Y., "A novel defrosting control method based on the degree of refrigerant superheat for air source heat pumps," *International Journal of Refrigeration,* vol. 36, pp. 2227-2288, 2013.

[89] Xiao, J., Wang, W., Zhao, Y. H., and Zhang, F. R., "An analysis of the feasibility and characteristics of photoelectric technique applied in defrost-control," *International Journal of Refrigeration,* vol. 32, pp. 1350-1357, 2009.

[90] Liu, Z. L., Wang, H. Y., Zhang, X. H., Meng, S., and Ma, C. F., "An experimental study on minimizing frost deposition on a cold surface under natural convection conditions by use of a novel anti-frosting paint. Part I. Anti-frosting performance and comparison with the uncoated metallic surface," *International Journal of Refrigeration,* vol. 29, pp. 229-236, 2006.

[91] Ozkan, D. B. and Ozil, E., "Experimental study on the effect of frost parameters on domestic refrigerator finned tube evaporator coils," *Applied Thermal Engineering,* vol. 26, pp. 2490-2493, 2006.

[92] Na, B. and Webb, R. L., "New model for frost growth rate," *International Journal of Heat Mass Transfer,* vol. 47, pp. 925-936, 2004.

[93] Lee, J., Byun, J. S., Jeon, C. D., and Jung, J. H., "The application of photo-coupler for frost detecting in an air-source heat pump," *International Journal of Refrigeration,* vol. 29, pp. 191-198, 2006.

[94] Buick, T. R., Mcmullan, J. T., Morgan, R., and Murry, R. B., "Ice detection in heat pumps and coolers," *International Journal of Energy Research,* pp. 85-98, 1978.

[95] Baxter, V. D. and Mogers, J. C., "Field-measured cycling, frosting and defrosting losses for a high-efficiency air-source heat pump," *ASHRAE Transactions 91,* pp. 537-554, 1985.

[96] Wang, W., Xiao, J., Guo, Q. C., Lu, W. P., and Feng, Y. C., "Field test investigation of the characteristics for the air source heat pump under two typical mal-defrost phenomena," *Applied Energy,* vol. 88, pp. 4470-4480, 2011.

[97] Zhu, J., Sun, Y., Wang, W., Ge, Y., and Liu, L. L. J., "A novel Temperature–Humidity–Time defrosting control method based on a frosting map for air-source heat pumps," *International Journal of Refrigeration,* vol. 54, pp. 45-54, 2015.

[98] Zhu, J. H., Sun, Y. Y., Wang, W., Deng, S. M., Ge, Y. J., and Li, L. T., "Developing a new frosting map to guide defrosting control for air source heat pump units," *Applied Thermal Engineering,* vol. 90, pp. 782-791, 2015.

[99] Wattlet, J. P., J.C.Chato, and Christoffersen, B. R., "Heat Transfer Flow Regimes of Refrigerants in a Horizontal-Tube Evaporator," *ACRC Technical Report 55 and ACRC Technical Report 2*.

[100] Dobson, M. K. and Chato, J. C., "Condensation in smooth horizontal tubes," *Journal of Heat Transfer-Transactions of the Asme,* vol. 120, pp. 193-213, 1976.

[101] Gnielinski, V., "New equation for heat and mass transfer in turbulent pipe and channel flow," *International Chemical Engineering Science,* vol. 16, pp. 359-368, 1976.

[102] Kays, W. M. and London, A. L., *Compact Heat Exchangers*, 3 ed.: Krieger Pub Co, 1998.

[103] Cengel, Y. A. and Boles, M. A., *Thermodynamics. An Engineering Approach*, 7 ed.: McGraw-Hill Higher Education, 2010.

[104] Incropera, F. P. and Dewitt, D. P., *Fundamentals of Heat Transfer*, Second ed.: John Wiley and Sons, 1985.

[105] Lemmon, E. W., Huber, M. L., and McLinden, M. O., "NIST Reference Fluid Thermodynamic and Transport Properties—REFPROP," NIST2013.

[106] O'Neal, D. L., "The effect of frost formation on the performance of a parallel plate heat exchanger," Doctor of Philosophy, Mechanical Engineering, Purdue University, 1982.

[107] Eckert, E. R. and Drake, R. M., *Analysis of heat and mass transfer*. New York: McGraw-Hill, 1972.

[108] Yonko, J. D. and Sepsy, C. F., "An investigation of the thermal conductivity of frost while forming on a flat horizontal plate," *ASHRAE Transactions,* vol. 73, pp. I.1.1-I.1.11, 1967.

[109] Chen, H., Thomas, L., and Besant, R. W., "Fan supplied heat exchanger fin performance under frosting conditions," *International Journal of Refrigeration*, vol. 26, pp. 140-149, 2003.